



Investigation of micro and nano structured materials for acoustic band gaps engineering in electro-acoustic devices

Yu Du

► **To cite this version:**

Yu Du. Investigation of micro and nano structured materials for acoustic band gaps engineering in electro-acoustic devices. Micro and nanotechnologies/Microelectronics. Ecole Centrale de Lille, 2015. English. <NNT : 2015ECLI0020>. <tel-01284060>

HAL Id: tel-01284060

<https://tel.archives-ouvertes.fr/tel-01284060>

Submitted on 7 Mar 2016

HAL is a multi-disciplinary open access archive for the deposit and dissemination of scientific research documents, whether they are published or not. The documents may come from teaching and research institutions in France or abroad, or from public or private research centers.

L'archive ouverte pluridisciplinaire **HAL**, est destinée au dépôt et à la diffusion de documents scientifiques de niveau recherche, publiés ou non, émanant des établissements d'enseignement et de recherche français ou étrangers, des laboratoires publics ou privés.

Numéro d'ordre: 277

ÉCOLE CENTRALE DE LILLE THESE

Présenté en vue d'obtenir le grade de

DOCTEUR

En

**Spécialité: Micro et Nanotechnologies, Acoustique et
Télécommunications**

Par

Yu DU

DOCTORAT DELIVRE PAR L'ÉCOLE CENTRALE DE LILLE

Titre de la thèse:

**Etude et développement de matériaux micro/nano structurés
pour l'ingénierie des bandes interdites dans les dispositifs
électro-acoustiques à ondes de surface**

Soutenance prévue le 5 Octobre 2015 devant le jury d'examen:

Président	M. Bahram DJAFARI-ROUHANI	Professeur à l'Université de Lille 1, IEMN
Rapporteur	M. Bruno MORVAN	Professeur à l'Université du Havre, LOMC
Rapporteur	M. Badreddine M. ASSOUAR	Chargé de Recherche CNRS, IJL, l'Université de Lorraine
Examineur	M. Bernard BONELLO	Directeur de Recherche CNRS, INP, l'Université Pierre et Marie Curie
Examineur	Mme. Ouarda LEGRANI	Maître de Conférences à Centrale-Supélec Campus de Metz
Examineur	M. Olivier BOU MATAR	Professeur à l'Ecole Centrale de Lille, IEMN
Directeur de thèse	M. Philippe PERNOD	Professeur à l'Ecole Centrale de Lille, IEMN
Co-directeur de thèse	M. Abdelkrim TALBI	Maître de Conférences à l'Ecole Centrale de Lille, IEMN
Co-directeur de thèse	M. Vladimir PREOBRAZHENSKY	Professeur à l'Ecole Centrale de Lille, Directeur de Recherche, IPGASM, IEMN

Thèse préparée dans le Laboratoire International Associé LICs/LEMAC

Institut d'Electronique de Microélectronique et de Nanotechnologies

(IEMN, UMR CNRS 8520, France)

Ecole Doctorale SPI 072 (Lille I, Lille III, Artois, ULCO, UVHC, EC Lille)

PRES Université Lille Nord de France

Contents

Contents	3
Acknowledgements	6
List of Abbreviations	7
List of Tables	8
List of Figures	9
Résumé en français	14
Introduction	14
Analyse par la méthode des éléments finis des structures de bandes d'un matériau micro-structuré.....	15
Design, fabrication et caractérisation de réseaux de micro-plot sur la surface du LiNbO ₃	18
Conclusion et perspectives	20
Introduction	22
Chapter 1: State of the art	26
1.1 Historical context.....	26
1.2 Existing technologies.....	29
1.2.1 Simulation methods.....	29
1.2.2 Experimental study for microfabricated phononic crystals	30
1.3 Application of phononic crystals	37
1.3.1 Acoustic insulators	38
1.3.2 Acoustic diodes	40
1.3.3 Phononic crystal waveguides, cavities and filters	41
1.3.4 Thermal metamaterials and heat management	42
1.4 Motivation	44
Chapter 2: Theoretical foundations of phononic crystals	49
2.1 Elasticity	49
2.1.1 Generalized Hooke's Law	49

2.1.2 Basic equations of elastodynamics.....	51
2.2 Surface acoustic waves on piezoelectric substrates	52
2.2.1 Plane waves.....	53
2.2.2 Surface acoustic waves	55
2.2.3 Rayleigh waves on LiNbO ₃ substrate with different cut directions	56
2.2.4 Piezoelectric consideration.....	58
2.2.5 Boundary conditions	60
2.3 Lattice and band theory	61
2.3.1 Lattice	61
2.3.2 Bloch Theorem.....	63
2.3.3 Band structures.....	65
2.4 PnC band gap mechanisms and properties	67
2.4.1 Bragg scattering	68
2.4.2 Local resonance.....	69
2.5 Conclusion.....	72
Chapter 3: Modeling of phononic crystals by the finite element method.....	73
3.1 Principles of finite element method	73
3.2 Modeling of band structures	74
3.3 Evidence of band gaps in pillar-based PnCs.....	79
3.4 Effect of pillar's geometry.....	82
3.4.1 Effect of pillar's height	82
3.4.2 Effect of pillar's radius	85
3.4.3 Evolution of polarization by varying geometrical parameters	88
3.5 Effect of anisotropy	91
3.6 Material consideration	97
3.7 Temperature coefficients of frequency for surface modes.....	99
3.8 Calculation of transmission spectrum.....	102
3.8.1 Pillar-based PnCs with a square lattice on a Y128-X LiNbO ₃ substrate.....	104
3.8.2 Pillar-based PnCs with triangular lattices on a Y-Z LiNbO ₃ substrate	106
3.8.3 Discussion about Young's Modulus	107

3.9 Conclusion.....	108
Chapter 4: Design, fabrication and characterization of pillar-based phononic crystals	110
4.1 Selection of materials	110
4.2 Device design	111
4.3 Fabrication of IDTs and PnCs	114
4.3.1 Substrate cleaning	115
4.3.2 Patterning by photolithography	116
4.3.3 Metallic deposition.....	123
4.3.4 Plasma-Enhanced Chemical Vapor Deposition (PECVD).....	124
4.3.5 Etching	125
4.3.6 Electroplating of Nickel pillars	127
4.3.7 Procedure	134
4.4 Characterization.....	137
4.4.1 PnCs morphology.....	137
4.4.2 Transmission spectrum measured by a vector network analyzer	139
4.5 Conclusion.....	148
Chapter 5: Ongoing work	149
5.1 Fabrication of 2D Si pillar-based phononic crystals.....	149
5.2 Self-assembly of magnetic nanoparticles	153
5.3 Fabrication of nickel nanowires by electroplating.....	155
5.4 Conclusion.....	157
Conclusion and Perspectives	158
Conclusion.....	158
Perspectives	159
Reference	160

Acknowledgements

This Ph-D work was carried out at the International Associated Laboratory on Nonlinear Magnetoacoustics of the Condensed matter (LICS-LEMAC), group of the Institute of Electronics, Microelectronics and Nanotechnologies (IEMN, CNRS/UMR 8520, France), associated with Ecole Centrale de Lille.

First, I would like to thank my three thesis directors: Mr. Philippe PERNOD, professor of Ecole Centrale de Lille; Mr. Vladimir PREOBRAZHENSKY, professor of Ecole Centrale de Lille; Mr. Abdelkrim TALBI, assistant professor of Ecole Centrale de Lille. Thanks to them, I got the opportunity to do my Ph-D research work in their team for three years. I would like also thank to Mme Hongzhe TANG, associated professor of Ecole Centrale de Pékin, who proposed me this opportunity.

I am sincerely grateful to the members of the jury, who accepted to evaluate this work, especially to the two reporters who reviewed this manuscript.

I address the most sincere gratitude to Mr. Abdelkrim TALBI and Mr. Jean-Claude GERBEDOEN, who taught me and helped me a lot during the three years. Without your support or patience, it would be much more difficult to obtain all the achievements of today. I really appreciate your generous giving.

I want to also thank to all my colleagues, the professors, the engineers, as well as the secretaries. Thanks for their company and selfless help.

I acknowledge China Scholarship Council who gave me the financial support for 48 months, which provided me a good living condition in France.

At last but the most important gratitude should be addressed to my parents, my whole family and all of my friends who have supported me from the beginning to the end, who have shared my joys and sorrows, whom I have been loving forever.

List of Abbreviations

AAO	Anodic aluminum oxide
ABG	Acoustic band gap
BAW	Bulk acoustic wave
FDTD	Finite difference time domain
FEM	Finite element method
FSE	Fourier series expansion
IDT	Inter-digital transducer
MEMS	Micro-electro-mechanical system
MST	Multiple scattering theory
PECVD	Plasma-enhanced chemical vapor deposition
PtC	Photonic crystal
PnC	Phononic crystal
PWE	Plane wave expansion
RF	Radio frequency
RFID	Radio frequency identification
SAW	Surface acoustic wave
SEM	Scanning electron microscope
SFIT	Slanted finger inter-digital transducer
TCf	Temperature coefficient of frequency
TMM	Transfer matrix method
UHF	Ultra high frequency
VHF	Very high frequency
VNA	Vector network analyzer
VSM	Vibrating sample magnetometer

List of Tables

I. Band-structure-related properties of three periodic systems.....	23
2.1. Bravais lattices, reciprocal lattices, first Brillouin zones and irreducible Brillouin zones of the normal two-dimensional lattices.	64
2.2. Comparison of Bragg Scattering Phononic Crystals and Locally Resonant Phononic Crystals.	71
3.1. Periodic conditions for square, triangular-X, triangular-Y, hexagonal-X and hexagonal-Y lattice.	77
3.2. LiNbO ₃ Y128-X cut substrate material parameters.....	79
3.3. The frequency ranges and central frequencies of each band gap for square, triangular-X, triangular-Y, hexagonal-X and hexagonal-Y lattice symmetries.	81
3.4. Frequency ranges and central frequencies of the band gaps of PnCs with different lattice symmetries.	93
3.5. The density and Young's modulus for gold, diamond, nickel and LiNbO ₃	98
3.6. Elastic parameters of LiNbO ₃ Y128-X and Ni for T ₀ =300K.	100
3.7. Temperature coefficients of density, elastic constant and Young's Modulus of LiNbO ₃ Y128-X and Ni... ..	100
3.8. Elastic parameters of LiNbO ₃ Y128-X and Ni for T ₀ =340K.	100
3.9. Aluminum parameters related in the calculation of the transmission spectrum.	103
4.1. Composition of Watts solution.....	130
4.2. Operating conditions for the Watts solution.....	130
4.3. Typical mechanical properties of Watts nickel electrodeposits and wrought nickel.....	131

List of Figures

1. Des diagrammes de bande au sein de différents réseaux de symétries.....	15
2. Polarisation pour les deux premiers modes dans le cas du réseau carré triangulaire-X et triangulaire-Y.....	16
3. Les valeurs TCF sur la fonction de fréquences pour les deux premiers modes propres des plots au sein du réseau carré triangulaire-X et triangulaire-Y avec deux hauteurs 2,5 μm et 5 μm	17
4. Le diagramme de bande et le spectre de transmission calculés d'un CPn composé du réseau carré de plots cylindriques de nickel.....	18
5. Modèle du dispositif utilisé pour étudier la propagation des ondes acoustiques de surface dans un réseau périodique de plots sur un substrat semi-infini.....	19
6. Le processus de fabrication.....	19
7. Les spectres de transmission relative et des images de MEB pour des CPn.....	20
1.1. Kinematic sculpture by Eusebio Sempere used as the first demonstration of band gaps in phononic crystals.....	27
1.2. First locally resonant phononic crystal.....	28
1.3. Scanning electron micrograph pictures of a patterned glass surface.....	31
1.4. Schematic diagram and SEM pictures of air/Si phononic crystal and slanted finger inter-digital transducers.....	32
1.5. Top view and the cross section of the fabricated devices with the hexagonal lattice PC structure in the middle and the transducer electrodes on each side.....	33
1.6. A phononic crystal realized by etching square arrays of low-acoustic impedance air hole inclusions.....	33
1.7. Micro acoustic bandgap (ABG) slab composed of Al capped W rods in SiO ₂ matrix with integrated AlN electro-acoustic couplers.....	34
1.8. SEM picture of the hole structure of a phononic crystal.....	35
1.9. SEM pictures of the phononic crystal membrane with Au pillars deposited on the AlN/Mo/Si membrane.....	36
1.10. Schematic of the experimental setup used for investigating the propagation of surface phonons in a periodic arrays of nickel pillars on a semi-infinite substrate and a SEM picture of the phononic crystal.....	36
1.11. Applications according to the phononic spectrum.....	37
1.12. Phononic crystals applied for different working frequency ranges: (a) sound (kHz); (b) Ultrasound (MHz); (c) Hypersound (GHz); (d) Heat (THz).....	38
1.13. Photographs of the honeycomb structure (a) and the triangular structure (b) used for the attenuation of surface waves.....	39
1.14. Attenuation spectra of the honeycomb structure (a); the triangular structure (b).....	40

1.15. An acoustic diode made of nonlinear acoustic medium and a 1D PnC.....	41
1.16. SEM image of a W2 waveguide realized by removing two rows of tungsten scattering inclusions from a square lattice W/SiO ₂ phononic crystal plate.	42
1.17. Normalized transmission of the W2 waveguide device of a W/SiO ₂ PnC.	42
1.18. Thermal metamaterials. (a) a thermal shield; (b) a thermal concentrator; (c) a thermal inverter.....	43
1.19. Schematic description of the sample consisting of 20 uniaxial films of TbCo ₂ (5nm)/FeCo(5nm) deposited on a Y-cut LiNbO ₃ substrate and the associated coordinate system.....	44
1.20. Comparisons between the theoretical calculations (solid and dashed lines) and experimental results (points) for the wave velocity variation of Rayleigh waves (a) and shear horizontal waves (b) on function of the amplitude of the external magnetic field applied along the difficult axis.....	45
1.21. Diagram of the surface acoustic wave device used to calculate the transmission spectra through a phononic crystal composed of TbCo ₂ (5nm)/FeCo(5nm) pillars within square lattice deposited on a Y128-X LiNbO ₃ substrate between two inter-digital transducers.....	45
1.22. Variation of the lower frequency (solid line) and the upper frequency (dashed line) of the 7 th mode according to the amplitude of the external magnetic field.....	46
1.23. AFM pictures of 1D periodic oxide lines array on Ni film: (a) topography; (b) phase.	46
1.24. Frequency dependences of transmission function S ₂₁ for the structure with N=150 oxide lines, height h=3.5nm in the constant magnetic field (solid line) and without it (dashed line): period a=500nm (a) and for a=200nm (b).	47
1.25. Schematic description of the surface acoustic wave radio frequency identification in real proportions.	47
1.26. Comparison between the time response of fabricated RFID SAW tag (dashed line) and the calculated response for the case of thin aluminum film parameters (solid line).....	47
2.1. Illustration of P, SH, SV wave.	55
2.2. Rayleigh waves.	55
2.3. Schematic diagram of the piezoelectric wafers with Y128-X cut, Y-X cut and Y-Z cut.	57
2.4. z-dependence of displacement of a Rayleigh wave propagating on LiNbO ₃ Y128-X (a), Y-X (b) and Y-Z (c) cut substrates, where λ is the SAW wavelength and z=0 corresponds to the surface.	58
2.5. The polarization of a Rayleigh wave mode in three directions with the same phase on LiNbO ₃ Y128-X, Y-X and Y-Z cut substrates.	58
2.6. Structure of diatomic chain.	65
2.7. Vibration spectra for one-dimensional diatomic lattice.	67
2.8. Bragg's Law.	68
3.1. Discretization of a domain using triangular shape finite elements.....	74

3.2. Unit cells of square lattice (a), triangular-X lattice (b), triangular-Y lattice (c), hexagonal-X lattice (d), hexagonal-Y lattice (e).	76
3.3. Models of unit cells with mesh used in Comsol for square (a), triangular-X (b), triangular-Y (c), hexagonal-X (d), hexagonal-Y (e) lattice.	77
3.4. Band structures of a pillar-based PnC for square (a), triangular-X (b), triangular-Y (c), hexagonal-X (d), hexagonal-Y (e) lattice with nickel pillars and LiNbO ₃ Y128-X cut substrate. The geometrical parameters are as follows: $a = 9\mu\text{m}$, $r = 3\mu\text{m}$ and $h = 5\mu\text{m}$	80
3.5. The total displacement of the six surface modes at the Point K in the irreducible Brillouin zone corresponding to the band structures for square, triangular-X, triangular-Y, hexagonal-X and hexagonal-Y lattice.	82
3.6. Band structures of pillar-based PnCs for square (a and a'), triangular-X (b and b'), triangular-Y (c and c'), hexagonal-X (d and d'), hexagonal-Y (e and e') lattice with nickel pillars and LiNbO ₃ Y128-X cut substrate. The geometrical parameters are as follows: $a = 9\mu\text{m}$, $r = 3\mu\text{m}$ and $h = 2.5\mu\text{m}$ left or $5\mu\text{m}$ (right). ...	83
3.7. The evolution of eigenfrequencies of the first six acoustic at the boundary of irreducible Brillouin zone by varying pillar's height for PnC with square lattice and $a = 9\mu\text{m}$, $r = 3\mu\text{m}$	85
3.8. The polarization of pillars in square lattice with different heights for surface acoustic modes, $h=2.5\mu\text{m}$ and $h=5\mu\text{m}$ with $r=3\mu\text{m}$ and $a=9\mu\text{m}$	85
3.9. Band structures of pillar-based PnCs for square (a and a'), triangular-X (b and b'), triangular-Y (c and c'), hexagonal-X (d and d'), hexagonal-Y (e and e') lattice with nickel pillars and LiNbO ₃ Y128-X cut substrate. The geometrical parameters are as follows: $a = 9\mu\text{m}$, $h = 5\mu\text{m}$ and $r = 1.5\mu\text{m}$ left or $3\mu\text{m}$ (right). ...	86
3.10. The evolution of eigenfrequencies of the first six acoustic at the boundary of irreducible Brillouin zone by varying pillar's radius for PnC with square lattice and $a = 9\mu\text{m}$, $h = 5\mu\text{m}$	87
3.11. The polarization of pillars in square lattice with different radius for surface acoustic modes, $r=1.5\mu\text{m}$ and $r=3\mu\text{m}$ with $h=5\mu\text{m}$ and $a=9\mu\text{m}$	88
3.12. Schematic drawing of the study on the variation of polarization on function of the pillar's radius.	89
3.13. The evolution of pillar's polarization by varying radius (left) and heights (right) of pillars within square (a and d), triangular-X (b and e) and triangular-Y lattices (c and f).	90
3.14. Band structures of pillar-based PnCs for square (a), triangular-X (b), triangular-Y (c) lattices with nickel pillars and LiNbO ₃ Y128-X cut substrate. The geometrical parameters are as follows: $a = 9\mu\text{m}$, $h = 4\mu\text{m}$ and $r = 3\mu\text{m}$	92
3.15. Displacement components of pillars within square, triangular-X and triangular-Y lattices for the first four eigenmodes in three directions.	94
3.16. Polarization of pillars for the first two resonant modes within square, triangular-X, triangular-Y lattices for different phases.	96
3.17. Wave propagation along direction x through pillar-based PnCs within square (a), triangular-X (b) and triangular-Y (c) lattices.	96
3.18. The band structures for PnCs based on gold (a), nickel (b) and diamond (c) pillars on LiNbO ₃ Y128-X cut semi-infinite substrate.	99
3.19. The TCf values as a function of frequencies for the first two eigenmodes of the pillars within square (a and a'), triangular-X (b and b') and triangular-Y (c and c') lattices with two heights $2.5\mu\text{m}$ (left) and $5\mu\text{m}$ (right).	101

3.20. Models of device used for the calculation of SAW transmission through PnC of square lattice (left), triangular-X lattice (middle) and triangular-Y lattice (right) in COMSOL.	103
3.21. The calculated band structure and transmission spectra of the PnC composed of square arrays of cylindrical nickel pillars. The lattice constant $a = 9\mu m$, pillar's height $h = 4\mu m$, pillar's radius $r = 3\mu m$	104
3.22. Displacement components of pillars with square lattice. The lattice constant $a = 9\mu m$, pillar's height $h = 4\mu m$, pillar's radius $r = 3\mu m$	105
3.23. Normalized elastic displacement distribution in the delay line for four frequencies: (a) $f=89\text{MHz}$, (b) $f=95\text{MHz}$, (c) $f=149\text{MHz}$, (d) $f=160\text{MHz}$	105
3.24. Calculated band structures and transmission spectrum of the PnC composed of triangular-X (a) and triangular-Y (b) arrays of cylindrical nickel pillars. The lattice constant $a = 9\mu m$, pillar's height $h = 3.5\mu m$, pillar's radius $r = 3\mu m$	107
3.25. Normalized elastic displacement distribution for triangular-X lattice at the frequencies $f=110.5\text{MHz}$ (a) and $f=120\text{MHz}$ (b); for triangular-Y lattice at the frequencies $f=104.6\text{MHz}$ (c) and $f=107.5\text{MHz}$ (d).	107
3.26. Transmission spectrum of PnCs with different Young's Modulus of pillars.	108
4.1. Model of device used for investigating the propagation of surface acoustic waves in a periodic array of pillars on a semi-infinite substrate.....	112
4.2. Schematic of IDTs used in this work.	113
4.3. Symmetries of crystals used in this thesis, square lattice (a), triangular-X lattice (b), triangular-Y lattice (c), hexagonal-X lattice (d), hexagonal-Y lattice (e).	113
4.4. Micro-fabricating Process of the device.....	114
4.5. Photolithography in the clean room of IEMN.....	117
4.6. The design of photomasks for PnCs with dispersive IDTs.	118
4.7. The design of photomasks for PnCs with slanted IDTs.	119
4.8. SEM photos of the negative photoresist AZ15nXT (diluted 10:1) with different exposure time and the same development. Exposure time is respectively 23s (a), 21s (b), 19s (c) and 17s (d).....	121
4.9. SEM photos of the negative photoresist AZ15nXT (diluted 10:1) with different development time. Development time is respectively 2min15s (a), 2min45s (b) and 3min15s (c).	123
4.10. Schematic of the sputtering.	124
4.11. Schematic of PECVD realized by OXFORD Plasmalab 80 Plus.....	125
4.12. Representation of a voltammetry bench with three electrodes.....	128
4.13. Overview of the electrodeposition bench.	129
4.14. SEM pictures of the pillar-based PnCs over deposited by electrolyse.	134
4.15. SEM pictures of the PnCs with a 30 second electrical short circuit during the electroplating.	134
4.16. Micro-fabricated dispersive IDTs (a) (b) and slanted IDTs (c) (d).	137

4.17. PnCs based on Ni pillars with a height of 4 μm . Front sections of PnCs with different lattice symmetries, including square lattice (a), triangular lattice (b) and hexagonal lattice (c); lateral sections of PnCs (d)(e)(f)(g)(h).....	138
4.18. The vector network analyzer in the characterization center of IEMN.....	139
4.19. Experimental response of dispersive IDTs (a and b) on a Y128-X LiNbO ₃ substrate and slanted IDTs (c and d) a Y-Z LiNbO ₃ substrate for low frequency (left) and high frequency (right) measured by a network analyzer.	140
4.20. Low frequency (left) and high frequency relative (right) transmission spectrum of PnCs with square (a and d), triangular (b and e), hexagonal (c and f) arrays of nickel pillars.....	142
4.21. Relative transmission spectrum of PnCs with a linear defect for square (a and a'), triangular-X (b and b') and hexagonal-Y (c and c') lattices measured low frequency IDTs (left) and high frequency IDTs (right).	143
4.22. The transmission spectrum with and without PnCs composed of square (a) and hexagonal-X (b) arrays of pillars.	144
4.23. Frequency dependence of relative transmission ΔS_{21} (a and c) and the phase delay $\Delta\phi_{21}$ (b and d) measured experimentally (solid line) and obtained by FEM calculation (dashed line) for pillar height $h=2.3\ \mu\text{m}$ (a and b) $h=3.4\ \mu\text{m}$ (c and d).....	146
4.24. The experimental relative transmission spectrum for triangular-X and triangular-Y lattices and the SEM picture of the sample.	147
4.25. Theoretical relative transmission spectrum and the band structures for triangular-X and triangular-Y lattices. The top and bottom radius of the pillars are respectively 3.5 μm and 3 μm . The height is 2.5 μm	147
5.1. Nickel electroplating through a 50 μm thickness silicon plate.....	150
5.2. Fabrication process of the silicon pillar-based phononic crystals.	151
5.3. SEM picture of silicon pillar-based PnCs.	152
5.4. The relative transmission spectra and the cumulative phase difference of the silicon pillar-based PnC with square lattice.....	152
5.5. SEM pictures of the Fe nanoparticles and nanochains: (a) N=1, X=0; (b) N=10, X=0; (c) N=5, X=0.05; (d) N=10, X=0.1.....	154
5.6. Magnetic hysteresis loops of the Fe nanoparticles and nanochains for different concentration of reagents measured by VSM.	154
5.7. The whatman anodisc inorganic filter membrane used in this work.	155
5.8. SEM pictures of the AAO template before electroplating (a), nickel nanowires before NaOH bath (b) and nickel nanowires after NaOH bath.	156
5.9. Magnetic hysteresis loops for both the nickel film (a) and the nickel nanowires (b) fabricated by electroplating.....	156

Résumé en français

Ce travail porte sur l'étude l'ingénierie des structures de bandes pour les ondes élastiques en utilisant des matériaux micro et nano structurés déposés sur un substrat piézo électrique. En particulier on s'intéresse à l'interaction des ondes élastiques de surface avec des structures périodiques constitués de micro-plots arrangés suivant différentes symétries cristallographiques.

Introduction

La propagation des ondes élastiques dans les matériaux structurés est différente de celle dans les matériaux homogènes. Dans un matériau homogène les ondes de surface sont généralement non dispersives. En revanche dans un matériau structuré qu'on qualifiera d'inhomogène, la propagation des ondes peut présenter des singularités : forte dispersion, vitesse de groupe négative, branche plate dans le diagramme de bandes et la présence de bande interdite. Les structures qui présentent une bande interdite sont appelées en général les cristaux phononiques (CPn) [1, 2] qui sont analogues aux cristaux photoniques [3].

L'apparition d'une bande interdite dans la structure de bandes d'un matériau microstructuré s'explique en général par deux mécanismes : la diffraction de Bragg [2] qui donne naissance à des interférences destructives lorsque la longueur d'onde est de même ordre de grandeur que la périodicité introduite dans le matériau par la micro structuration. Par conséquent, la périodicité et la distribution des inclusions deviennent les paramètres clés pour optimiser la largeur et la position des bandes interdites. Toutefois, il est également possible d'obtenir des bandes interdites à des fréquences beaucoup plus basses que le seuil de la diffraction de Bragg, sans augmenter la maille élémentaire du cristal. Ce mécanisme est appelé le mécanisme des branches plates ou également le mécanisme des résonances locales [4]. En effet la maille élémentaire artificiellement induite par la micro-structuration présente des modes de résonances propres, qui peuvent être couplés aux modes qui se propagent dans la structure et faire apparaître ainsi des branches plates. L'objectif de cette thèse est d'étudier théoriquement et expérimentalement dans le cas d'un matériau

piézoélectrique combiné à des microstructures sous forme de plots déposés en surface le mécanisme d'interaction des ondes de surface avec les modes de résonances de ces microstructures.

Analyse par la méthode des éléments finis des structures de bandes d'un matériau micro-structuré

Le modèle développé est implémenté dans le logiciel commercial Comsol Multiphysics. La plate-forme proposée est constituée d'un substrat de niobate de lithium et de micro-plots de nickel déposés en surface et arrangés suivant différentes symétries. L'axe z est choisi perpendiculaire à la surface du substrat et parallèle à l'axe des plots. La distance entre deux plots adjacents (centre à centre) est a , la hauteur des plots est h et le rayon est r .

Un exemple de diagrammes de bandes est montré sur la Figure 1. Il montre les structures de bandes de différents réseaux de plots de Ni. Les paramètres géométriques utilisés sont $a = 9\mu\text{m}$, $h = 4\mu\text{m}$, $r = 3\mu\text{m}$. Les courbes en bleu correspondent aux modes de surface, les zones hachurées quant à elle représentent les modes diffractés vers le volume et également les modes de surface rapide qui ont une grande profondeur de pénétration dans le volume. Ces deux zones sont délimitées par les ondes de Rayleigh dans le substrat.

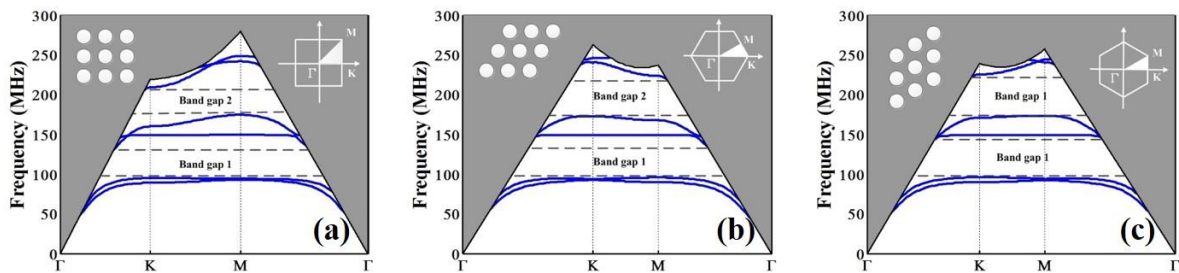


FIG. 1. Des diagrammes de bande au sein de différents réseaux de symétries : carré (a), triangulaire-X (b) et triangulaire (c) avec les paramètres géométriques de la manière suivante: $a = 9\mu\text{m}$, $h = 4\mu\text{m}$, $r = 3\mu\text{m}$.

Les branches plates dans les diagrammes de bandes confirment l'existence de résonances localisées au niveau des micro-plots. Les champs de déformations des deux premiers modes sur chaque diagramme sont illustrés sur la Figure 2. On y voit clairement la localisation des résonances dans les plots avec une différence dans la polarisation. C'est l'un

des points clés qu'on va tenter d'analyser dans cette thèse. En effet si l'on observe le digramme du réseau carré et du réseau triangulaire que l'on appelle Y, on constate que ces modes présentent la même polarisation. Cependant, la polarisation du réseau triangulaire-X (rotation de 90° de Y) est complètement différente. L'observation en dynamique de cette polarisation montre un mode de flexion combiné à une rotation dans le sens des aiguilles d'une montre ou dans le sens inverse. On confirme par cette étude que la polarisation des modes dépend fortement de la symétrie du réseau, ce point est très original au vue de toutes les conclusions qu'on peut trouver dans la littérature. Nous avons également mené une série de simulations pour étudier l'effet des paramètres géométriques sur la polarisation des modes et plusieurs conclusions originales ont été tirées.

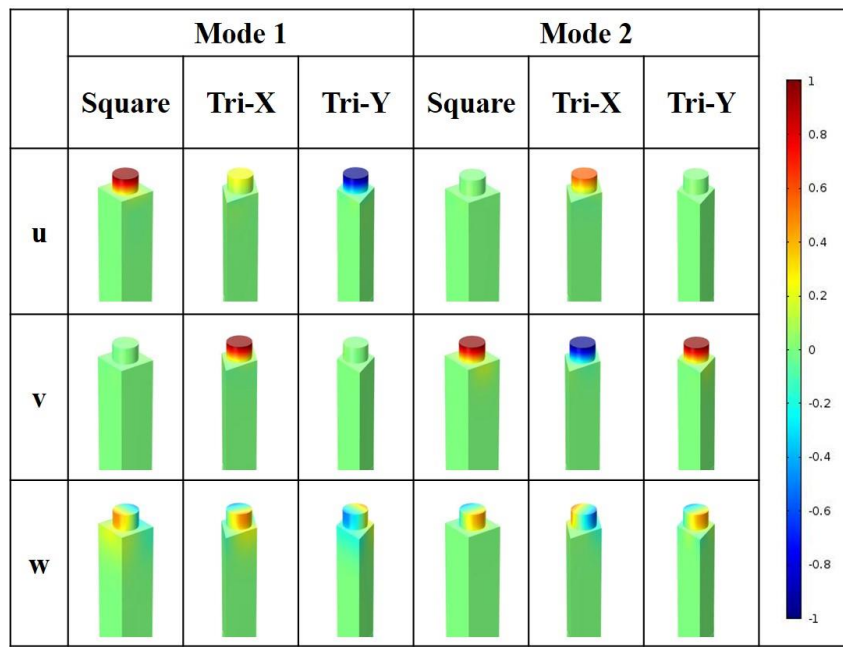


FIG. 2. Polarisation pour les deux premiers modes dans le cas du réseau carré triangulaire-X et triangulaire-Y.

Dans le même contexte, nous avons étudié l'effet de la température sur les modes de surface. Le coefficient de température en fréquence pour les deux modes de surface et pour chaque réseau est illustré sur la Figure 3. On y observe également que la sensibilité des modes dépend de la symétrie du réseau par le biais de la polarisation des modes. Ainsi les modes de surface dans le triangulaire-X sont plus sensibles que les modes de surface dans le réseau carré et triangulaire-Y.

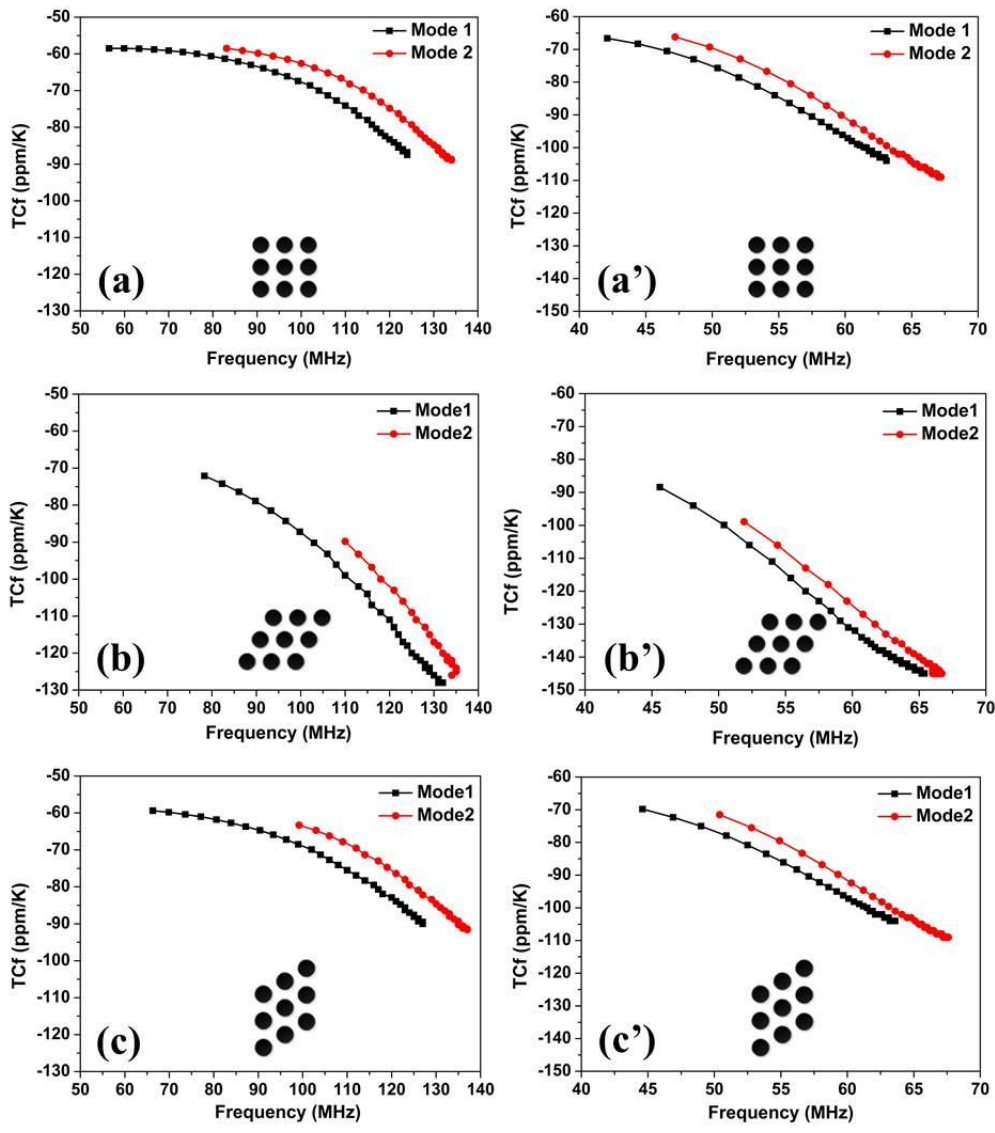


FIG. 3. Les valeurs TCf sur la fonction de fréquences pour les deux premiers modes propres des plots au sein du réseau carré triangulaire-X et triangulaire-Y avec deux hauteurs $2,5\mu\text{m}$ et $5\mu\text{m}$.

Pour comprendre comment cet effet se traduit sur une transmission, nous avons développé et implémenté un modèle sous Comsol. Un exemple de résultat est illustré sur la Figure 4, il présente la transmission d'un mode de Rayleigh à travers un réseau de plots de Ni arrangés suivant une symétrie carrée. On observe clairement l'excitation des modes de surfaces, qui se traduit par un pic d'absorption sur la transmission lorsque le couplage avec l'onde existe. Comme l'onde excitée est une onde quasi-sagittale, seuls les Modes 1, 3 et 4 sont excités. Nous avons également mené une série de simulation en considérant l'effet du réseau, de la rigidité des plots, et des paramètres géométriques.

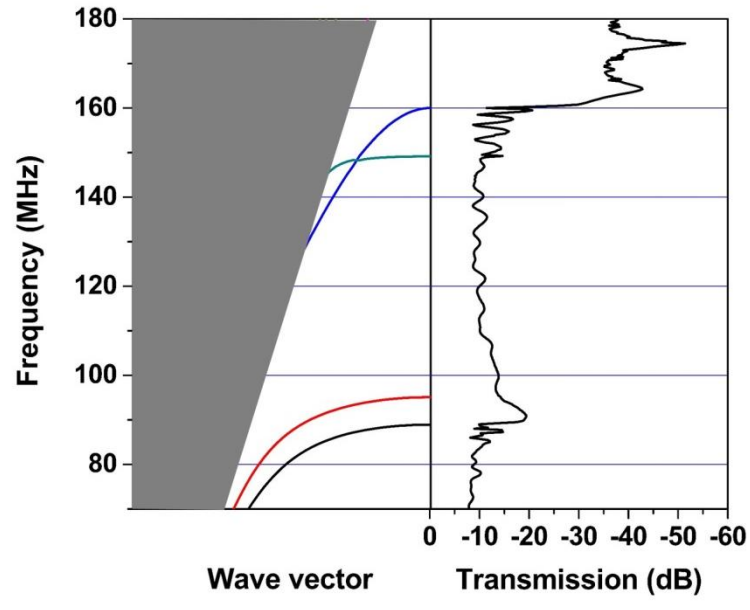


FIG. 4. Le diagramme de bande et le spectre de transmission calculés d'un CPn composé du réseau carré de plots cylindriques de nickel. Les constantes sont : $a = 9\mu\text{m}$, $h = 4\mu\text{m}$ et $r = 3\mu\text{m}$.

Design, fabrication et caractérisation de réseaux de micro-plot sur la surface du LiNbO_3

La structure élaborée est schématisée sur la Figure 5. Le substrat choisi est le LiNbO_3 coupe Y128 avec une propagation suivant x. Les micro-plots sont constitués de Ni électrodéposés et arrangés suivant un réseau carré triangulaire, et hexagonal. Deux transducteurs à électrodes inter-digités sont déposés à la surface du LiNbO_3 permettant l'excitation et la détection large bande des ondes de Rayleigh. Les mesures électriques sont faites à l'aide d'un analyseur de réseaux. Les transducteurs ont été conçus pour couvrir toute la plage des fréquences d'intérêt à savoir 50MHz-400MHz. Les constantes de maille a pour le réseau carré et les réseaux triangulaires sont respectivement $10\mu\text{m}$ et $9\mu\text{m}$. Le rayon des plots cylindriques est respectivement de $4\mu\text{m}$ pour le réseau carré et $3\mu\text{m}$ pour des réseaux triangulaires. L'épaisseur du substrat D peut être considérée comme semi-infinie ($D = 500\mu\text{m} \gg h$) où h est la hauteur de plots.

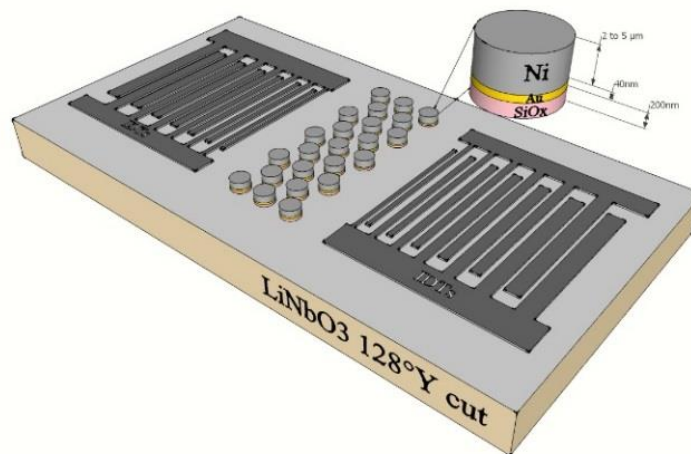


FIG. 5. Modèle du dispositif utilisé pour étudier la propagation des ondes acoustiques de surface dans un réseau périodique de plots sur un substrat semi-infini.

Le procédé de fabrication est illustré sur la Figure 6. Il fait intervenir des étapes de lithographie, de dépôt par plasma, de gravure, et d'électrodéposition.

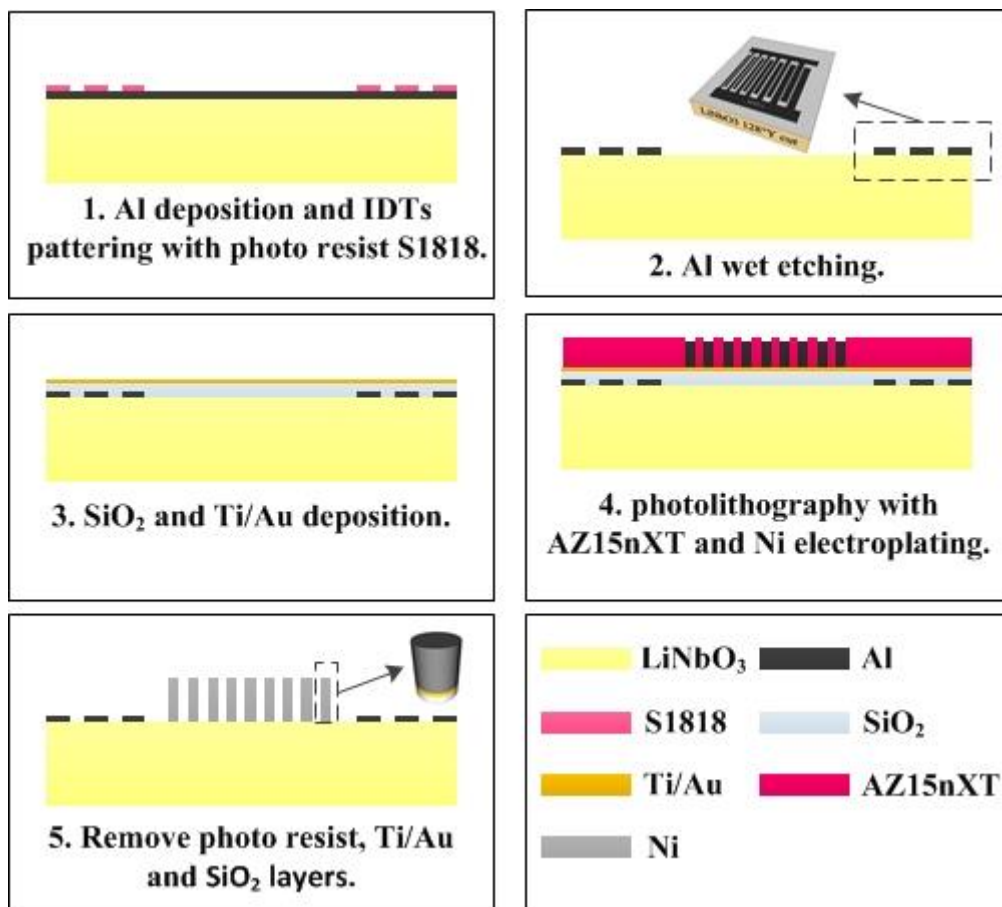


FIG. 6. Le processus de fabrication.

Un exemple de résultat sur les spectres de transmission est illustré sur la Figure 6. Il présente la transmission des ondes de Rayleigh à travers des réseaux de plots de type carré et triangulaires-X et triangulaires-Y. Les résultats obtenus confirment les conclusions faites sur les résultats de calcul. En effet la transmission à travers le réseau carré et triangulaire-Y présente la même évolution au voisinage du Mode 1 de surface, cependant le triangulaire-X présente une série de pics d'absorption.

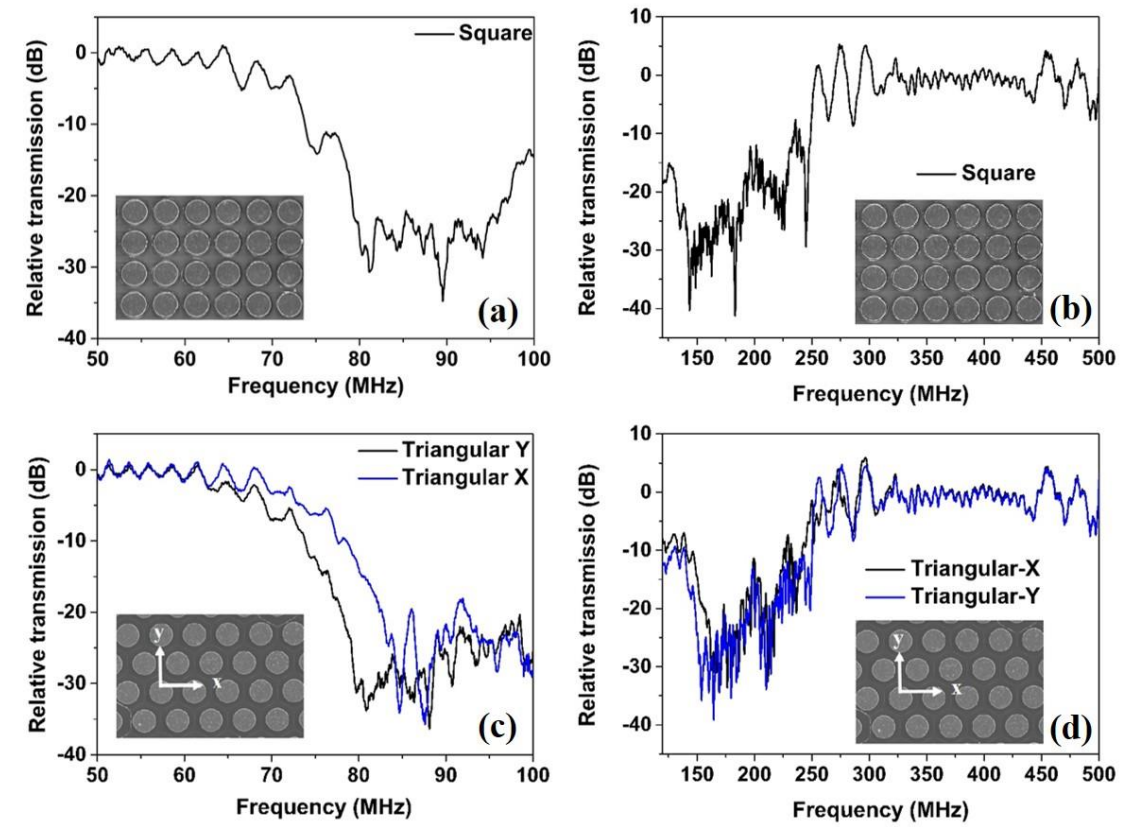


FIG. 7. Les spectres de transmission relative et des images de MEB pour des CPn avec le réseau carré (a et b), triangulaires (c et d) pour des basses fréquences (a et c) et des hautes fréquences (b et d).

Conclusion et perspectives

Dans cette travail, l'étude des matériaux micro et nano structurés pour l'ingénierie acoustique des bandes interdites dans les dispositifs électro-acoustiques a été présentée, notamment pour l'étude des cristaux phononiques deux dimensionnels basés sur des plots de nickel. Certaines propriétés sur la propagation des ondes élastiques dans les structures périodiques dues à la résonance locale ont été introduites. Du point de vue de la polarisation des plots, certaines

observations ont été proposées et analysées théoriquement. En outre, un processus complet de fabrication basé sur des techniques de micro-fabrication a été présenté en détails.

Ce travail a induit beaucoup de recherches en cours et inachevées.

Comme perspectives, le premier travail qui doit être fait est l'analyse théorique sur le couplage des modes de propagation. Jusqu'à présent, nous avons seulement observé les phénomènes et donné une explication visualisée. Un modèle théorique doit être élaboré pour expliquer profondément la physique.

Deuxièmement, depuis le concept de CPn proposé pour la première fois il y a plus de deux décennies, beaucoup de travail a été réalisé pour l'étude sur le mécanisme et les propriétés du CPn. Cependant peu de réalisations ont été réalisées pour les applications. Dans ce travail, nous avons proposé une idée de capteurs thermiques qui peuvent être considérés comme une application potentielle pour des CPn.

En outre, il y a beaucoup de travail en cours, qui doit être fini et étudié plus. Bien que ce soit la fin de ma carrière de PhD, cela est aussi un nouveau départ de la recherche pour les matériaux et les structures périodiques.

Introduction

Human cognitive process of crystals started with embedding the colorful gemstones in the imperial crowns of their kings in the ancient times. These glittering and translucent gemstones, which symbolized wealth and power in that period, were the so-called crystals. With the development of science, people's attention concerned not only the beautiful appearance of crystals, but also why they were looked like that, which opened the study of solid state physics.

There is a general consensus in the scientific community that the investigation of solid state physics started with the discovery in the X-ray diffraction for crystals. Why crystals were chosen, not the amorphous? That's because crystals can give the best description of some electronic properties. For example, the band gap property of semiconductors needs to rely on the periodic structures of crystals. Subsequent research has shown that this discovery can be seen as an important technological revolution, because inspired by the theory of electron energy band in natural crystals, lots of research has been done around the propagation of classic waves in periodic composite materials or structures. For these materials or structures, there are some frequency ranges, in which the propagation of some kind of classic waves is forbidden. These frequency ranges are the so-called band gaps. And the periodic composite materials or structures that have the band gap property are called Wave Crystals. For example, the materials or structures, which have electromagnetic wave band gaps and a distribution of periodic dielectric constants, are called Photonic Crystals (PnCs). Similarly, the materials or structures, which have elastic wave band gap properties and a distribution of elastic constants, are called Phononic Crystals (PnCs), which is the topic of this thesis.

In fact, our daily life is the result of technological revolutions. One of the most important marks of technological revolution is the improved ability to manipulate electrons and photons. For example, the control of electrons brought us into digital times with the products such as laptops, mobile phones and digital cameras. On the other hand, with the development of artificial structures and devices used to control photons, the wireless communication and the use of optical fibres and microwaves were achieved. Inspired by the success of the manipulation of electrons and photons, people believe that the control of phonons which are responsible for the transmission of sound and heat can also lead to a great

contribution to the society. Analogous to the utilization of PtCs, controlling the phonon flows with PnCs is a direct and common method which has attracted significant attention in recent decades.

TAB. I. Band-structure-related properties of three periodic systems [2].

Property	Electronic crystal	Photonic crystal	Phononic crystal
Materials	Crystalline (nature or grown)	Constructed of two dielectric materials	Constructed of two elastic materials
Parameters	Universal constants, atomic numbers	Dielectric constants of constituents	Mass densities, sound speeds c_l, c_t of constituents
Lattice constant	10-50nm (microscopic)	0.1 μ m – 1cm (mesoscopic or macroscopic)	Mesoscopic or macroscopic
Waves	de Broglie (electrons) ψ	Electromagnetic or light (photons) \mathbf{E}, \mathbf{B}	Vibration or sound (phonons) \mathbf{u}
Polarization	Spin \uparrow, \downarrow	Transverse: $\nabla \cdot \mathbf{D} = \mathbf{0}$ ($\nabla \cdot \mathbf{E} \neq \mathbf{0}$)	Coupled trans.-longit. ($\nabla \cdot \mathbf{u} \neq \mathbf{0}$, $\nabla \times \mathbf{u} \neq \mathbf{0}$)
Differential equations	Schrodinger equation	Maxwell equations	Elastic wave equation
Free particle limit	$W = \frac{\hbar^2 k^2}{2m}$ (electrons)	$\omega = \frac{c}{\sqrt{\epsilon}} k$ (photons)	$\omega = c_{t,l} k$ (phonons)
Band gap	Increases with crystal potential; no electron states	Increases with $ \epsilon_a - \epsilon_b $; no photons, no light	Increases with $ \rho_a - \rho_b $, etc. no vibration, no sound
Spectral region	Radio wave, microwave, optical, X-ray	Microwave, optical	$\omega \leq 1 \text{ GHz}$

The pioneers of the investigation of PnCs have compared the peculiarities of phononic crystals, as well as electronic and photonic crystals, (see Table I_[2]). From the table, we can find that these three crystals have many properties in common. However, different from electromagnetic waves, which are transverse, sound waves in solids can be longitudinal and transverse. Even though in a homogenous solid medium, there are 3 independent elastic constants, density and 2 lamé constants. For electromagnetic waves, the two components of polarization are both transverse. And there is no coupling between them. The dielectric constant is the only independent parameter in a homogenous medium. Therefore, the investigation of PnCs has more abundant physical connotation than PtCs.

This work is about the investigation of micro and nano structured materials for acoustic band gaps engineering in electro-acoustic devices, especially for the study of two-

dimensional pillar-based phononic crystals. The objectives of this work are to achieve several goals as follow:

- Study the propagation of surface acoustic waves in periodic structures like PnCs. Understand the mechanisms of a PnC which refer to Bragg scattering and local resonance.
- Build the theoretical models to study band structures and transmission spectrum of a two dimensional pillar-based PnC by the finite element method.
- Discuss the effect of geometrical and elastic parameters on the locally resonant PnCs.
- Study the anisotropy of a pillar-based PnC and the temperature coefficient of frequency for a PnC.
- Develop a microfabrication process based on microfabricating techniques and the electroplating.
- Validate the simulation results by measuring the transmission spectrum through a network analyzer.
- Explore the possibility of other periodic structures based on magnetic nanoparticles, silicon pillars and nickel nanowires.

The content of this thesis is divided into five chapters with an introduction and the conclusion-perspectives:

Chapter 1 gives the bibliography of materials with periodic structures and brings up the concept of phononic crystals. The history of PnCs, theoretical and experimental existing methods and technologies, application of PnCs are also presented, as well as the motivation of this thesis.

In the Chapter 2, we will review the theoretical foundation of PnCs used in this work, including essential elastic theory, the propagation of elastic waves, lattice and band theories as well as the mechanisms of PnCs.

Chapter 3 describes the theoretical models built by the finite element method using COMSOL software in order to study the band structures and transmission spectrum of PnCs. Different geometrical parameters such as pillar's height and pillar's radius will be discussed as well as the consideration of material composition of a PnC. By the observation of pillar's polarization at the eigenfrequencies, a new explanation of the effect of PnC's anisotropy will be brought out. In addition, the temperature coefficient of frequency of a PnC will also be discussed in this chapter.

The design and microfabrication process of the two dimensional pillar-based PnCs will be presented in Chapter 4. Pictures taken by a scanning electron microscope are depicted

to show the morphology of the sample and discuss the microfabricating techniques. Experimental transmission spectrum is measured by a network analyzer to validate the simulation results.

In Chapter 5, other attempts to fabricate the micro and nano periodic structures in this work will be talked about, including the PnCs composed of two dimensional silicon pillars, assembly of magnetic nanoparticles and nickel nanowires fabricated by electroplating through an anodic aluminum oxide template.

To finish this thesis, a conclusion and perspectives about this work will be discussed.

Chapter 1: State of the art

1.1 Historical context

The investigation of phononic crystals is on the base of the theory of elastic waves' propagation in periodic structures, which can date back to Floquet's research on one-dimensional Mathieu Equation in 1883. Then in 1887, Rayleigh pioneered the study on the propagating characteristics of elastic waves in continuous periodic structures. He indicated that some frequency ranges existed, in which waves cannot propagate, in continuous periodic structures.

Time came to the 20th century. In 1953, Brillouin conducted a systematic in-depth study on the propagating characteristics in periodic materials_[5]. The idea of reflecting sound waves using a periodic organization appears in 1965 with the introduction of acoustic Bragg mirrors_[6]. Indeed, these stacks of alternating layers of different materials formed a version of one-dimensional phononic crystal.

As we have mentioned previously, the study of photonic crystals has an important significance of the inspiration for phononic crystals. In 1987, the work of E. Yablonovitch_[7] and J. Sajeev_[8] have shown that the systems composed of periodic structures of dielectric materials for dispersive components of the electromagnetic waves, can provide, in some cases, one or more frequency bands in which the electromagnetic waves are completely reflected by the crystal. These frequency ranges are called photonic band gaps. Inspired by the investigation of photonic crystals, in 1992, M. M. Sigalas and E.N.Economou demonstrated theoretically the existence of band gaps of elastic waves propagating in periodic structures_[1]. In 1993, Kushwaha put forward clearly the concept of phononic crystals and predicted the applications in the domain of high precision and no vibration environment_[2]. Next year, Kushwaha and Halevi presented several basic rules on the two-dimensional structures involving metal cylinders in a solid matrix_[9]:

- ✓ The quantity and width of band gaps depend on filling ratio, which describes the volume fraction of inclusions in the phononic crystal.

- ✓ The organization in a hexagonal lattice is more favorable to the appearance of band gaps than in a square lattice. More generally, it indicates that the symmetry of a phononic crystal can influence the opening of band gaps.
- ✓ Band gaps appear more easily when the materials involved have a big contrast of density and other elastic constants.
- ✓ Inclusions with acoustic velocity less than that of the matrix favors the appearance of stop bands.

Until then, all the pioneering exploration about PnCs was limited to the theoretical aspect. In order to demonstrate the simulation results, a compelling experiment was quite needed. The first demonstration with a band gap in a 2-dimensional phononic crystal was presented in 1995 by Martinez-Sala et al._[10] using a minimalist sculpture by Eusebio Sempere exposed to Madrid which we can see in Figure 1.1. From the experimental point of view, the existence of band gaps in PnCs was firstly confirmed. Since then, the investigation of PnCs caused widespread concern.



FIG. 1.1. Kinematic sculpture by Eusebio Sempere used as the first demonstration of band gaps in phononic crystals [10].

During the research process of PnCs, another important discovery was presented by the work of Prof. Liu et al._[4]. Before 2000, all the PnCs were simulated or constructed on the theoretical basis of Bragg diffusion, which requires lattice parameters corresponding to the wavelengths. That is the limitation of the construction of PnCs. In addition, new artificial

phononic structures were designed and have been the subject of studies on the propagation and diffusion of acoustic waves with large wavelength relative to the periodicity of structures. In 2000, Liu et al. achieved a new PnC, called locally resonant phononic crystal (LRPnC) capable of opening band gaps in the sonic regime using a periodicity much smaller than the wavelengths that are propagated, shown in Figure 1.2. They showed that their PnCs behave as a medium with a negative effective elastic constant, which integrate into the category of acoustic meta-materials. This discovery developed another area of research of PnCs.

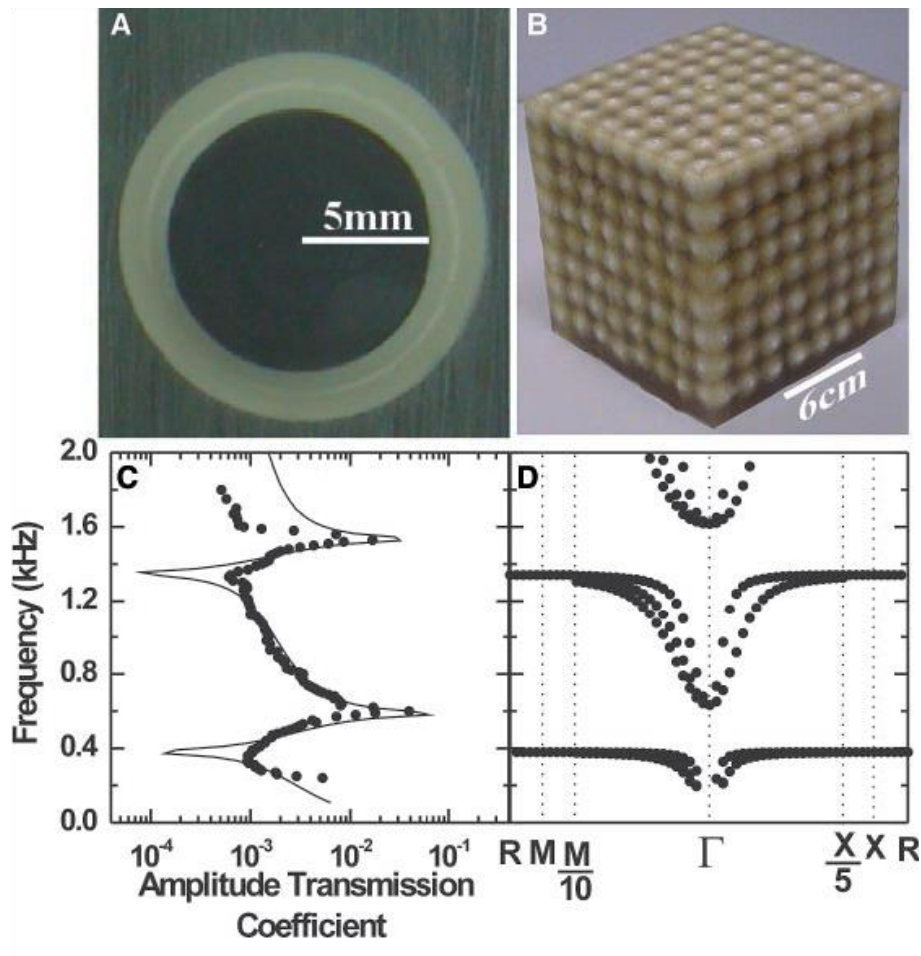


FIG. 1.2. The first locally resonant phononic crystal [4]. (A) Cross section of a coated lead sphere that forms the basic structure unit. (B) For an 8×8×8 sonic crystal. (C) Calculated (solid line) and measured (circles) amplitude transmission coefficient along the [100] direction are plotted as a function of frequency. (D) From 200 to 2000 Hz, of a simple cubic structure of coated spheres. Three modes (two transverse and one longitudinal) are distinguishable in the [110] direction, to the left of the G point. The two transverse modes are degenerate along the [100] direction, to the right of the G point. Note the expanded scale near the G point.

Besides these most important discoveries which we have mentioned above, in the whole research process of PnCs, there are also lots of great achievements in this domain,

which have made enormous contributions to the subsequent research. The first 2-dimensional PnC in the laboratory was achieved simultaneously by Vasseur et al._[11] and Sanchez-Perez et al._[12] in 1998. In the same year Sprik et al._[13] proposed the idea of transferring 2D PnCs to 3D PnCs. Then two years later, the first demonstration of a three-dimensional phononic was born_[4]. Time came to the mid-2000s, many practical demonstrations had been done but they were all in macroscopic scales. Until the work of Wu's group_[14] which presented the first achievement of a microscopic PnC, the research of PnCs were transferred from the macroscopic scales into the microscopic scales. The investigation of PnCs were not limited to bulk waves, some demonstrations of microscopic PnCs were achieved by using surface acoustic waves (SAW)_[15, 16] et Lamb waves_[17-19].

1.2 Existing technologies

1.2.1 Simulation methods

With the deepening of the investigation of wave propagation, many numerical simulation methods have been applied for analyzing the resolution of Maxwell Equations in the complex systems. Among all the research domains, photonic crystals have been studied by many numeric methods, such as Plane Wave Expansion (PWE)_[20], Transfer Matrix Method (TMM)_[21], Multiple Scattering Theory (MST)_[22], Fourier Series Expansion (FSE)_[23] Finite Difference Time Domain (FDTD)_[24] and Finite Element Method (FEM)_[25]. During the last two decades, these numerical methods were also applied for the theoretical investigation of the propagation of elastic waves in phononic crystals_[2, 26-30].

Among all the numerical methods, PWE, FDTD and FEM were the most common in applications of elastic wave propagation in PnCs. The plane wave expansion is based on the representation of the acoustic field by a linear superposition of plane waves propagating through a phononic crystal. This method does not allow for the transmission of a finite phononic crystal, but provides the calculation for band structures of an infinite phononic crystal. It can lead to inconsistent results, especially when handling solid-fluid hybrid systems, or when the difference between the acoustic parameters of the different materials is too large_[31]. In addition, it is provided for infinite systems in all directions. It can be also modified to model the behaviour of surface acoustic waves in a two-dimensional phononic

crystal_[32] or the system for Lamb waves_[33]. It allows modeling of a phononic crystal in accordance with the experiments_[34], but the calculations become too long for complex structures. Another disadvantage is that the commercial software for PWE does not exist.

Finite difference time domain considers the system by discretizing the space and time, which allows approximating the partial derivative of the differential equations governing the system locally by differences between the values of the acoustic fields presenting in different nodes and different steps in time. This method provides both the band structure of an infinite PnC and the transmission of a finite PnC. This method is quite extensive in the literature and showed results in agreement with the experiment. However, there is no commercial software for the simulation of phononic crystals.

Finite element method uses the discretization of space as the FDTD method, but uses a polynomial interpolation of acoustic fields between mesh nodes. It uses a variational formulation for solving partial differential equations defining the local behavior of the system. Similarly as FDTD, it provides the calculation for both the band structures and the transmissions through a phononic crystal. Its main drawback is the long duration of the necessary calculations, especially for the complex structures in transmission, for which meshes can quickly reach several hundreds of thousands of nodes. Its main advantage is that there are software offering finite element modeling in which the main formulations are already programmed.

1.2.2 Experimental study for microfabricated phononic crystals

Since the complete phononic bandgaps were firstly experimentally observed_[12, 35, 36], phononic crystals have attracted much attention. As a result, a great deal of progress has been achieved especially in the theoretical analysis. For the experimental aspect, the primitive achievements of PnCs devices have been mainly constructed by hands, assembling scattering inclusions in a viscoelastic medium, predominantly air, water or epoxy_[12, 34, 36-46], resulting in large structures limited to frequencies below 1 MHz. These hand-assembled devices were inherently lossy, time consuming and costly to manufacture, and difficult to reproducibly construct_[47].

With the development of microfabrication techniques, PnC based devices were capable to be miniaturized. Consequently, these PnC based devices could be realized and

experimentally verified at very high frequencies (VHF: 30-300 MHz) and ultra high frequencies (UHF: 300-3000 MHz)_[47].

An example of one-dimensional PnCs was constructed by etching a grating of lines in a glass substrate for the investigation of surface acoustic waves (SAWs) at a working frequency range of a few GHz_[48], shown in Figure 1.3. One of the first realization of 3D micro-phononic crystals was achieved by the self-assembly of polystyrene nanosphere inclusions on a glass substrate subsequently back filled with a silicon oil matrix_[49].

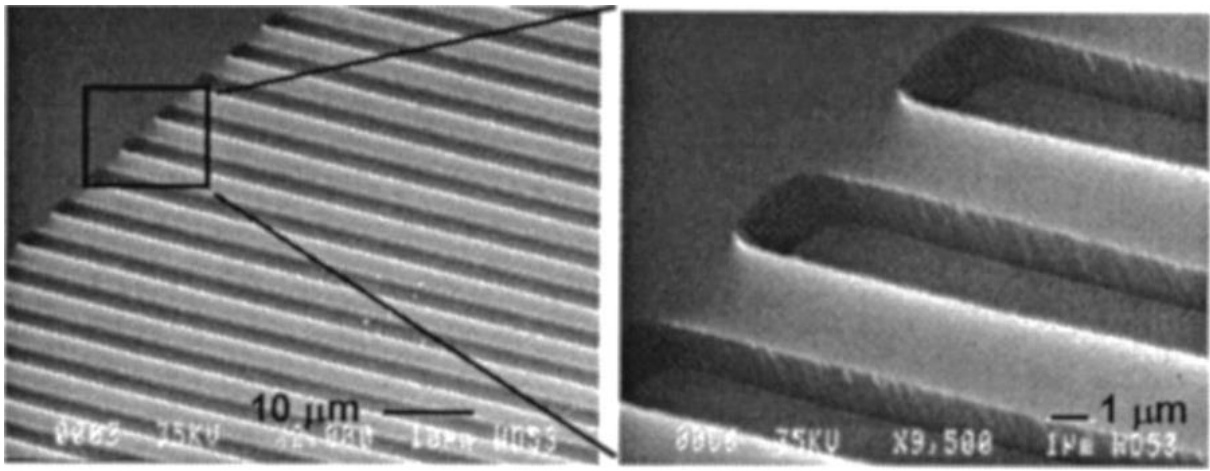


FIG. 1.3. Scanning electron micrograph pictures of a patterned glass surface. The sample has a grating period of 3 μm and a relief depth of 1.15 μm [48].

Now we talk about the two-dimensional PnCs which have attracted the highest attention because of the abundant physical connotation. 2D PnCs always focused on a semi-infinite substrate or a slab. The 2D periodic arrays of inclusions are on or in the host matrix. The PnC band gaps were both observed for in several material systems including Si/air_[14, 18, 50-52], SiC/air_[53], AlN-TiN/air_[54], LiNbO₃/air_[55-57], Si/W_[58] and SiO₂/W_[17, 47, 59-63]. Solid/solid PnCs have been demonstrated less sensitivity to lithography when compared to solid/air PnCs_[64], allowing scaling to higher frequency operation important to radio frequency (RF) and thermal applications. Certain devices, such as cavities, requiring very low material damping have been best realized in solid/air materials systems using high-Q materials such as Si_[50] and SiC_[53].

To my knowledge, the first experimental demonstration of 2D micromachined PnC was achieved by Wu_[14] from the Institute of Applied Mechanics in National Taiwan University. The Chinese group etched cylindrical air holes inclusions in Si matrix to construct a 2D PnC shown in Figure 1.4. The lattice constant was chosen as 10 μm , the radius of the

circular cylinder is thus equal to $3.5\mu\text{m}$ and the depth of the air holes was $80\mu\text{m}$ considering that the energy of SAW modes should be mostly confined to a depth of one to two wavelengths of the SAW. Another important contribution of Wu was the utilization of slanted finger inter-digital transducers (SFITs) which allowed widening the bandwidth of a single SAW transducer to cover the frequency range for SAW PnC characterization.

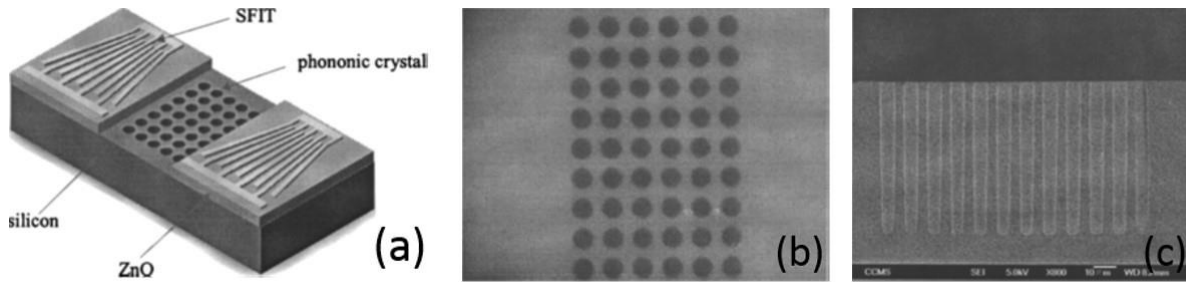


FIG. 1.4. (a) Schematic diagram of air/Si PnC and SFITs; (b) a microscopic picture of the 2D PnC; (c) cross section of the 2D PnC [14].

To be inspired by Wu's work, Saeed Mohammadi from Georgia Institute of Technology has shown the evidence of the existence of large complete PnC band gaps in 2D PnCs formed by embedding hexagonal arrays of cylindrical air holes in a freestanding Si Plate_[18, 50, 65]. In this work, a freestanding Si slab with a thickness of $15\mu\text{m}$ was penetrated. The lattice constant was $15\mu\text{m}$ and the diameter of the air holes was approximately $12.8\mu\text{m}$ shown in Figure 1.5. This results open a new direction in the implementation of high frequency practical PC structures with a possible higher performance over the conventional micromechanical devices used in a variety of applications especially in wireless communication devices and sensing systems.

On the other hand, the air holes were not only etched in a Si matrix but also in a lithium niobate host material_[55-57] by Sarah Benchabane, Abdelkrim Khelif and Vincent Laude's group from Institut FEMTO-ST. In their work, a PnC was realized by etching square arrays of low-acoustic impedance air hole inclusions with a depth of $10\mu\text{m}$ in a $500\mu\text{m}$ thick high-acoustic impedance, Y-cut lithium niobate wafer, shown in Figure 1.6._[55]. The diameter of the air holes was $9\mu\text{m}$ and lattice constant was $10\mu\text{m}$, resulting in a $1\mu\text{m}$ minimum feature size and a volume filling fraction of 0.9. IDTs used to launch and detect the acoustic waves necessary for characterizing the PnC were realized on the two sides of the PnC by patterning 150nm thick aluminum electrodes on the lithium niobate substrate.

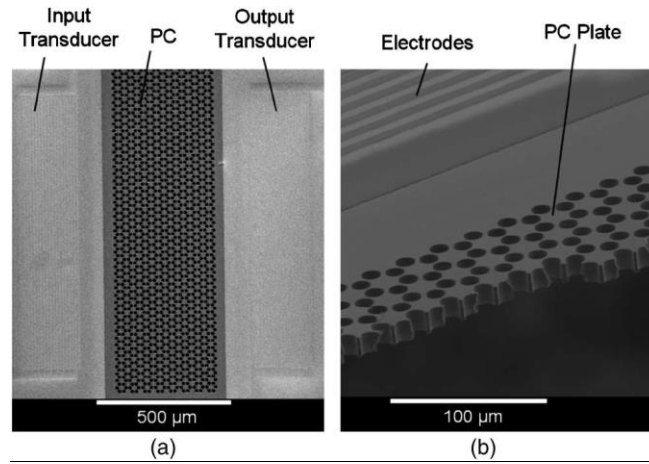


FIG. 1.5. (a) Top view of the fabricated devices with the hexagonal lattice PC structure in the middle and the transducer electrodes on each side; (b) cross sectional view of the same structure [18, 50, 65].

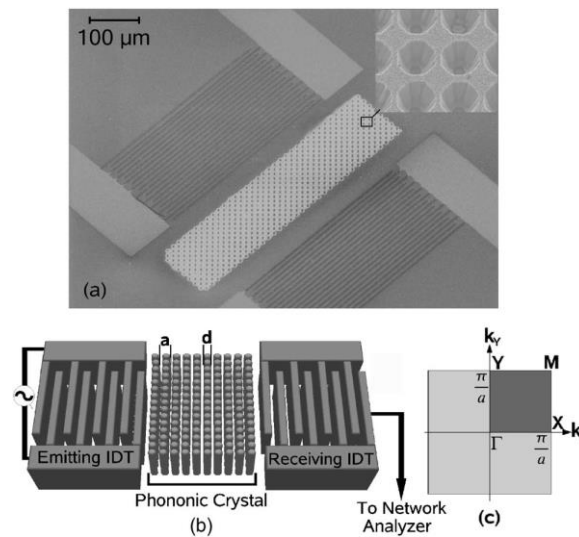


FIG. 1.6. (a) Scanning electron microscope picture of a PnC for SAWs. The structure, consisting of 9 μm diameter air holes with a 10 μm pitch, is surrounded by a pair of IDTs to ensure surface wave transduction. The inset in the top-right corner shows a more detailed view of the holes etched in the lithium niobate single crystal substrate; (b) schematic of the experimental setup used for an electrical characterization of the crystal; (c) sketch of the first Brillouin zone [55].

Beside these air/solid PnCs, solid/solid PnCs were also investigated. An example of this kind of PnC was given by I. El-Kady and R. H. Olsson III's group from Sandia National Laboratories of the USA. Their investigations were mainly about the W/SiO₂ based micro and nano fabricated phononic crystals [17, 59, 61-63]. A PnC slab constructed by square arrays of high-acoustic impedance W scattering inclusions in a low-acoustic impedance SiO₂ matrix [59, 61] is shown in Figure 1.7. The lattice constant was 45 μm and the radius of the W inclusions was 14.4 μm, yielding a filling fraction of 0.32. In the center of each tungsten

inclusion was a release hole with a radius of $5\mu\text{m}$. These holes were required to undercut the PnC and suspend it from the substrate. Aluminum nitride (AlN) transducers were utilized on each side of the PnC for electrical characterization. Similar to the slanted SAW transducer discussed in Wu's work_[14], the AlN couplers were tapered to provide the wide bandwidth necessary for characterizing a PnC bandgap. The W inclusions were formed by etching holes through the SiO_2 matrix and back filling these holes with W using chemical vapor deposition (CVD). In this work, the PnC in a square lattice have been measured at 67MHz with greater than 30dB of acoustic rejection and bandwidths exceeding 25% of the midgap.

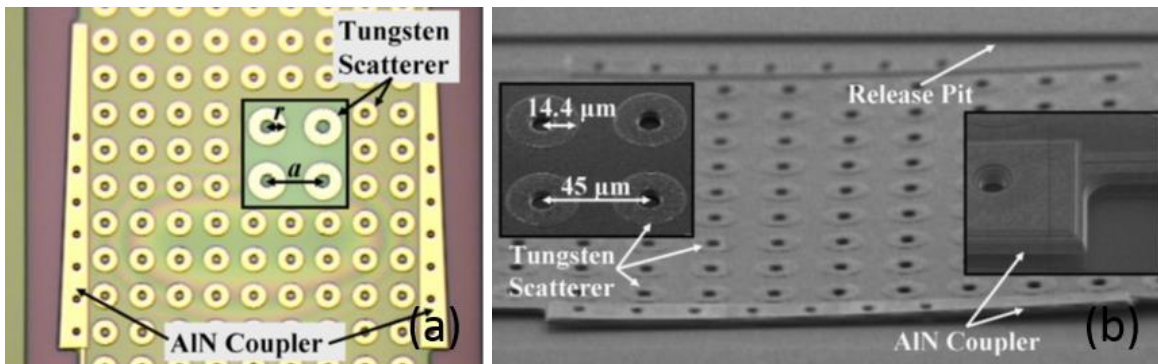


FIG. 1.7. (a) Micro acoustic band gap (ABG) slab with integrated AlN electro-acoustic couplers. The ABG was realized by embedding W scatterers in an oxide matrix. Acoustic frequencies within the gap cannot pass between the AlN couplers. Inset shows close up image of the W scatterers and release holes; (b) SEM image of the micro-ABG slab. Inset show (left) close up SEM of Al capped W rods in SiO_2 matrix (right) close up SEM of an AlN coupler [59, 61].

As the further investigation of the W/ SiO_2 based micro and nano fabricated PnC done by this group, single and multimode acoustic waveguides have been realized by defecting the acoustic crystals through removal of a subset of the W scatterers. These waveguides achieved relative transmission of up to 100% for the propagating modes_[59]. In addition, they experimentally realized the PnC, designed to operate at gigahertz frequencies_[63]. These Gigahertz-frequency PnCs were well poised to find usage as high-Q resonators, waveguides, and coupling elements in a variety of application areas including RF communications.

For the recent experimental research about the 2D PnCs, one working direction is to fabricate the PnC devices operating at ultra high frequencies which means about gigahertz. A method for designing and fabricating a Love wave resonator utilizing the PnC as the reflectors was presented by Wu's team_[66]. In this work, the PnCs were formed by depositing 2D, periodically etched silica film on a quartz substrate. A one-port resonator that contained a set

of IDTs inside the resonant cavity bonded by two PnC arrays was designed. With sub-micrometer structures, the resonator was designed to operate at 1.25 GHz. The SEM pictures of PnCs designed and fabricated in this work is shown in Figure 1.8.

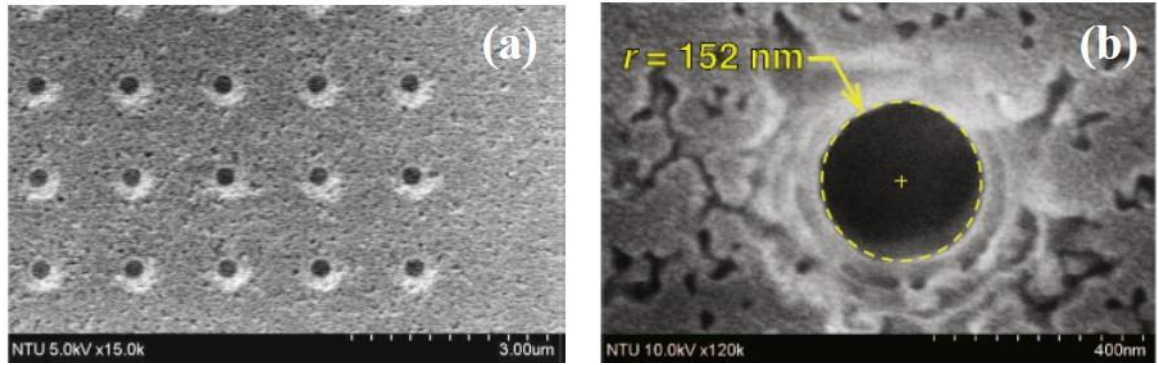


FIG. 1.8. (a) A SEM picture of the hole structure of the PnC; (b) close-up of a single hole [66].

Another interesting idea of the recent research of the 2D experimental PnCs is the realization of pillar-based PnCs. The early investigations of PnCs always use bulk acoustic waves (BAW) which are easier to understand. However the use of BAW is limited in the microscopic experimental aspects because it is really hard to achieve punching spaced holes with a diameter of $1\mu\text{m}$ in a material which has a thickness of several hundred micrometers [67]. As a result, PnCs using SAWs have broader application prospects [68-70]. SAW are guided along the surface, and are confined in the direction perpendicular to the surface. The PnCs using SAW were always based on periodic holes [16, 71, 72] in the previous investigations. Recently the utilization of pillar-based PnCs [73-76] on the surface was proposed. Comparing with holes-based PnCs, pillar-based PnCs can avoid the limitation of the thickness of host material. In addition, pillar-based PnCs have a new geometrical parameter (the height of pillars) which can adjust the frequency of acoustic mode and the position of band gaps, along with other parameters [73, 77]. As a result, it makes the physics of propagation and confinement of acoustic waves in pillar-based structures more complex than the hole-based structures [78].

Reza Pourabolghasem et al. [79] have presented an experimental evidence for the existence of a complete PnC band gap for Lamb waves in the high frequency regime (about 800MHz) for a pillar-based PnC membrane with a triangular lattice of gold pillars on top shown in Figure 1.9. The membrane was composed of an aluminum nitride film stacked on thin molybdenum and silicon layers. A large attenuation of at least 20dB was observed in the

three major crystallographic directions of the PnC lattice in the frequency range of 760MHz-820MHz.

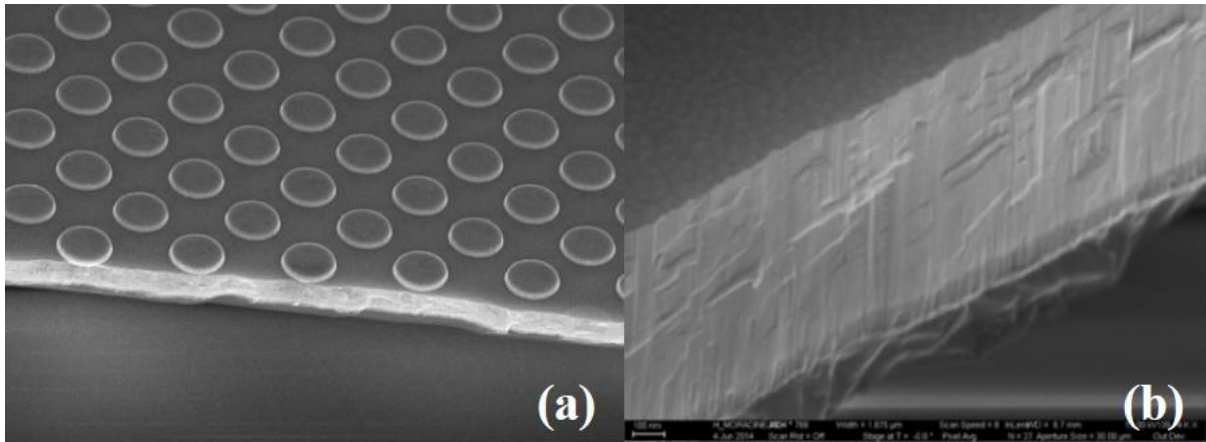


FIG. 1.9. (a) SEM picture of the PnC membrane with Au pillars deposited on the AlN/Mo/Si membrane; (b) SEM picture of the cross-section of the AlN/Mo/Si membrane. [79].

Another approach for pillar-based PnCs was realized by Younes Achaoui et al. [73]. In his work, he reported on the experimental study of the propagation of surface guided waves in periodic arrangement of pillars on a semi-infinite medium. Samples composed of nickel pillars grown on a lithium niobate substrate were prepared and wide bandwidth transducers were used for the electrical generation of surface elastic waves. Both of local resonant type band gap and Bragg scattering type band gap were identified. The schematic diagram of the experimental setup and the SEM picture of the PnCs were shown in Figure 1.10.

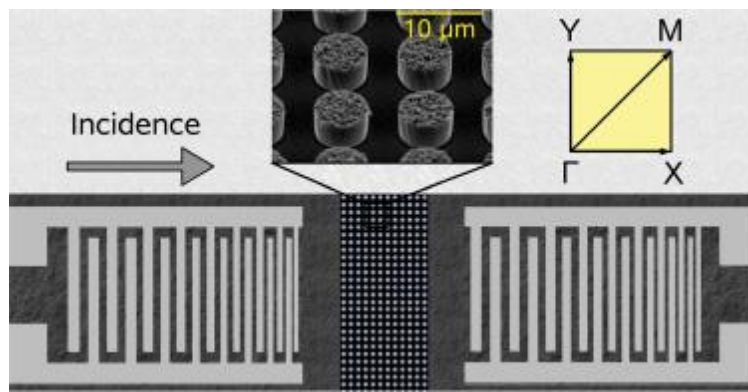


FIG. 1.10. Schematic of the experimental setup used for investigating the propagation of surface phonons in a periodic arrays of pillars on a semi-infinite substrate. The nickel pillars shown as an inset have a radius of $3.2\mu\text{m}$ and a height of $4.7\mu\text{m}$. They are arranged according to a square lattice with a pitch of $10\mu\text{m}$. Two chirped IDTs generate and detect surface phonons due to the piezoelectric properties of the lithium niobate substrate. [73].

1.3 Application of phononic crystals

With the development of PnCs in both theoretical and experimental aspects, scientists began to explore the applications of PnCs. There is no lack of some typical applications among them, including sound insulation_[80], anti-seismic structures_[68] and filters, signal processing as well_[41, 81-84].

People's daily lives have been improved remarkably through manipulating electrons and photons. For example, thanks to the control of electrons in semi-conductor materials, many electronic products, such as laptops, mobile phones and digital cameras, came out leading our lives into a digital time. Analogously with electrons, the development of photons devices contributes to the wireless communication and the use of optical fibers and micro waves_[85]. As that electrons and photons play important roles in electronics and optics, phonons as another important kind of particles are responsible for the transmission of sound and the heat in acoustics and thermotics. That's because both sound and heat can be described as the mechanical vibration in the atomic lattices. The difference is that acoustic waves oscillate at low frequencies and propagate over a large distance, whereas most heat vibrations oscillate at high frequencies and travel small distance. Applications of phonons can be classified by working wave frequency ranges shown in Figure 1.11.

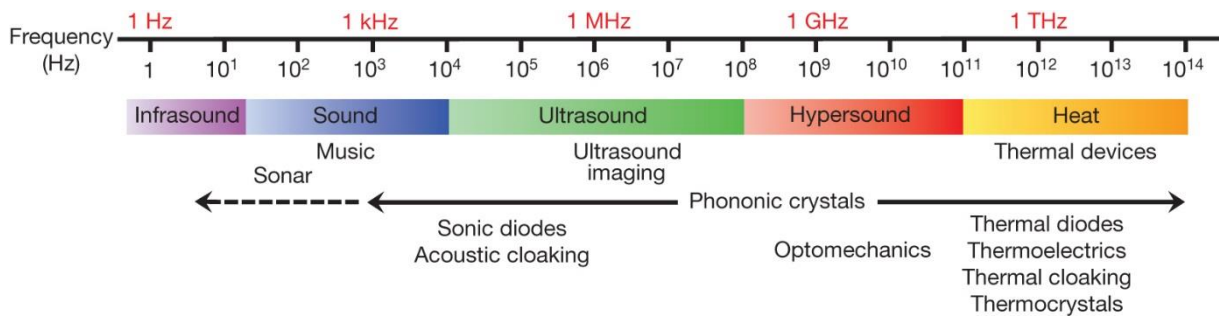


FIG. 1.11. Applications according to the phononic spectrum_[85].

Seen from Figure 1.11, we can find that phononic crystals have a large working frequency range (from 1KHz to 100THz), which gives phononic crystals a big potential of applications. In phononic crystals, elastic waves with frequencies within a specific range are not allowed to propagate through the periodic structure. As a result, a band gap of frequencies appears. Due to the wave interferences, the relevant wavelengths should be comparable to the structure periodicity. Consequently, the size of the phononic crystal is inversely proportional

to the working frequency. Here are several achievements of phononic crystals with different working frequencies shown in Figure 1.12.

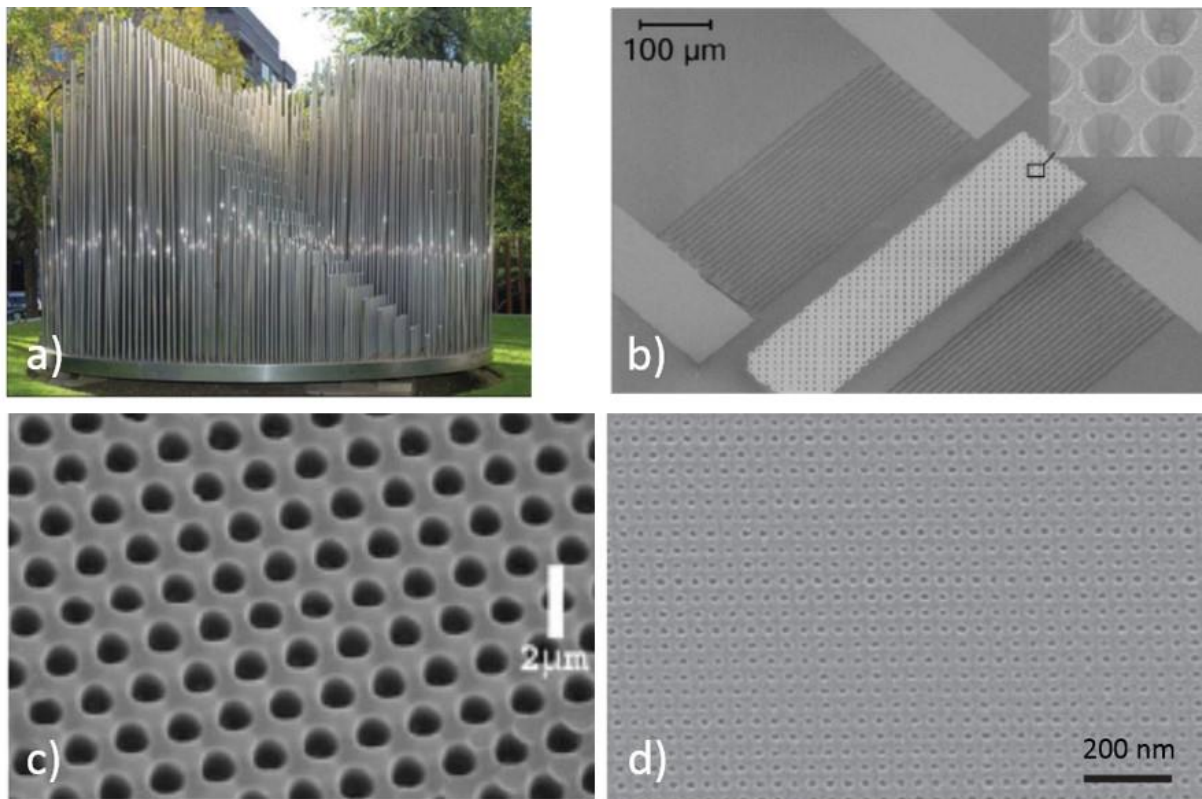


FIG. 1.12. Phononic crystals applied for different working frequency ranges: (a) sound (kHz) [10]; (b) Ultrasound (MHz) [55]; (c) Hypersound (GHz) [86]; (d) Heat (THz) [87].

As a new concept, PnCs have been proposed since two decades. It is too early to have some applications which can affect our everyday life. However, from another perspective, PnCs offer us a broad field to develop the applications. Understanding and controlling the PnCs' properties provides opportunities to thermally insulate building, reduce environmental noise, transform waste heat into electricity and develop earthquake protection. Here I list some recent progress and the development of new ideas and devices that make use of PnCs to control both sound and heat.

1.3.1 Acoustic insulators

The most general and easiest to understand is an acoustic insulator, due to the band gap property of PnCs. Indeed, for all frequencies contained in a complete band gap, a phononic crystal behaves like an acoustic shield, sending back all incident waves. With this principle, PnCs can be applied in someplace where there is too much noise or somewhere silence is

required, such as highways, construction sites, schools, hospitals, etc. As we know, the human being's auditory sense is typically sensitive from 20Hz to 20000Hz. So if a phononic crystal, whose band gap in that frequency range, is constructed on the propagation path of acoustic waves, the noise can be well cancelled.

The second application as an acoustic insulator for a phononic crystal is the attenuation of surface waves in seismic movement like the earthquake. Indeed, the earthquake can be understood as the vibration of guided waves. When the waves strike an obstacle, they will be partially scattered in all directions. The interferences resulting from multiple scattering on a periodic lattice of obstacles could thus lead to an important reduction of the amplitude of waves. As a result, the energy of earthquake can be reduced. F. Meseguer et al. [68] achieved the structure of the honeycomb and triangular structures of 6cm diameter cylindrical holes on the surface of the marble quarry shown in Figure 1.13. By measuring the transmission spectra, the attenuation of the seismic waves was found (Figure 1.14).

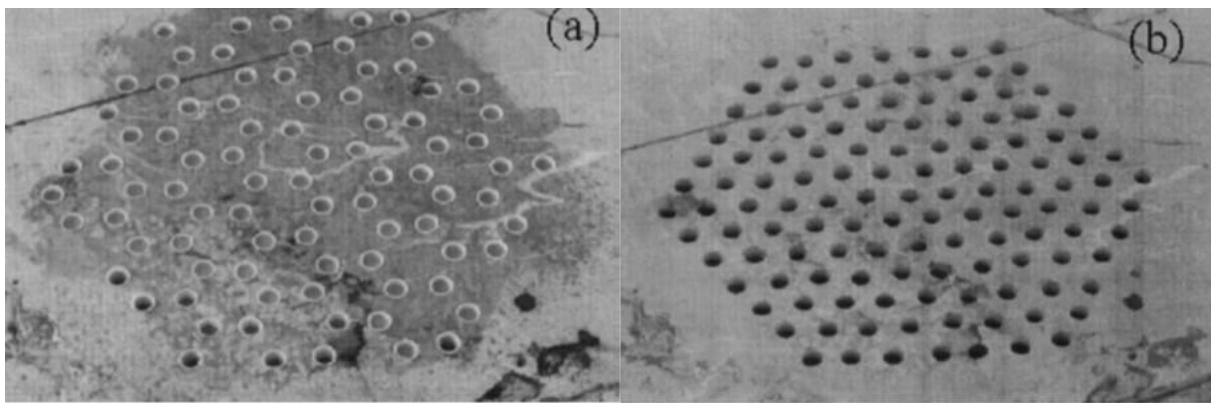


FIG. 1.13. Photographs of the honeycomb structure (a) and the triangular structure (b) used for the attenuation of surface waves [68].

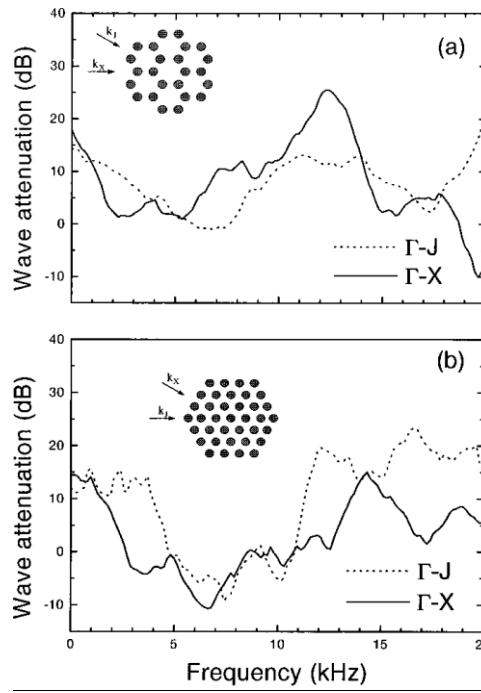


FIG. 1.14. Attenuation spectra of the honeycomb structure (a); the triangular structure (b) [68].

1.3.2 Acoustic diodes

Another application of PnCs is an acoustic diode. When we talk about diodes, we will think about the electronic devices which allows the current to pass in one direction but not in the opposite direction. The similar principle has been recently demonstrated for acoustic waves_[88-90]. An unidirectional sonic diode based on one dimensional PnC was achieved by Liang et al._[88] (see Figure 1.15). This PnC was made of alternating layers of glass and water, connected with a nonlinear acoustic medium. When an incident acoustic wave with frequency ω inside the band gap enters into the device from the left side, it will be partially converted within the nonlinear medium to a secondary wave with a frequency 2ω . The original wave is reflected when it propagates to the entrance of PnC because ω is in the band gap. Instead, the secondary wave with a frequency 2ω can propagate freely through the PnC. On the other hand, if the wave with a frequency ω is incident from the right side, it will be reflected also because of the band gap. In this way, an acoustic diode realized the unidirectional transmission. Acoustic diodes have been predicted with a potential medical application_[89].

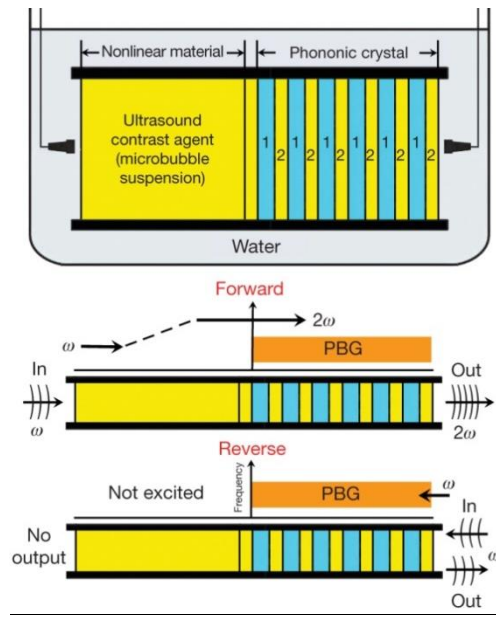


FIG. 1.15. An acoustic diode made of nonlinear acoustic medium and a 1D PnC [88].

1.3.3 Phononic crystal waveguides, cavities and filters

Placing point or linear defects in a PnC by removing scattering inclusions can be used to create functional devices such as waveguides [40, 83], cavities [41] and filters [42], which are useful for miniaturizing microwave devices used in signal processing.

Figure 1.16 represents an example of PnC waveguide [59]. A W2 waveguide realized by removing two rows of tungsten scattering inclusions from a square lattice W/SiO₂ phononic crystal plate. The measured normalized transmission of the suspended membrane W2 waveguide with the PnC is presented in Figure 1.17. Several modes where acoustic transmission is permitted through the defected bandgap crystal are seen in Figure 1.17, with a dominant mode at 68MHz where the relative transmission is equal to 1, indicating that no additional loss is created by the waveguiding.

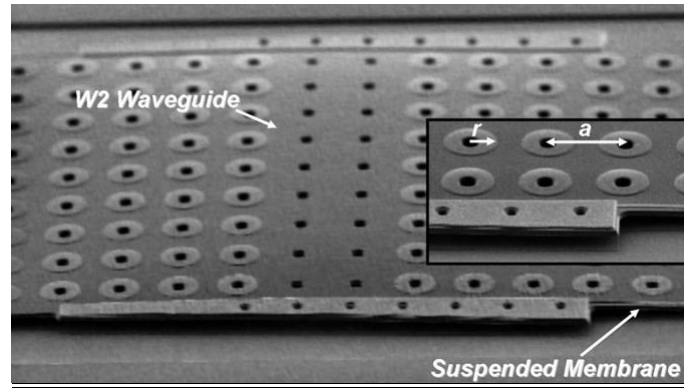


FIG. 1.16. SEM picture of a W2 waveguide realized by removing two rows of tungsten scattering inclusions from a square lattice W/SiO₂ phononic crystal plate [59].

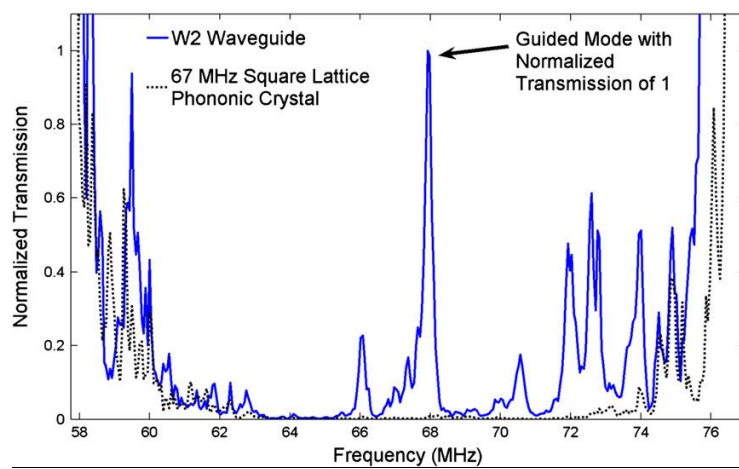


FIG. 1.17. Normalized transmission of the W2 waveguide device of a W/SiO₂ PnC [59].

1.3.4 Thermal metamaterials and heat management

Another interesting potential application of PnCs is to apply the metamaterial methods that are used for sound manipulation to the management of heat conduction. The heat flow is realized to manipulate by designing the thermal metamaterials_[91].

A new class of artificial materials for thermal conduction made of a multilayered composite approach was used to control the diffusive heat flow by shielding, concentrating and inverting heat current. These were not only theoretical concepts but also realized experimentally by constructing a thermal shield made of alternating concentric cylinders of latex rubber and a silicone elastomer and placing the shield within an agar-water matrix shown in Figure 1.18a. A constant temperature profile is obtained under a thermal gradient in the shield's inner region while the temperature profile outside is almost undistorted. On the other hand, by intentionally arranging the materials along the radial direction, the shell can act

as a thermal concentrator, with the thermal energy considerably enhanced within the shell and remaining uniform as shown in Figure 1.18b. In addition, for a spiral arrangement of the layer in the shell, heat rotates within the composite shell in a spiral manner such that heat flux changes its sign within the inner region of the shell, creating an apparent negative thermal conductivity shown as Figure 1.18c.

Besides these examples which we have mentioned above, to our knowledge, phononic crystals have many interesting features which provide enormous potential applications. But as a young subject, both theoretically and experimentally, there is much work which has not been dabbled yet. For example, the various combination of materials, different geometries and symmetries, different structures of inclusions (nanowires and nanoparticles), explorer of the fabrication methods, optimization of simulation, etc., all of which, need to be investigated. For the application aspect, the existent applications are not mature enough to be applied in our daily lives. Consequently, the investigation of PnCs has a large space to be improved.

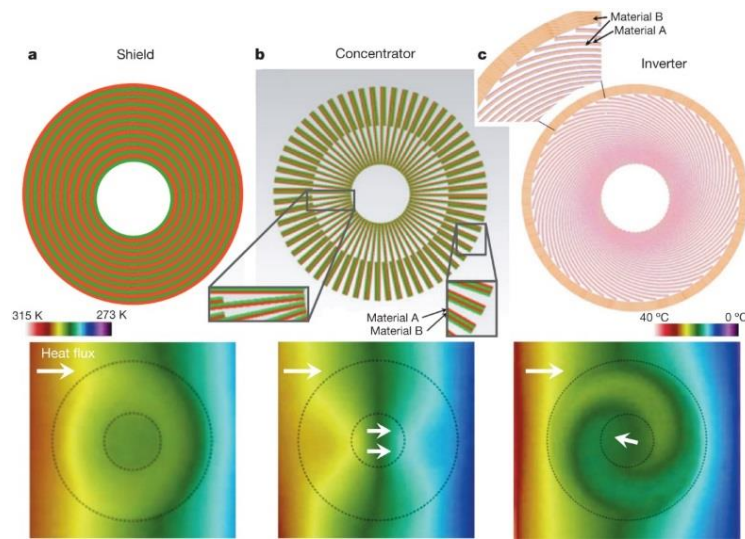


FIG. 1.18. Thermal metamaterials. (a) A thermal shield made of a concentric layered structure of latex rubber and silicone elastomer (top). The measured temperature profile for horizontal heat flux (white arrow): the shell maintains the inner region at constant temperature (bottom). (b) A thermal concentrator made of azimuthally alternating layers of latex and elastomer (top). The temperature profile, where heat flux is increased by 44% in the inner region (bottom). (c) A thermal inverter made of a spiral arrangement of copper and polyurethane (top). The temperature profile showing inversion of the heat flux (bottom) [85, 91].

1.4 Motivation

As a hot topic, active materials with periodic structures have been widely used to fabricate the magneto-electro-acoustic devices to manipulate surface acoustic waves. In my group, during the last several years, much work has been done in this subject.

Huan ZHOU_[92] and Noura GASMI_[93] worked on the theoretical and experimental study of the system based on magneto-elastic multi-layer films deposited on a piezoelectric substrate. In particular, Huan discussed the magnetic field dependence of acoustic wave's velocity in the multi-layer magneto-elastic films for different modes including sagittal and transverse waves. The schematic description is depicted in Figure 1.19. Theoretical and experimental results are shown in Figure 1.20.

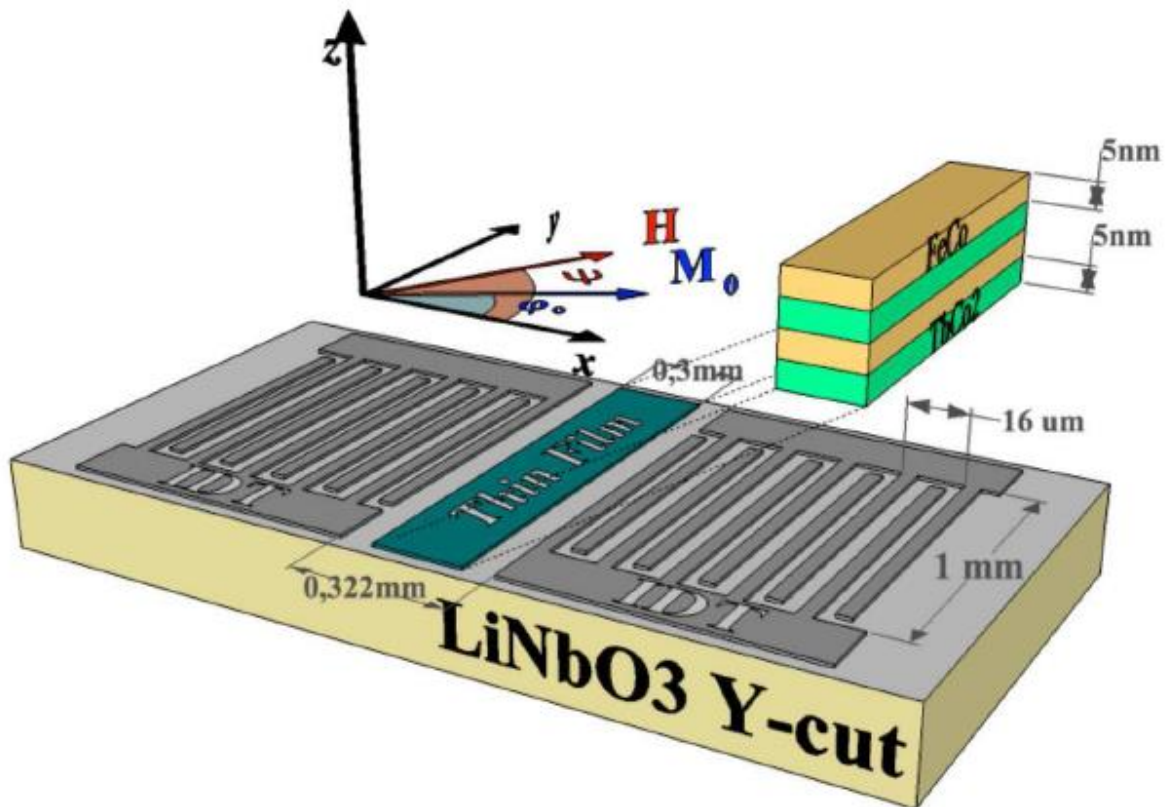


FIG. 1.19. Schematic description of the sample consisting of 20 uniaxial films of $\text{TbCo}_2(5\text{nm})/\text{FeCo}(5\text{nm})$ deposited on a Y-cut LiNbO_3 substrate and the associated coordinate system [92].

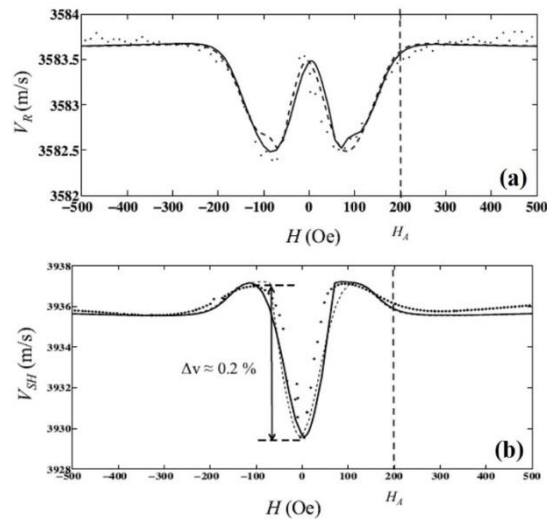


FIG. 1.20. Comparisons between the theoretical calculations (solid and dashed lines) and experimental results (points) for the wave velocity variation of Rayleigh waves (a) and shear horizontal waves (b) on function of the amplitude of the external magnetic field applied along the difficult axis. The solid and dash lines respectively correspond to a decreasing and an increasing intensity of the magnetic field [92].

Noura calculated more about the dispersion relations for the multi-layer system by using a polynomial method. In addition, Noura also worked on the theoretical study of magneto-elastic locally resonant phononic crystals composed of $\text{TbCo}_2/\text{FeCo}$ cylinder pillars on a LiNbO_3 substrate, shown in Figure 1.21. The effect of geometrical pillars and magnetic field was discussed about by calculating the band structures and transmission spectrum through a finite element method. The resonant frequency of a pillar can be controlled by the external magnetic field, shown in Figure 1.22.

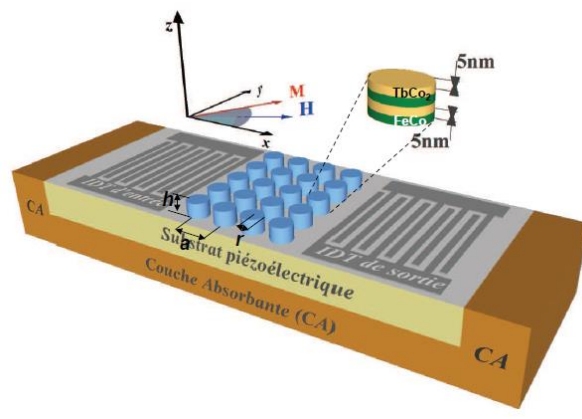


FIG. 1.21. Diagram of the surface acoustic wave device used to calculate the transmission spectra through a phononic crystal composed of $\text{TbCo}_2(5\text{nm})/\text{FeCo}(5\text{nm})$ pillars within square lattice deposited on a Y128-X LiNbO_3 substrate between two inter-digital transducers [93].

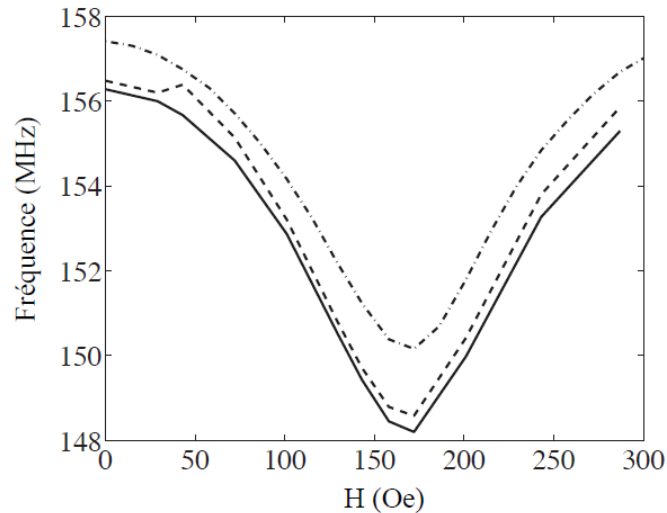


FIG. 1.22. Variation of the lower frequency (solid line) and the upper frequency (dashed line) of the 7th mode according to the amplitude of the external magnetic field. The dash-dot curve represents the change in the resonant frequency of the 7th mode of a pillar fixed on the bottom face on a function of the amplitude the external magnetic field [93].

In the thesis of Anastasia Pavlova_[94], the fabrication of submicron structures on ferromagnetic films using two different lithographic techniques: scanning probe lithography and electron-beam lithography for potential applications in spintronics and magnetically tunable SAW devices was experimentally investigated. The fabrication of one dimensional and two dimensional phononic crystals based on nickel inclusions for 2-6GHz frequencies using electron beam lithography was developed. The AFM pictures of 1D periodic oxide lines array on Ni film are depicted in Figure 1.23. The experimental results of frequency dependences of transmission function S_{21} for the structure with and without magnetic field are shown in Figure 1.24.

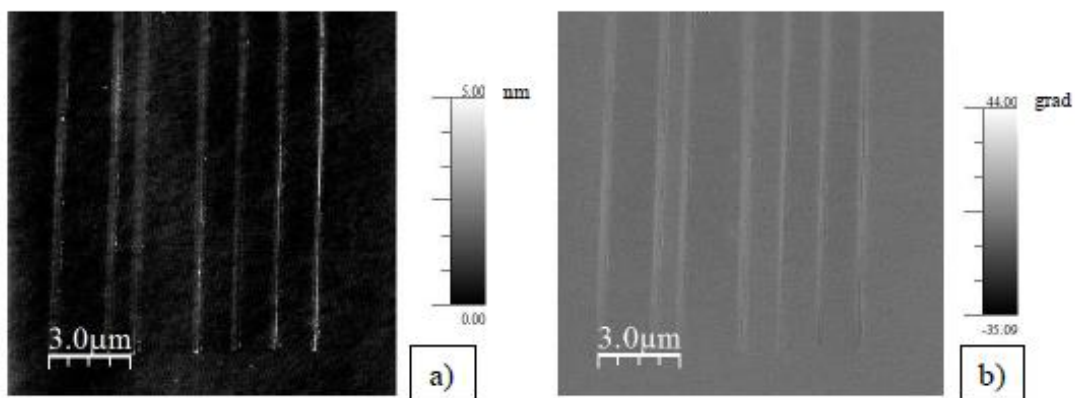


FIG. 1.23. AFM pictures of 1D periodic oxide lines array on Ni film: (a) topography; (b) phase [94].

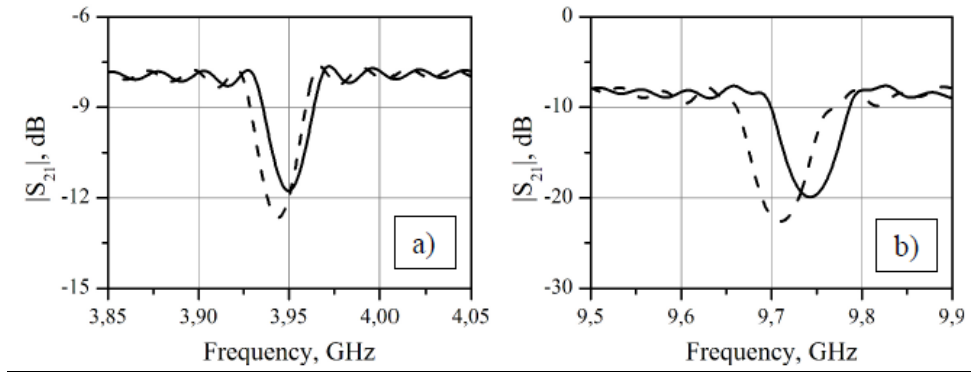


FIG. 1.24. Frequency dependences of transmission function S_{21} for the structure with $N=150$ oxide lines, height $h=3.5\text{nm}$ in the constant magnetic field (solid line) and without it (dashed line): period $a=500\text{nm}$ (a) and for $a=200\text{nm}$ (b). [94].

Furthermore, Sergey Yankin [95] investigated the surface acoustic wave radio frequency identification (SAW RFID) tag. The schematic description of SAW RFID tag is depicted in Figure 1.25. The comparison between theoretical and experimental results is shown in Figure 1.26. In addition, he has also contributed to the study of two dimensional nickel pillar-based phononic crystals. The theoretical models for the calculation of band structures and transmission spectrum for the PnCs with square lattice was built in his work.

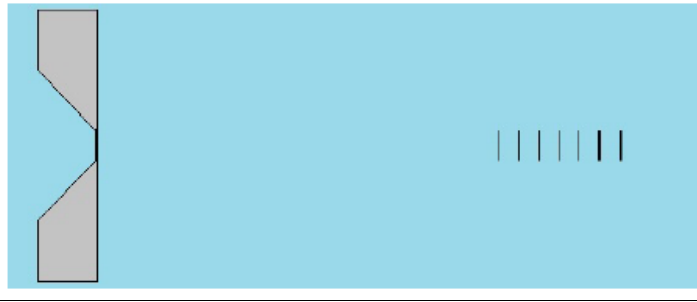


FIG. 1.25. Schematic description of the surface acoustic wave radio frequency identification in real proportions. [95].

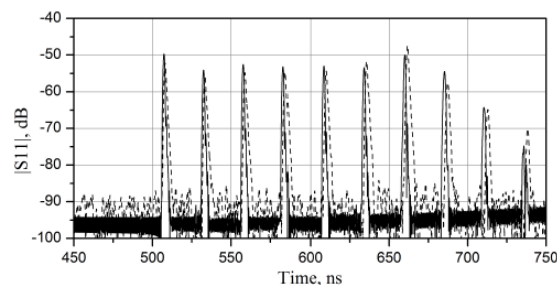


FIG. 1.26. Comparison between the time response of fabricated RFID SAW tag (dashed line) and the calculated response for the case of thin aluminum film parameters (solid line). [95].

My work can be regarded as a continuation of the study about the active materials with periodic structures. Although pillar-based phononic crystals have attracted more attention in recent years, not only in our group, there are still some problems which have not yet been solved, such as the effect of anisotropy of the PnCs, the coupling of different propagating modes, etc. The new composition of materials and geometrical parameters are required to be exploited. For the experimental aspect, there is no report on the detailed fabrication process of the pillar-based PnC using microfabrication techniques. And only a few structures of pillars and lattice symmetries were achieved.

Moreover, locally resonant pillar-based PnCs have a wide application potential for high-Q sensors. We are very interested in the temperature coefficient of frequency of a PnC. As a result, that may lead to an application of a thermal sensor.

For the consideration of magnetic properties, nickel was also chosen as the pillars' material for the PnCs, preparing for the following magnetic utilization.

Chapter 2: Theoretical foundations of phononic crystals

Phononic crystals are periodic composite materials or structures which have elastic waves' band gap property. So we can regard PnCs as the extension of the concept of crystals in solid state physics. The goal of the investigation of PnCs is essentially to study the propagation of elastic waves in periodic inhomogeneous media. Therefore, elasticity, as well as the lattice and band theories are the theoretical foundations of the investigation of PnCs.

In this chapter, firstly we will introduce some concepts and basic equations of dynamic elasticity. Then the propagation of surface acoustic waves on piezoelectric substrates will be studied, especially for the Rayleigh waves on lithium niobate semi-infinite substrate with different cut directions, considering with the boundary conditions. After that, theories of band structures and crystal lattice in solid state physics will be presented. Based on this, the PnC band gap mechanisms and properties will be summarized in this chapter. This chapter is served as a theoretical foundation of phononic crystal research.

2.1 Elasticity

2.1.1 Generalized Hooke's Law

As we have already known, for one point inside the media, if there is an external force acting at this point, it will generate a stress and a strain, which are both second order tensors with 6 independent components. Under the ideal conditions, for one point inside the media, it should satisfy the linear relationship between stress and strain, as shown in Equation (2.1), which is called generalized Hooke's Law.

$$\begin{bmatrix} \sigma_{xx} \\ \sigma_{yy} \\ \sigma_{zz} \\ \sigma_{yz} \\ \sigma_{xz} \\ \sigma_{xy} \end{bmatrix} = \begin{bmatrix} c_{11} & c_{12} & c_{13} & c_{14} & c_{15} & c_{16} \\ c_{21} & c_{22} & c_{23} & c_{24} & c_{25} & c_{26} \\ c_{31} & c_{32} & c_{33} & c_{34} & c_{35} & c_{36} \\ c_{41} & c_{42} & c_{43} & c_{44} & c_{45} & c_{46} \\ c_{51} & c_{52} & c_{53} & c_{54} & c_{55} & c_{55} \\ c_{61} & c_{62} & c_{63} & c_{64} & c_{65} & c_{66} \end{bmatrix} \begin{bmatrix} \epsilon_x \\ \epsilon_y \\ \epsilon_z \\ \gamma_{yz} \\ \gamma_{xz} \\ \gamma_{xy} \end{bmatrix} \quad (2.1)$$

In Equation (2.1), coefficients c_{mn} ($m, n = 1, 2, \dots, 6$) are called elastic coefficients which form a tensor of 36 components, called elastic tensor (stiffness tensor).

If the object is made of inhomogeneous media, elastic coefficients are functions of coordinates x, y, z . Conversely, if the object is made of homogeneous media, it can be proved that $[c_{mn}]$ is a symmetric tensor with constants, with $c_{mn} = c_{nm}$ ($m, n = 1, 2, \dots, 6$). Totally, there are 21 independent components. Specially, for isotropic homogeneous media, there are only 2 independent elastic coefficients. As a result, Equation (2.1) can be simplified in Equation (2.2).

$$\begin{cases} \sigma_{xx} = \lambda\theta + 2\mu\varepsilon_x, & \sigma_{yz} = \mu\gamma_{yz} \\ \sigma_{yy} = \lambda\theta + 2\mu\varepsilon_y, & \sigma_{xz} = \mu\gamma_{xz} \\ \sigma_{zz} = \lambda\theta + 2\mu\varepsilon_z, & \sigma_{xy} = \mu\gamma_{xy} \\ \theta = \varepsilon_x + \varepsilon_y + \varepsilon_z \end{cases} \quad (2.2)$$

In Equation (2.2), there are 2 independent elastic coefficients λ, μ called Lamé constants. Using dumb index, Equation (2.2) can be written as

$$\sigma_{ij} = \lambda\theta\delta_{ij} + 2\mu S_{ij} \quad (2.3)$$

$$\text{with } \delta_{ij} = \begin{cases} 1, & i = j \\ 0, & i \neq j \end{cases}$$

Taking the sum of the first three equations of Equation (2.2), we get

$$\Theta = (3\lambda + 2\mu)\theta = K\theta \quad (2.4)$$

Equation (2.4) expresses the relationship between volume stress and volume strain, which is called Hooke's Law for volume strain, with $\theta = \varepsilon_x + \varepsilon_y + \varepsilon_z$ called volume strain, $\Theta = \sigma_{xx} + \sigma_{yy} + \sigma_{zz}$ called volume stress and $K = 3\lambda + 2\mu$ called volume elastic modulus. We also have the relationship between Young's Modulus E , Shear Modulus G and Lamé constants, shown as below:

$$\begin{cases} E = \frac{(3\lambda+2\mu)\mu}{\lambda+\mu}, & G = \mu \\ \lambda = \frac{E\nu}{(1+\nu)(1-2\nu)} = \frac{G(E-2G)}{3G-E}, \\ \mu = \frac{E}{2(1+\nu)}, & \nu = \frac{\lambda}{2(\lambda+\mu)} = \frac{E-2G}{2G} \end{cases} \quad (2.5)$$

ν in this equation is called Poisson's ratio.

2.1.2 Basic equations of elastodynamics

According to the theory of elastodynamics, for continuous isotropic homogeneous completely linear elastic material with micro deformation and without initial stress, we consider an arbitrarily small micro volume element (mass point). We can build three kinds of basic equations to describe the relationship among force, displacement, stress and strain, as shown below:

Differential equation of motion (expression of force and displacement),

$$\sigma_{ij,j} + \rho f_i = \rho \ddot{u}_i \quad (2.6)$$

Geometrical equation (expression of displacement and strain),

$$S_{ij} = \frac{1}{2}(u_{i,j} + u_{j,i}) \quad (2.7)$$

Physical equation (expression of stress and strain),

$$\sigma_{ij} = \lambda \theta \delta_{ij} + 2\mu S_{ij} \quad (2.8)$$

In Equation (2.6), f_i is the external force acting on unit mass, ρ is the mass density of media, u_i is the displacement, \ddot{u}_i is the second order derivation of displacement with respect to time. The geometrical equation and the physical equation have been already mentioned above. Here for all equations, $i, j = x, y, z$.

In Cartesian coordinate system, there are 15 equations belonging to the three kinds of equations above, including 3 equations of motion, 6 geometrical equations and 6 physical equations with 15 unknowns, including 6 components of stress tensor, 6 components of strain tensor and 3 components of displacement u_x, u_y, u_z . All of them are unknown functions of space coordinates x, y, z and time t . These 15 equations constitute a closed equation system, called basic equations of elastodynamics based on Cartesian coordinate system.

Among all the equations, not each of them includes all the unknown functions. So we can choose some of unknown functions as basic unknown functions, which can be solved firstly. Then on the basis of these solved basic unknown functions, all the others can be solved

as well. As a result, we have 2 methods to solve this problem according to the choice of basic unknown function. For the first method, stress is chosen as the basic unknown function. For the second, displacement is chosen. In the equations of motion, there are partial derivative of stress and derivation of displacement-time, which is very hard to solve by the first method. So we always choose displacement as basic unknown functions to solve the equations of motion in elastodynamics. First, geometrical equation (2.7) is introduced into physical equation (2.8) to get the stress components expressed by displacement, which is introduced into equation of motion (2.6) for the second step. Finally the problem is solved. The equation of motion which chooses displacement as basic unknown function is called the Wiener Equation,

$$\rho \ddot{u}_i = \rho f_i + \sum_{j=1}^3 \left\{ \frac{\partial}{\partial x_i} \left(\lambda \frac{\partial u_j}{\partial x_j} \right) + \frac{\partial}{\partial x_j} \left[\mu \left(\frac{\partial u_i}{\partial x_j} + \frac{\partial u_j}{\partial x_i} \right) \right] \right\} \quad (2.9)$$

In Equation (2.9), $i, j = 1, 2, 3$. x_1, x_2, x_3 are corresponding to x, y, z . And u_1, u_2, u_3 are corresponding to u, v, w . Equation (2.9) can also be written as a vector form as

$$\rho \ddot{\mathbf{u}} = \rho \mathbf{f} + \nabla [[\lambda(\mathbf{r}) + 2\mu(\mathbf{r})](\nabla \cdot \mathbf{u})] - \nabla \times [\mu(\mathbf{r}) \nabla \times \mathbf{u}] \quad (2.10)$$

Because of the formula $\nabla^2 \mathbf{u} = \nabla(\nabla \cdot \mathbf{u}) - \nabla \times \nabla \times \mathbf{u}$, Equation (2.10) can be written in another form,

$$\rho \ddot{\mathbf{u}} = \rho \mathbf{f} + (\lambda + \mu) \nabla(\nabla \cdot \mathbf{u}) + \mu \nabla^2 \mathbf{u} \quad (2.11)$$

2.2 Surface acoustic waves on piezoelectric substrates

Because of the elasticity, every mass point in the media has an interaction with the adjacent mass points to reach an equilibrium state. If one point in the media has a disturbance, the relative positions among the adjacent points change. As a result, an elastic force between the disturbed point and the adjacent points appears. Therefore all the points around the disturbed points are into motion. This action is passed around to constitute a fluctuation started by a disturbance. We call this propagation process elastic wave. Since the dimension and size of the substrate where waves propagate can be different, the propagating properties are related to the imposed boundary conditions. Elastic waves can be divided into several types, such as bulk waves, surface acoustic waves (SAWs) and Lamb waves.

In this work, we are interested in the propagation of SAWs on piezoelectric substrates. In the following paragraphs, first of all, we present a little review about plane waves which are more simple and general.

2.2.1 Plane waves

Plane waves are a kind of elastic waves propagating in an isotropic bulk material. Here we try to seek a solution to the wave equation in the form of a progressive monochromatic plane wave propagating along a direction defined by a wave vector \mathbf{k} :

$$u_i = U_i e^{j(\omega t - \mathbf{k} \cdot \mathbf{x})} \quad (2.12)$$

Where U_i is a constant vector indicating polarization along the direction i , \mathbf{k} is the wave vector, \mathbf{x} is position, and ω is the angular frequency. Substituting Equation (2.12) in the differential equation of motion (2.6) with the definition of a unit vector $\mathbf{n} = \frac{\mathbf{k}}{|\mathbf{k}|}$, we obtain the Christoffel Equation:

$$\rho v^2 u_i = c_{ijkl} n_j n_k u_l \quad (2.13)$$

where v is the propagating velocity of elastic waves and c_{ijkl} is the stiffness tensor. Introducing the Christoffel tensor Γ , which is a second order tensor, $\Gamma_{il} = c_{ijkl} n_j n_k$, Equation (2.13) can be written as:

$$\Gamma_{il} u_l = \rho v^2 u_i \quad (2.14)$$

In the system of plane waves, the propagation equation (2.14) has solutions for elastic modes whose polarization is an eigenvector of Γ . The eigenvalues allow us to go back to the velocities.

Lamé and Helmholtz have proved that an elastic wave field satisfies the condition as below:

$$\mathbf{u} = \nabla \phi + \nabla \times \boldsymbol{\psi} \quad (2.15)$$

In the case of a homogeneous medium, according to Equation (2.11) and (2.15), we have:

$$v_L^2 \nabla^2 \phi = \frac{\partial^2 \phi}{\partial t^2} \quad (2.16)$$

That equation describes longitudinal compression waves propagating in the medium with a velocity $v_L^2 = \frac{\lambda+2\mu}{\rho}$. While we have another equation (2.17), which describes transversal shear waves propagating with a velocity $v_T^2 = \frac{\mu}{\rho}$.

$$v_T^2 \nabla^2 \psi = \frac{\partial^2 \psi}{\partial t^2} \quad (2.17)$$

Since these two equations are uncoupled, transversal and longitudinal waves in the infinite homogeneous, isotropic medium propagate independently to each other. The velocities ratio, given by:

$$\frac{v_L}{v_T} = \sqrt{\frac{\lambda+2\mu}{\mu}} = \sqrt{\frac{2-2\nu}{1-2\nu}} \quad (2.18)$$

depends only on the Poisson ratio ν of the medium. The Poisson ratio generally varies from 0 to 0.5, while for most materials it is around 0.33. This corresponds a sound velocity ratio of 1.41 for $\nu = 0$ and 1.99 for $\nu = 0.33$, respectively. The sound velocity ratio goes to infinity as ν approaches 0.5, which is the Poisson ratio typical for incompressible materials, such as fluids, that do not support shear waves.

From Equation (2.16) and (2.17), we can find a vector elastic field including wave equations of both longitudinal and transversal waves. And the velocity of longitudinal waves is faster than the velocity of transversal waves, so the former is called primary wave (P wave for short) and the latter is called secondary wave (S wave for short). Since the polarization direction of P wave is always parallel with normal direction of wave surface, so it is very easy to define. However, for S wave, it is more complex because the polarization direction of S wave can be any direction perpendicular with normal direction of wave surface. If the polarization direction of S wave is parallel with the horizontal axis x_3 , we call this kind of S wave SH wave. If the polarization direction of S wave is parallel with the vertical plan (x_10x_2), we call this kind of S wave SV wave. There is always a coupling between P waves and SV waves. In another word, one kind of waves can generate the other kind of waves by scattering. Conversely, SH waves are decoupled with neither P waves nor SV waves, which means the scattering of SH waves can only generate SH waves. P, SH and SV waves are shown in Figure 2.1.

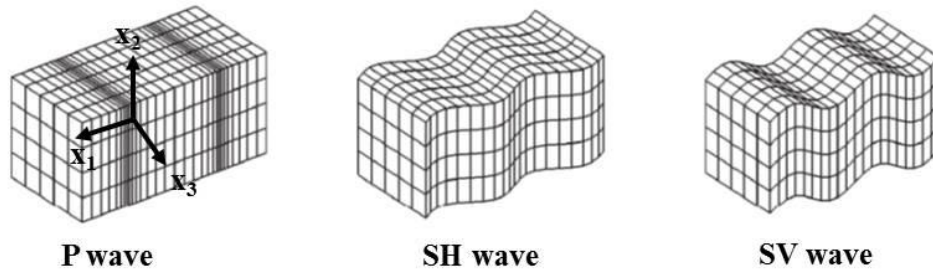


FIG. 2.1. Illustration of P, SH, SV wave [96].

2.2.2 Surface acoustic waves

If we impose a homogeneous free surface as a physical limitation to the medium of waves' propagation, the boundary conditions will affect the properties of waves propagating in the medium. In this case, there is a particular type of waves whose amplitude decreases exponentially with the depth and affect the substrate with only a thickness of the order of the wavelength of the mode. Indeed, these surface waves have a displacement vector whose normal component is evanescent. In particular, the so-called Rayleigh waves shown in Figure 2.2 were discovered by Lord John Rayleigh in 1885. These waves propagate with a velocity lower than that of bulk acoustic waves and have an elliptical polarization. In addition, Rayleigh wave is not dispersive and have a quasi-null attenuation while propagating in a substrate. In this thesis, the SAWs are referred to as Rayleigh waves.

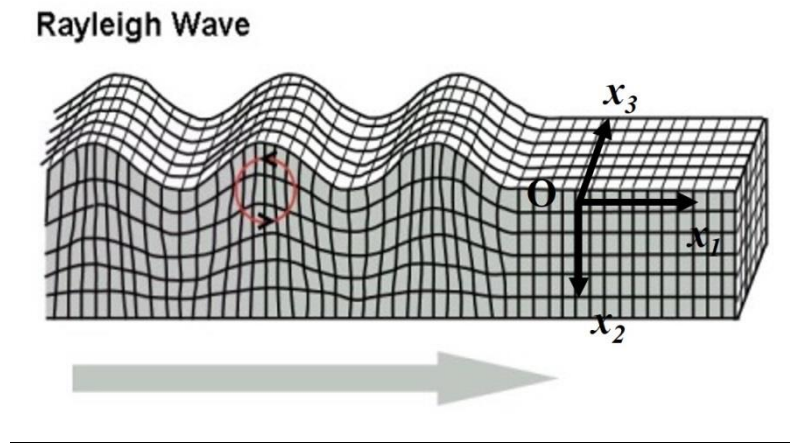


FIG. 2.2. Rayleigh waves [97].

We take the reference coordinate shown in Figure 2.2 to study the Rayleigh waves. Therefore, Ox_2 is perpendicular to the free surface and Ox_1 is the direction of propagation. The term :

$$u_l = u_{l0} e^{-\chi k x_2} e^{i(\omega t - k x_1)}, \quad \text{Re}[\chi k] > 0 \quad (2.19)$$

represents a wave (inhomogeneous) whose components of displacements decrease with the depth in direction Ox_2 , where χ is the decay constant, k is the wave vector.

The velocity v being considered as a parameter to determine the condition of compatibility is an equation of the sixth degree ($i\chi$). The exponential coefficients of $i\chi$ are real. There are three pairs of conjugate roots. Only three are acceptable $i\chi_r$ ($r=1, 2, 3$) as $\text{Re}[\chi_r k] > 0$. The others with $\text{Re}[\chi_r k] < 0$, leading to a wave whose amplitude increases with x_2 . For each of the values χ_r , the system provides the mechanical displacements u_{l0} to a proportionality coefficient. The general solution is a combination of these three partial waves of the same velocity v :

$$u_l = \left(\sum_{r=1}^3 A_r u_{l0}^r e^{-\chi_r k x_2} \right) e^{i(\omega t - k x_1)} \quad (2.20)$$

where A_r are the partial wave amplitudes and σ_{i2} is the normal stress. The mechanic free boundary condition at the surface requires that:

$$\sigma_{i2} = 0 \text{ or } \sum_{r=1}^3 \sigma_{i2}^{(r)} A_r = 0. \quad (2.21)$$

2.2.3 Rayleigh waves on LiNbO₃ substrate with different cut directions

As a kind of common piezoelectric materials, LiNbO₃ is widely used in the SAW devices for communicating, signal processing and sensing. Because of the anisotropy of LiNbO₃, the crystal cut direction can affect the propagation of acoustic waves on the surface of LiNbO₃ substrate.

In this work, the propagation of Rayleigh waves on LiNbO₃ substrate with different cut directions, including Y128-X cut, Y-X cut and Y-Z cut was calculated. The schematic diagram of the piezoelectric wafers with Y128-X cut, Y-X cut and Y-Z cut is depicted in Figure 2.3. The propagating velocity is different because of the different cut directions. For example, SAWs propagate on a Y128-X LiNbO₃ substrate with a velocity of 3980m/s; but if the LiNbO₃ substrate is Y-X cut or Y-Z cut, the corresponding velocities are 3762m/s and 3488m/s.

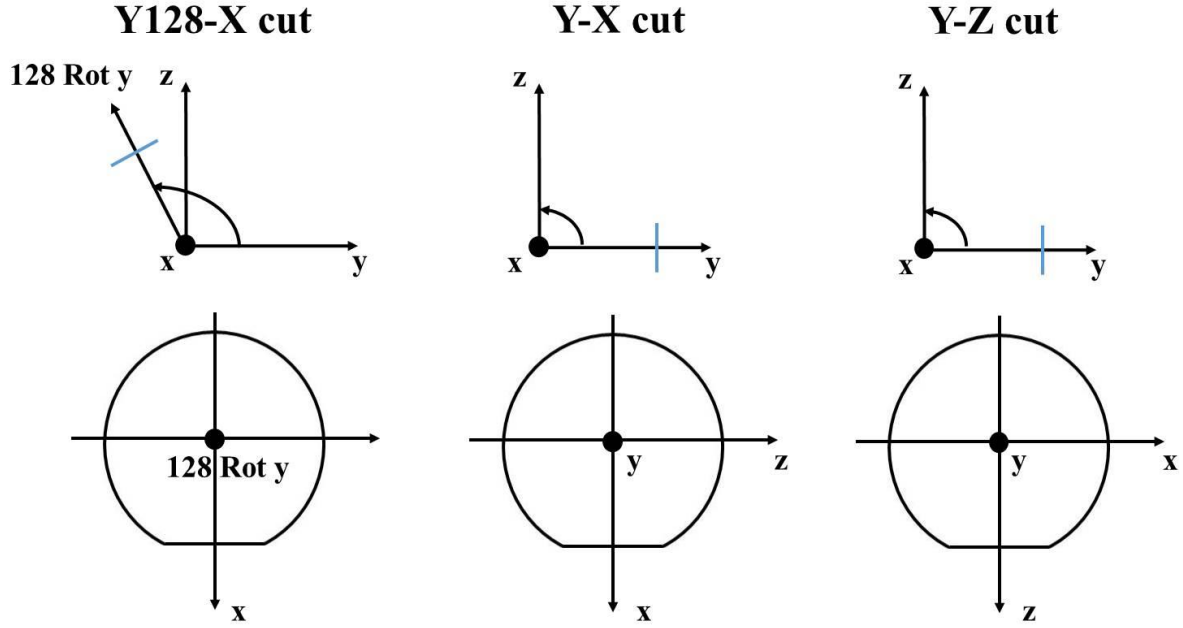


FIG. 2.3. Schematic diagram of the piezoelectric wafers with Y128-X cut, Y-X cut and Y-Z cut.

Besides the propagating velocities, the different cut for piezoelectric substrate can also affect the polarization. Normalized absolute values of the mechanical displacement components u , v , w along respectively direction x , y , z on function of depth in direction z for LiNbO_3 with Y128-X cut, Y-X cut and Y-Z cut were calculated. The results are depicted in Figure 2.4. In addition, the polarization of a Rayleigh wave mode in three directions with the same phase are shown in Figure 2.5. From Figure 2.4, we can observe that the displacement component w along direction z increases with the decrease of depth until to the surface. In x -direction, we find a zero crossing of $|u|$ at $z \approx -0.2\lambda$. It reveals that u changes sign at that point. That means that the motion of a single particle in the solid changes its rotation direction from clockwise (for $z > -0.2\lambda$) to counterclockwise (for $z < -0.2\lambda$). The transversal component of the displacement v increases slowly with the decrease of depth for Y128-X cut and Y-X LiNbO_3 . In these two cases, comparing with the components u and w , v is very weak, but it can't be ignored. However, v keeps zero all along in the case of Y-Z LiNbO_3 , which means Y-Z LiNbO_3 substrate can generate only saggital Rayleigh waves which has no transversal component. This phenomena can also be observed in Figure 2.5.

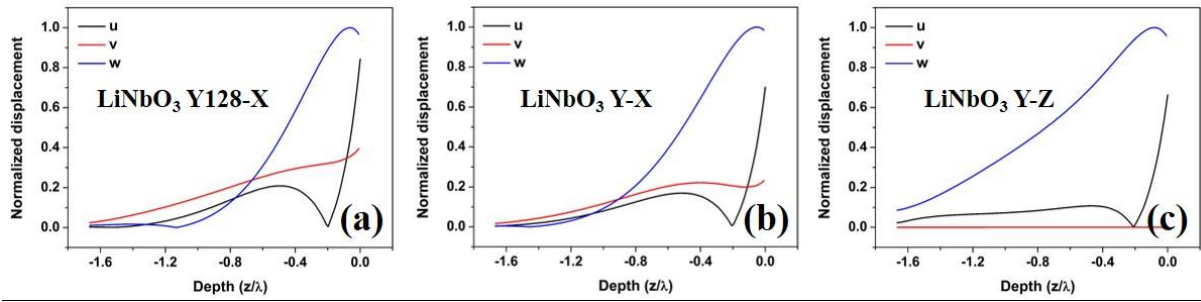


FIG. 2.4. z-dependence of displacement of a Rayleigh wave propagating on LiNbO₃ Y128-X (a), Y-X (b) and Y-Z (c) cut substrates, where λ is the SAW wavelength and $z=0$ corresponds to the surface.

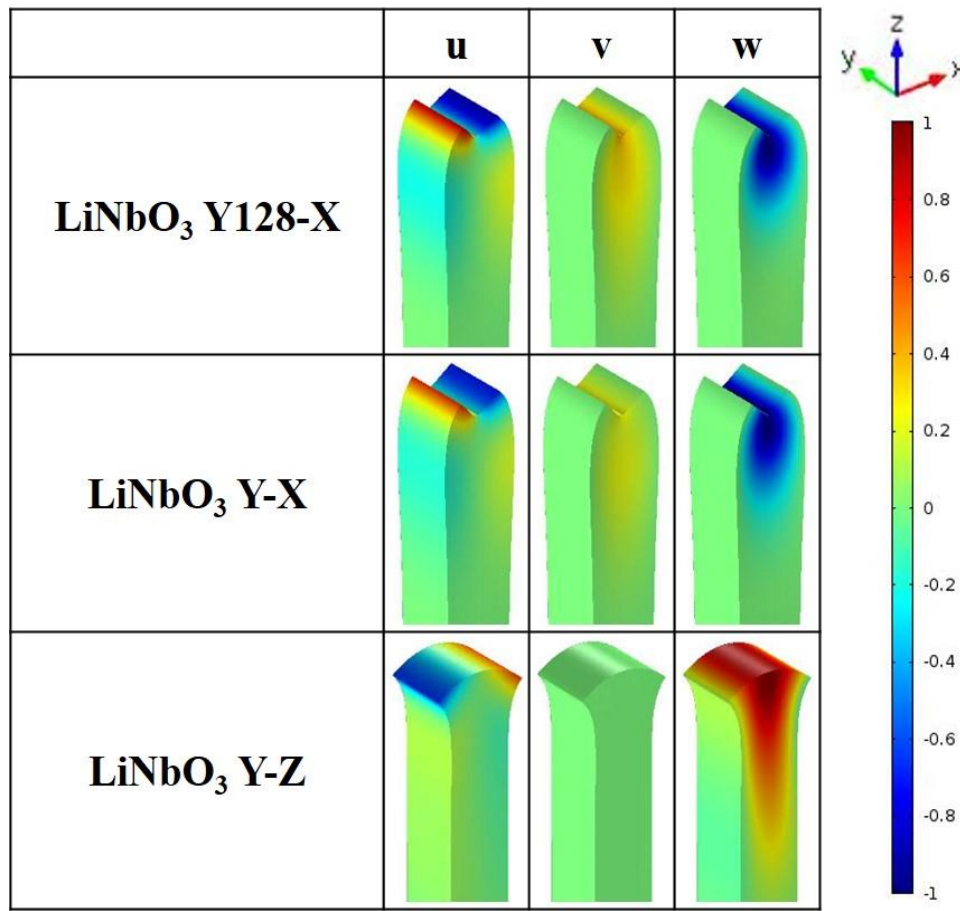


FIG. 2.5. The polarization of a Rayleigh wave mode in three directions with the same phase on LiNbO₃ Y128-X, Y-X and Y-Z cut substrates.

2.2.4 Piezoelectric consideration

A piezoelectric material is a material in which electric fields are established as a result of a mechanical deformation and vice versa. In this work, the piezoelectric substrate was used to generate SAWs. Consequently, the equation of motion (Equation 2.6) should be reconsidered with a piezoelectric term.

We start with the general form of the equation of motion without any external forces. Equation 2.6 turns to be :

$$\rho \frac{\partial^2 u_i}{\partial t^2} = \sum_j \frac{\partial \sigma_{ij}}{\partial x_j}, i, j \in \{1,2,3\} \quad (2.22)$$

with density ρ , elastic deformation u_i and stress tensor σ_{ij} . In an anisotropic piezoelectric medium, the generalized Hooke's Law shown in Equation 2.1 should also take into account a piezoelectric term. As a result, stress tensor σ_{ij} is a function of the stiffness tensor c_{ijkl} , the strain components S_{ij} mentioned in Equation 2.7, the piezoelectric tensor e_{ijk} and the electric field:

$$\sigma_{ij} = \sum_{k,l} c_{ijkl} S_{kl} - \sum_k e_{kij} E_k \quad (2.23)$$

The electric displacement D in a piezoelectric material is given by

$$D_i = \sum_j \epsilon_{ij} E_j + \sum_{j,k} e_{ijk} S_{jk} \quad (2.24)$$

where ϵ_{ij} is the dielectric tensor.

Since propagating velocity of elastic waves is typically five orders of magnitude smaller than the velocity of light, the electric field may be considered under the quasi-static approximation. Consequently, the electric field can be written as the gradient of a potential function ϕ :

$$\mathbf{E} = -\nabla\phi \quad (2.25)$$

Inserting Equation 2.23 and 2.26 into Equation 2.22, the equation of motion becomes:

$$\rho \frac{\partial^2 u_i}{\partial t^2} = \sum_{j,k} \left(e_{kij} \frac{\partial^2 \phi}{\partial x_j \partial x_k} + \sum_l c_{ijkl} \frac{\partial^2 u_k}{\partial x_j \partial x_l} \right) \quad (2.26)$$

As there are no free charges on the surface of the substrate for insulating solids, according to Poisson's Equation $\nabla \cdot \mathbf{D} = 0$ which is applied to Equation 2.24, we have

$$\sum_{i,j} \left(\epsilon_{ij} \frac{\partial^2 \phi}{\partial x_i \partial x_j} - \sum_k e_{ijk} \frac{\partial^2 u_j}{\partial x_i \partial x_k} \right) = 0 \quad (2.27)$$

Equation 2.26 and 2.27 yield four equations relating the four unknown quantities u and ϕ . By adding the appropriate boundary conditions, the coupled acoustic and electrical waves in a piezoelectric solid will be complete.

2.2.5 Boundary conditions

For a real problem, we need to define specific interfaces and borders and translate them in equations. Thus, equations of boundary conditions on displacement field \mathbf{u} and $\boldsymbol{\sigma}$ are the constraints expressed on these borders according to their nature which may be free, fixed or have a periodicity property.

1). Free and fixed boundary conditions

The free or fixed boundary conditions for one or more boundaries of domains are attached to the wave propagation. A free surface undergoes no constraints in any of its points. For example, there is a free surface at $z=z_1$, whose normal vector is \mathbf{n}_z along with the direction of axis z of the cartesian coordinate system. The free boundary condition is expressed by:

$$\boldsymbol{\sigma}_{z=z_1} \cdot \mathbf{n}_z = 0 \quad (2.28)$$

In the case of a fixed surface, no movement is possible for any particles of the medium. Thus, the fixed boundary condition can be expressed by a displacement field of zero $\mathbf{u}=\mathbf{0}$, which means $u_x=u_y=u_z=0$ for all of the points on this surface.

2). Periodic boundary conditions

Periodic boundary conditions are usually used to build periodic systems which are supposed to be very large or even infinite. The idea is to reduce the resolution to a periodic element to constitute a unit cell which is the new field of study. Periodic boundary conditions are introduced on the boundaries of this cell according to the periodicity along with the directions in order to express the fact that the conditions of the input acoustic waves are the same as the output of the cell, with a definite phase shift. The simulated system is theoretically infinite. A formulation given by the Bloch-Floquet Theorem is used to express the periodic behaviors of the displacement field and constraints of the elastic propagation. Thus, for a periodic infinite domain, the periodic boundary conditions can be written in forms of :

$$u_I(\vec{X} + \vec{a}) = e^{-i\vec{k}\cdot\vec{a}} u_I(\vec{X}) \quad (2.29)$$

and

$$\sigma_I(\vec{X} + \vec{a}) = e^{-i\vec{k}\cdot\vec{a}} \sigma_I(\vec{X}) \quad (2.30)$$

where u_I and σ_I are respectively displacement field and constraints, \vec{a} is a periodic vector of the structure.

All of the three boundary conditions mentioned above will be applied in this thesis, which will be discussed in details in the following chapters.

2.3 Lattice and band theory

Phononic crystals can be regarded as the extension of the concept of crystals in solid state physics. If the periodic parameter of a crystal turns to be microscopic or macroscopic, periodic atoms are replaced by elastic scatterers, the influence of PnCs on elastic waves is similar to the influence of atomic periodic potential field on electrons. Because of this similarity, the investigation of PnCs adopts directly definitions, concepts, describing methods and main conclusions of lattice and band theories in solid state physics.

2.3.1 Lattice

We use a point to represent a basic cell which is repeated indefinitely in crystals. Then the crystal can be regarded as a space matrix of points. There are many parallel lines and plans through these points to build up a grid, which is called a lattice.

Lattice has an important property called translational periodicity. It means a crystal can be built up by translating the unit cell along with 3 noncoplanar vectors \mathbf{a}_1 , \mathbf{a}_2 , \mathbf{a}_3 , which are the basic vectors of the lattice. The coordinates of each point in the crystal can be expressed by a linear composition of the 3 basic vectors.

$$\mathbf{R}_n = n_1 \mathbf{a}_1 + n_2 \mathbf{a}_2 + n_3 \mathbf{a}_3 \quad (2.31)$$

Among them, \mathbf{R}_n is the lattice vector, n_1, n_2, n_3 are integers. The lattice composed of endpoints of lattice vectors is called the Bravais Lattice.

Another important property of lattice is spatial symmetry, which means symmetric operations such as rotation and center inversion won't change either lattices or crystals.

Because of the spatial periodicity of crystals, for any point, its physical quantity at position \mathbf{r} $f(\mathbf{r})$ (such as density, Lamé constants, etc.) also has periodicity which satisfies Equation 2.32.

$$f(\mathbf{r} + \mathbf{R}_n) = f(\mathbf{r}) \quad (2.32)$$

\mathbf{R}_n is a direct lattice vector. Since $f(\mathbf{r})$ is a periodic function, it can be expanded in form of Fourier series,

$$f(\mathbf{r}) = \sum_{\mathbf{h}} F(\mathbf{G}_h) e^{i\mathbf{G}_h \cdot \mathbf{r}} \quad (2.33)$$

Introducing Equation 2.33 into Equation 2.32, we have

$$\mathbf{G}_h \cdot \mathbf{R}_n = 2\pi k \quad (2.34)$$

k is an integer.

\mathbf{G}_h is called a reciprocal lattice vector. We define $\mathbf{b}_1, \mathbf{b}_2, \mathbf{b}_3$ as a group of basic vectors for a reciprocal lattice.

$$\mathbf{G}_h = h_1 \mathbf{b}_1 + h_2 \mathbf{b}_2 + h_3 \mathbf{b}_3 \quad (2.35)$$

h_1, h_2, h_3 are integers.

The relationship between basic vectors for direct lattices and reciprocal lattices is shown below:

$$\mathbf{a}_i \cdot \mathbf{b}_j = 2\pi \delta_{ij} \quad i, j = 1, 2, 3 \quad (2.36)$$

If the volume of a unit cell is Ω , reciprocal lattice vectors can be expressed by direct lattice vectors.

$$\begin{cases} b_1 = 2\pi \frac{[a_2 \times a_3]}{\Omega} \\ b_2 = 2\pi \frac{[a_3 \times a_1]}{\Omega} \\ b_3 = 2\pi \frac{[a_1 \times a_2]}{\Omega} \end{cases} \quad (2.37)$$

As the definition of Bravais Lattice, the lattice composed of endpoints of reciprocal lattice vectors is called Reciprocal Lattice.

2.3.2 Bloch Theorem

As we have presented above, crystals have spatial periodicity and symmetry. As a result, the eigenfrequencies and eigenmodes have a certain symmetry as well. So when we study the eigenfield, the problem can be relatively simplified.

If a system described by the linear operator \hat{L} has translational periodicity for lattice vector \mathbf{R}_n (\hat{L} is commutative with translational operator $\hat{T}_{\mathbf{R}_n}$) which satisfies Equation 2.38, then the eigenvector of \hat{L} can be written in form as Equation 2.39, the corresponding eigenvalue $\lambda_{\mathbf{k},n}$ satisfies Equation 2.40. $\mathbf{u}_{\mathbf{k},n}(\mathbf{X})$ is periodic with a translation \mathbf{R}_n , which satisfies Equation 2.41. Eigenequation of \hat{L} turns into eigenequation of $\hat{L}_{\mathbf{k}}$ 2.42 which has an eigenvector $\mathbf{u}_{\mathbf{k},n}(\mathbf{X})$. \mathbf{k} can be any Bloch vector. \mathbf{G}_m is the reciprocal lattice vector of direct lattice vector \mathbf{R}_n .

$$[\hat{L}, \hat{T}_{\mathbf{R}_n}] = \hat{L}\hat{T}_{\mathbf{R}_n} - \hat{T}_{\mathbf{R}_n}\hat{L} = 0 \quad (2.38)$$

$$\boldsymbol{\Psi}_{\mathbf{k},n}(\mathbf{X}) = e^{i\mathbf{k}\cdot\mathbf{X}}\mathbf{u}_{\mathbf{k},n}(\mathbf{X}) \quad (2.39)$$

$$\lambda_{\mathbf{k},n} = \lambda_{\mathbf{k}+\mathbf{G}_{m,n}} \quad (2.40)$$

$$\mathbf{u}_{\mathbf{k},n}(\mathbf{X} + \mathbf{R}_n) = \mathbf{u}_{\mathbf{k},n}(\mathbf{X}) \quad (2.41)$$

$$\hat{L}_{\mathbf{k}}\mathbf{u}_{\mathbf{k},n} = e^{-i\mathbf{k}\cdot\mathbf{X}}\hat{L}e^{i\mathbf{k}\cdot\mathbf{X}}\mathbf{u}_{\mathbf{k},n} = \lambda_{\mathbf{k},n}\mathbf{u}_{\mathbf{k},n} \quad (2.42)$$

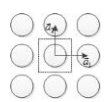
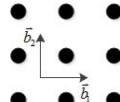
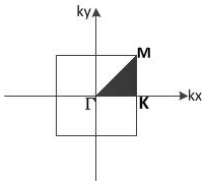
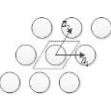
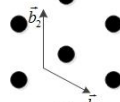
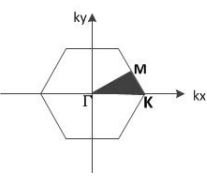
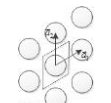
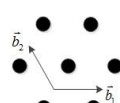
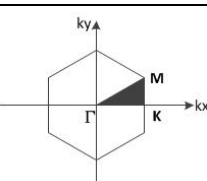
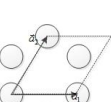
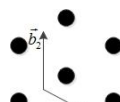
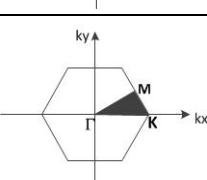
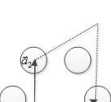
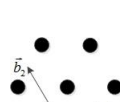
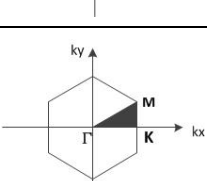
The Bloch Theorem tells us that any linear system of translational periodicity, whose eigenfield can be written in form of Equation 2.39, can be regarded as an amplitude-modulated plane wave, which has the same translational periodicity as crystals. \mathbf{k} is the wave vector. Therefore, waves in periodic systems are also called Bloch waves. In the other hand, its eigenvalue is translational periodic in reciprocal lattice, as shown in Equation 2.40. We

call the Weigner-Seitz cell in reciprocal lattice the first Brillouin zone. Equation 2.41 tells us that there isn't any new eigenvalue out of first Brillouin zone. Consequently, all values of \mathbf{k} are in the first Brillouin zone, which much reduces the ranges of \mathbf{k} .

In addition, if crystals have a certain point group symmetry, its eigenspectra has the same symmetry. Thus the range of wave vector \mathbf{k} can be further reduced. We call the new zone the irreducible Brillouin zone.

Bravais lattices, reciprocal lattices, first Brillouin zones and irreducible Brillouin zones of the normal two-dimensional lattices which will be talked about in the following parts are shown in Table 2.1.

TAB. 2.1. Bravais lattices, reciprocal lattices, first Brillouin zones and irreducible Brillouin zones of the normal two-dimensional lattices.

Lattice's name	Bravais lattice	Reciprocal lattice	First and Irreducible Brillouin zones	Direct and Reciprocal basic vectors
Square lattice				$\begin{cases} a_1 = a(1,0) \\ a_2 = a(0,1) \end{cases} \begin{cases} b_1 = \frac{2\pi}{a}(1,0) \\ b_2 = \frac{2\pi}{a}(0,1) \end{cases}$
Tri-X lattice				$\begin{cases} a_1 = a(1,0) \\ a_2 = a\left(\frac{1}{2}, \frac{\sqrt{3}}{2}\right) \end{cases} \begin{cases} b_1 = \frac{2\pi}{a}\left(1, -\frac{\sqrt{3}}{3}\right) \\ b_2 = \frac{2\pi}{a}\left(0, \frac{2\sqrt{3}}{3}\right) \end{cases}$
Tri-Y lattice				$\begin{cases} a_1 = a\left(\frac{\sqrt{3}}{2}, \frac{1}{2}\right) \\ a_2 = a(0,1) \end{cases} \begin{cases} b_1 = \frac{2\pi}{a}\left(\frac{2\sqrt{3}}{3}, 0\right) \\ b_2 = \frac{2\pi}{a}\left(-\frac{\sqrt{3}}{3}, 1\right) \end{cases}$
Hex-X lattice				$\begin{cases} a_1 = \sqrt{3}a(1,0) \\ a_2 = \sqrt{3}a\left(\frac{1}{2}, \frac{\sqrt{3}}{2}\right) \end{cases} \begin{cases} b_1 = \frac{2\pi}{\sqrt{3}a}\left(1, -\frac{\sqrt{3}}{3}\right) \\ b_2 = \frac{2\pi}{\sqrt{3}a}\left(0, \frac{2\sqrt{3}}{3}\right) \end{cases}$
Hex-Y lattice				$\begin{cases} a_1 = \sqrt{3}a\left(\frac{\sqrt{3}}{2}, \frac{1}{2}\right) \\ a_2 = \sqrt{3}a(0,1) \end{cases} \begin{cases} b_1 = \frac{2\pi}{\sqrt{3}a}\left(\frac{2\sqrt{3}}{3}, 0\right) \\ b_2 = \frac{2\pi}{\sqrt{3}a}\left(-\frac{\sqrt{3}}{3}, 1\right) \end{cases}$

2.3.3 Band structures

When we study the motion of electrons in solid, for any given wave vector \mathbf{k} , we can get a series of eigenvalues and the corresponding eigenvectors by solving Equation 2.42. Every eigenvalue and the corresponding eigenvector represents an inherent frequency and the corresponding motion state. As Bloch wave vector \mathbf{k} is a continuous variable, every eigenvalue is no longer a simple number but a function of \mathbf{k} . Thus, the function is usually called an eigenband. The corresponding vector is called an eigenmode. We choose \mathbf{k} as the horizontal axis and the eigenvalues as the vertical axis. The relationship between them is called band structure or dispersion diagram. As we have mentioned above, we know that for almost all the computations of band structures, \mathbf{k} is required only traversing the boundary of irreducible Brillouin zone. Here we use a classic example, the vibration of a diatomic chain, to explain the band structure. The structure of diatomic chain is shown in Figure 2.6.

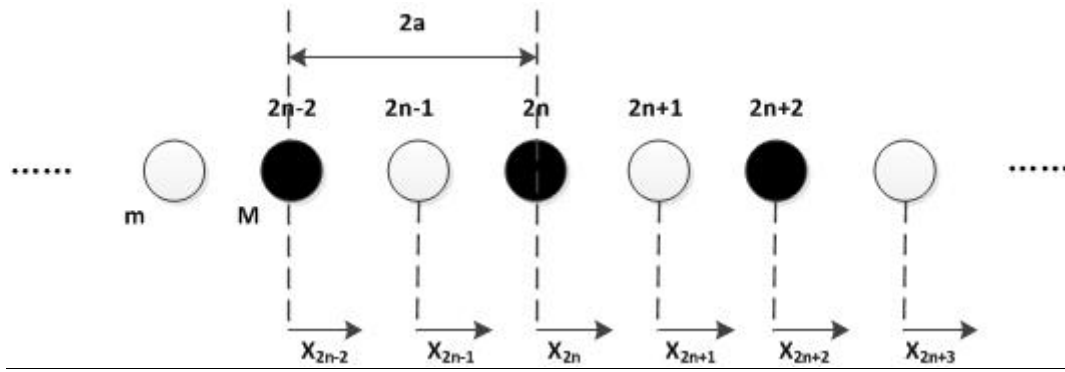


FIG. 2.6. Structure of diatomic chain.

We suppose that the unit cell of a one-dimensional diatomic chain is composed of two kinds of atoms, whose mass are m and M . The distance between two adjacent same atoms is $2a$ as the lattice constant. The atoms whose numbers are $2n-2, 2n-1, 2n, 2n+1, 2n+2$ are at positions $x_{2n-2}, x_{2n-1}, x_{2n}, x_{2n+1}, x_{2n+2}$. The interaction potential between two adjacent atoms is $U(a)$ at equilibrium position. $\delta = x_{2n+1} - x_{2n}$ is the relative displacement. The interaction potential becomes $U(a+\delta)$. By Taylor expansion, we have:

$$U(a + \delta) = U(a) + \left(\frac{dU}{dr}\right)_a \delta + \frac{1}{2} \left(\frac{d^2U}{dr^2}\right)_a \delta^2 + \dots \quad (2.43)$$

In Equation 2.43, the first term is a constant. The second term is 0 because the potential is minimum at equilibrium position. When δ is very small, the vibration is weak, the expansion terms can be kept to second order. Thus we have,

$$-\frac{dU}{d\delta} = -\left(\frac{d^2U}{dr^2}\right)_a \delta = -\beta\delta \quad (2.44)$$

β is the restoring force constant.

Motion equations for points $2n+1$ and $2n+2$ are:

$$\begin{cases} m \frac{d^2 x_{2n+1}}{dt^2} = \beta(x_{2n+2} + x_{2n} - x_{2n+1}) \\ M \frac{d^2 x_{2n+2}}{dt^2} = \beta(x_{2n+3} + x_{2n+1} - x_{2n+2}) \end{cases} \quad (2.45)$$

Here we suppose $M > m$.

The stable solution of Equation 2.45 can be written in form of harmonic vibration with an angular frequency ω .

$$\begin{cases} x_{2n+1} = Ae^{i[k(2n+1)a - \omega t]} \\ x_{2n+2} = Be^{i[k(2n+2)a - \omega t]} \end{cases} \quad (2.46)$$

In Equation 2.46, k is the wave vector, A and B are amplitudes for these 2 kinds of atoms. Take Equation 2.46 into Equation 2.45, we have,

$$\begin{cases} (2\beta - m\omega^2)A - (2\beta \cos ka)B = 0 \\ -(2\beta \cos ka)A + (2\beta - M\omega^2)B = 0 \end{cases} \quad (2.47)$$

If it exists some propagating modes, Equation 2.47 should have nonzero solutions, so the determinant of coefficients of Equation 2.47 must be equal to 0.

$$\begin{vmatrix} 2\beta - m\omega^2 & -2\beta \cos ka \\ -2\beta \cos ka & 2\beta - M\omega^2 \end{vmatrix} = 0 \quad (2.48)$$

By solving Equation 2.48, we can get,

$$\omega^2 = \frac{\beta}{mM} \left\{ (m + M) \pm [m^2 + M^2 + 2mM \cos 2ka]^{\frac{1}{2}} \right\} \quad (2.49)$$

According to Equation 2.49, we find that there are 2 kinds of dispersion relationships between angular frequency ω and wave vector k , as shown in Equation 2.50 and 2.51.

$$\omega_1^2 = \frac{\beta}{mM} \left\{ (m + M) + [m^2 + M^2 + 2mM \cos 2ka]^{\frac{1}{2}} \right\} \quad (2.50)$$

$$\omega_2^2 = \frac{\beta}{mM} \left\{ (m + M) - [m^2 + M^2 + 2mM \cos 2ka]^{\frac{1}{2}} \right\} \quad (2.51)$$

The dispersion relationship in the first Brillouin zone is displayed in Figure 2.7. Since $M > m$, the minimum of ω_1 is even bigger than the maximum of ω_2 , which means the frequency of dispersion branch ω_1 is always higher than that of ω_2 . We call ω_1 an optical branch and ω_2 an acoustic branch. We notice that there is no dispersion curve in the shadow part between the optical branch and the acoustic branch, which means that it doesn't exist any propagating modes, corresponding to the waves whose frequencies are in the shadow part for one-dimensional diatomic lattice. Consequently, the vibration in that frequency range can't propagate stably in the one-dimensional diatomic lattice. The frequency range is called a band gap. The band gap property is always regarded as the most important property of phononic crystals because the existence and the position of band gaps of PnCs can be designed in order to control the propagation of elastic waves. That's the significance of investigation of PnCs.

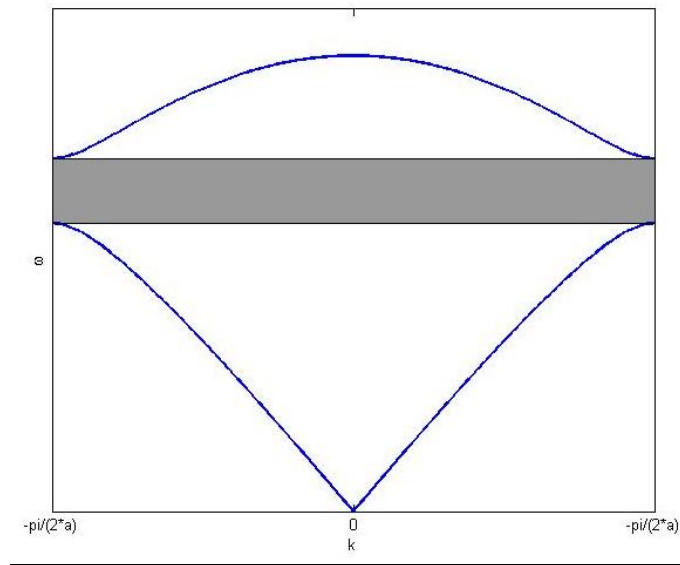


FIG. 2.7. Vibration spectra for one-dimensional diatomic lattice.

2.4 PnC band gap mechanisms and properties

According to the comparison of lattice constant and wavelength corresponding to the frequency of band gap, band gaps can be classified into 2 kinds. One is due to Bragg scattering (lattice constant and wavelength corresponding to the frequency of band gap are in the same order of magnitude). The other is due to local resonance (wavelength corresponding

to the frequency of band gap is much greater than lattice constant). Generally speaking, the two mechanisms are both the results of periodic structures and Mie scattering of single scatterers. Nevertheless, for Bragg scattering type PnCs, the interaction of primitive cells, in another word, the periodic structures are the dominant factors. For local resonance type PnCs, the resonance of single scatterers plays the leading role.

2.4.1 Bragg scattering

W. H. Bragg and W. L. Bragg established Bragg's Law based on the investigation of X ray scattering in crystals_[98], which can be applied more generally in the scattering of a plane wave in periodic media. They interpreted these results by equating the crystal structure consisting of a periodic arrangement of parallel planes and explaining the reflection spectrum obtained by an interference phenomenon between waves X. The waves reflected by the successive layers interfere constructively if the difference in propagation path is a multiple of 2π , building to the enunciation of Bragg's law, which can be deduced intuitively enough of geometrical optics, such as shown in Figure 2.8.

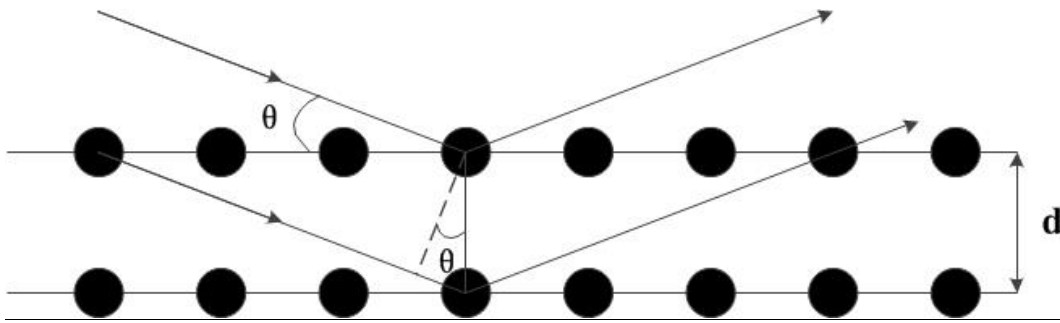


FIG. 2.8. Bragg's Law.

Bragg's Law can be written in form of:

$$n\lambda = 2d\sin\theta \quad (2.52)$$

where n is an integer, λ is the wavelength, d is the distance between two crystallographic planes and θ is the angle between the incident beam and the crystal surface.

If a wave propagates in the periodic media which has two different permittivities ϵ_1 and ϵ_2 , the Bragg's wavelength is:

$$\lambda_{\text{Bragg}} = 2 \cdot n_{\text{eff}} \cdot a \quad (2.53)$$

Where n_{eff} is the effective index, a is the periodicity. With this condition, the reflectivity is maximum. We consider a normal incident plane wave with a wave vector \vec{k} whose wavelength satisfies Bragg's Law. The reflected wave is in the same phase and has a wave vector $-\vec{k}$. Therefore in the case of Bragg mirror, the transmission is null, where there is constructive interference between incident waves and reflected waves. In another word, there are band gaps for which the propagation is impossible.

When the media of Bragg type PnCs is liquid or gas, there are only longitudinal waves. The band gap is due to the constructive interference of waves reflected by adjacent cells. The central frequency of the first band gap is always nearby $c/2a$. c is the propagating velocity in media, a is the lattice constant. On the other hand, when the media is solid, there is the conversion of transversal waves and longitudinal waves. Thus the band gap mechanism is much more complex.

Bragg type PnCs have 2 main characteristics: (1) Magnitude of the wavelength corresponding to the frequency in the band gap is always of the same order as the lattice constant. (2) The biggest attenuation usually appears around the central frequency of the band gap.

2.4.2 Local resonance

According to the Bragg scattering mechanism which we have mentioned above, we know that the lattice constant should be half of the wavelength in the media. For example, if we want to achieve the acoustic insulation for 500 Hz in the water, we need to construct a Bragg type PnC with a lattice constant which is equal to 1.5 m. On the other hand, Bragg scattering is related to the periodicity, so several periodic structures are needed. The whole size of PnC is several meters. Obviously it is not very practical. Therefore PnCs which are not restricted by the lattice constant are required.

Locally resonant phononic crystals were first proposed by Zhengyou LIU in 2000_[4]. Composites which have a simple micro-structure unit consisting of lead balls with relatively high density and a coating of elastically soft material silicone rubber are embedded in epoxy media to form a three dimensional PnC with three components. The theoretical and experimental results all show that the wavelength corresponding to the band gap of the PnC is much greater than the lattice constant. This discovery broke through the restriction of Bragg

scattering mechanism. They also found that the existence of band gaps without periodic structures. As a result, locally resonant mechanism for elastic wave's band gaps was proposed.

According to the locally resonant mechanism, various scatterers resonate with the excitation of elastic waves with certain frequencies. Because of the resonant scattering, elastic waves are attenuated sharply during the propagation, resulting in the prohibition of the waves' propagation. Since the generation of locally resonant band gaps depends on the interaction between the scatterers' resonant characteristic and the progressive waves, the relevant band gap frequencies are related to the inherent vibration characteristic. That explains why the relevant wavelength of the band gap can be much greater than the lattice constant.

There are several essential characteristics for locally resonant PnCs:

(1). Relevant frequency of band gap is much lower than that of Bragg scattering band gap, which leads to the control of big wavelengths with small sizes of scatterers. Generally, the lattice constant of locally resonant PnCs is two orders of magnitude lower than the relevant wavelength of band gap.

(2). There are flat band gaps in the band structures. Locally resonant phenomena exists in the internal wave field. It means the waves with different directions and different values have the same vibration mode.

(3). The width of the band gaps increases with the increasing of filling fraction.

All these characteristics will be shown in the band structures in the following parts of the thesis.

To control a band gap, we need to know where the band gap is and how much the attenuation is. And also we need to know the main factors for these two points.

(1). Influencing factors of band gap frequencies.

The starting frequency of a band gap is related to the equivalent mass and the equivalent stiffness of local oscillators. Thus, all the materials and structural parameters which can bring about changes in local oscillators' equivalent mass and equivalent stiffness can affect the starting frequency of a band gap. For the cut-off frequency, besides all these

factors above, the parameters which can bring about changes in the equivalent mass of media can also take effect.

(2). Influencing factors of band gap attenuation

Theoretical frequency ranges of locally resonant band gaps are related to the equivalent mass and stiffness of oscillators and media. Devices can be designed to have a relatively wide frequency range. However experimentally, the attenuation in the band gap of a PnC with a finite structure is anti-symmetric_[4, 99, 100]. There is always a sharp attenuation peak at the resonant frequency of oscillators, but for the other frequencies in the band gap, the relevant attenuation is very small. This feature is totally different from the band gap characteristics of Bragg scattering PnCs. Much research has demonstrated that the contrast of equivalent stiffness of oscillators and media of a locally resonant PnC is the main factor which can affect the band gap attenuation_[101-103].

In conclusion, the propagation of elastic waves in both Bragg Scattering PnCs and Locally Resonant PnCs is a complicated multiple-scattering resulting in the existence of band gaps. The comparison of these two kinds of PnCs is shown in Table 2.2. Though the inner mechanisms of band gaps are very complicated, we can distinguish the two kinds of PnCs simply by the relevant wavelengths in the band gaps.

Table 2.2. Comparison of Bragg Scattering PnCs and Locally Resonant PnCs.

PnC type	Bragg Scattering PnC	Locally Resonant PnC
Mechanism	Interaction between primitive cells of the periodic structure	Locally resonant characteristics of a single scatterer
Frequency range	High frequency	Low frequency
Relevant wavelength	Two times the lattice constant	Two orders of magnitude greater than lattice constant
Band gap features	Large band gaps with the biggest attenuation around the central frequency	Flat bands exist in band structures; Sharp attenuation peaks at the resonant frequencies of oscillators
Influencing factors	Contrast of materials' densities and elastic constants, filling fractions, lattice forms and symmetries of scatterers	All the parameters related to the inherent locally resonant characteristics of a single scatterer

When the wavelength in PnCs is of the same order as the lattice constant ($\lambda \approx a$), we usually talk about Bragg Scattering PnCs.

When the wavelength in PnCs is at least one order of magnitude greater than the lattice constant ($\lambda \gg a$), we usually talk about Locally Resonant PnCs.

When the wavelength in PnCs is much smaller than the lattice constant ($\lambda \ll a$), we can regard this case as the propagation of elastic waves in a homogeneous medium.

2.5 Conclusion

In this chapter, we have mainly talked about the theoretical background of this work. We started with the discussion of elasticity by revealing the generalized Hooke's Law and the basic equations of elastodynamics. Then we have talked about the surface acoustic waves on piezoelectric substrates, for example LiNbO_3 in this work. Beginning with the plane waves, the solution of SAWs, especially for the Rayleigh waves were discussed, considering the case of piezoelectric medium and adding the boundary conditions. Furthermore, as phononic crystals are a kind of periodic structures, we reviewed some concepts and properties related to the lattice and band theory, as well as the band structures. At last, we presented the two well-known mechanisms of phononic crystals, referring to Bragg scattering and local resonance.

The background mentioned in this chapter can be regarded as the theoretical preparation of this work. In this work, we will mainly investigate the pillar-based locally resonant phononic crystals for surface acoustic waves. This system first proposed in the work of A. Khelif et al. [29, 40-42, 73-75, 77-79]. N. Gasmı [93] and S. Yankin [76, 95] have also contributed to this domain during their Ph-Ds. To summarize the previous work, it was always focused on the appearance of band gaps and the locally resonant frequencies. Pillar's polarization has not been deeply discussed. From my point of view, the polarization of pillars can reflect many intrinsic properties relating to the resonance of pillars. Consequently, in this work, pillar-based locally resonant PnCs will be investigated from the viewpoint of pillar's polarization. Furthermore, as the exploration of the potential application for high-Q thermal PnC sensors, temperature coefficient of frequency for surface modes will be first studied in this work.

Chapter 3: Modeling of phononic crystals by the finite element method

In this chapter, the simulation is realized by Finite Element Method (FEM) using the commercial software Comsol Multiphysics v4.3a. The diagrams of the band structures and the transmissions of PnCs with different symmetric lattices are calculated. The evidence of pillar-based PnC band gaps is shown. The effect of pillar's geometrical parameters including radius and height on locally resonant PnC band gaps are discussed, as well as the effect of anisotropy which refers to the lattice symmetries of PnCs. Pillar's polarization are mainly mentioned in this chapter. Furthermore, material consideration is given to show the influence of elastic parameters such as Young's Modulus and density on band gaps. In addition, temperature coefficients of frequency of surface modes which can be applied in the thermal PnC sensors are studied in this chapter. This chapter starts with the introduction of the finite element method.

3.1 Principles of finite element method

The Finite Element Method can be used in various physical problems by solving the differential equations. The calculations for the band structures and transmissions of PnCs by common analytical methods seem to be impractical when the system becomes complex. To solve this problem, FEM provides the discretization of the continuous irregular geometries.

The prerequisite of the utilization of FEM is that one irregular domain can be divided into small regular pieces in which the differential equations can be approximately solved. Then these differential equations for small regions are assembled to compute the behavior of the system over the entire domain. The divided small regions are regarded as elements and the process of division is called the discretization. These elements are connected at specific points, called nodes, and the assembly process requires that the solution be continuous along common boundaries of adjacent elements_[104]. A discretized domain composed of triangular elements is shown in Figure 3.1.

The solution of the differential equation applied to the subdomain of each single element is replaced by a continuous function approximating the distribution of the primary field variables, expressed at each nodal point of the element_[105]. A system of equations in terms of each node can be computed for each element and subsequently they are assembled to form a piecewise approximation problem for the entire domain.

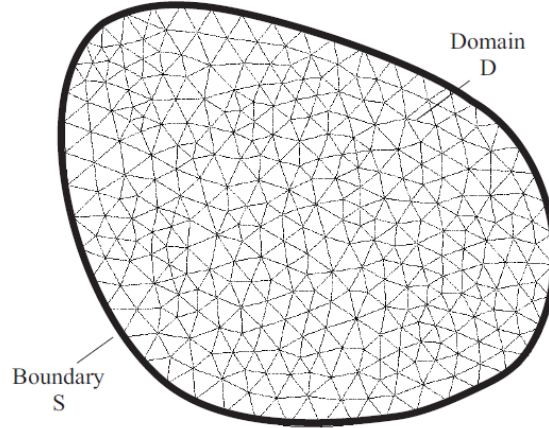


FIG. 3.1. Discretization of a domain using triangular shape finite elements [106].

3.2 Modeling of band structures

In this work, FEM was used for the eigenfrequency analysis. We computed the SAW mode spectra for different designs of PnCs using COMSOL MULTIPHYSICS software. The computation of the acoustic wave propagation in this software starts with the dynamic equations for anisotropic electro-elastic material shown in Equation 3.1, when body forces, current density and variation of electric charge density are disregarded:

$$\begin{cases} \frac{\partial u_i}{\partial t^2} = \frac{1}{\rho_0} \frac{\partial T_{ij}}{\partial x_j} \\ \frac{\partial D_i}{\partial x_i} = 0 \end{cases} \quad (3.54)$$

with the following constitutive equations

$$\begin{cases} T_{ij} = C_{ijkl} \frac{\partial u^l}{\partial x_k} + e_{kij} \frac{\partial \phi_e}{\partial x_k} \\ D_i = \epsilon_{ij} \frac{\partial \phi_e}{\partial x_j} + e_{kij} \frac{\partial u_j}{\partial x_k} \end{cases} \quad (3.55)$$

Here u_i is the displacement field, T_{ij} is the stress tensor, D_i is the electric displacement, ρ_0 is the density, C_{ijkl} is the elasticity tensor, e_{kij} is the coupling tensor, ϵ_{ij} is the relative permittivity and ϕ_e is the electric potential.

To calculate the band structure of a phononic crystal constituted of anisotropic electro-elastic materials, we seek a solution in the form of plane waves:

$$u_i = u_i^0 e^{-jk_x x} e^{-jk_y y} e^{j\omega t} \quad (3.56)$$

The system of equations is then transformed in an eigenvalue/eigenvector problem, which can be written in the following form (and directly implemented in the commercial Finite Element Method software COMSOL MULTIPHYSICS):

$$\lambda^2 e_a \bar{u}^0 - \lambda d_a \bar{u}^0 + \nabla \cdot \Gamma = F \quad (3.57)$$

where

$$e_a = \begin{bmatrix} -\rho_0 & 0 & 0 & 0 \\ 0 & -\rho_0 & 0 & 0 \\ 0 & 0 & -\rho_0 & 0 \\ 0 & 0 & 0 & 0 \end{bmatrix} \quad (3.58)$$

$$d_a = 0 \quad (3.59)$$

$$\Gamma = \begin{bmatrix} T_{11}^0 & T_{12}^0 & T_{13}^0 \\ T_{12}^0 & T_{22}^0 & T_{23}^0 \\ T_{13}^0 & T_{23}^0 & T_{33}^0 \\ D_1^0 & D_2^0 & D_3^0 \end{bmatrix} \quad (3.60)$$

$$F = \begin{bmatrix} jk_x T_{11}^0 + jk_y T_{12}^0 \\ jk_x T_{12}^0 + jk_y T_{22}^0 \\ jk_x T_{13}^0 + jk_y T_{23}^0 \\ jk_x D_1^0 + jk_y D_2^0 \end{bmatrix} \quad (3.61)$$

Here the eigenvalue is linked to the pulsation by the relation $\lambda = -j\omega$, and the periodic boundary condition is

$$\bar{u}^0(x + a) = \bar{u}^0(x) \quad (3.62)$$

Then the system of equations can be recast in a $k(\omega)$ formulation to calculate isofrequency or to introduce losses. This calculation method is used for continuous periodic conditions as a general method. Besides that, in this work, the Floquet periodic conditions were also involved.

In this work, pillar-based PnCs realized in square, triangular-X, triangular-Y, hexagonal-X and hexagonal-Y lattices were investigated. The unit cells chosen for the calculation of band structures for these 5 lattices are shown in Figure 3.2.

The unit cell used in Comsol software is composed of a LiNbO₃ Y128-X cut substrate and a Ni pillar. The thickness of the substrate is H . The height and the radius of the pillar are respectively h and r . The substrate is divided equally into two parts. The under part is responsible for the damping and loss. A three-dimensional tetrahedral mesh is used to mesh the unit cell. The element size for the substrate is chosen as 2 μm and the one for the pillar ranges from 50 nm to 1 μm . The models of unit cell with mesh used in Comsol for square, triangular-X, triangular-Y, hexagonal-X, hexagonal-Y lattice are shown in Figure 3.3.

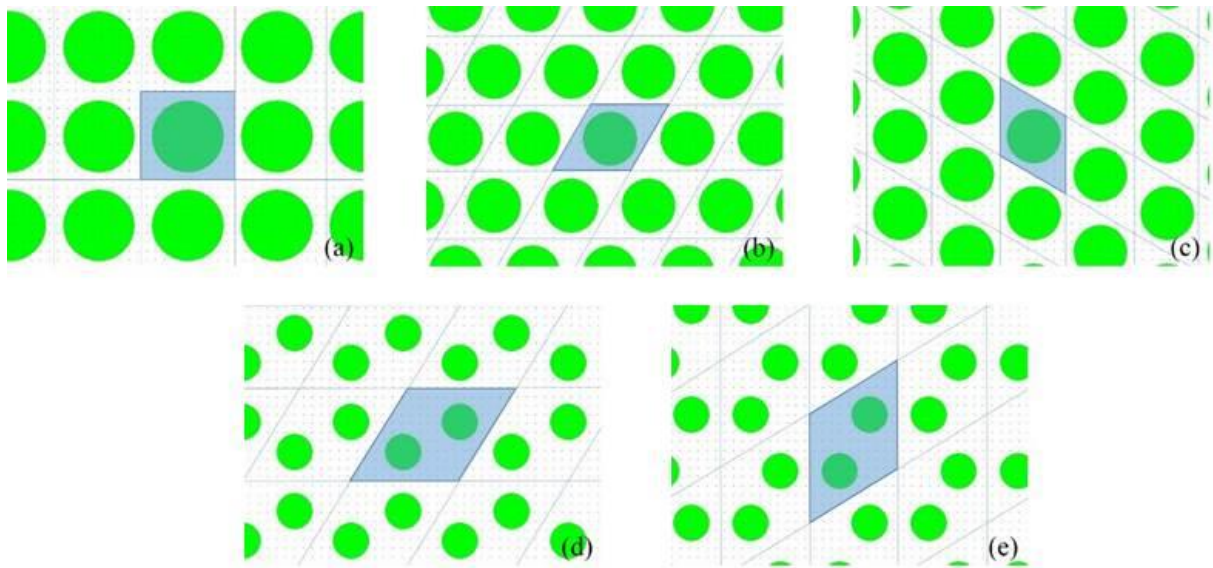


FIG. 3.2. Unit cells of square lattice (a), triangular-X lattice (b), triangular-Y lattice (c), hexagonal-X lattice (d), hexagonal-Y lattice (e).

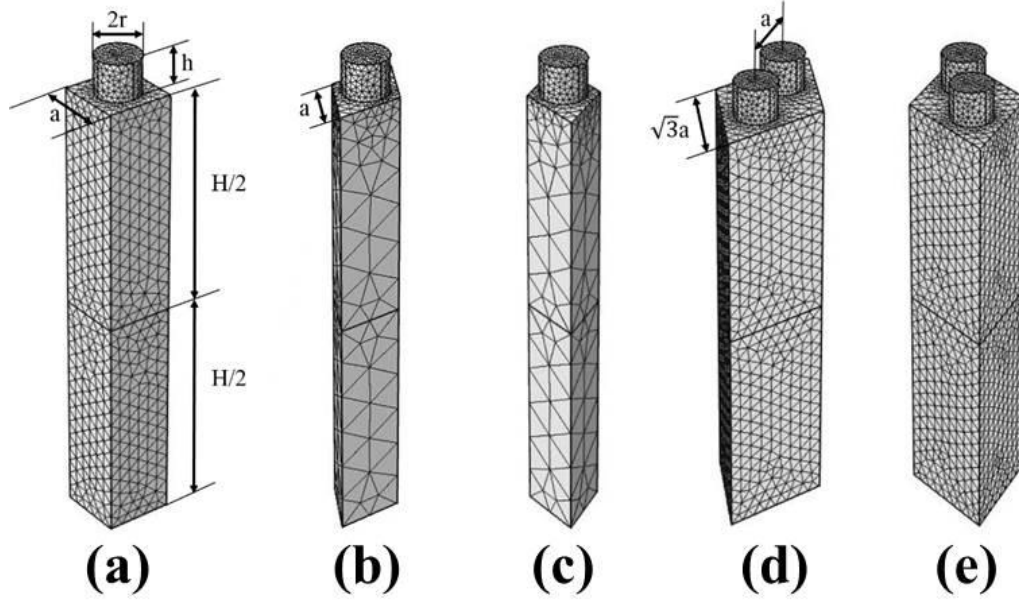
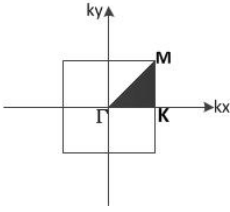
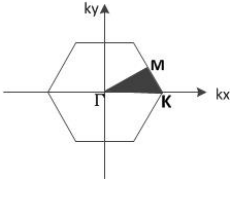
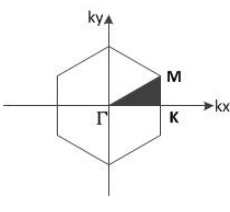
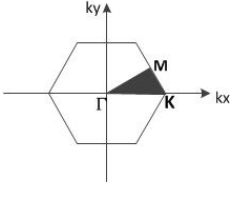
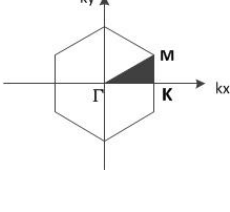


FIG. 3.3. Models of unit cells with mesh used in Comsol for square (a), triangular-X (b), triangular-Y (c), hexagonal-X (d), hexagonal-Y (e) lattice.

The whole structure can be constructed by the repetition of the periodic infinite unit cells along the two directions of the basic vectors. Periodic conditions expressed as Equation (3.10) are applied along the x and y directions, which are the lateral sides of the unit cell to represent the infinity of PnCs, where \vec{u}_{dst} and \vec{u}_{src} are the displacement vectors of the destination and the source, \vec{r}_{dst} and \vec{r}_{src} are the vectors of the destination and the source, \vec{k}_F is the wave vector. The Floquet periodic conditions for these 5 lattices are shown in Table 3.1.

$$\vec{u}_{dst} = \vec{u}_{src} e^{-i\vec{k}_F \cdot (\vec{r}_{dst} - \vec{r}_{src})} \quad (3.63)$$

TAB. 3.1. Periodic conditions for square, triangular-X, triangular-Y, hexagonal-X and hexagonal-Y lattice.

Lattice	Irreducible zone	ΓK	KM	$M\Gamma$
Square		$\begin{pmatrix} k \\ 0 \\ 0 \end{pmatrix}$ $0 < k < \pi/a$	$\begin{pmatrix} \frac{\pi}{a} \\ a \\ k \\ 0 \end{pmatrix}$ $0 < k < \pi/a$	$\begin{pmatrix} \frac{\pi}{a} - \frac{k}{\sqrt{2}} \\ \frac{\pi}{a} - \frac{k}{\sqrt{2}} \\ 0 \end{pmatrix}$ $0 < k < \sqrt{2}\pi/a$
Triangular-X		$\begin{pmatrix} k \\ 0 \\ 0 \end{pmatrix}$ $0 < k < \frac{4\pi}{3a}$	$\begin{pmatrix} \frac{4\pi}{3a} - \frac{k}{2} \\ k \cdot \frac{\sqrt{3}}{2} \\ 0 \end{pmatrix}$ $0 < k < \frac{2\pi}{3a}$	$\begin{pmatrix} \frac{\pi}{a} - k \cdot \frac{\sqrt{3}}{2} \\ \frac{\pi}{\sqrt{3}a} - \frac{k}{2} \\ 0 \end{pmatrix}$ $0 < k < \frac{2\pi}{\sqrt{3}a}$
Triangular-Y		$\begin{pmatrix} k \\ 0 \\ 0 \end{pmatrix}$ $0 < k < \frac{2\pi}{\sqrt{3}a}$	$\begin{pmatrix} \frac{2\pi}{\sqrt{3}a} \\ k \\ 0 \end{pmatrix}$ $0 < k < \frac{2\pi}{3a}$	$\begin{pmatrix} \frac{2\pi}{\sqrt{3}a} - k \cdot \frac{\sqrt{3}}{2} \\ \frac{2\pi}{3a} - \frac{k}{2} \\ 0 \end{pmatrix}$ $0 < k < \frac{4\pi}{3a}$
Hexagonal-X		$\begin{pmatrix} k \\ 0 \\ 0 \end{pmatrix}$ $0 < k < \frac{4\pi}{3\sqrt{3}a}$	$\begin{pmatrix} \frac{4\pi}{3\sqrt{3}a} - \frac{k}{2} \\ k \cdot \frac{\sqrt{3}}{2} \\ 0 \end{pmatrix}$ $0 < k < \frac{2\pi}{3\sqrt{3}a}$	$\begin{pmatrix} \frac{\pi}{\sqrt{3}a} - k \cdot \frac{\sqrt{3}}{2} \\ \frac{\pi}{3a} - \frac{k}{2} \\ 0 \end{pmatrix}$ $0 < k < \frac{2\pi}{3a}$
Hexagonal-Y		$\begin{pmatrix} k \\ 0 \\ 0 \end{pmatrix}$ $0 < k < \frac{2\pi}{3a}$	$\begin{pmatrix} \frac{2\pi}{3a} \\ k \\ 0 \end{pmatrix}$ $0 < k < \frac{2\pi}{3\sqrt{3}a}$	$\begin{pmatrix} \frac{2\pi}{3a} - k \cdot \frac{\sqrt{3}}{2} \\ \frac{2\pi}{3\sqrt{3}a} - \frac{k}{2} \\ 0 \end{pmatrix}$ $0 < k < \frac{4\pi}{3\sqrt{3}a}$

3.3 Evidence of band gaps in pillar-based PnCs

In order to study the occurrence of band gaps in pillar-based PnCs, we examine the band structures of the five lattice symmetries which have been mentioned above (square, triangular-X, triangular-Y, hexagonal-X and hexagonal-Y) calculated using finite element methods. The geometrical parameters are as follows: $a = 9\mu m$, $r = 3\mu m$ and $h = 5\mu m$, where a , r and h are respectively lattice constant, cylindrical pillar's radius and height. The thickness of the substrate is regarded as infinite comparing with the height of the pillars. The pillar's material is chosen as isotropic nickel with the key elastic parameters, density ρ and Young's modulus E are as follows: $\rho = 8900 \text{ kg/m}^3$, $E = 219 \text{ GPa}$. The substrate material LiNbO₃ Y128-X cut wafer is anisotropic. The density ρ is 4700 kg/m^3 . The stiffness tensor c_{ij} , the piezoelectric constants e_{ij} and the relative dielectric constants ϵ_{ij} are shown in Table 3.2. The corresponding band structures are shown in Figure 3.4.

TAB. 3.2. LiNbO₃ Y128-X cut substrate material parameters.

Elastic constants c_{ij} (GPa)					
198.39	66.31	53.54	6.96	0	0
66.31	186.56	80.50	6.31	0	0
53.54	80.50	208.99	6.10	0	0
6.96	6.31	6.10	75.02	0	0
0	0	0	0	56.62	-4.01
0	0	0	0	-4.01	74.56
Piezoelectric constants e_{ij} (C/m ²)					
0	0	0	0	4.3977	0.3648
-1.7223	4.5333	-1.3519	0.2174	0	0
1.7263	-2.4540	2.5953	0.7352	0	0
Relative dielectric constants ϵ_{ij}					
45.6		0		0	
0		38.2845		-9.3634	
0		0		33.6155	

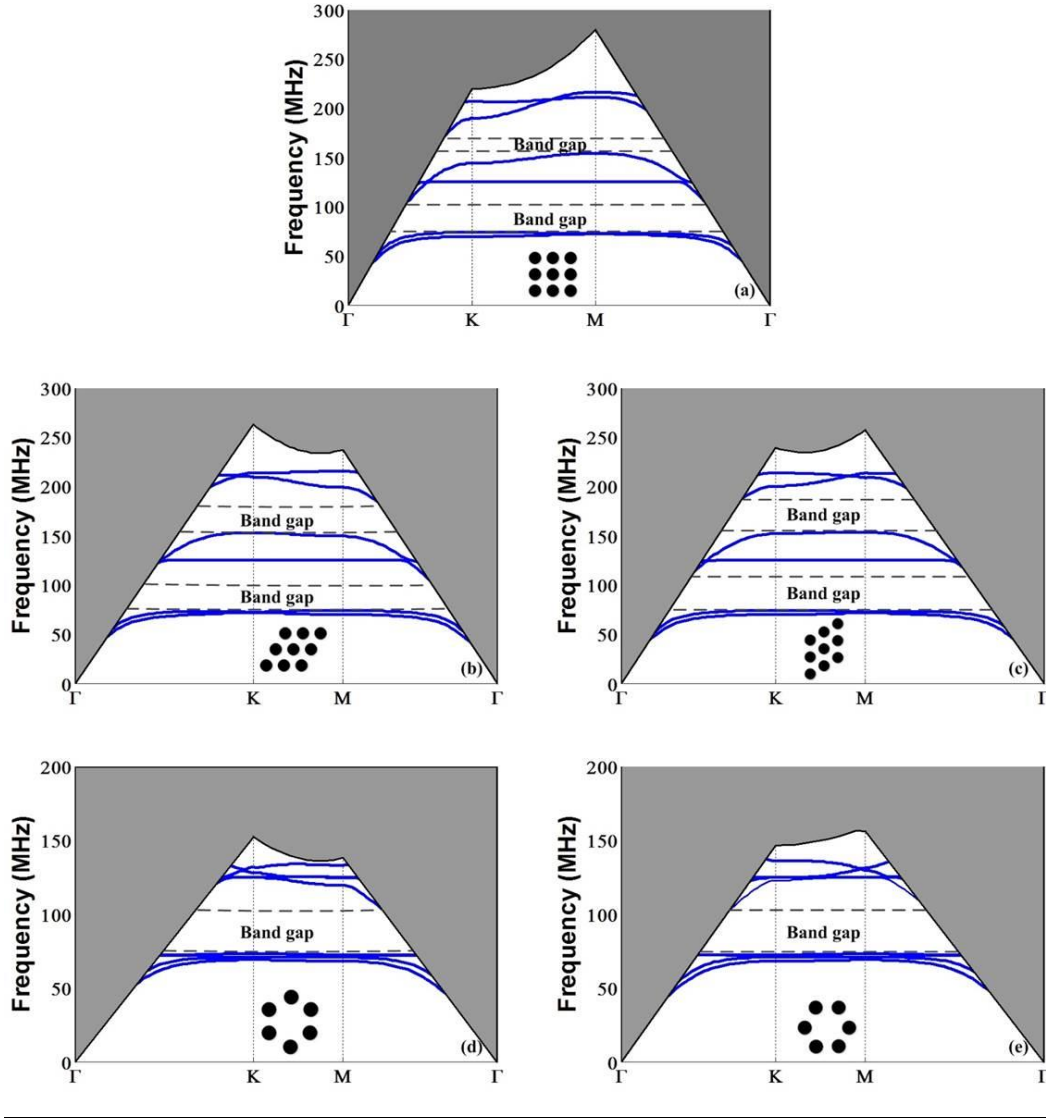


FIG. 3.4. Band structures of a pillar-based PnC for square (a), triangular-X (b), triangular-Y (c), hexagonal-X (d), hexagonal-Y (e) lattice with nickel pillars and LiNbO₃ Y128-X cut substrate. The geometrical parameters are as follows: $a = 9\mu\text{m}$, $r = 3\mu\text{m}$ and $h = 5\mu\text{m}$.

The gray part in the graph represents the radiation zone, which is the zone of bulk wave modes excitation. Surface modes appear below the black curve which represents the propagating mode in homogeneous LiNbO₃ Y128-X cut substrate. The slope of the black curve represents the propagating velocity in the substrate for all directions according to the dispersion relation $v = \frac{2\pi f}{k}$. For example, in this problem, the wave's propagating velocity in homogeneous LiNbO₃ Y128-X cut substrate along the direction ΓK is 3980 m/s . The 6 blue branches stand for 6 surface acoustic eigenmodes in the irreducible Brillouin zone. A complete band gap with a width about 30MHz is observed in the band structures for all the lattice symmetries around the central frequency 90MHz. The difference is that for square,

triangular-X and triangular-Y lattice, the first band gap appears between the second and the third branch. For hexagonal-X and hexagonal-Y lattice, this band gap appears between the third and the fourth branches as a result of the shift of the third branch. Moreover, another complete band gap is observed between the fourth and the fifth branches in the band structures for square, triangular-X and triangular-Y lattice but not for hexagonal-X nor hexagonal-Y lattice. The frequency ranges and central frequencies of each band gap for all the five lattice symmetries are shown in Table 3.3. We can find that the lower edges of each band gap for all the five lattice symmetries are almost the same but the upper edges have a little shift because of the different arrays of pillars.

TAB. 3.3. The frequency ranges and central frequencies of each band gap for square, triangular-X, triangular-Y, hexagonal-X and hexagonal-Y lattice symmetries.

	Band gap 1		Band gap 2	
	Frequency range (MHz)	Central frequency (MHz)	Frequency range (MHz)	Central frequency (MHz)
Square	74-105	90	154-172	163
Triangular-X	74-107	91	153-184	169
Triangular-Y	74-115	95	154-188	171
Hexagonal-X	73-103	88	--	--
Hexagonal-Y	73-103	88	--	--

Besides the band structure, to better understand the locally resonant band gaps, the polarization of the pillars for eigenmodes has always been studied. The total displacement of the six surface modes corresponding to the band structures for square, triangular-X, triangular-Y, hexagonal-X and hexagonal-Y lattice are depicted in Figure 3.5. The wave vector k is chosen as the limit of the direction ΓK in the irreducible Brillouin zone. From Figure 3.5, we can find that for square, triangular-X and triangular-Y lattice, the first two modes are the bending modes. The third mode is an expanding mode in x - y plan, and the fourth mode is a tensile mode along the direction z . The last two modes are mixed modes composed of an expanding mode and a bending mode. Comparing with square, triangular-X and triangular-Y lattice, the polarization of pillars within hexagonal-X and hexagonal-Y arrays have a large difference. The first four modes are bending modes and the last modes are expanding modes for both of the lattice symmetries, but the fifth mode is an expanding mode for hexagonal-X and the one for hexagonal-Y is a tensile mode. Moreover, we find that for hexagonal-Y lattice, the two pillars in the unit cell have the same polarization, but for hexagonal-X lattice, the two pillars in the unit cell have a different polarization. As the

polarization is the only way to distinguish the propagating modes, we will discuss it in detail later in the following parts.

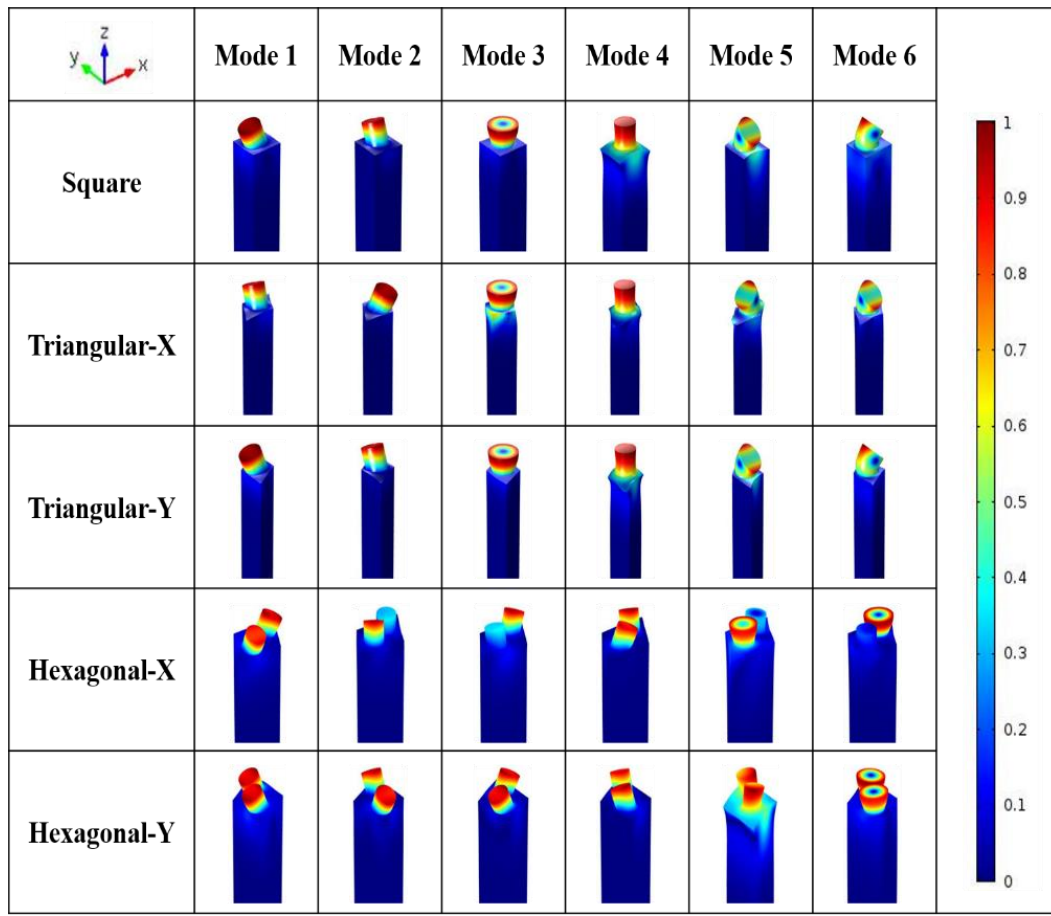


FIG. 3.5. The total displacement of the six surface modes at the Point K in the irreducible Brillouin zone corresponding to the band structures for square, triangular-X, triangular-Y, hexagonal-X and hexagonal-Y lattice.

3.4 Effect of pillar's geometry

3.4.1 Effect of pillar's height

To further understand the band gap property of a pillar-based PnC, we have studied the evolution of the band gaps with the variation of pillar's geometrical parameters, such as pillar's height and pillar's radius. Figure 3.6 illustrates the evolution of band gaps of PnCs with pillar's height being $2.5\mu\text{m}$ and $5\mu\text{m}$ for square, triangular-X, triangular-Y, hexagonal-X and hexagonal-Y lattices. The pillar remains a cylinder with a radius being $3\mu\text{m}$.

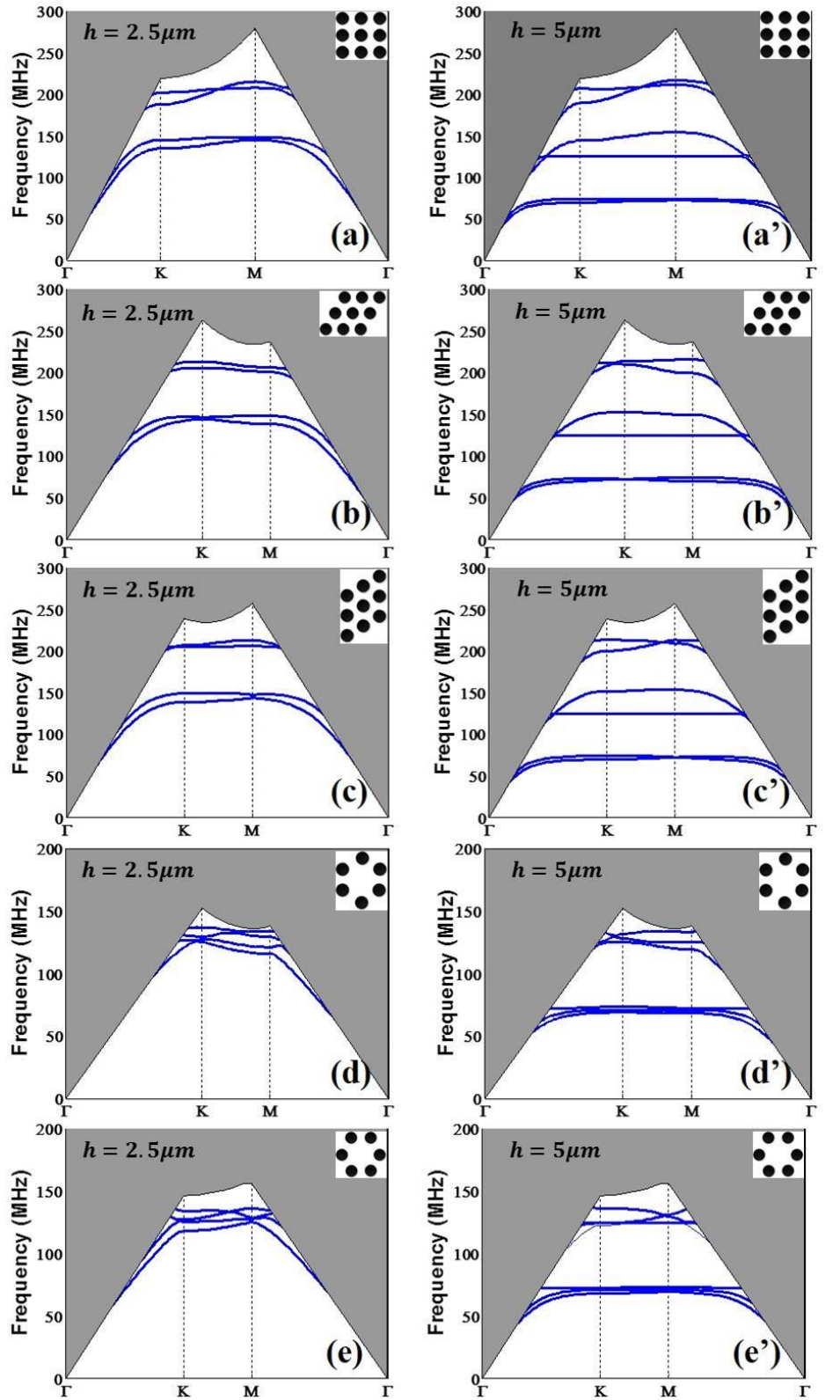


FIG. 3.6. Band structures of pillar-based PnCs for square (a and a'), triangular-X (b and b'), triangular-Y (c and c'), hexagonal-X (d and d'), hexagonal-Y (e and e') lattice with nickel pillars and LiNbO₃ Y128-X cut substrate. The geometrical parameters are as follows: $a = 9\mu\text{m}$, $r = 3\mu\text{m}$ and $h = 2.5\mu\text{m}$ (left) or $5\mu\text{m}$ (right).

Comparing the two groups of band structures of PnCs with different pillar's height, we find that in the case of $2.5\ \mu\text{m}$, there are four surface acoustic modes and a complete band gap between the second and the third modes for square and triangular lattices but no band gaps observed for hexagonal lattices. But for the case of $5\ \mu\text{m}$, there are six acoustic modes and two band gaps for square and triangular lattices. The first band gap appears between the second and the third modes as the case of $2.5\ \mu\text{m}$. The second band gap appears between the fourth and the fifth modes. But for hexagonal lattices, only one band gap can be observed between the third and fourth modes. In addition, the first mode in the latter case has a lower frequency. That is the phenomena which can be observed for all the lattice symmetries.

The evolution of eigenfrequencies of the first six acoustic modes at the boundary of the irreducible Brillouin zone by varying pillar's height is depicted in Figure 3.7. In this case, the PnC composed of square arrays of nickel pillars is chosen as an example. The lattice constant a and the pillar's radius r are respectively $9\ \mu\text{m}$ and $3\ \mu\text{m}$. Pillar's height h varies from $0.9\ \mu\text{m}$ to $9\ \mu\text{m}$ with a step of $0.9\ \mu\text{m}$ resulting in the variation of h/a from 0.1 to 1 with a step of 0.1. From Figure 3.7, we observe that with the increase of h/a , the eigenfrequencies at the boundary of the irreducible Brillouin zone have a tendency to decrease, which means that the local resonances can be excited in lower frequencies. The first two modes almost coincide when h/a is close to 1. The third mode and the fourth mode have an intersection when $h/a=0.43$. As a result, the polarization of mode 3 turns to be the polarization of mode 4 and the polarization of mode 4 at the beginning turns to be the polarization of mode 3, when $h/a>0.43$. Another intersection can be seen between mode 5 and mode 6 when $h/a= 0.32$. The comparison of polarization of pillars with heights $h=2.5\ \mu\text{m}$ and $5\ \mu\text{m}$ resulting in $h/a=0.27$ and 0.56 is depicted in Figure 3.8.

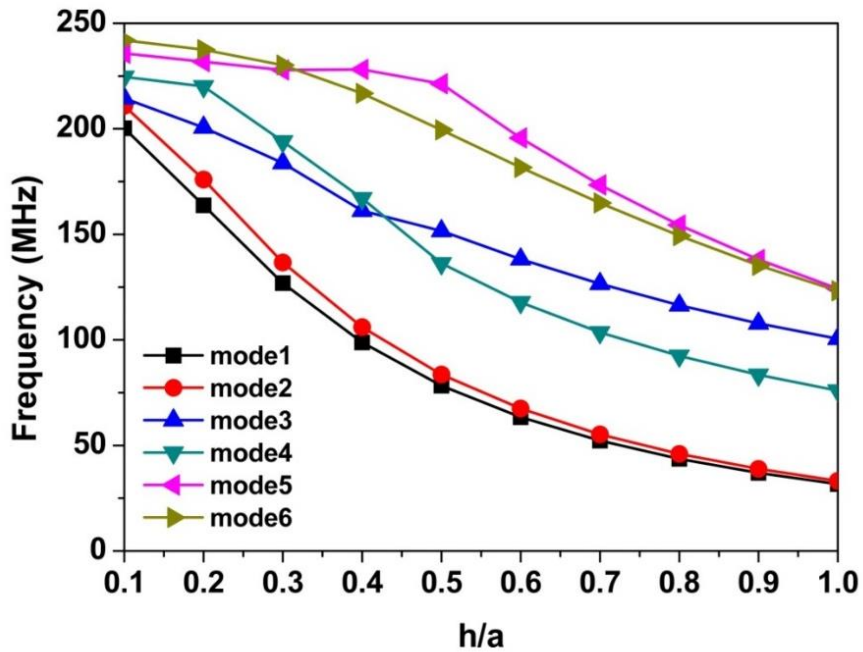


FIG. 3.7. The evolution of eigenfrequencies of the first six acoustic at the boundary of irreducible Brillouin zone by varying pillar's height for PnC with square lattice and $a = 9\mu\text{m}$, $r = 3\mu\text{m}$.

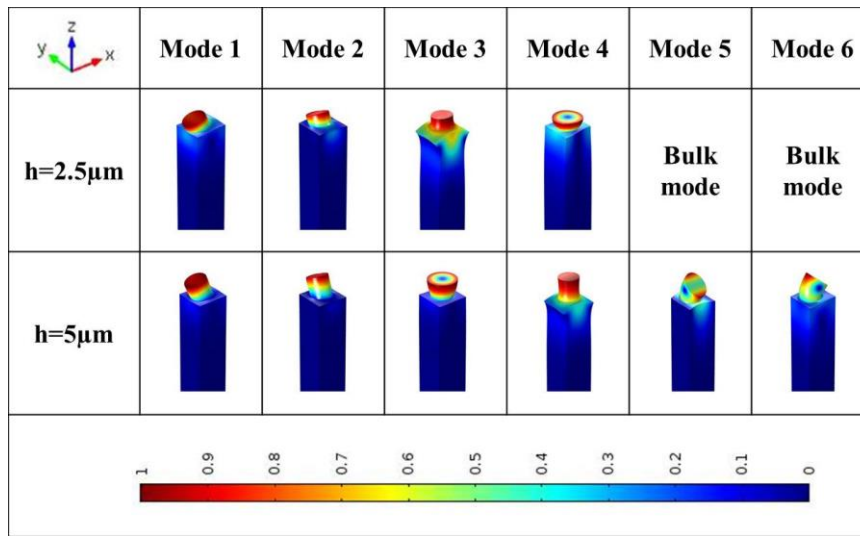


FIG. 3.8. The polarization of pillars in square lattice with different heights for surface acoustic modes, $h=2.5\mu\text{m}$ and $h=5\mu\text{m}$ with $r=3\mu\text{m}$ and $a=9\mu\text{m}$.

3.4.2 Effect of pillar's radius

Figure 3.9 illustrates the evolution of band gaps of PnCs with pillar's radius being $1.5\mu\text{m}$ and $3\mu\text{m}$ for square, triangular-X, triangular-Y, hexagonal-X and hexagonal-Y lattices. The pillar's height is kept at $5\mu\text{m}$.

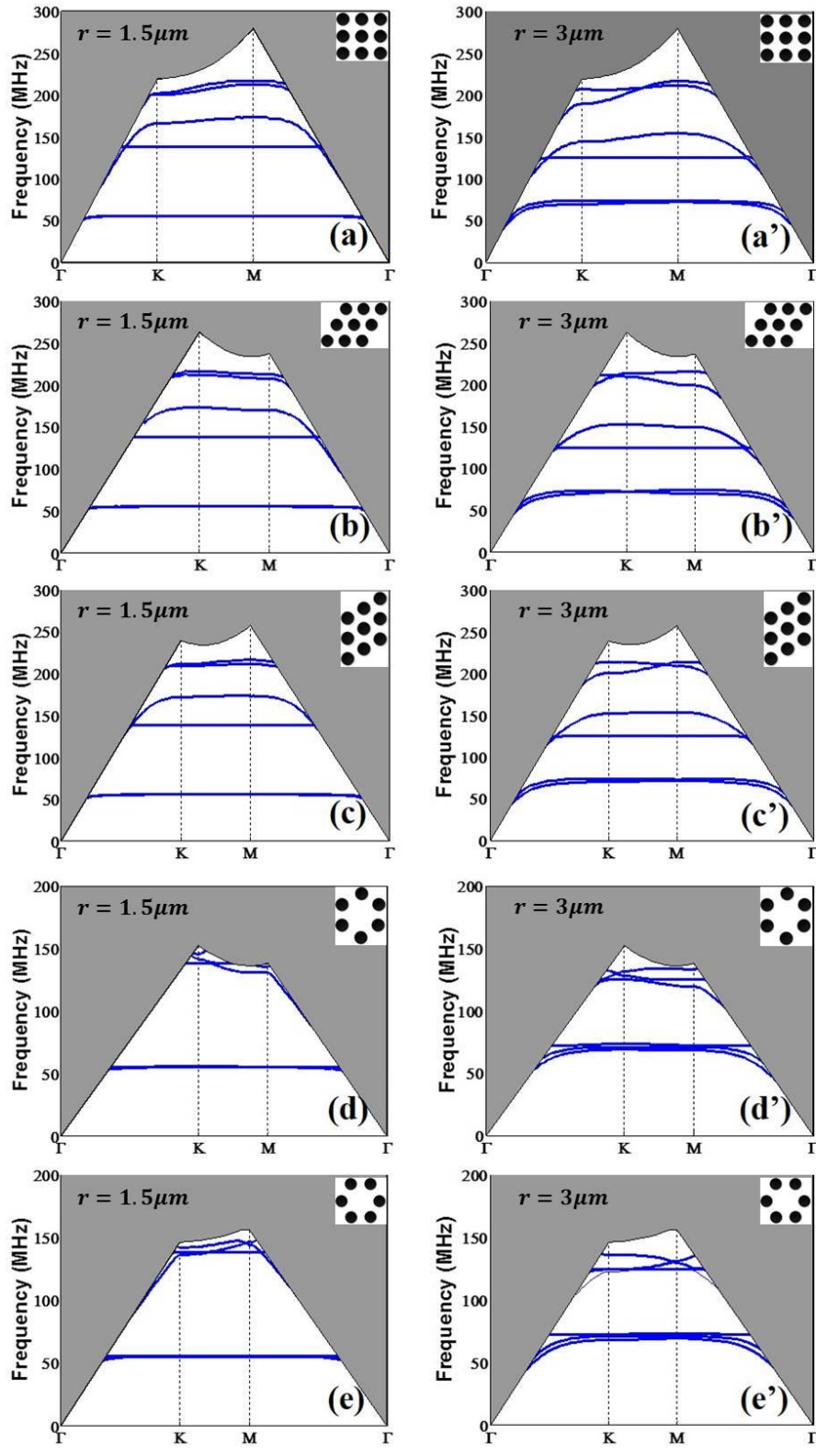


FIG. 3.9. Band structures of pillar-based PnCs for square (a and a'), triangular-X (b and b'), triangular-Y (c and c'), hexagonal-X (d and d'), hexagonal-Y (e and e') lattice with nickel pillars and LiNbO_3 Y128-X cut substrate. The geometrical parameters are as follows: $a = 9\mu\text{m}$, $h = 5\mu\text{m}$ and $r = 1.5\mu\text{m}$ (left) or $3\mu\text{m}$ (right).

Different from the case of the variation of pillar's height, when the radius turns from $3\mu\text{m}$ to $1.5\mu\text{m}$, the band structures don't change a lot. However there are still some small changes observed. In the case of $r = 1.5\mu\text{m}$, the first two surface modes almost coincide and appear at lower frequencies comparing with the case of $r = 3\mu\text{m}$. But the third and fourth modes appear at higher frequencies. The last two modes almost stay at the same frequencies but also coincide. Similar situations can be observed for all of the lattice symmetries.

The evolution of eigenfrequencies of the first six acoustic modes at the boundary of the irreducible Brillouin zone by varying pillar's radius is depicted in Figure 3.10. The lattice constant a and the pillar's height h are respectively $9\mu\text{m}$ and $5\mu\text{m}$. Pillar's radius r varies from $0.45\mu\text{m}$ to $3.6\mu\text{m}$ with a step of $0.45\mu\text{m}$ resulting in the variation of r/a from 0.05 to 0.4 with a step of 0.05. Different from what we have seen in Figure 3.7, the first two modes have a tendency to increase with the increase of radius. This can be explained by the polarization of pillars. Shown in Figure 3.11, the first two modes are the bending modes. When the pillar's height increases, the rigidity decreases. But for a thicker pillar, the rigidity increases. In addition, with the increase of radius, the first two modes are better separated. And an intersection of mode 5 and mode 6 is observed when $r/a=0.21$.

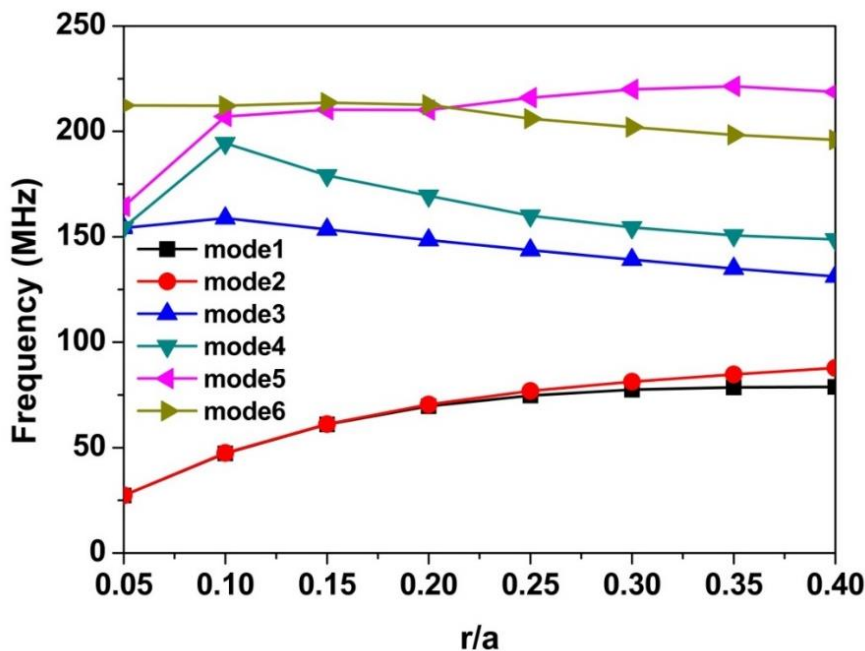


FIG. 3.10. The evolution of eigenfrequencies of the first six acoustic at the boundary of irreducible Brillouin zone by varying pillar's radius for PnC with square lattice and $a = 9\mu\text{m}$, $h = 5\mu\text{m}$.

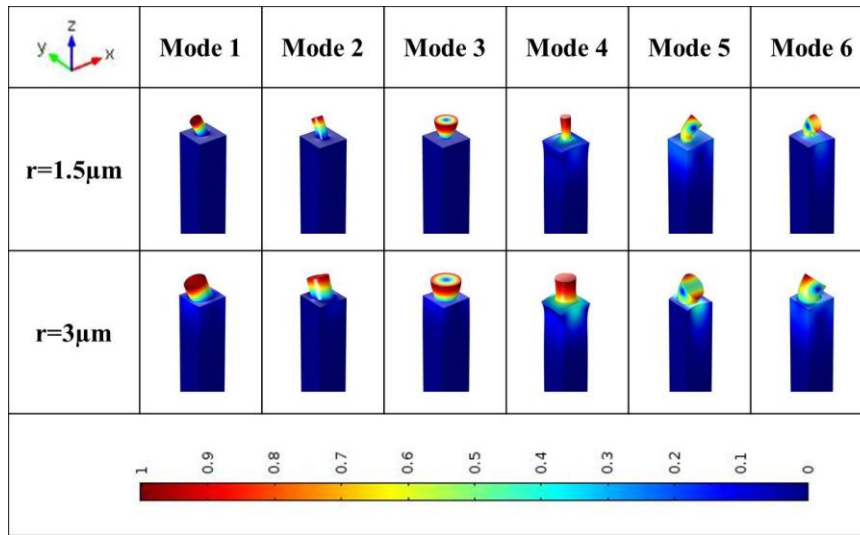


FIG. 3.11. The polarization of pillars in square lattice with different radius for surface acoustic modes, $r=1.5\mu\text{m}$ and $r=3\mu\text{m}$ with $h=5\mu\text{m}$ and $a=9\mu\text{m}$.

3.4.3 Evolution of polarization by varying geometrical parameters

When we study the locally resonant band gaps of a PnC or the eigenmodes of the pillars, the polarization of pillars is always very important, because it can reflect some intrinsic properties. We found that the polarization changed while varying the geometrical parameters. Inspired by this observation, we will talk about the evolution of polarization by varying geometrical parameters in this part.

We observe that the polarization for the first two bending modes varies with the variation of the pillar's radius. To get more information about that, we focus on a fixed point on the surface of the pillar to study the variation of polarization as a function of the pillar's radius. As shown in Figure 3.12, O is the original position of the fixed point and O' is its new position. φ represents the angle between the direction y and the polarization direction. We have $\varphi = \tan^{-1} \text{abs}(u/v)$, where u , v represent the deformation along direction x and direction y .

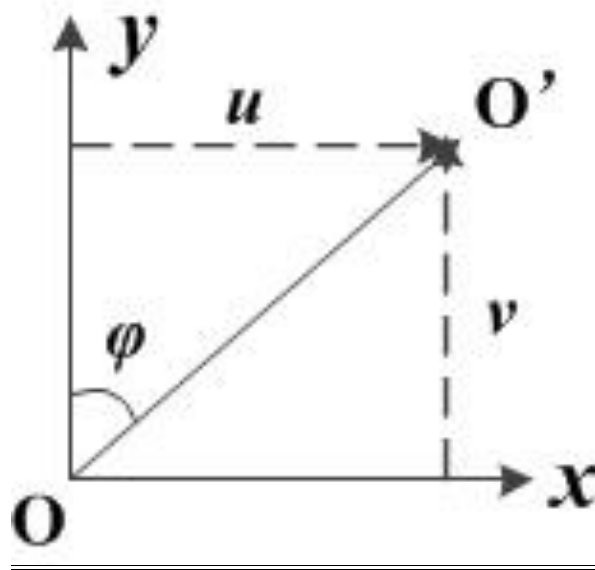


FIG. 3.12. Schematic drawing of the study on the variation of polarization on function of the pillar's radius.

The evolution of pillar's polarization by varying radius and heights of pillars within square, triangular-X and triangular-Y lattices are depicted in Figure 3.13. First of all, we take a look at the figures on the left. The pillar's radius varies from $0.5\ \mu\text{m}$ to $3.5\ \mu\text{m}$. The lattice constant a and the pillar's height h are respectively $9\ \mu\text{m}$ and $4\ \mu\text{m}$. For pillars within square lattice, we can find that the polarization changes when the radius is greater than about $1.1\ \mu\text{m}$. However the change is not gradual. The polarization switches from direction y to direction x or contrarily. Then the polarization turns to be stable when the radius increases to $1.2\ \mu\text{m}$. To see what happens exactly, we zoom the part between $1.1\ \mu\text{m}$ and $1.2\ \mu\text{m}$. We find that the polarization in that period oscillates. This phenomenon can be explained by the coupling between the first two modes in the case that the radius is between $1.1\ \mu\text{m}$ and $1.2\ \mu\text{m}$. In addition, the polarization of mode 1 and mode 2 are always symmetric. Similar situation has been also observed for pillars within triangular-Y lattice but the case for triangular-X lattice is very different. When the radius is smaller than $1.0\ \mu\text{m}$, the polarization for Mode 1 and Mode 2 stays respectively along direction y and direction x . Then with the increase of radius, the polarization for the two modes begins to rotate and have a tendency to coincide. When the radius increases to about $2\ \mu\text{m}$, the polarization for the two modes becomes to be stable and φ is about 45° , which means the displacement u along direction x and the displacement v along direction y are almost equal. The polarization of the two modes is also symmetric all the time.

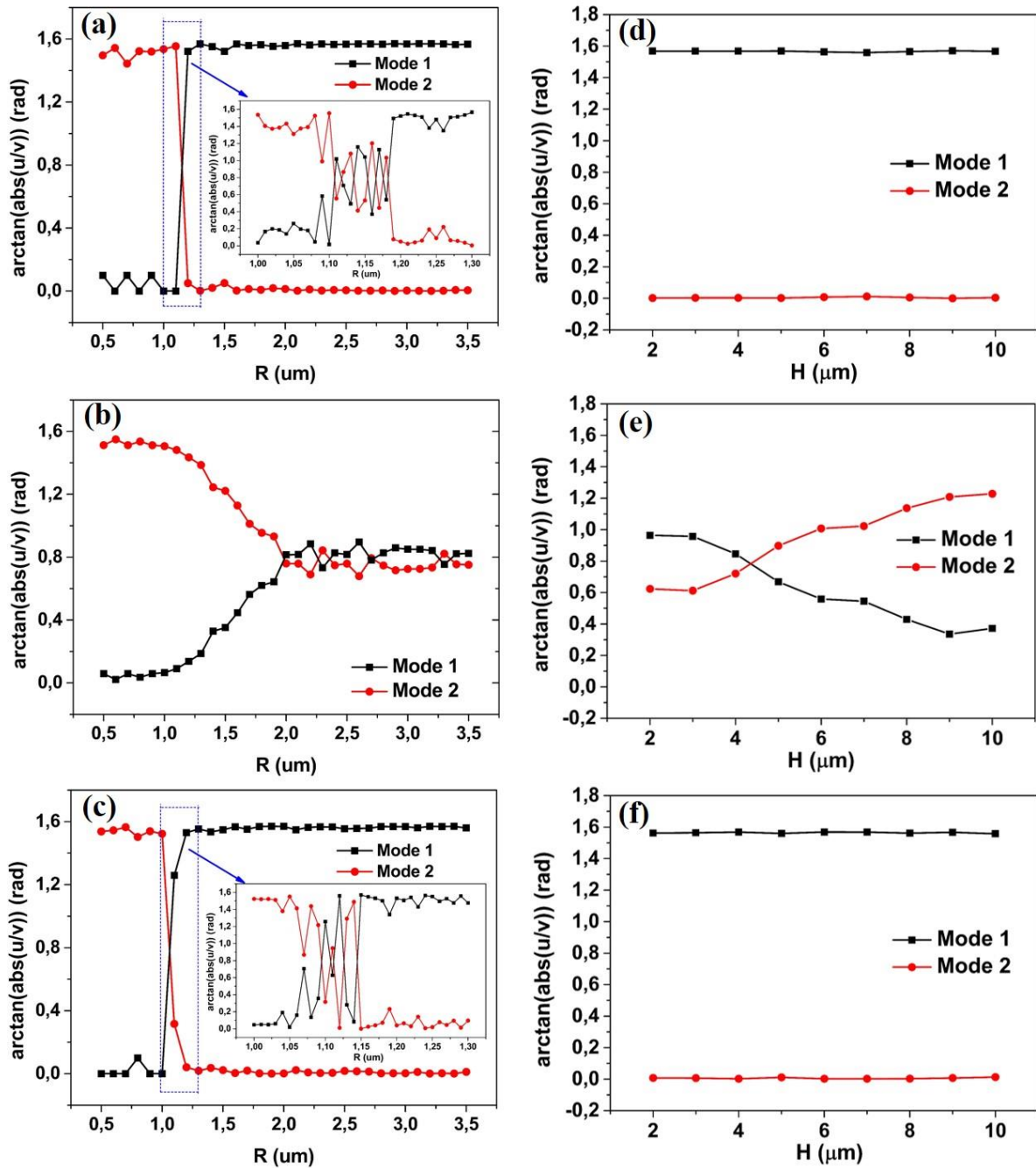


FIG. 3.13. The evolution of pillar's polarization by varying radius (left) and heights (right) of pillars within square (a and d), triangular-X (b and e) and triangular-Y lattices (c and f).

Since the polarization has an evolution with the variation of pillar's radius, we wondered what would happen if we vary the pillar's height. Consequently, The evolution of pillar's polarization by varying heights of pillars within square, triangular-X and triangular-Y lattices are depicted in Figure 3.13 (right). Different from the case by varying radius, when pillar's heights change, the polarization of pillars within square and triangular-Y lattices for the first two modes doesn't change. The lattice constant and the radius of the pillars are respectively $9\mu\text{m}$ and $3\mu\text{m}$. As a result, the polarization for Mode 1 is along direction x and

the polarization for Mode 2 is along direction y . The case within triangular-X lattice is a little more complex. φ varies from 55 degree to 20 degree when the height varies from $2\mu\text{m}$ to $10\mu\text{m}$ for the first mode. Symmetrically, φ varies from 35 degree to 70 degree for the second mode. In addition, a crossing of the curves is observed when the height is about $4.5\mu\text{m}$, which means the two modes share the same polarization with this height.

3.5 Effect of anisotropy

Much work has been done to demonstrate that the formation of locally resonant band gaps only depends on the pillar's materials and geometries and not on the lattice symmetries_[73, 77]. A. Khelif et al._[77] have indicated theoretically that the locally resonant band gaps are invariant with respect to the lattice symmetries, which means that the discrete acoustic modes of pillars, those inducing the band gaps are not affected by the arrays. In addition, Y. Achaoui et al._[73] have further proved this argument experimentally.

However, according to our study of the influence of anisotropy of PnCs, something different has been found. So the main objective of this part of work is to demonstrate that the lattice symmetries can affect the surface localized modes. This dependency is investigated in a 2D PnC model composed of Ni Pillars deposited on a LiNBO_3 Y128-X cut piezoelectric substrate for square, triangular-X and triangular-Y lattices. The lattice constant a is $9\mu\text{m}$, pillar's height h is $4\mu\text{m}$ and pillar's radius r is $3\mu\text{m}$ for all these three lattice symmetries. Band structures of PnCs with square, triangular-X and triangular-Y lattices are shown in Figure 3.14.

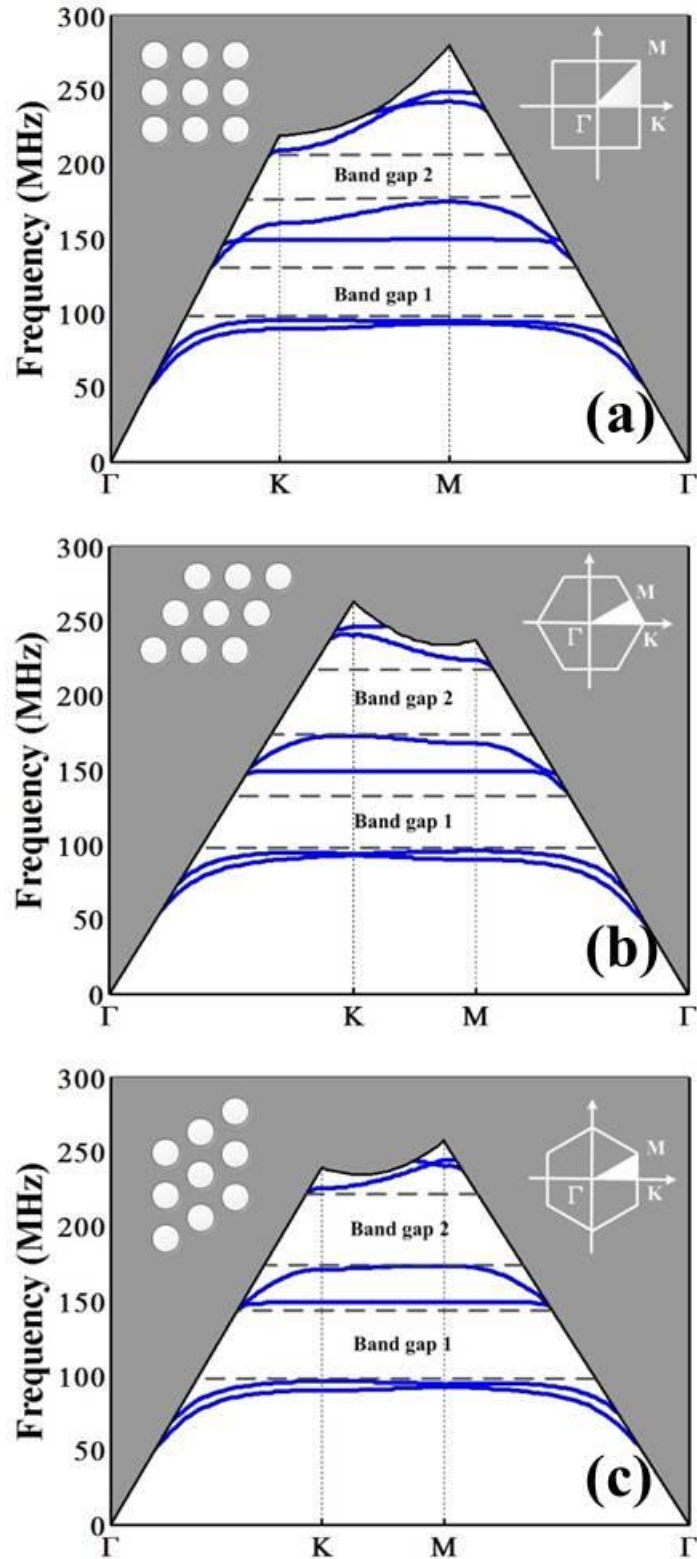


FIG. 3.14. Band structures of pillar-based PnCs for square (a), triangular-X (b), triangular-Y (c) lattices with nickel pillars and LiNbO_3 Y128-X cut substrate. The geometrical parameters are as follows: $a = 9\mu\text{m}$, $h = 4\mu\text{m}$ and $r = 3\mu\text{m}$.

TAB. 3.4. Frequency ranges and central frequencies of the band gaps of PnCs with different lattice symmetries.

		Square	Tri-X	Tri-Y
Band gap 1	Frequency range (MHz)	95.1-131.4	95.7-135.5	96.0-144.1
	Central frequency (MHz)	113.3	115.6	120.0
Band gap 2	Frequency range (MHz)	174.6-205.0	172.8-219.9	173.7-222.9
	Central frequency (MHz)	189.8	196.4	198.3

6 eigenmodes are observed for the band structure of each lattice. Two complete band gaps are found in the band structures for square, triangular-X and triangular-Y lattice. From the first view of the band structures, it seems that the two band-gaps appear approximately at similar frequency ranges for the different lattice symmetries, especially for the bottom edge of each band gap. The frequencies of band gaps edge of the PnCs with different lattice symmetries are shown in Table 3.4. We also observe that the widths of first band gap for square, triangular-X and triangular-Y lattices are respectively 36.3MHz, 39.8MHz and 48.1MHz. The central frequencies are respectively around 113.3MHz. Moreover, the width of the second band gap is 30.4MHz for square lattice and 47.1MHz for triangular-X and 49.2MHz for triangular-Y lattice. The central frequency is 189.8MHz for square lattice and 196.4MHz for triangular-X and 198.3MHz for triangular-Y lattice. Therefore, we can summarize that since the PnCs with different lattice symmetries share the same pillars and the lattice constant, the band gaps appear at the similar frequency with the similar widths. Nevertheless, the influence of the lattice symmetries still exists, resulting in the small shifts of the band gaps. To explain this shift, we will focus on the shape deformation corresponding to each surface localized mode principally the two lower modes.

Figure 3.15 shows the shape deformation for the first four modes in the case of square, triangular X and triangular Y lattice symmetries. The wave vector \mathbf{k} is chosen as the limit of the direction ΓK in the irreducible Brillouin zone. The total displacement of a unit cell can be divided into 3 components u , v and w representing respectively the displacement in the direction x , y and z . First of all, we observe that the three lattices share the same Mode 3 and Mode 4. But for the first two modes, it's different. For example, the polarization of square and triangular-Y lattices is along the direction x for Mode 1 and along direction y for Mode 2. But the polarization of triangular-X lattice has two components along two direction x and y for both Mode 1 and Mode 2. So we can conclude that even for the same pillar and the same lattice constant, pillars may have different polarization.

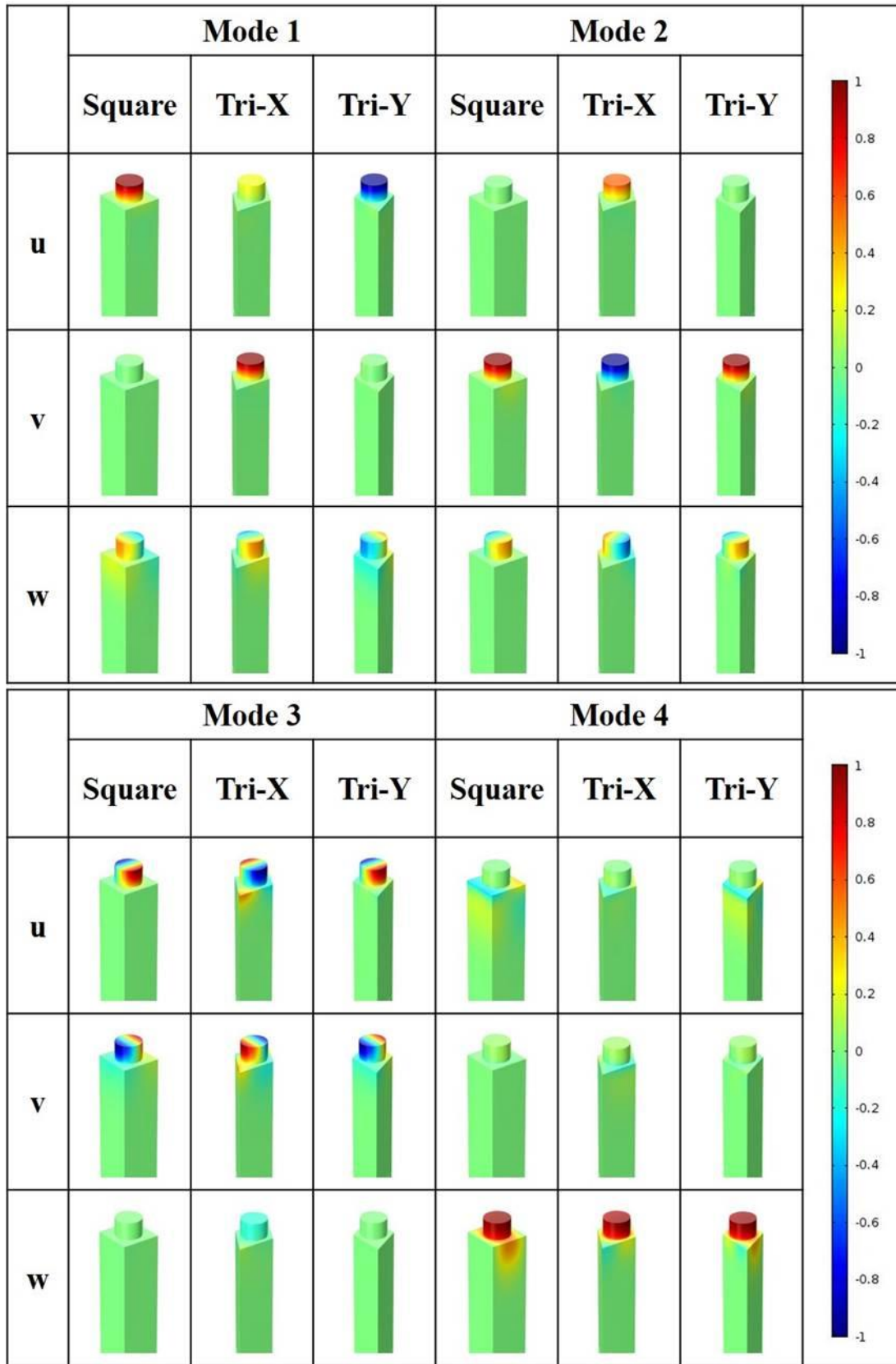


FIG. 3.15. Displacement components of pillars within square, triangular-X and triangular-Y lattices for the first four eigenmodes in three directions.

As we have presented above, the first two modes are bending modes in plan xy . The third mode is an expanding mode in plan xy but the displacement field is isotropic. The fourth mode is a tensile mode along direction z and has no component in plan xy . Since the PnC is anisotropic in plan xy due to the different lattice symmetries, the polarization of Mode 3 and Mode 4 are independent from the anisotropy in plan xy . As a result, the polarization of pillars within these three lattices for Mode 3 remains unchanged, as well as Mode 4. But for the first two bending modes, the displacement field in plan xy is no longer isotropic. When the pillar bends to a direction, it is affected by the adjacent pillars. Consequently, the distribution of pillars may have an influence on the polarization of pillars.

Another observation is that the polarization of pillars for the bending modes (Mode 1 and Mode 2) within square lattice and triangular-Y lattice is much similar but totally different from the one within triangular-X lattice, shown in Figure 3.15. In the cases of square and triangular-Y lattices, the polarization is along direction x for Mode 1 and along direction y for Mode 2. However for the case of triangular-X lattice, the polarization has two components along direction x and y for both the two modes. To know more about the vibration of pillars within different lattice symmetries, Figure 3.16 illustrates the polarization of pillars for the first two resonant modes within different lattice symmetries for different phases. From Figure 3.16, we can observe that the first mode for square lattice and triangular-Y lattice is along direction x and the second mode is along direction y . However for triangular-X lattice, instead of the oscillation along one axis, the pillar rotates counterclockwise for Mode 1 and clockwise for Mode 2.

This phenomenon can be explained by the band structures shown in Figure 3.14. At the point K, which is the boundary of the irreducible Brillouin zone, the first two modes are well separated for the cases of square and triangular-Y lattices, but for the case of triangular-X lattice, the first two modes are very close, which means that there is a coupling between the two modes, resulting in an unstable polarization. Just as shown in Figure 3.13, the polarization of pillars with certain geometrical parameters within a triangular-X lattice rotates from the axis x to y or contrarily for the first two modes.

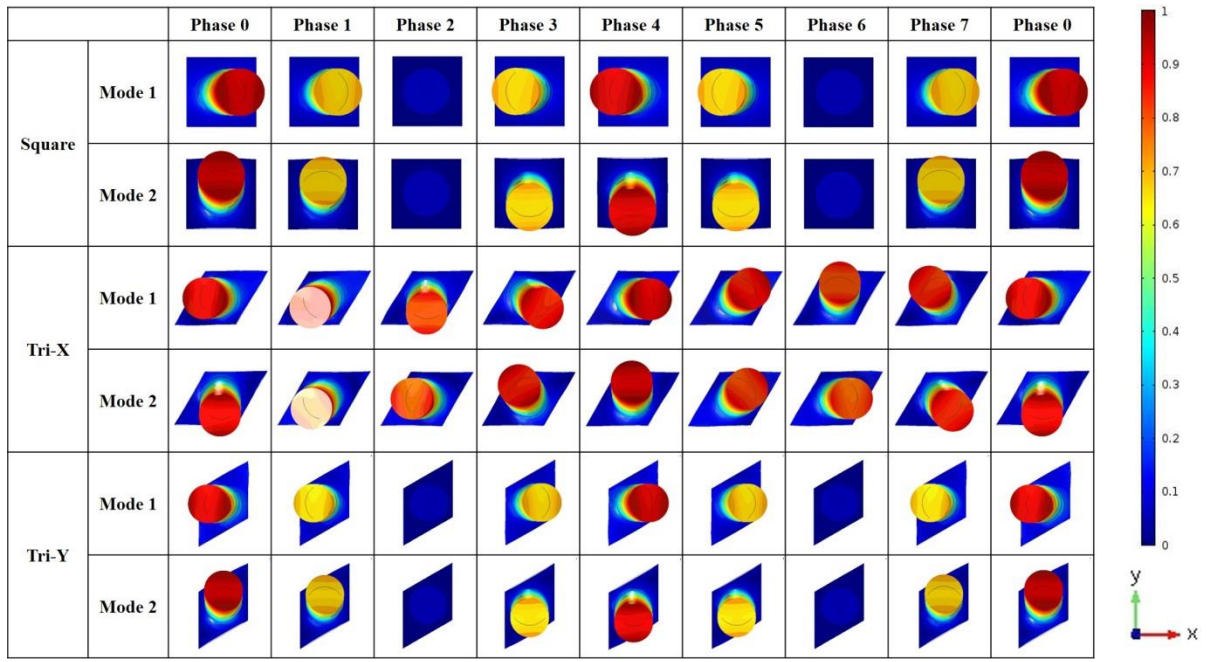


FIG. 3.16. Polarization of pillars for the first two resonant modes within square, triangular-X, triangular-Y lattices for different phases.

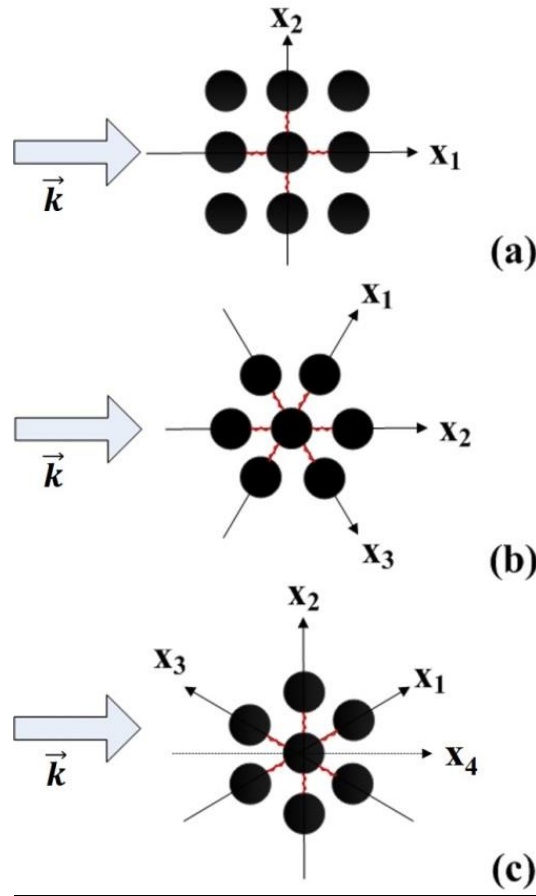


FIG. 3.17. Wave propagation along direction x through pillar-based PnCs within square (a), triangular-X (b) and triangular-Y (c) lattices.

From the point of view of lattice symmetries, we can also explain this observation. As shown in Figure 3.17, the square lattice has symmetry of order 2 and the wave vector is along one of the symmetric axis x_1 . The triangular lattices share symmetry of order 3. The wave vector is along the symmetric axis x_2 for triangular-X lattice, but for triangular-Y lattice, the wave vector is not along any symmetric axis (x_1 , x_2 and x_3). We mark the direction of this wave vector x_4 . Considering the propagation direction, the four interactions between pillars along the direction x_1 and x_3 are identical. According to the symmetry, triangular-Y lattice can be regarded as symmetry of order 2 with two axes x_2 and x_4 , just like the square lattice. Consequently, under the effect of anisotropy, pillars within square lattice and triangular-Y lattice share the similar polarization and different from the one for triangular-X lattice.

3.6 Material consideration

To study band gaps is very meaningful for the investigation of a PnC because the band gap can give much physical information about the PnCs. Many parameters including elastic parameters such as Young's modulus and density, as well as the geometrical parameters such as the pillar's height and form can be discussed via the band structures. In the following part of this chapter, the consideration of material composition, the influence of pillar's form, the effect of the lattice symmetries will all be discussed.

It is known that the formation of a PnC band gap is due to the diffraction of phonons propagating in a crystal at the interface between the matrix and inclusion materials. The physical origins of PnC band gaps can be understood by describing the Bragg and Mie resonance based on scattering of acoustic waves propagating within the crystal.

To simplify the model, both of the matrix and inclusions materials are considered isotropic. ρ and E are the density and Young's modulus. The subscript i and m represent inclusions and matrix. The propagating velocity in a material is given by

$$V_{i,m} = \sqrt{\frac{E_{i,m}}{\rho_{i,m}}} \quad (3.64)$$

$$Z_{i,m} = \sqrt{E_{i,m}\rho_{i,m}} \quad (3.65)$$

The amount of acoustic power reflected at the interface between the inclusion and the matrix is

$$\Gamma^2 = \left(\frac{Z_i - Z_m}{Z_i + Z_m}\right)^2 \quad (3.66)$$

According to Equation 3.13, large acoustic impedance Z (ρ , E) mismatch between the matrix and inclusion is necessary for achieving wide PnC band gaps.

As we know, the density and the Young's Modulus are the key parameters for the Bragg type PnCs. In the next part, we are going to talk about how they act in the locally resonant PnCs.

In this work, LiNbO₃ Y128-X cut substrate is chosen as the matrix material of which the material parameters are depicted in Table 3.2. For the selection of the pillars' materials, gold and diamond are chosen respectively because of their large density and high Young's modulus, compared to nickel. The density and Young's modulus for gold, diamond, nickel and LiNbO₃ are shown in Table 3.5.

TAB. 3.5. The density and Young's modulus for gold, diamond, nickel and LiNbO₃.

	Gold	Nickel	Diamond	Lithium Niobate
Density ρ (kg/m^3)	19300	8900	3520	4700
Young's modulus E (GPa)	70	219	1220	--
$V_{i,m} = \sqrt{\frac{E_{i,m}}{\rho_{i,m}}}$ (m/s)	1904	4961	18617	--

The band structures for PnCs based on gold (a), nickel (b) and diamond (c) pillars on LiNbO₃ Y128-X cut semi-infinite substrate are depicted in Figure 3.18. The PnC is composed of square arrays of cylindrical pillars. The pillars' height and radius are respectively 5 μ m and 3 μ m. From Equation 3.11, we know that eigenfrequencies increase when Young's modulus increases or density decreases. As shown in Figure 3.18, gold pillars have lower eigenfrequencies compared to nickel pillars and diamond pillars because of their large density. On the other hand, diamond pillars have relatively high eigenfrequencies as a result of large Young's modulus. On the other hand, we observe that the modes are very flat in the band structure for the gold pillars, which means the material with a large density and a small Young's Modulus can give a high Q factor.

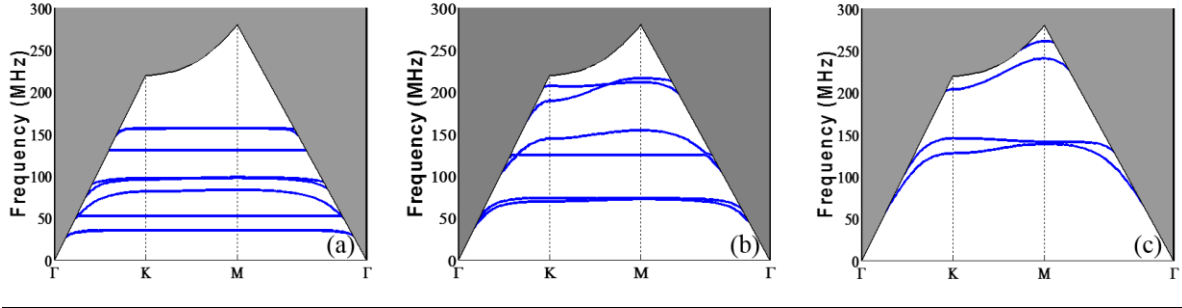


FIG. 3.18. The band structures for PnCs based on gold (a), nickel (b) and diamond (c) pillars on LiNbO₃ Y128-X cut semi-infinite substrate.

3.7 Temperature coefficients of frequency for surface modes

After the discussion about the effect of geometrical and material parameters on the PnCs, now we take a look at the influence of the temperature, which leads to the study of the temperature coefficients of frequency for surface modes.

In this work, the PnC is based on LiNbO₃ Y128-X cut substrate and nickel pillars. Two temperatures are chosen as $T_0=300K$, $T_1=340K$. With the variation of temperature, the elastic properties of materials also change by inserting a new parameter which is the temperature coefficient. For example, the density, the elastic constant and the Young's Modulus can be expressed in Equation 3.14, 3.15 and 3.16 as follow:

$$\rho' = \rho(1 + T\rho(T_1 - T_0)) \quad (3.67)$$

$$C'_{ij} = C_{ij}(1 + TC_{ij}(T_1 - T_0)) \quad (3.68)$$

$$E' = E(1 + TE(T_1 - T_0)) \quad (3.69)$$

where, ρ and ρ' are the density for $T_0=300K$ and $T_1=340K$; C_{ij} and C'_{ij} are the elastic constant for $T_0=300K$ and $T_1=340K$; E and E' are the Young's Modulus for $T_0=300K$ and $T_1=340K$. $T\rho$, TC_{ij} and TE are respectively the temperature coefficients of density, elastic constant and Young's Modulus. All these parameters for $T_0=300K$ are shown in Table 3.6. Temperature coefficients of density, elastic constant and Young's Modulus are shown in Table 3.7. And the calculated parameters for $T_1=340K$ are shown in Table 3.8.

TAB. 3.6. Elastic parameters of LiNbO₃ Y128-X and Ni for T₀=300K.

T ₀ =300K					
LiNbO ₃ Y128-X					
Density ρ=4680kg/m ³					
Elastic constants C _{ij} (GPa)					
203	69	59	12.5	0	0
69	195	90.5	9.3	0	0
59	90.5	221	9.16	0	0
12.5	9.3	9.16	75	0	0
0	0	0	0	55.7	-3.5
0	0	0	0	-3.5	76
Ni					
Density ρ=8900 kg/m ³					
Young's Modulus E=219 GPa					

TAB. 3.7. Temperature coefficients of density, elastic constant and Young's Modulus of LiNbO₃ Y128-X and Ni.

LiNbO ₃ Y128-X					
Temperature coefficient of density $T\rho = -38 \cdot 10^{-6} K^{-1}$					
Temperature coefficient of elastic constant $TC_{ij} (10^6 K^{-1})$					
-35	-14.4	-10.8	0.28	0	0
-14.4	-38	-11.5	0.016	0	0
-10.8	-11.5	-35	-1.47	0	0
0.28	0.016	-1.47	-11.8	0	0
0	0	0	0	-11.4	-0.9
0	0	0	0	-0.9	-11
Ni					
Temperature coefficient of density $T\rho = -39 \cdot 10^{-6} K^{-1}$					
Temperature coefficient of density Young's Modulus $T\rho = -81 \cdot 10^6 K^{-1}$					

TAB. 3.8. Elastic parameters of LiNbO₃ Y128-X and Ni for T₀=340K.

T ₀ =340K					
LiNbO ₃ Y128-X					
Density ρ=4672.89 kg/m ³					
Elastic constants C _{ij} (GPa)					
201.6	68.424	58.568	12.511	0	0
68.424	193.48	90.04	9.301	0	0
58.568	90.04	219.6	9.101	0	0
12.511	9.301	9.101	74.528	0	0
0	0	0	0	55.244	-3.536
0	0	0	0	-3.536	75.56
Ni					
Density ρ=8886.12kg/m ³					
Young's Modulus E=215.76GPa					

With these parameters above, band structures of PnCs for the temperatures $T_0=300K$ and $T_1=340K$ can be calculated. In this work, PnCs composed of nickel cylindrical pillars

within square, triangular-X and triangular-Y lattices are studied. Pillar's radius is $3\ \mu\text{m}$. Two heights of pillars $2.5\ \mu\text{m}$ and $5\ \mu\text{m}$ are chosen.

The temperature coefficient of frequency can be expressed as Equation 3.17.

$$TCf = \frac{1}{f_0} \frac{\partial f}{\partial T} \quad (3.17)$$

It is a key parameter to describe the sensitivity of a sensor. The TCf values as a function of frequencies for the first two eigenmodes of the pillars within square, triangular-X and triangular-Y lattices with two heights $2.5\ \mu\text{m}$ and $5\ \mu\text{m}$ are depicted in Figure 3.19.

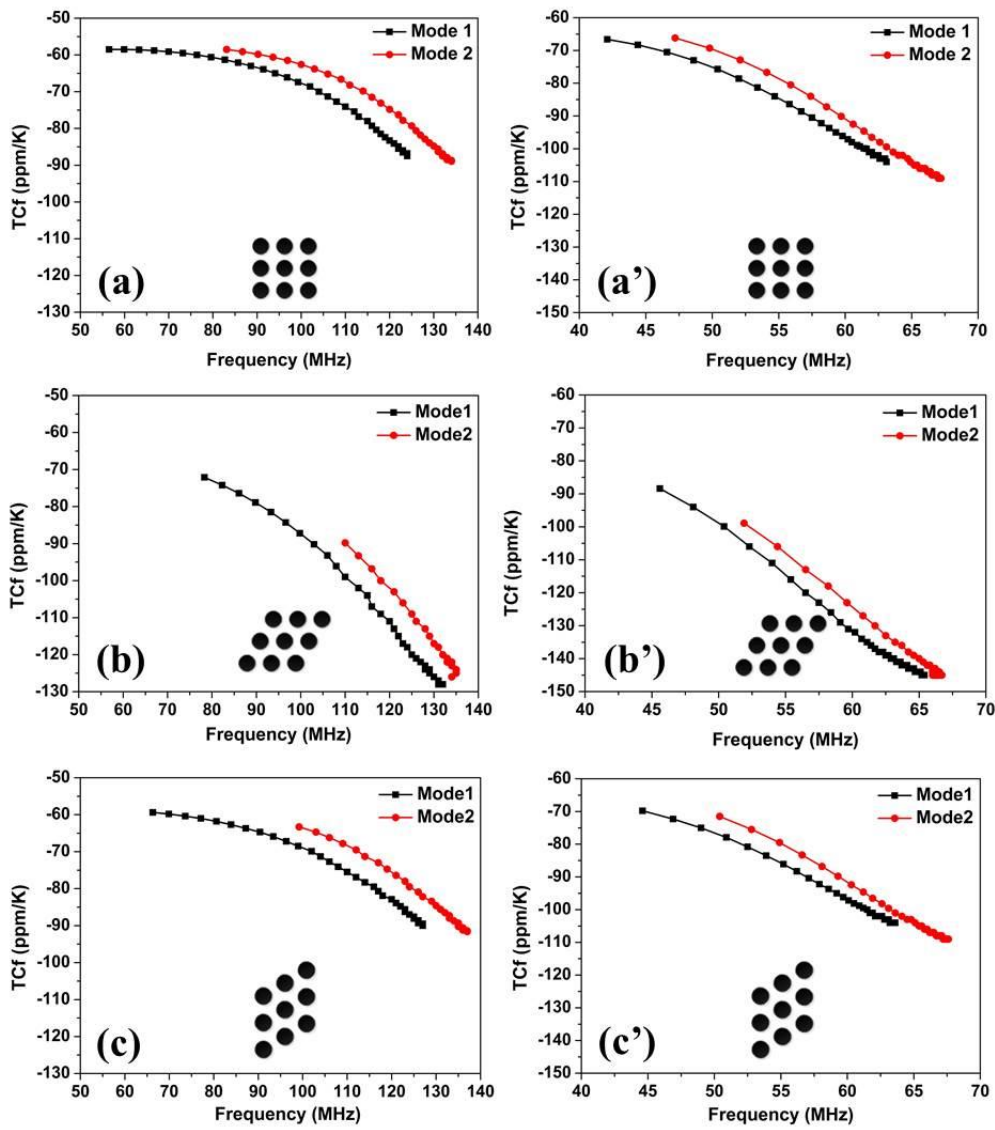


FIG. 3.19. The TCf values as a function of frequencies for the first two eigenmodes of the pillars within square (a and a'), triangular-X (b and b') and triangular-Y (c and c') lattices with two heights $2.5\ \mu\text{m}$ (left) and $5\ \mu\text{m}$ (right).

Comparing the cases with the same lattice symmetries and different pillar's heights, we find that pillars with a height of $5\ \mu\text{m}$ have a higher TCf than pillars with a height of $2.5\ \mu\text{m}$. That is because the TCf of nickel is higher than the value of LiNbO_3 . For the case with a higher pillar, the surface waves propagate more in the nickel pillars, as a result, the TCf is closer to the pure nickel case. We can conclude that higher nickel pillars have a greater sensitivity for temperature.

Another observation is about the anisotropy of PnC. If we fix the pillar's height, and compare the TCf for different lattice symmetries, we can find that the case for square and triangular-Y lattices are almost the same, but lower than the case for triangular-X lattice. This observation has already been explained in the front part. Consequently, the anisotropy of PnCs also has an influence on the TCf .

To sum up, when the wave vector is close to the boundary of the irreducible Brillouin zone, the group velocity is close to zero. The modes become flat leading to a high sensitivity of the temperature. The sensitivity can also depend on the geometrical parameters and the anisotropy of the crystals. Imitating the discussion about the TCf , there are also other mechanical and thermodynamic parameters which can be discussed. The meaning of this study is that the controllable high sensitivity may lead to the applications of sensors based on PnCs.

3.8 Calculation of transmission spectrum

In order to understand the obtained results of band structures, we have also calculated the transmission spectrum. The band structures show the results about the intrinsic properties of the PnCs, such as the resonance, the polarization, etc. It's more like an ideal infinite model. Therefore it is necessary to calculate the transmission spectrum of a finite tridimensional PnC to confirm the theoretical results obtained by the calculation of band structures and to create a complete theoretical foundation for the experimental realization.

The theoretical calculation of the transmission spectrum was realized by simulating a SAW device composed of two parts of aluminum inter-digital transducers (IDTs) and a PnC formed by arrays of Ni pillars located between IDTs, as well as a semi-infinite Y128-X cut propagating LiNbO_3 substrate. The lattice constant is a for all the structures. The models built

for square, triangular-X and triangular-Y lattice symmetries in COMSOL are shown in Figure 3.20. Wave propagation is along direction x . Periodic boundary conditions are applied along with the direction y which is perpendicular to the propagating direction. The lattice constant is a for all the structures. The widths of the models are respectively $a, \sqrt{3}a$ and a for square, triangular-X and triangular-Y lattices. The semi-infinite piezoelectric substrates are surrounded by layers of absorption which can be used to absorb the undesired reflections from the boundary. Input IDTs on the left side are given a harmonic voltage signal to excite the incident waves which propagate through the phononic crystal in the middle and received by the output IDTs on the right side. The transmission spectrum is calculated by measuring the output voltage amplitude.

Anisotropic LiNbO_3 is chosen as the substrate material. Isotropic nickel is chosen as the pillar's material, whose density and Young's Modulus are shown in Table 3.4. Aluminum is chosen as the material of IDTs. The aluminum parameters related in the calculation are shown in Table 3.9.

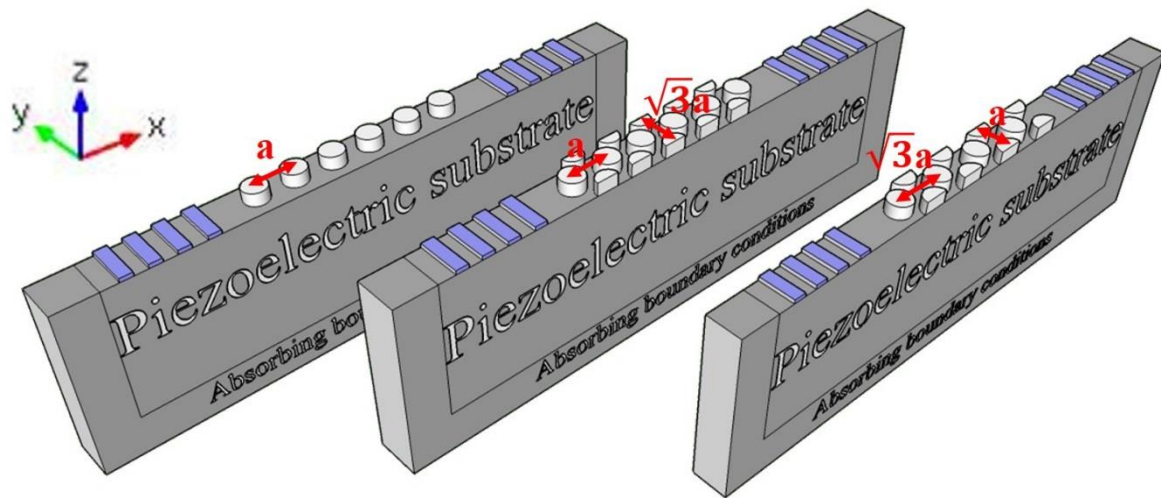


FIG. 3.20. Models of device used for the calculation of SAW transmission through PnC of square lattice (left), triangular-X lattice (middle) and triangular-Y lattice (right) in COMSOL.

TAB. 3.9. Aluminum parameters related in the calculation of the transmission spectrum.

Relative permittivity	1
Density	2700 kg/m^3
Young's Modulus	70 GPa
Poisson's ratio	0.33

3.8.1 Pillar-based PnCs with a square lattice on a Y128-X LiNbO₃ substrate

Figure 3.21 illustrates the calculated band structure and transmission spectra of the PnC composed of square arrays of cylindrical nickel pillars on a Y128-X LiNbO₃ substrate. The lattice constant $a = 9\mu\text{m}$, pillar's height $h = 4\mu\text{m}$, pillar's radius $r = 3\mu\text{m}$. From the band structure calculated along the boundary ΓK of the irreducible Brillouin zone, four surface acoustic modes can be clearly observed respectively at the frequencies 89MHz, 95MHz, 149MHz and 160MHz. In the transmission spectra, Mode 1, Mode 3 and Mode 4 are related to three picks at the same frequencies shown in the band structures. But for Mode 2, we can't find any information about it in the transmission spectra. This phenomenon can be explained by the polarization of pillars for each mode, which is depicted in Figure 3.22. In this study, LiNbO₃ Y128-X substrate can only generate sagittal acoustic waves who has the polarization in direction x and z (very weak in direction y). From Figure 3.22, we can find that the polarization of pillars for Mode 2 is primarily in direction y (weakly in direction z). Consequently, Mode 2 cannot be observed in the transmission spectra. After 160MHz, a big gap appears, resulting in attenuation about 40dB to 50dB. That may be caused by Bragg scattering and the radiation of surface acoustic waves turning into bulk acoustic waves. Figure 3.23 illustrates the interaction of surface acoustic waves on the four frequencies: $f = 89\text{MHz}$, 95MHz , 149MHz and 160MHz . As shown in Figure 3.23 (a)(c)(d), the energy of the waves transferred from one pillar to another can be blocked and delayed in the pillar array at the these frequencies. For the case around the second mode shown in Figure 3.23(b), after the first pillar, no more pillars deform.

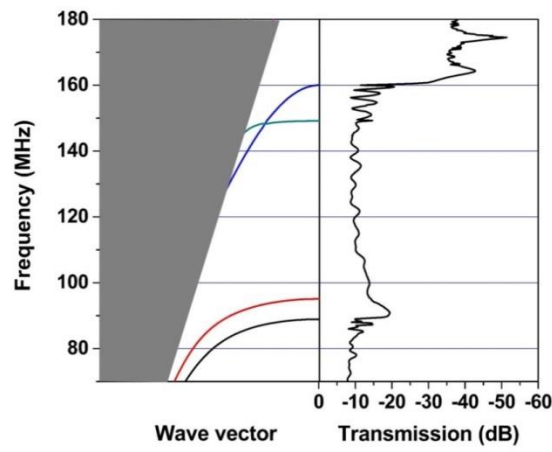


FIG. 3.21. The calculated band structure and transmission spectra of the PnC composed of square arrays of cylindrical nickel pillars. The lattice constant $a = 9\mu\text{m}$, pillar's height $h = 4\mu\text{m}$, pillar's radius $r = 3\mu\text{m}$.

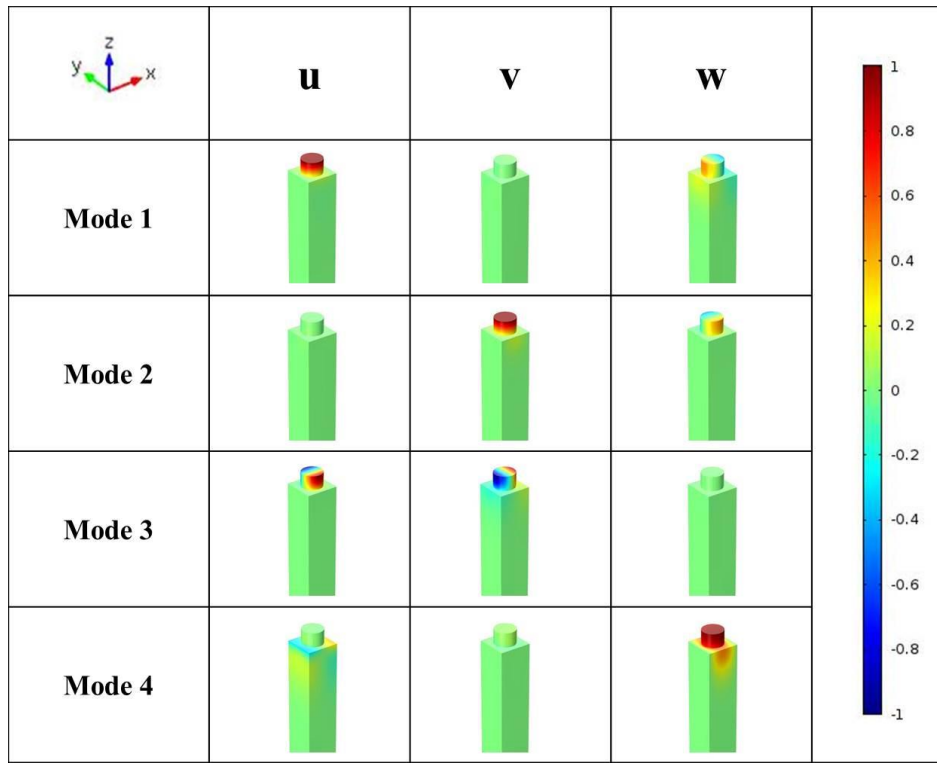


FIG. 3.22. Displacement components of pillars with square lattice. The lattice constant $a = 9\mu\text{m}$, pillar's height $h = 4\mu\text{m}$, pillar's radius $r = 3\mu\text{m}$.

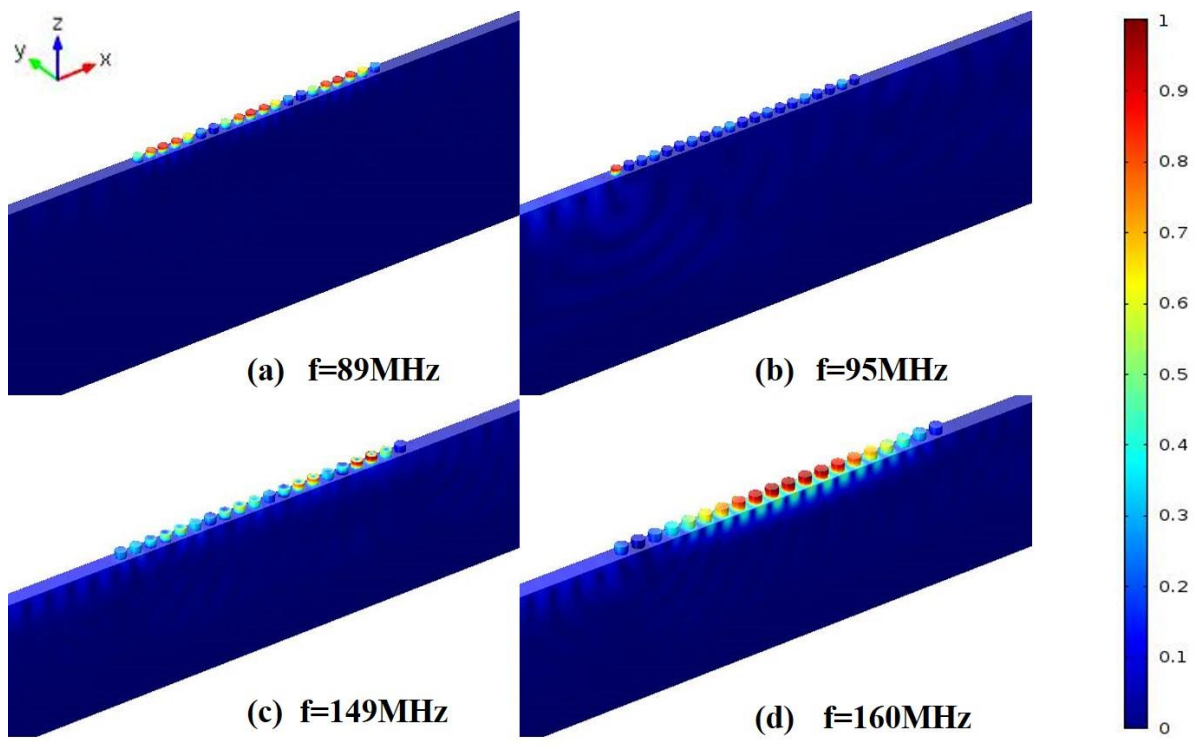


FIG. 3.23. Normalized elastic displacement distribution in the delay line for four frequencies: (a) $f=89\text{MHz}$, (b) $f=95\text{MHz}$, (c) $f=149\text{MHz}$, (d) $f=160\text{MHz}$.

3.8.2 Pillar-based PnCs with triangular lattices on a Y-Z LiNbO₃ substrate

Figure 3.24 illustrates the calculated band structures and transmission spectrum of the PnC composed of triangular-X and triangular-Y arrays of cylindrical nickel pillars on a Y-Z LiNbO₃ substrate which can generate only pure sagittal Rayleigh waves. The lattice constant $a = 9\mu m$, pillar's height $h = 3.5\mu m$, pillar's radius $r = 3\mu m$. From Figure 3.24, we can observe that the two modes for triangular-X lattice are very close on the boundary of the irreducible Brillouin zone, resulting in much oscillation at the corresponding frequencies in the transmission spectra due to the collective resonance. After the oscillation part, a wide band gap about 20dB loss is observed. The case for the PnC with triangular-Y lattice is different. The two modes are well separated, resulting a band gap of more than 20dB. Different from the case for triangular-X lattice, there is no coupling between the modes.

Figure 3.25 illustrates the normalized elastic displacement distribution for both triangular-X and triangular-Y lattices. For the case with triangular-X lattice, we observe the displacement at two frequencies, $f=110.5\text{MHz}$ which in the oscillation part and $f=120\text{MHz}$ which in the band gap. We observe that the energy transfers for one pillar to another. Almost all the pillars have a deformation along the direction x and z because the wave is sagittal, shown in Figure 3.25(a). However for the frequency in the band gap, when the wave arrives at the first pillar, almost all the waves are diffracted to the substrate, shown as Figure 3.25(b). There is no energy transferring to the other side. For the case with triangular-Y lattice, we have the similar displacement field. At the frequency $f=104.6\text{MHz}$, shown in Figure 3.25(c), the wave transfers and all the pillars deform. But at the frequency $f=107.5\text{MHz}$, shown in Figure 3.25(d), the waves are diffracted into substrate when they arrive the first pillar as we have observed in the case with triangular-X lattice.

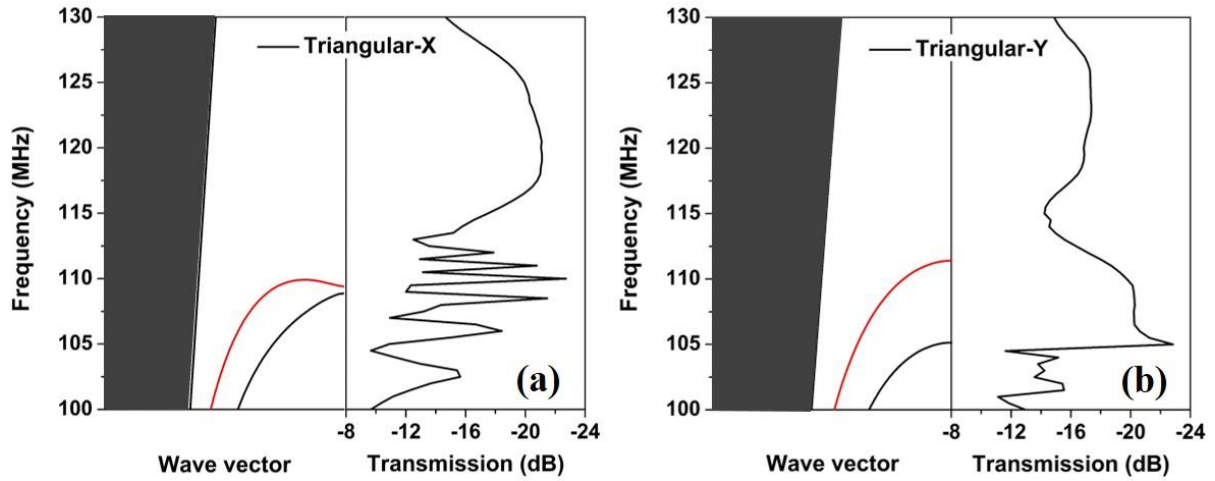


FIG. 3.24. Calculated band structures and transmission spectrum of the PnC composed of triangular-X (a) and triangular-Y (b) arrays of cylindrical nickel pillars. The lattice constant $a = 9\mu\text{m}$, pillar's height $h = 3.5\mu\text{m}$, pillar's radius $r = 3\mu\text{m}$.

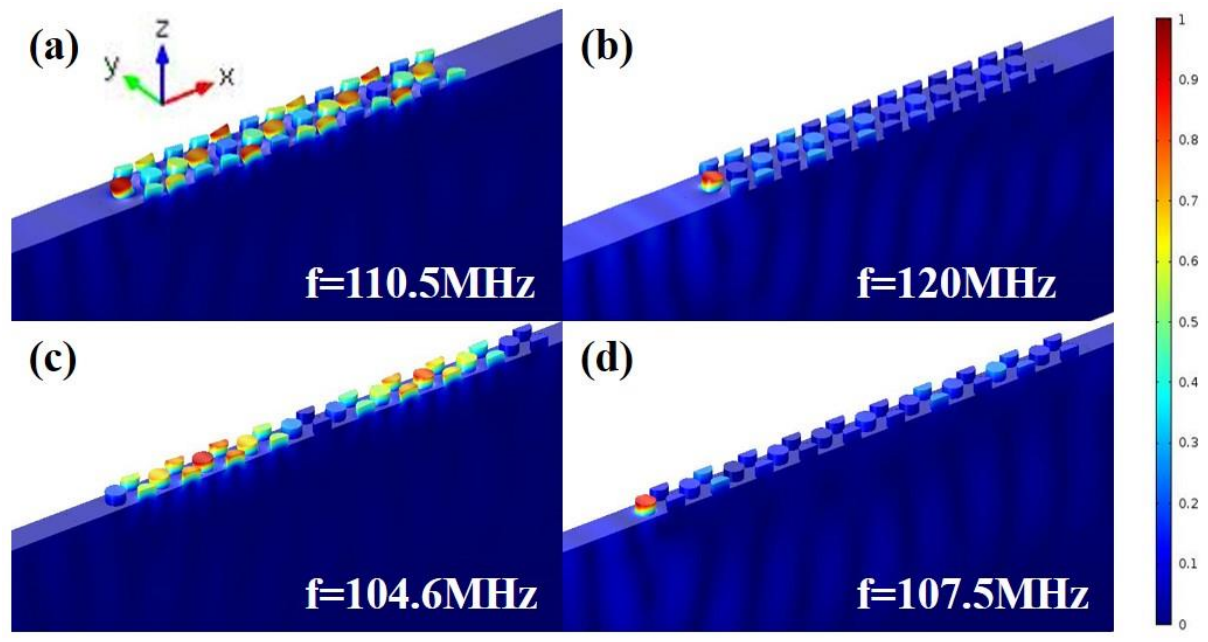


FIG. 3.25. Normalized elastic displacement distribution for triangular-X lattice at the frequencies $f=110.5\text{MHz}$ (a) and $f=120\text{MHz}$ (b); for triangular-Y lattice at the frequencies $f=104.6\text{MHz}$ (c) and $f=107.5\text{MHz}$ (d).

3.8.3 Discussion about Young's Modulus

In the previous part of this chapter, we have discussed the effect of elastic parameters of pillars on band structures (Figure 3.18). We have found that with the increase of Young's Modulus, the frequencies within the band gaps increase. Here we discuss again the Young's Modulus from the point of view of transmission spectrum.

As the previous part, Y128-X LiNbO₃ is chosen as the material of the substrate. The cylindrical pillars are made of diamond with different Young's Modulus: 75GPa, 150GPa, 300GPa and 1075GPa. The pillar's height is 5 μm and the radius is 3 μm . Figure 3.26 illustrates the transmission spectrum with different Young's Modulus. From this figure, we can find that with the increase of Young's Modulus, the band gaps are put forward to higher frequencies, which well matches with the results of Figure 3.18. On the other hand, we notice that with the increase of Young's Modulus, the band gaps become wider, which means the coupling between the pillars and the waves become stronger.

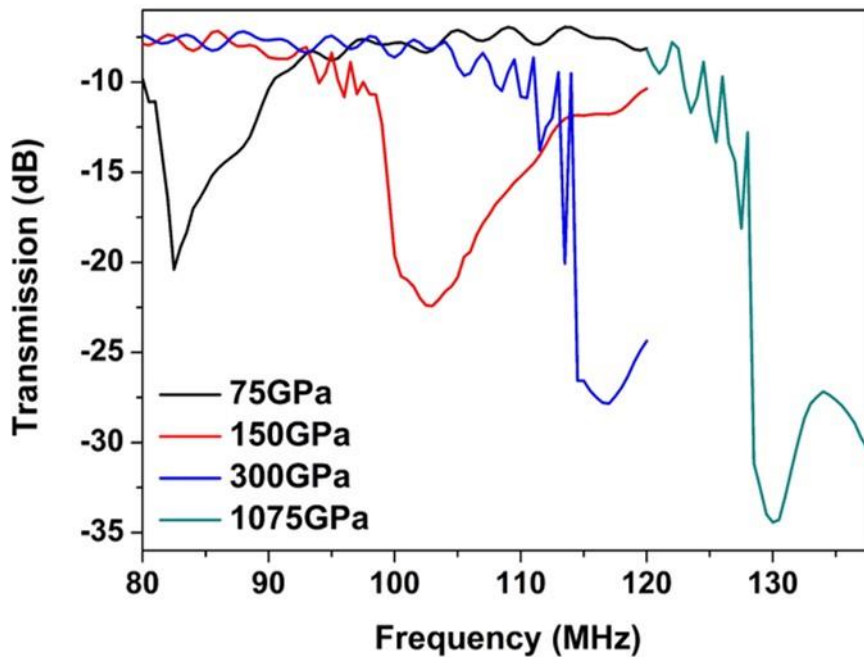


FIG. 3.26. Transmission spectrum of PnCs with different Young's Modulus of pillars.

3.9 Conclusion

In this chapter, we have talked about the modeling of phononic crystals by the finite element method. We started with the introduction of the FEM. Then by using this method in COMSOL software, band structures of pillar-based PnCs within different lattice symmetries were built. We have shown the evidence of locally resonant PnC band gaps and talked about the physics. Meanwhile, we focused on the effect of pillar's geometrical parameters such as radius and height on the band gaps, as well as the effect of PnC anisotropy. Different from the previous work, we have mainly talked about the polarization of pillars, which represents

always the intrinsic properties of elastic wave propagation through a PnC. Next, we gave the material consideration, compared the PnCs composed of pillars of materials with different density and Young's Modulus. We also studied the temperature coefficient of frequency for surface modes and observed that the sensitivity could be affected by the geometrical parameters and the anisotropy of the PnCs, which is very meaningful for the application of the sensors based on PnCs. At last, to prove the results obtained from band structures and to prepare for the experimental realization, calculations of transmission spectrum were made.

Chapter 4: Design, fabrication and characterization of pillar-based phononic crystals

Theoretical aspect of pillar-based phononic crystals has been presented about in the previous sections. In this chapter, the experimental realization of pillar-based phononic crystals and inter-digital transducers used in this work will be presented in details. The design idea is based on the theoretical calculation. The fabrication was realized in the clean room of IEMN (Institut d'Electronique de Microélectronique et de Nanotechnologie) by Micro-fabricating techniques, such as photo lithography, sputtering, etching, etc. In addition, nickel pillars were fabricated by electroplating which is an electro-chemical method.

4.1 Selection of materials

Before the fabrication, the first problem that should be considered is the selection of materials. In this work, the substrate is required to be able to generate surface acoustic waves by a given electric signal; so the piezoelectric materials such as quartz, LiTaO_3 , ZnO and LiNbO_3 are considered. To study the propagation of surface acoustic waves, we consider the substrate as a homogeneous semi-infinite substrate, in which Rayleigh waves are susceptible to propagate. In this work, LiNbO_3 Y128-X cut and Y-Z cut substrates were chosen as the material of the substrate.

The most common material for inter-digital transducers is the aluminum. First, aluminum has the best electrical conductivity among the metals after silver, copper and gold which are much more expensive than aluminum. Secondly, the deposition of a 200nm aluminum layer is easy to achieve by sputtering. Moreover, the chemical property of aluminum is relatively stable, so the sample can be preserved easily. In addition, the aluminum can be also easily removed by the acid solution if the sample is not proper enough.

For the consideration of the PnCs, we have exploited several possibilities, including assembled Fe/FeO nanoparticles in a magnetic field, etched silicon pillars, electroplated nanowires through an anodic aluminum oxide template and self-assembled polystyrene or silica nanospheres. These exploitations will be discussed in the following chapter. Since all these exploitations are not experimentally mature enough, in this work, we chose the nickel pillar-based PnCs realized by electroplating. The reason to choose nickel as the pillar's material is that we expect to study the magnetic property of PnCs in the following investigation, which is one of the main subject of our group. Compared with iron and cobalt which are very easy to be oxidized, nickel has a more stable chemical property. Another reason is that the fabrication of nickel pillars can be achieved by electroplating, which is already a mature method. To my knowledge, it's impossible to fabricate metal pillars with a height of several micro meters by sputtering or evaporation. The only and most common method is electroplating. And nickel is happened to be a good electroplating material.

Besides the materials of the substrate, IDTs and PnCs, some seed and adhesion layers, as well as photoresists should all be well considered. This will be discussed in the fabrication part of this chapter.

4.2 Device design

The objective is to design the SAW devices composed of two dispersive or slanted interdigital transducers (IDTs) between which there is a pillar-based PnC with various symmetries. The model of device used in this work is shown in Figure 4.1.

The IDTs here were regarded as a source which is used for generation and reception of surface acoustic waves. It was made of comb-shaped arrays of metallic electrodes. Aluminum was chosen as the material for IDTs. Figure 4.1 clearly shows us the SAW device in which we were using two IDTs where one IDT was used for emitting waves and the other one was used for receiving waves. These metallic electrodes should be deposited on the surface of a piezoelectric substrate, such as quartz or lithium niobate, to form a periodic structure.

The working mechanism of the device is that when a voltage is applied at the input IDT, the substrate deforms because of the piezoelectric effect of the LiNbO₃ substrate, which can generate SAWs propagating though the PnCs. On the other hand, when the SAWs arrive

at the output side, the deformation generates an electric field because of the inverse piezoelectric effect. Then the mechanical signals are back to the electrical signals received by the output IDT which is always connected a network analyzer.

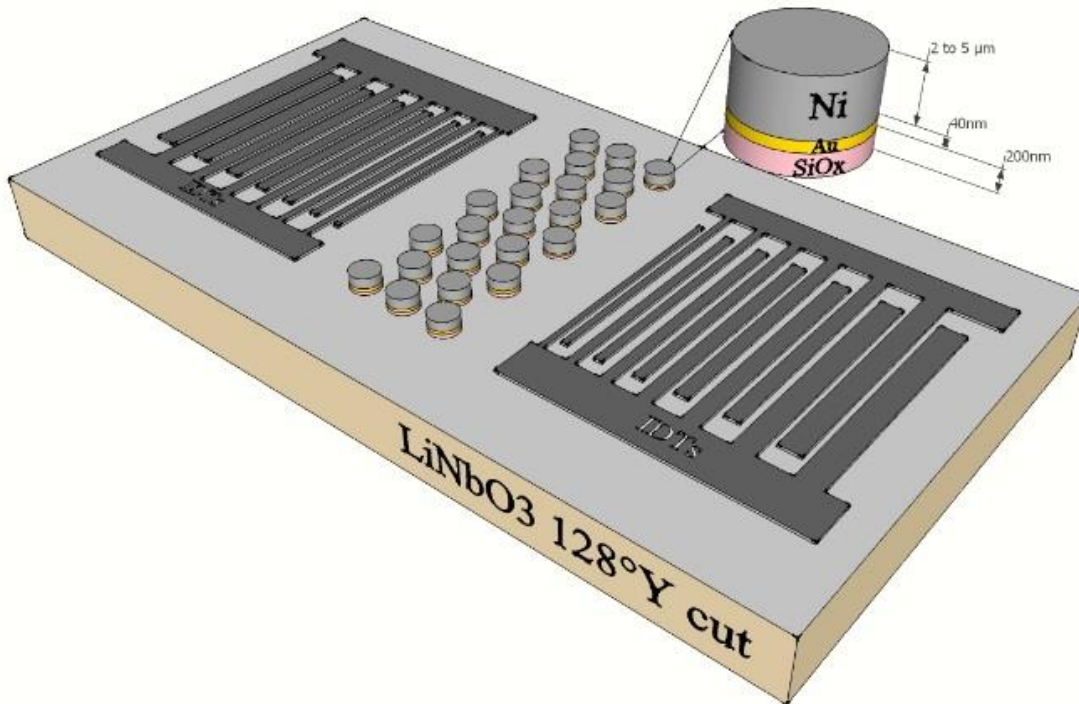


FIG. 4.1. Model of device used for investigating the propagation of surface acoustic waves in a periodic array of pillars on a semi-infinite substrate.

In this work, for the design of dispersive IDTs, the transducers are permitted to cover the entire operation frequency range of interest enabling the easy observation of opening band gap for the designed phononic crystal. In our design, we have two different kinds of IDTs. One is applied for low frequency, the periodicity of the corresponding IDTs ranges from $24\mu\text{m}$ to $76\mu\text{m}$. The other one is applied for high frequency, the periodicity d of the correspondent IDTs ranges from $12\mu\text{m}$ to $36\mu\text{m}$. The periodicity d is equal to the generated wave length λ as shown in Figure 4.2. The propagating velocity of the Rayleigh waves in LiNbO_3 Y128-X cut substrate is 3980m/s . The working frequency is $f = v/\lambda$. So in this work, the working frequency range applied for low frequency is from 52MHz to 166MHz and for high frequency is from 111MHz to 332MHz . Besides the dispersive IDTs, we have also the slanted IDTs designed by a commercial company.

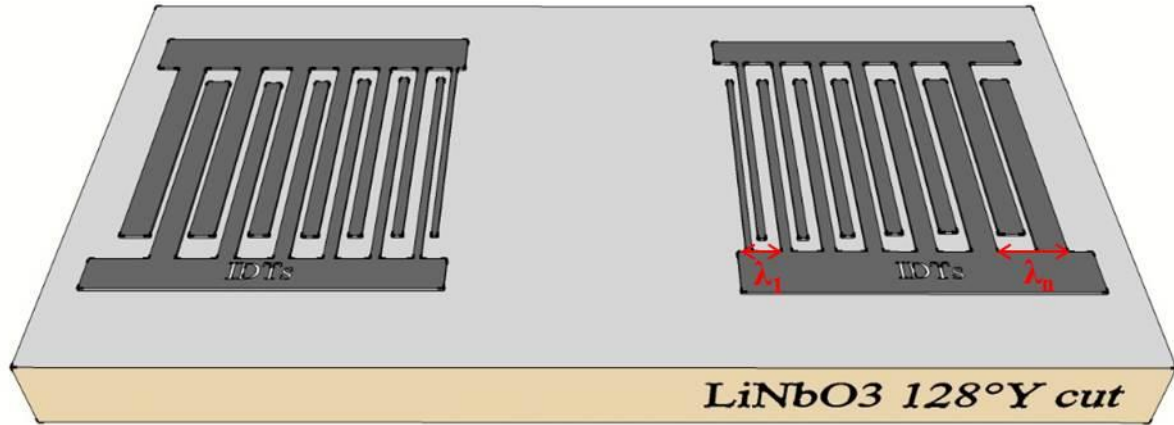


FIG. 4.2. Schematic of IDTs used in this work.

For the design of phononic crystals located between two IDTs, we consider different symmetries such as square, triangular-X, triangular-Y, hexagonal-X and hexagonal-Y arrays of cylindrical pillars. The symmetries of crystals are shown in Figure 4.3. The distance between two centers of adjacent pillars a is respectively $10\mu\text{m}$ for square lattice, $9\mu\text{m}$ for triangular lattices and $7\mu\text{m}$ for hexagonal lattices. And the radius of the cylindrical pillars is respectively $4\mu\text{m}$ for square lattice, $3\mu\text{m}$ for triangular lattices and $2\mu\text{m}$ for hexagonal lattices. The thickness of the substrate is D which can be seen as semi-infinite ($D=500\mu\text{m}\gg h$), where h is the height of pillars.

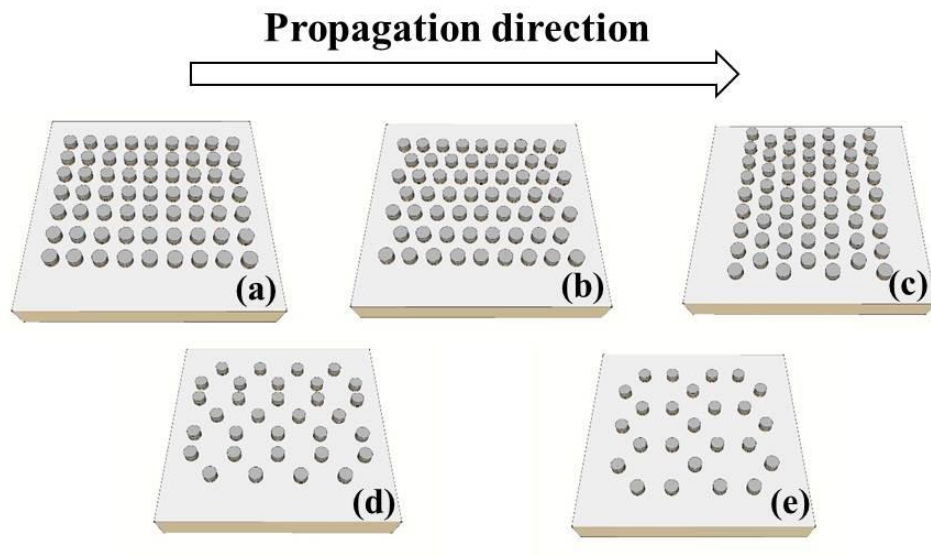


FIG. 4.3. Symmetries of crystals used in this thesis, square lattice (a), triangular-X lattice (b), triangular-Y lattice (c), hexagonal-X lattice (d), hexagonal-Y lattice (e).

4.3 Fabrication of IDTs and PnCs

The fabrication process starts with the LiNbO_3 Y128-X cut wafer, the substrate is favorable for generating sagittal type Raleigh wave modes. The IDTs were fabricated by sputtering an aluminum thin film and the photo lithography process. Then a layer of SiO_2 (200nm) was deposited by PECVD to protect the IDTs before the sputtering of Ti/Au layer (10nm/40nm). The Au film acts as a seed layer for Ni electroplating, and the Ti film is the adhesion layer between the Au film and SiO_2 layer. A Nickel thick layer (4 μm) was then electroplated inside a photoresist mould (AZ15nXT) of thickness around 4.5 μm . In the electroplating, the current density was $20\text{mA}/\text{cm}^2$, the electroplating bath was controlled at 40°C and the Ni deposition rate was $0.1\ \mu\text{m}/\text{min}$. At last, etching was used by RIE process along the nickel pillars and all the rest of Ti/Au and SiO_2 was removed. Schematic of the whole fabricating process is shown in Figure 4.4. In the following parts, every step of the fabricating process will be presented in details.

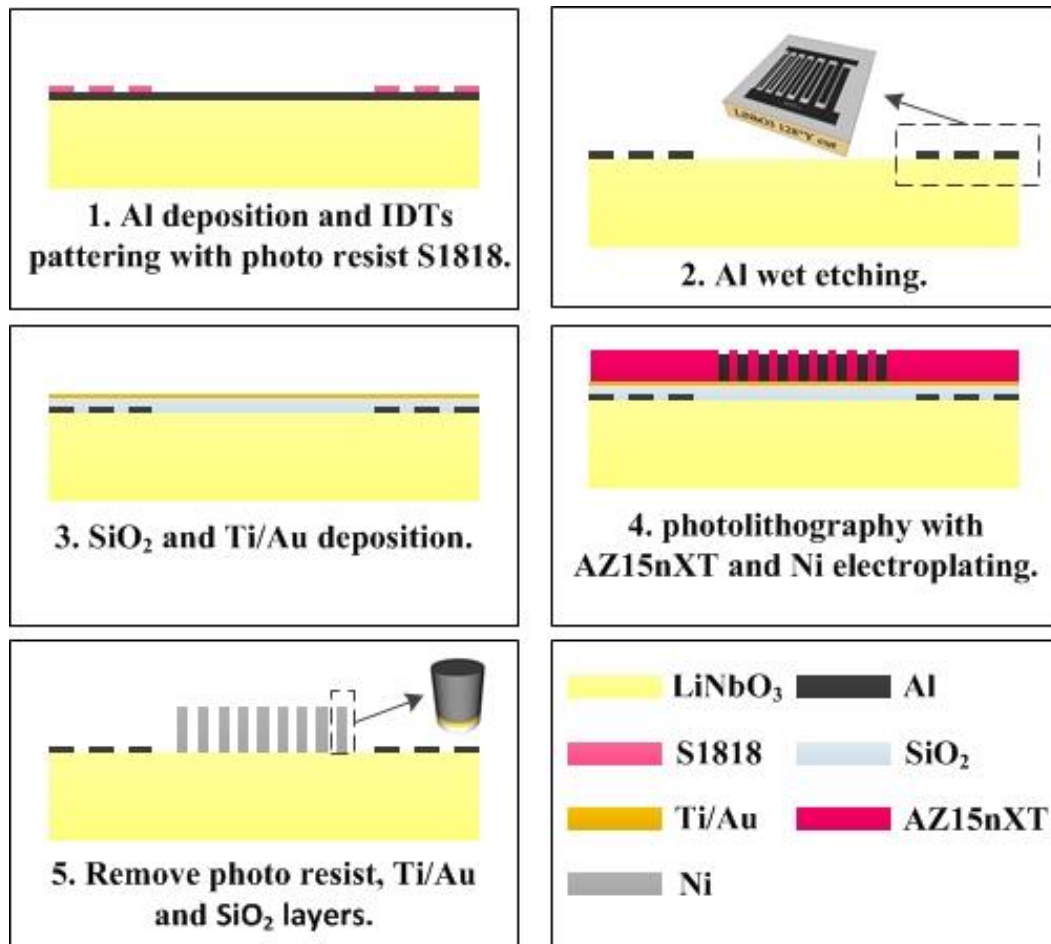


FIG. 4.4. Micro-fabricating Process of the device.

4.3.1 Substrate cleaning

In this work, LiNbO₃ Y128-X cut wafer was chosen as the substrate because of its piezoelectric property. However it is an expensive and fragile wafer, so normally we do a test on the Silicon wafer. Then when all the material and techniques are well tested, the real sample will be fabricated with the LiNbO₃ substrate. No matter which substrate we use, the first step is always cleaning the substrates.

The objective of the substrate cleaning is to remove unwanted organic and inorganic impurities, such as residual photoresist, dust and other particulates from the substrate surface. Wafer cleaning and treatment of surface is usually a complex and important step in the semiconductor manufacturing. If the surface is not proper enough, the following steps are just a waste of time. Normally, when the wafer is new or almost clean, to be sure, a simple cleaning process is still required as follows:

1. Ultrasonic cleaning with deionized (DI) water for 3 minutes and rinsing with DI water.
2. Ultrasonic cleaning with acetone for 3 minutes and rinsing with acetone.
3. Rinsing with isopropanol alcohol (IPA).
4. Dry with Nitrogen (N₂).
5. Place on hot plate for 5 minutes at 180 °C.

DI water can be used to remove the inorganic particulates. The acetone is reasonably successful at removing organic from the surface, and the IPA serves to remove the residue left behind by the acetone. The solvents and water that remain on the wafer can be blown off by N₂ and evaporated on the hot plate.

For the wafer which has photoresist or other impurities on the surface, besides the normal cleaning method mentioned above, some special cleaning methods are necessary. Wafers with photoresist on them can be cleaned by submersion in the appropriate remover, such as Remover PG, SVC14, etc. Appropriate heating and ultrasonic treatment can also be useful to remove the residual photoresist. To eliminate the photoresist which is very hard to be removed in remover, an oxygen plasma etch is recommended for several minutes. This method is very powerful and efficient, but it should be very careful to select the right mode. Otherwise, there will be the risk that the surface may be etched too. Particularly stubborn contaminants may require the use of a more aggressive cleaning procedure such as Piranha (a mixture of 3:1 concentrated 96% sulfuric acid to 30% hydrogen peroxide solution) etch.

However, the Piranha etch should be very cautious to clean a LiNbO₃ wafer because the temperature will be increased sharply during the etching process, the wafer may be broken by the heat.

After the cleaning process, the substrate should be examined by microscope to ensure that the surface is clean enough to be continued.

4.3.2 Patterning by photolithography

The most common technique for patterning in microfabrication is lithography. According to the requirements of the pattern size, lithography can be divided into microlithography and nanolithography. Typically, features smaller than 10 μm are considered microlithographic, and features smaller than 100nm are considered nanolithographic. Photolithography is one of microlithography methods with a resolution about 1 μm, often applied to fabricate Micro-electro-mechanical systems (MEMS) devices. Photolithography generally uses a pre-fabricated photomask or reticle as a master from which the final pattern is derived. For the features in nanoscale, one of the nanolithography methods electron beam lithography will be applied with a resolution sub-10nm. Electron beam lithography as it is usually practiced is a form of maskless lithography, in that a mask is not required to generate the final pattern. Instead, the final pattern is created directly from a digital representation on a computer, by controlling an electron beam as it scans across a resist-coated substrate. However electron beam lithography has the disadvantage of being much slower and more expensive than photolithography. As the patterns in this work are in micro scale, photolithography was chosen as the patterning method.

Using photolithography, patterns with feature size greater than 1 μm can be readily transferred to a photoresist by high intensity radiation and a photomask. Photoresists are classified into two groups: positive resists and negative resists. A positive resist is a type of photoresist in which the portion of the photoresist that is exposed to light becomes soluble to the photoresist developer. The portion of the photoresist that is unexposed remains insoluble to the photoresist developer. A negative resist is a type of photoresist in which the portion of the photoresist that is exposed to light becomes insoluble to the photoresist developer. The unexposed portion of the photoresist is dissolved by the photoresist developer. Generally speaking, different types of photoresists vary significantly in their properties. Positive photoresists can typically achieve smaller feature sizes than negative photoresists, however,

negative photoresists are usually better at resisting wet-etching chemicals. In this work, the photoresist S1818 used for patterning the IDTs is a kind of positive resists. And the photoresist AZ15nXT used for patterning the phononic crystals is a kind of negative resists.

The basic procedure for patterning by photolithography is usually in the following steps: spin coating of photoresists, soft bake, mask alignment and exposure, post exposure bake if necessary and development. In this work, the photolithography was realized in the clean room of IEMN shown in Figure 4.5.



FIG. 4.5. Photolithography in the clean room of IEMN.

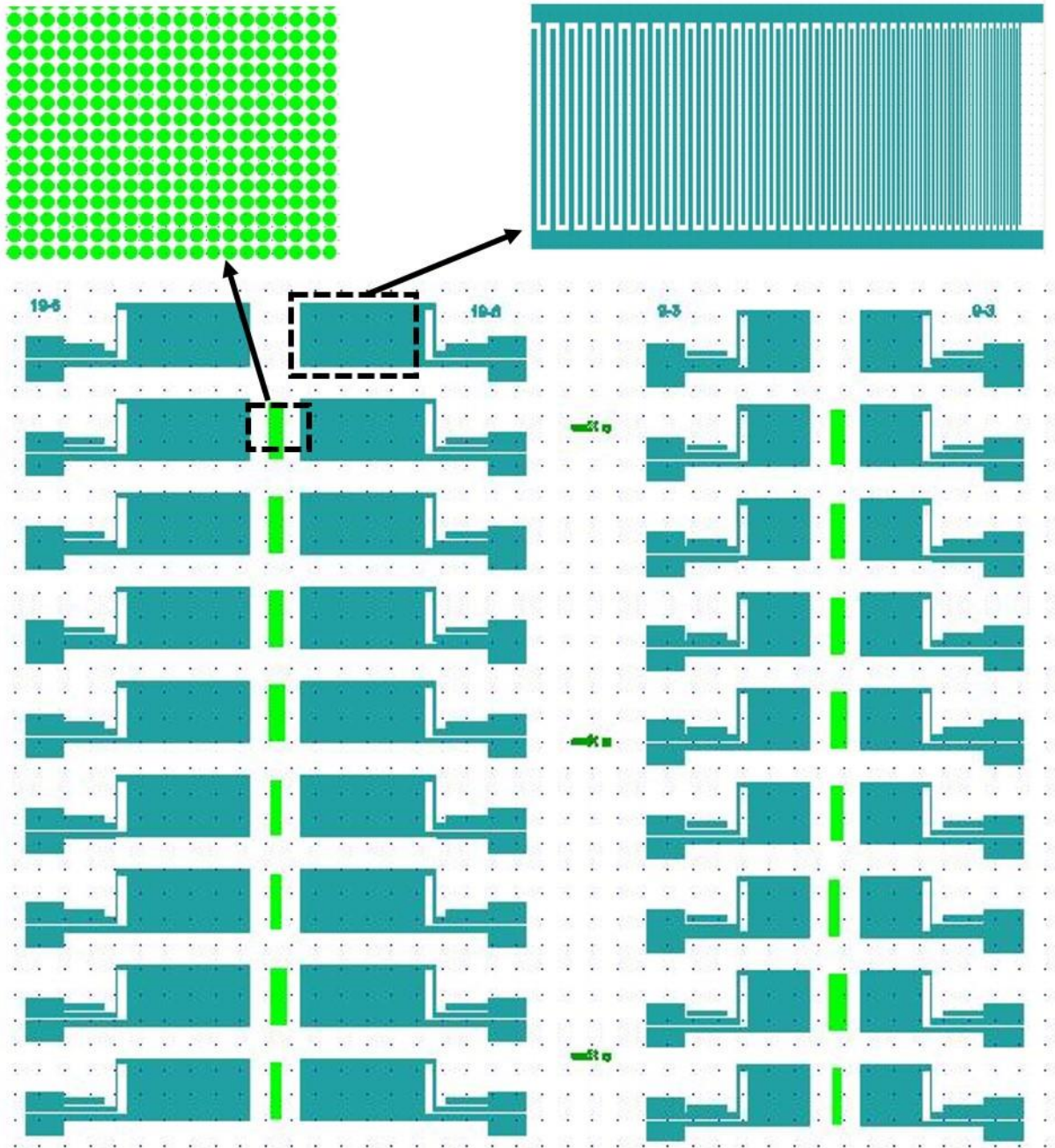


FIG. 4.6. The design of photomasks for PnCs with dispersive IDTs.

Before patterning, we need to have the suitable photomasks for both IDTs and phononic crystals. Since a positive photoresist S1818 was chosen for patterning IDTs, the photomask for IDTs should be also positive which means that the mask should be designed to block light in the regions where metal was to be deposited. In the other hand, a negative photoresist AZ15nXT was chosen for patterning phononic crystals, so the relevant photomask should be negative too which means that the mask should be designed to block light in the regions where the holes were to be etched.

The mask was designed by a software named Layout Editor. The export format should be gds. Then mask designs was transformed into a chrome film on glass by the engineers in IEMN by electron photolithography. The chrome acts as an absorber for light incident on the mask, and the glass is essentially transparent, allowing the photoresist coated substrate below to be preferentially exposed. The design of the mask was shown in Figure 4.6 (PnCs with dispersive IDTs) and Figure 4.7 (PnCs with dispersive IDTs).

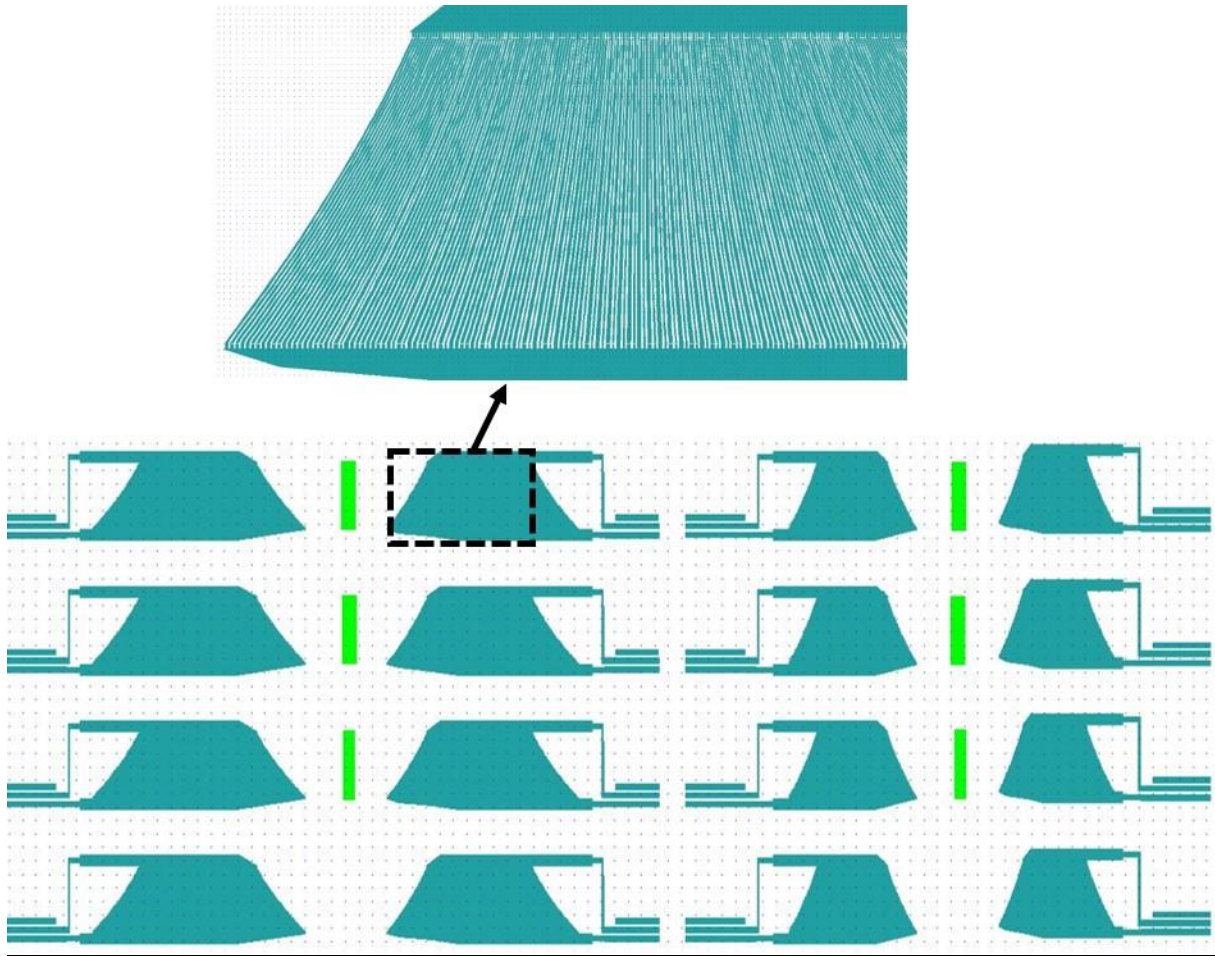


FIG. 4.7. The design of photomasks for PnCs with slanted IDTs.

When the photomask is ready, the patterning can be started with a spin coating which results in a uniform film deposited on the surface of a substrate. The spin coater used consisted of a vacuum chuck to securely hold and spin substrates at high revolutions per minute (rpm) in a well-controlled manner. The photoresist is dropped on the surface of the substrate with a dropper. The centrifugal force acts on the fluid to eject it off the edge of the substrate, leaving a film whose thickness varies with the spin time and rpm. Besides the parameters which can be set up, the thickness of the film is also related to the viscosity of the photoresist. Usually the thickness of photoresist h can normally be expressed as

$$h \propto \sqrt{\frac{v}{\omega}} \quad (4.70)$$

where v is the viscosity and ω is the spin speed. The exact parameters of a photoresist can be found in its own datasheet.

After the spin coating, the resist film contains a remaining solvent concentration depending on the resist, the solvent, the resist film thickness and the resist coating technique. The soft bake reduces the remaining solvent content in order to:

- ✓ Avoid mask contamination and/or sticking to the mask,
- ✓ Prevent popping or foaming of the resist by N_2 created during exposure,
- ✓ Improve resist adhesion to the substrate,
- ✓ Minimize dark erosion during development,
- ✓ Prevent dissolving one resist layer by a following multiple coating,
- ✓ Prevent bubbling during subsequent thermal processes.

The step following with soft bake is exposure which allows the careful alignment of a substrate to a photomask and delivers a well-defined dose to the exposed portions of photoresist. The photomask is absorbed by a supporter located on the sample. The mask aligner is equipped with a microscope that can be used to inspect the alignment of the sample to the mask. Since the mask is fixed, the sample can be translated or rotated to adjust the alignment. Different exposure modes such as soft/hard contact, low vacuum, vacuum etc., can be chosen according to the size of the pattern, the thickness of the film and the photoresist properties. The radiation source of exposure is provided by a UV lamp with a wavelength 365nm. And the light per unit area is $10\text{mW}/\text{cm}^2$. Another important parameter of exposure is the exposure time. The mask aligner is equipped with an electronic timer that opens and closes a shutter allowing for exposure times from a fraction of a second to several minutes. Normally, exposure time less than 20 seconds is a suitable choice. Higher exposure time results in diffracted light giving a significant dose to regions that are supposed to be sheltered, making the pattern extremely difficult to develop. Here we use an example to explain how the exposure time results in the sample. The negative photoresist AZ15nXT (diluted 10:1) was deposited on the substrate with a layer of Au/Ti. The objective is to etch the holes from the top to the gold layer. Four parallel tests were done with the same parameters besides the exposure time which was respectively 23s, 21s, 19s and 17s. After a post exposure bake of 1 minute at 120°C and the development in AZMIF326 for 2 minutes 15 seconds, the four

samples were characterized by a Scanning Electron Microscope (SEM). The photos are shown in Figure 4.8.

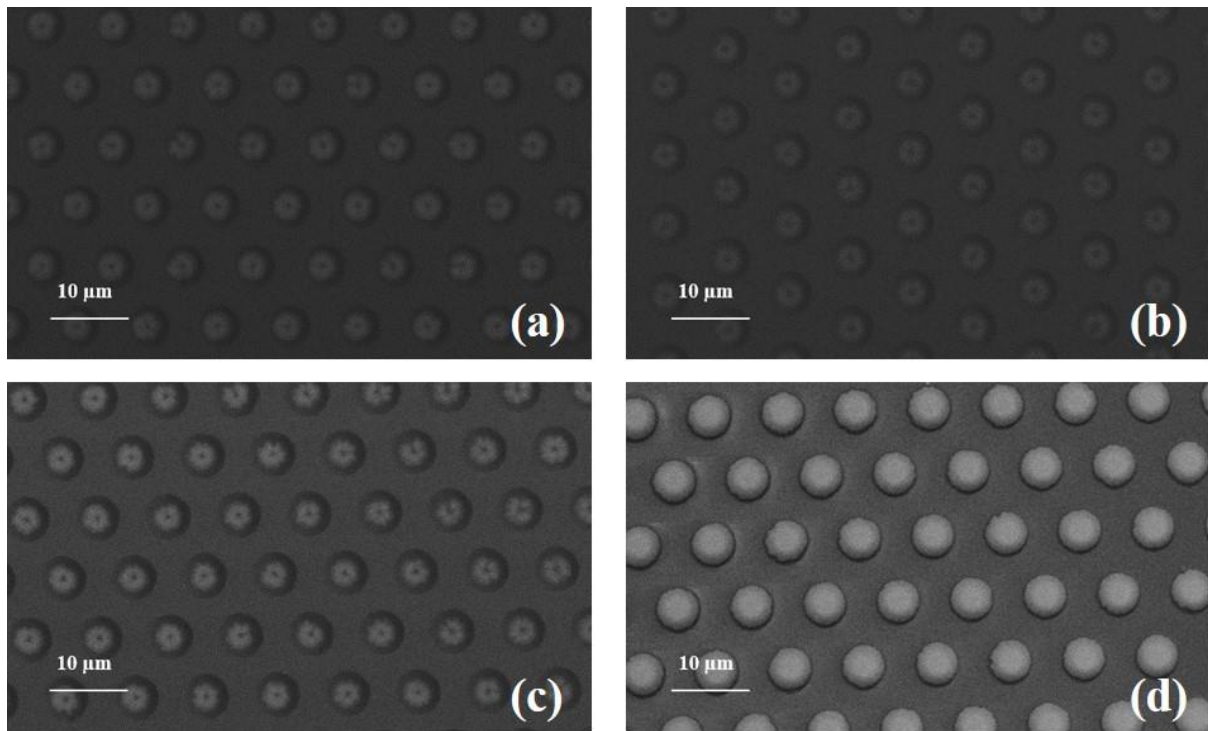


FIG. 4.8. SEM photos of the negative photoresist AZ15nXT (diluted 10:1) with different exposure time and the same development. Exposure time is respectively 23s (a), 21s (b), 19s (c) and 17s (d).

From these four SEM photos, we can find that with the reduction of the exposure time, the patterning works better. When the exposure time is 23s and 21s, the holes are not opened and the diameter is small, shown in Figure 4.8 (a) and (b). When the exposure time is reduced to 19s, the holes begin to be opened even though the form is not exactly a circle and there is still the residual photoresist in the center, as shown in Figure 4.8 (c). However when the exposure time is 17s, we find that the holes are well opened because we can see clearly the metal color and the bottom diameter is almost the same as the top, shown in Figure 4.8 (d).

After the exposure, a post exposure bake sometimes is required for 1-2 minutes at about 110 °C or 120 °C. The post exposure bake can be applied above the softening point of the resist without destroying the structures to be developed due to the still closed resist film. But the post exposure bake is not necessary all the time, which depends on the photoresist. For example, in our work, there is no post exposure bake in the patterning process of the photoresist S1818 which is used for patterning IDTs. In the other hand, for the photoresist

AZ15nXT which is used for patterning phononic crystals the post exposure bake is essential for the crosslinking mechanism initiated during the exposure.

The exposed film should be immersed into the photoresist developer for some time ranging from several seconds to several minutes to remove the undesired portion. During development, the photoresist pattern is undercut and the degree of undercut increases with the amount of time that the sample spends in the developer solution. Different photoresists require to be developed in its suitable developers. For example, in this work, Photoresist S1818 needs to be developed in MF-319 solution and photoresist AZ15nXT's suitable developer is AZ326MIF solution. Before the development, it is necessary to determine the approximate development time, which varies substantially with exposure time because it's always impossible to see the patterning by eyes.

In this work, AZ15nXT (diluted 10:1) was deposited on 3 substrates with a layer of Ti/Au on the surface. Except the development time, all the other patterning parameters are the same. The development time is respectively 2min15s, 2min45s and 3min15s. The sample was characterized by SEM and the photos are shown in Figure 4.9.

From Figure 4.9 (a), we can find when the development time is 2min15s, there is still residual photoresist in the center of the holes, which can be improved, when the development time is prolonged to 2min45s. If we continue to develop it, there is no strong change.

During the development, we should watch the sample carefully under the microscope to find the appropriate development time. When the development is done, the whole patterning process is finished.

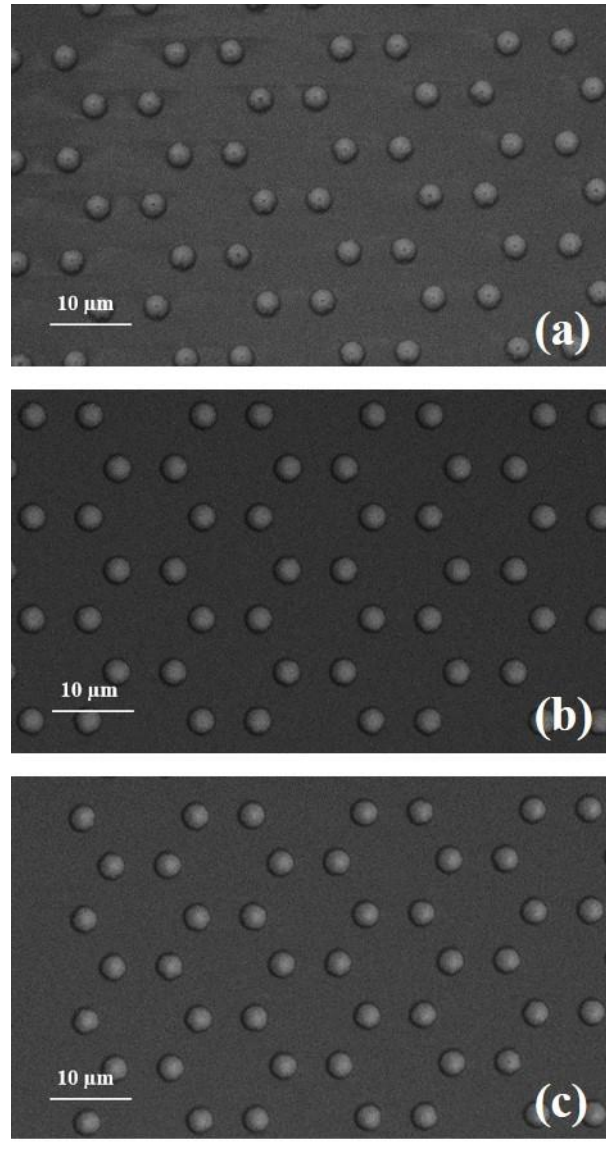


FIG. 4.9. SEM photos of the negative photoresist AZ15nXT (diluted 10:1) with different development time. Development time is respectively 2min15s (a), 2min45s (b) and 3min15s (c).

4.3.3 Metallic deposition

Besides photolithography, there are also other techniques required in this work. One of them is metallic deposition. In this work, a layer of aluminum with a thickness of 150nm was required as the material of IDTs. Moreover, a layer of Ti/Au with a thickness of 10nm/40nm was also needed as the bonding layer for Ni electroplating.

The metal deposits are used in all processes of production of electronic components, optoelectronics, sensors, micro mechanisms etc. They serve:

- Contacting the active layers in some types of components.

- Actuation mode for microsystems (shape memory alloys).
- Contacting pads for galling.
- Bonding layers in the case of electrolytic thickening.

The technique for metallic deposition used in this work is the cathodic pulverization (sputtering). Physical sputtering is driven by momentum exchange between the ions and atoms in the materials, due to collisions. The incident ions set off collision cascades in the target. When such cascades recoil and reach the target surface with an energy greater than the surface binding energy, an atom would be ejected, known as sputtering. The schematic of the sputtering is shown in Figure 4.10.

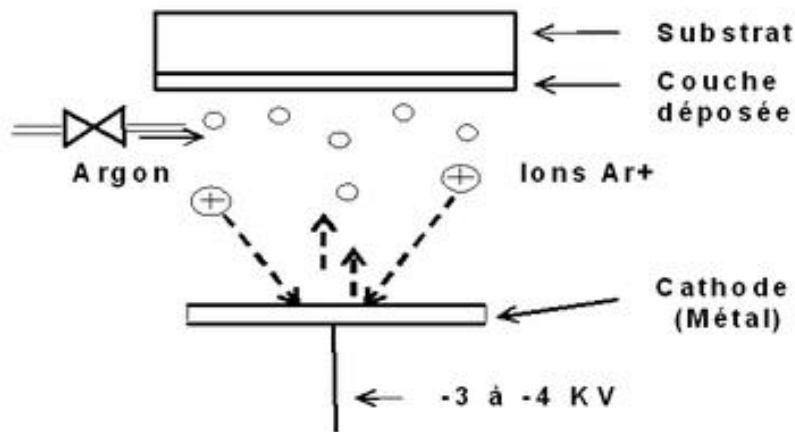


FIG. 4.10. Schematic of the sputtering.

4.3.4 Plasma-Enhanced Chemical Vapor Deposition (PECVD)

When IDTs were well fabricated, a layer of SiO_2 was deposited in order to protect the IDTs. The technique that we used to deposit a layer of SiO_2 is Plasma-enhanced chemical vapor deposition (PECVD) which is a process used to deposit thin films from a gas state (vapor) to a solid state on a substrate. Chemical reactions are involved in the process, which occur after creation of a plasma of the reacting gases. The plasma is generally created by RF (AC) frequency or DC discharge between two electrodes, the space between which is filled with the reacting gases. In this work, PECVD was realized by OXFORD Plasmalab 80 Plus whose schematic is shown in Figure 4.11.

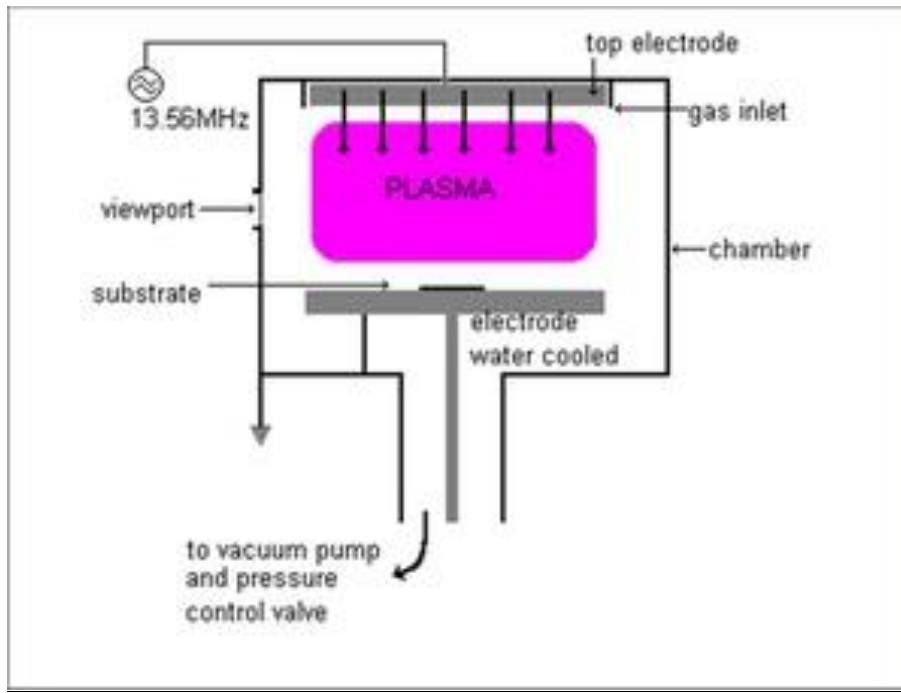


FIG. 4.11. Schematic of PECVD realized by OXFORD Plasmalab 80 Plus.

4.3.5 Etching

Etching is used in microfabrication to chemically remove layers from the surface of a wafer during manufacturing. During the etching process, part of the wafer is protected from the etchant by a mask which resists etching. The photoresists deposited by lithography is always chosen as the mask material. Etching can be classified by the phase of etchants into two parts which are wet etching and dry etching.

4.3.5.1 Wet etching

Wet etching is a material removal process that uses liquid chemicals or etchants to remove materials from a wafer. The specific patterns are defined by masks on the wafer. Materials that are not protected by the masks are etched away by liquid chemicals. These masks are deposited and patterned on the wafers in a prior fabrication step using lithography. A wet etching process involves multiple chemical reactions that consume the original reactants and produce new reactants. The wet etch process can be described by three basic steps.

- 1) Diffusion of the liquid etchant to the structure that is to be removed.

- 2) The reaction between the liquid etchant and the material being etched away. A reduction-oxidation reaction usually occurs. This reaction entails the oxidation of the material then dissolving the oxidized material.
- 3) Diffusion of the byproducts in the reaction from the reacted surface.

In this work, a layer of Aluminum with a thickness of 200nm partially protected by the photoresist S1818 was etched. There is always the formation of a very thin (a few nm) Al_2O_3 film at the surface of Al layer when Al is exposed in the air. This thin oxide layer makes Al very inert in many substances. Therefore Al etchants require at least compounds for dissolving Al_2O_3 as well as for etching (or respectively oxidizing) Al. As a result, the Aluminum etchants used in this work contains mixtures of 65% HNO_3 (for Al oxidation), 85% H_3PO_4 (to dissolve the Al_2O_3) and H_2O dilution to define the etch rate at room temperature by a volume ratio 1:4:1. Keep the sample immersed in the solution for 1-2 minutes until the parts without masque become clear. Then rinse the sample with DI water to remove the residual acid.

4.3.5.2 Dry etching

In dry etching, plasmas or etchant gasses remove the substrate material. The reaction that takes place can be done utilizing high kinetic energy of particle beams, chemical reaction or a combination of both. Here when we talk about the dry etching, it refers to the reactive ion etching (RIE) which is one of the most diverse and most widely used dry etching methods in industry and research. RIE uses both physical and chemical mechanisms to achieve high levels of resolution, which means the high energy collision from the ionization helps to dissociate the etchant molecules into more reactive species. Since the process combines both physical and chemical interactions, the process is much faster.

In this work, RIE was utilized to etch SiO_2 and Ti/Au with a mask of Nickel pillars. For SiO_2 etching, a mixture of gases CHF_3/CF_4 was used with a ratio 1:1. To etch the metal Ti/Au, a mixture of gases CF_4/O_2 was chosen with a ration 4:1 for Ti and 2:1 for Au. In addition, we can also use Argon to etch the metal, since the etching rate for Ti/Au is much faster than Ni.

4.3.6 Electroplating of Nickel pillars

4.3.6.1 Basic principles and electrodeposition bench set up

Electroplating is a process that uses electric current to reduce dissolved metal cations so that they form a coherent metal coating on an electrode. The part to be plated is the cathode of the circuit. In one technique, the anode is made of the metal to be plated on the part. Both components are immersed on a solution called an electrolyte containing one or more dissolved metal salt as well other ions that permit the flow of electricity. A power supply supplies a direct current to the anode, oxidizing the metal atoms that it comprises and allowing them to dissolve in the solution. At the cathode, the dissolved metal ions in the electrolyte solution are reduced at the interface between the solution and the cathode, such that they plate out onto the cathode. The rate at which the anode is dissolved is equal to the rate at which is plated, vis-à-vis the current through the circuit. In this manner, the ions in the electrolyte bath are continuously replenished by the anode.

Electroplating is a widely used electrochemical method for coating metal. Comparing with microsystem fabricating techniques such as sputtering and evaporation, electroplating is inexpensive and easy to operate. By controlling the composition of solution, the current amplitude, the agitation speed, the temperature and other parameters, the quality of the deposition can be guaranteed for a micro scale system. That's why that electroplating is chosen as the method for the fabrication of nickel pillars.

In our case, the electroplating bench is used for the electrodeposition of the small samples which means the substrate diameter is two inches or for the pieces of substrates. The beaker containing the electrochemical bath with a capacity of 2 liter, is placed on a magnetic stirrer with hotplate. The most basic electroplating bench is equipped with a power generator disposed between the cathode, formed by the sample to be electrodeposited and the anode can either be inert (for example Platinum) or consisted of material electrodeposited.

The electrodeposition bench set up in the framework of this thesis is based on the voltammetry. This technique allows observing the evolution of the current resulting from the reduction or oxidation of a sample during the application of a potential difference between the sample and a reference electrode. It is also possible to proceed in reverse manner, by

imposing the current and observing the potential difference relative to the reference electrode: this is the most suitable for electrodeposition configuration.

The presence of an additional electrode is required to allow the flow of electrical current through the electroplating bath. Voltammetry then requires three electrodes: (1) The working electrode, where occurs the studied oxidation or reduction process. In the case of electroplating, it consists of the sample, the surface of which occurs the reduction of the metal cations in the electrolyte solution. (2) The reference electrode whose potential is constant. The potential of the working electrode is measured with respect to this electrode. The electrodeposition bench described in this chapter uses a saturated chloride silver electrode. (3) The auxiliary electrode: it allows the passage of the current in the electrochemical cell. A mesh-shaped electrode of 12cm square was performed platinized titanium. This can cover a large area compared to a full electrode, while improving the quality of agitation. Platinized titanium electrodes finally have the advantage of being less costly.

The choice of the potentiostats for the realization of such electrochemical experiments by voltammetry is the VoltaLab 40 (PGZ-301) Radiometer Analytical. It is controlled by a computer, and allows the production of a large number of electrochemical experiments in potentiometric voltammetry (imposed potential, measured current) or galvanic (current imposed, measured potential). This allows providing alternating currents or current ramps. A block diagram is proposed in Figure 4.12 Figure 4.13 presents an overview of the electrodeposition bench used in this work.

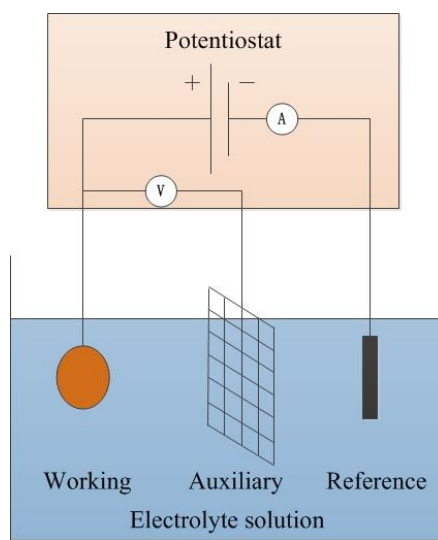


FIG. 4.12. Representation of a voltammetry bench with three electrodes.

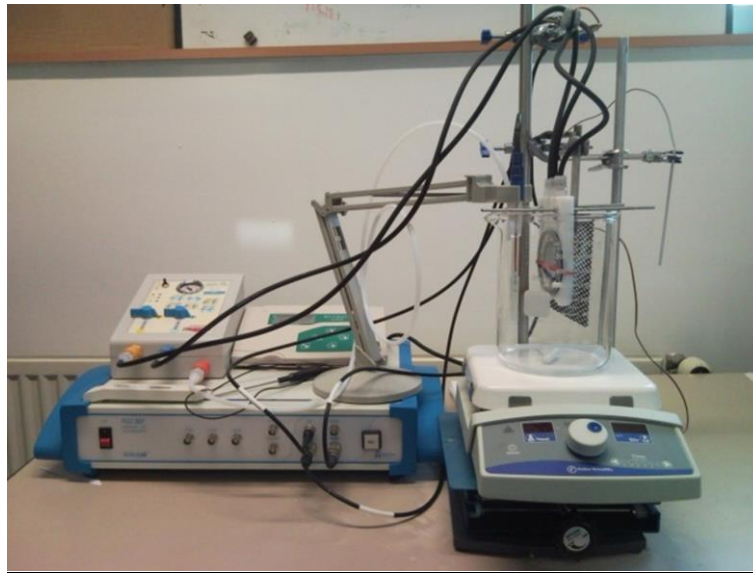


FIG. 4.13. Overview of the electrodeposition bench.

4.3.6.2 Nickel electrolyte solution preparation_[107]

Nickel coatings have long been applied to substrates of steel, brass, zinc and other metals in order to provide a surface that is resistant to corrosion, erosion and abrasive wear. Most of the nickel is used as decorative coatings 5 μm to 40 μm thick, usually under a topcoat of chromium about 0.3 μm thick that gives a no tarnishing finish. The nickel thereby provides a high added-value to the parts being plated.

In practice, a small percentage of the current passing to the cathode causes discharge of hydrogen ions, not nickel deposition, and hydrogen bubbles are formed. Therefore, the efficiency of the deposition of nickel is less than 100%. The practical figure is usually 96% to 98%, the exact value depending upon the plating conditions such as pH, cathodic current and additives used. In order to restrict the change of solution pH arising from discharge of hydrogen at the cathode, a buffer, usually boric acid, is added to the solution. Since boric acid is a weak acid, it exists in the solution as a mixture of borate ions and undissociated, or nonionized, boric acid. When hydrogen ions in the solution are discharged as hydrogen bubbles at the cathode in the presence of the boric acid, some of the boric acid dissociates to provide replacement hydrogen ions plus borate ions. The tendency for solution pH to rise is thereby greatly diminished. Conversely, when acid is added to the plating solution, free borate ions combine with the additional hydrogen ions forming undissociated boric acid; fall in pH is thereby diminished. As a result, the boric acid/borate ion buffer is able to maintain solution pH relatively constant over long working periods in normal operation.

Most nickel electroplating is carried out in solutions based on a mixture of nickel sulphate, nickel chloride and boric acid proposed by C. P. Watts in 1916[108]. The composition of the Watts nickel electroplating solution is shown in Table 4.1

TAB. 4.1. Composition of Watts solution.

Chemical Name	Formula	Metric (g/L)
Nickel sulphate	NiSO ₄ 6H ₂ O	240-300
Nickel chloride	NiCl ₂ 6H ₂ O	40-60
Boric acid	H ₃ BO ₃	25-40

In this solution, nickel sulphate acts as the chief source of nickel ions. Nickel chloride acts as a subsidiary source of nickel ions, increases the electrical conductivity of the solution, and assists in the dissolution of nickel anodes. The boric acid acts as a buffer and also improves the appearance of the nickel deposited.

The Watts solution is relatively cheap and simple. It is also easy to control and to keep free from impurities. Higher deposition rates can be used when the ratio of nickel chloride to nickel sulphate is increased, and the more conductive high-chloride solution formulations are frequently used in barrel plating in order to counteract the high electrical resistance at the perforated sides of immersed barrels and to increase the overall deposition rate in inclined barrels.

The operating conditions for the Watts solution are given in Table 4.2. The solution is operated over a temperature range of 25-60 °C with agitation, usually air agitation. Current density is usually held between 3 A/dm² and 7A/dm², equivalent to a deposition rate of 40 μm to 90 μm per hour, and the pH is held between 3.5 and 5.

TAB. 4.2. Operating conditions for the Watts solution.

Temperature	25-60 °C
Agitation	Usually air
pH	3.5-5
Cathode current density	3-7A/dm ²
Mean deposition rate	40-90 μm/h

The mechanical properties of the nickel electrodeposited from Watts solution are compared with those of wrought nickel in Table 4.3.

TAB. 4.3. Typical mechanical properties of Watts nickel electrodeposits and wrought nickel.

	Hardness HV	Ductility %	Tensile Strength MN/m ²	Tensile Stress MN/m ²
Hot rolled and annealed nickel	90-140	47	460	-
Watts nickel	130-200	25	420	150

Compared with wrought nickel, deposits from a Watts solution are usually harder, have lower ductility, and exhibit fairly high internal tensile stress. However, the values shown in Table 4.3 can be influenced by impurities in the solution. Mechanical properties are also dependent on the solution formulation, pH, temperature and the current density. Solution pH has little effect on deposit properties over the range 1.0 to 5.0. When pH is further raised to 5.5, however, deposit hardness, strength and internal tensile stress all increase while ductility falls.

Soft, ductile deposits with relative low internal stress are given at pH 3.0 temperature 50 °C to 60 °C, over the current density range 3 A/dm² to 7A/dm² in a solution formulated so that 75% of the nickel ions are furnished by nickel sulphate, 25% by nickel chloride. These soft deposits have a coarse-grained structure. Harder deposits produced at high pH have a finer-grain structure.

4.3.6.3 Electroplating photoresist

Electroplating with photoresist masks requires a chemically stable resist with a superior adhesion to the substrate and often also steep sidewalls. Beside a resist optimized for electroplating, also its processing strongly impacts on the demand to avoid underplating as well as a resist attack by the electrolyte. Here several basic requirements for electroplating photoresist are listed.

- Acidic and alkaline stability of the resist. Electroplating solution is the metal salt solution. In order to improve the conductive capacity, some acidic and alkaline solution is added in the electroplating solution. For example, in this work boric acid was added in nickel electroplating solution. Therefore, the acidic and alkaline stability of the resist is required. The cresol resin of some photoresists as AZ and TI photoresists makes the resist mask stable in common acidic electrolytes. And the alkaline stability of the resist film can be improved via a hardbake applied at temperature greater than 140 °C.

- Substrate adhesion of the resist. Resist swelling during electroplating in combination with a suboptimum resist adhesion often causes peeling of the resist with underplating as a consequence. The resist adhesion to the substrate can be improved by a suitable softbake and a hardbake after development.
- Metal adhesion. Metal is regarded as an electrode in the electroplating process. As a consequence, photoresists need to have a good metal adhesion. In the other hand, some resists require special developers for residual-free development. If unsuitable developers are used, or the subsequent rinsing is not sufficiently applied, thin and almost invisible resist residuals may stay on the substrate preventing a proper contact between the substrate and the deposited metal. In this work, the electroplating photoresist need to have a good gold adhesion.

In this work, nickel pillars whose height is smaller than 5 μm deposited on gold surface are required. We choose AZ15nXT diluted with PGMEA (2-methoxy-1-methylethylacetate) with a ratio 10:1 as the electroplating photoresist.

AZ15nXT is a cross-linking negative resist for resist film thicknesses up to approximately 30 μm . The high stability and superior adhesion make the AZ15nXT well suited for most electroplating applications. The resist sidewalls are very steep up to a film thickness of approximately 10 μm , towards higher resist film thicknesses the resist profiles becomes more and more negative allowing the electrodeposition of structures which narrow from bottom to top. AZ15nXT has these following properties.

- 5 ... 20 μm via single-coating (thickness smaller than 5 μm can be reached by dilution)
- Aqueous alkaline developers (such as the TMAH-based AZ 326/726/827 MIF)
- Excellent adhesion, no underplating
- Wide plating compatibility: Cu, Ni, Au ...
- Standard wet stripping processes.

As a simple and economic metallization method, electroplating is not like the sputtering, of which the parameters have already been strictly set up and the whole process is automatic. During the process of electroplating, the operators are required to be well concentrated. Here are several difficulties which should be overcome in the process of electroplating.

- The environment should be as clean as possible. When the sample is electroplated, the solution will be recycled and preserved for another utilization. And the quality of the electroplating solution is very important to the quality of the metallization. So the operators should try their best to keep the impurity away from the electroplating solution.
- The parameters are not strictly controlled. The parameters used in the electroplating, such as the current density, the temperature, the agitation speed, etc., are not fixed. They always vary in an interval. And the deposition rate is estimated by the selection of the parameters. To do a nice electroplating, much experience is required. And the process is always slow to make sure that every step is confirmed.
- The elastic parameters of the material are difficult to measure. In this work, nickel was electroplated to form pillars but it's very difficult to measure the density and Young's modulus of the electroplated nickel.

Here are several SEM pictures showing the failure of the electroplating. Since the deposition rate is an estimated parameter, to have a deposition almost reaching to the surface of the photoresist, the time of deposition is hard to control. Sometimes, the sample is over deposited, shown in Figure 4.14. From the SEM pictures of the pillar-based PnCs, we can find that the pillar's shape is like a mushroom. The cylindrical pillar is under a nickel 'hat'. That is because the time of electroplating is too long, the pillars have already run out of the photoresist which is regarded as the mask. Seen from Figure 4.14 (a) and (b), the tops of the pillars begin to connect up with each other to form a continuous nickel film. Moreover, according to Figure 4.14 (c) and (d), we can find that some pillars have already separated with the substrate. As shown in Figure 4.14 (d), we notice that there is a dark point in the bottom of the pillar. That is the result of some residual photoresist after development. As a result, the liaison force between the nickel pillars and the substrate is proper enough to fix all the pillars in the right positions.

When we do the electrodeposition, the electrical circuit is very import which should be proper during the whole process. A failure will be caused even a small problem for a second. Here is an example of the electrical short circuit and the SEM pictures of the sample are shown in Figure 4.15. During the electroplating process, the working electrode touched the auxiliary electrode unexpectedly for about 30 seconds, causing an electrical short circuit. Seen from Figure 4.15, we notice that the deposition is not homogeneous. The pillar's form is irregular.

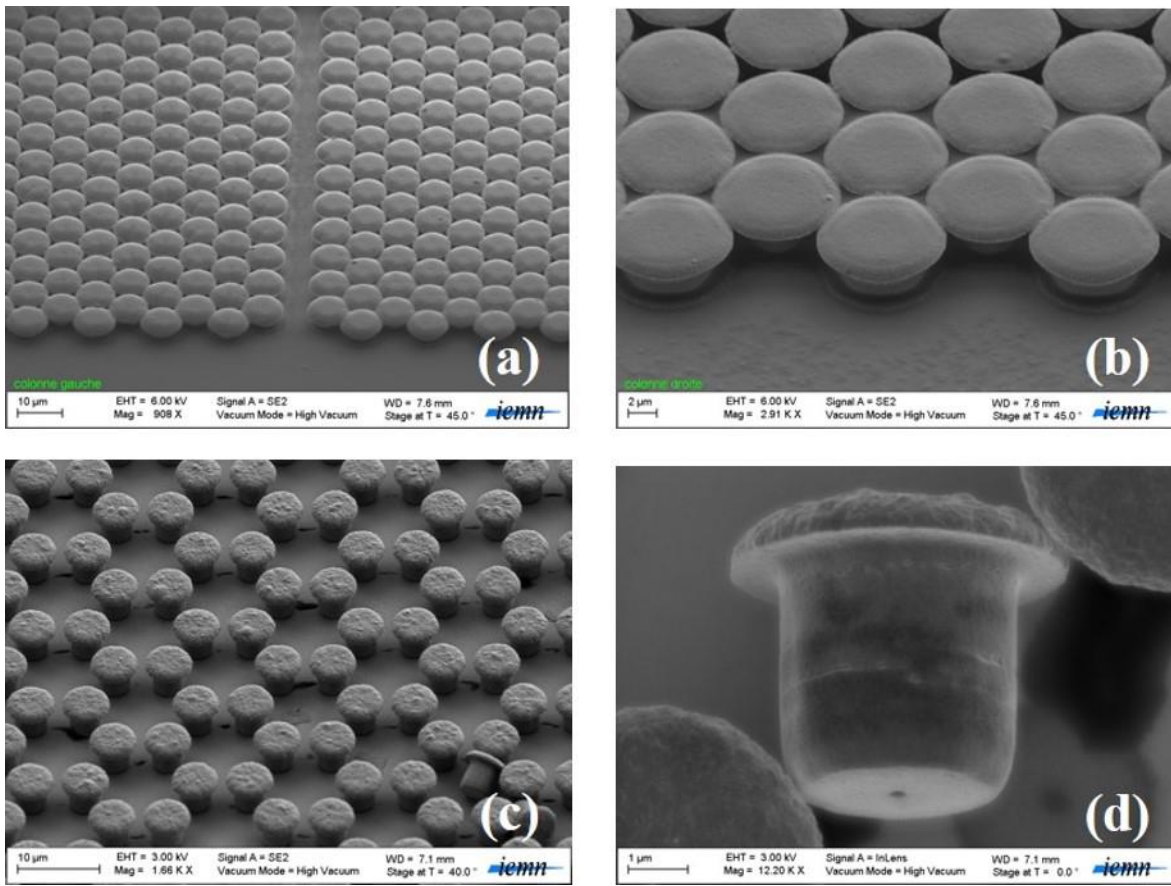


FIG. 4.14. SEM pictures of the pillar-based PnCs over deposited by electroplating.

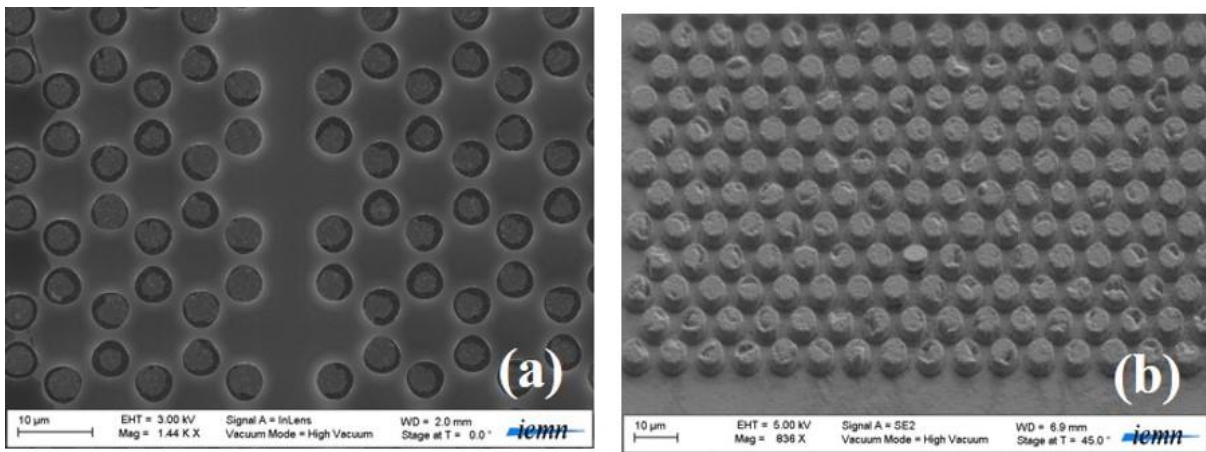


FIG. 4.15. SEM pictures of the PnCs with a 30 second electrical short circuit during the electroplating.

4.3.7 Procedure

In summary, the IDTs were fabricated by the following procedure:

Substrate cleaning

1. Ultrasonic cleaning with deionized (DI) water for 3 minutes and rinsing with DI water.
2. Ultrasonic cleaning with acetone for 3 minutes and rinsing with acetone.
3. Rinsing with isopropyl alcohol (IPA).
4. Dry with Nitrogen (N_2).
5. Place on hot plate for 5 minutes at 180 °C.

Fabrication of IDTs

6. Deposition of a layer of Aluminum with a thickness of 200nm by sputtering for two times of 150 seconds
7. Deposition of the photoresist S1818 in the closing mode with the speed 3000rpm for 12 seconds.
8. Soft bake at the temperature 110 °C for 1 minute.
9. Exposure using the mode hard contact for 3.8 seconds with a UV lamp of 365nm whose intensity is 10mW/cm².
10. Development in MF-319 developer for 1 minute.
11. Rinsing with DI water.
12. Dry with N_2 .
13. Wet etching in a mixture solution of HNO_3 , H_3PO_4 and H_2O at room temperature by a volume ratio 1:4:1.
14. Rinsing with DI water.
15. Dry with N_2 .
16. Rinsing with acetone.
17. Rinsing with IPA.
18. Dry with N_2 .

Fabrication of PnCs

19. Deposition of a layer of SiO_2 with a thickness of 200nm at the temperature of 80 °C.
20. Deposition of a layer of Ti/Au with a thickness of 10/40nm by sputtering for 20/50 seconds.
21. Deposition of the photoresist AZ15nXT (diluted 10:1) in the closing mode with the speed 2000rpm for 30 seconds.
22. Soft bake at the temperature 110 °C for 3 minutes.
23. A break time for 10 minutes.

24. Exposure using the mode vacuum for 17 seconds with a UV lamp of 365nm whose intensity is $10\text{mW}/\text{cm}^2$.
25. A break time for 10 minutes.
26. Post exposure bake at the temperature $120\text{ }^\circ\text{C}$ for 1 minute.
27. Development in AZ 326MIF developer for 3 minutes.
28. Rinsing with DI water.
29. Dry with N_2 .
30. Opening a little part of the photoresist to exposure the gold layer.
31. Sticking Aluminum paper to the gold layer and fixing it with Polydimethylsiloxane (PDMS).
32. Electroplating in the Nickel solution with the current intensity $20\text{mA}/\text{cm}^2$ for 10 minutes (for $4\mu\text{m}$).
33. Removing the photoresist AZ15nXT by plasma O_2 with the power 500W for 5 minutes.
34. Removing Ti/Au layer by plasma CF_4/O_2 with the power 200W for 7 minutes.
35. Removing SiO_2 layer by plasma CHF_3/CF_4 with the power 180W for 10 minutes.

4.4 Characterization

4.4.1 PnCs morphology

After the fabrication, the most direct way to check whether the device is well fabricated or not is to take a picture of the target device using a scanning electronic microscope (SEM). A SEM is a type of electron microscope that produces images of a sample by scanning it with a focused beam of electrons. SEM pictures of the micro-fabricated IDTs are shown in Figure 4.16, including dispersive IDTs (Figure 4.16 (a) and (b)) and slanted IDTs (Figure 4.16 (c) and (d)). SEM pictures of the pillar-based PnCs with a height of $4\mu\text{m}$ are shown in Figure 4.17.

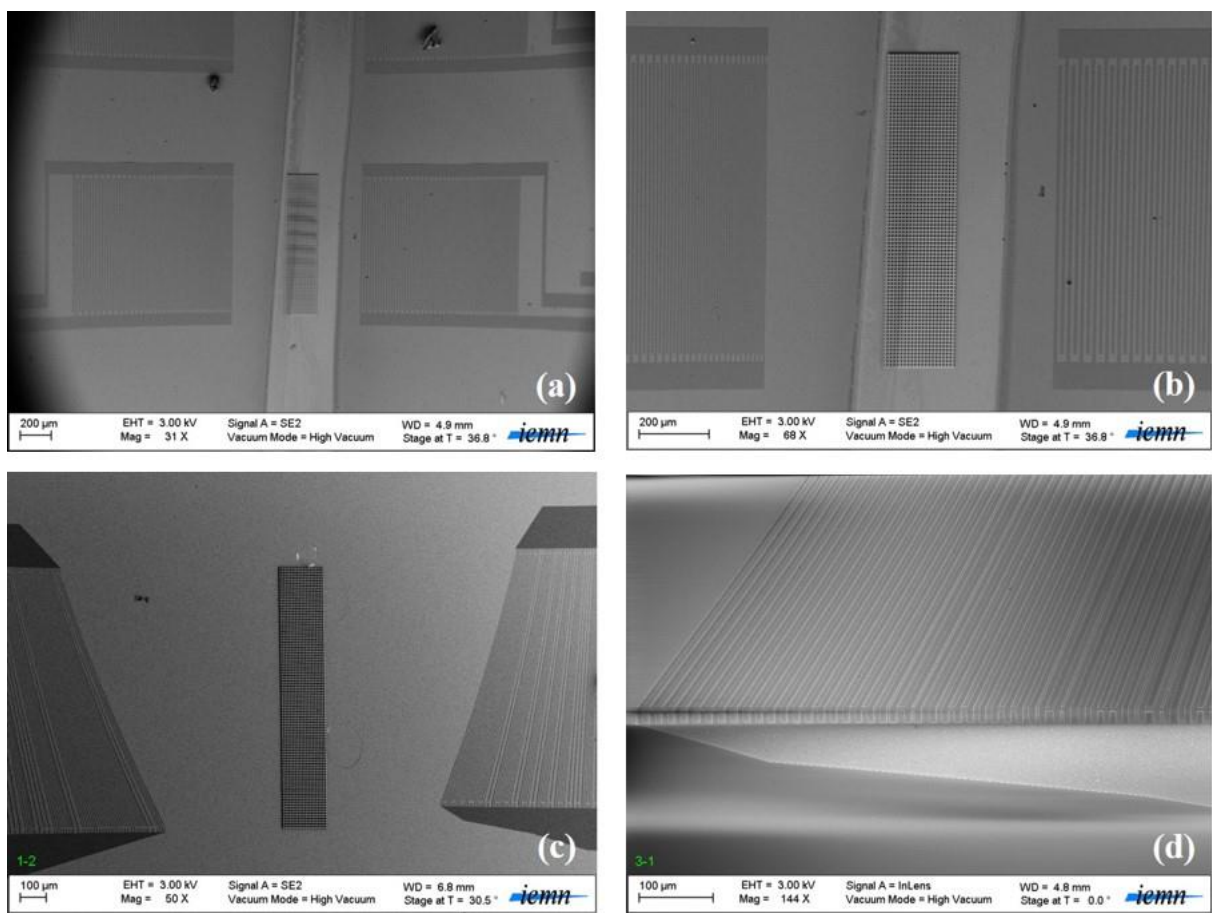


FIG. 4.16. Micro-fabricated dispersive IDTs (a) (b) and slanted IDTs (c) (d).

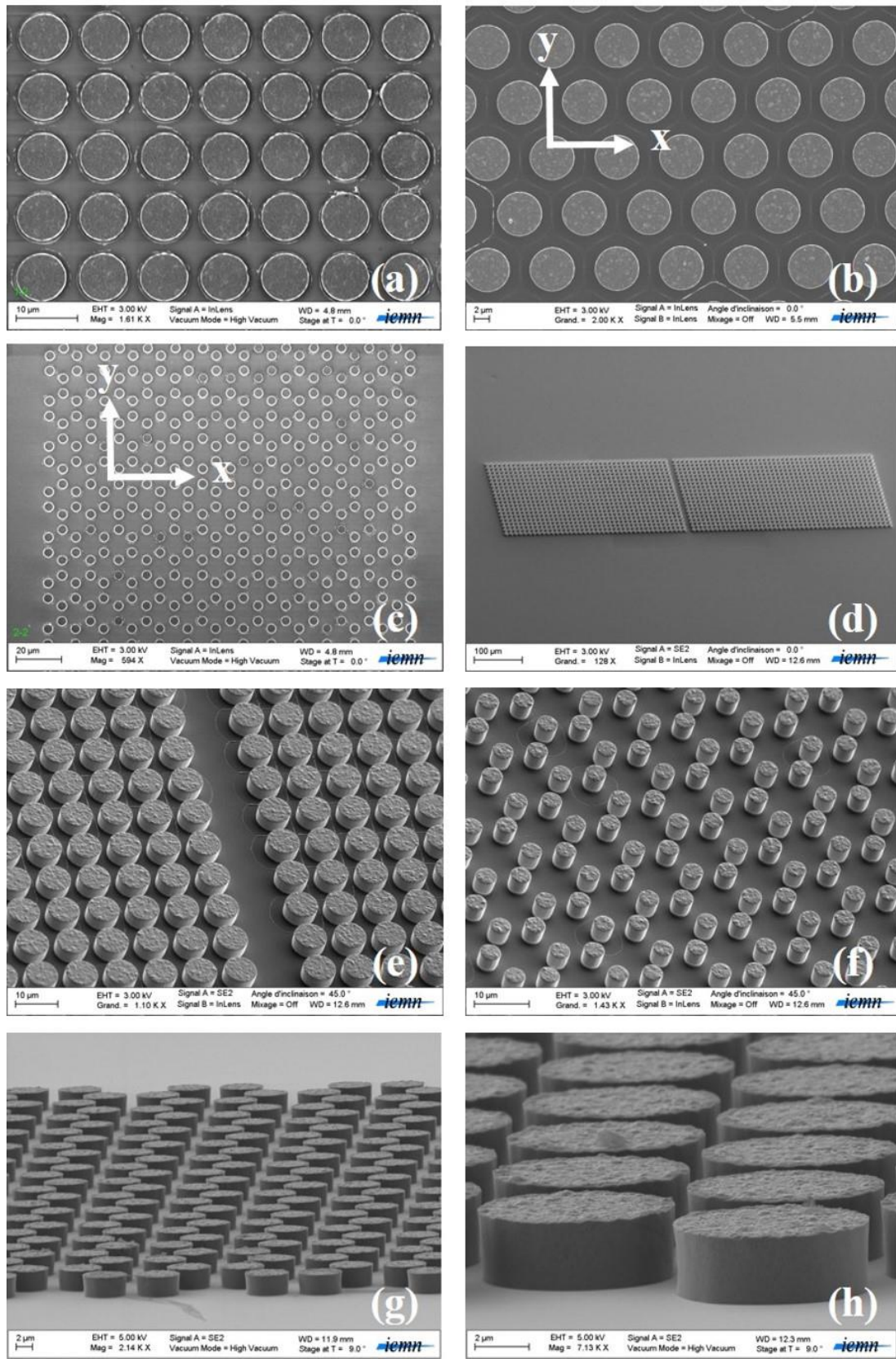


FIG. 4.17. PnCs based on Ni pillars with a height of 4 μm. Front sections of PnCs with different lattice symmetries, including square lattice (a), triangular lattice (b) and hexagonal lattice (c); lateral sections of PnCs (d)(e)(f)(g)(h).

4.4.2 Transmission spectrum measured by a vector network analyzer

Once the samples have been characterized by a SEM and they are proper enough, the next step will be the measurement of the transmission spectrum of the PnCs by a vector network analyzer (VNA). A VNA is an instrument that measures the network parameters of electrical networks. Here it refers to the S-parameters because we are more interested in the transmission spectrum of the PnCs. The VNA used in this work is an Agilent Network Analyzer 8753ES, shown in Figure 4.18. The characterization set up is composed of a VNA, a microscope and two micro electrodes. The two micro electrodes which are used to emit and receive electrical signals are connected respectively with the input and output IDTs. The results of the measured S-parameters are shown in the display window of the VNA. The VNA used in this work is a 2-port VNA. S_{11} is the input port voltage reflection coefficient. S_{12} is the reverse voltage gain. S_{21} is the forward voltage gain. S_{22} is the output port voltage reflection coefficient.

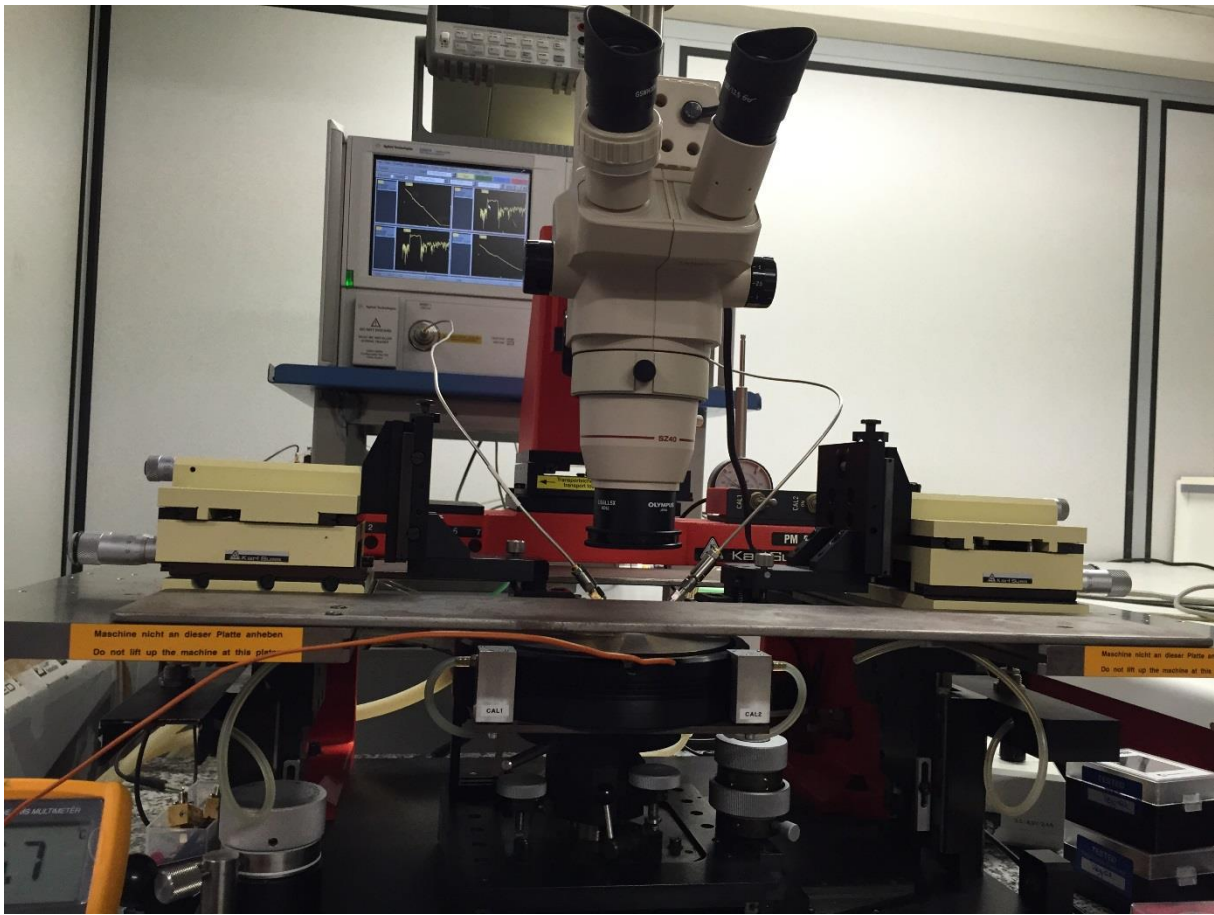


FIG. 4.18. The vector network analyzer in the characterization center of IEMN.

4.4.2.1 Experimental response of inter-digital transducers

As we have mentioned above, in this work, two kinds of inter-digital transducers, referred as dispersive IDTs and slanted IDTs were designed and fabricated for both low frequency and high frequency. The substrate used for dispersive IDTs was Y128-X LiNbO₃ and the one for slanted IDTs was Y-Z LiNbO₃. Their responses were measured by the network analyzer. The results were shown in Figure 4.19. Figure 4.19(a) and Figure 4.19(b) illustrate the response of dispersive IDTs for low frequency and high frequency. Figure 4.19(c) and (d) illustrate the response of slanted IDTs for low and high frequency. From these figures, large passbands are observed.

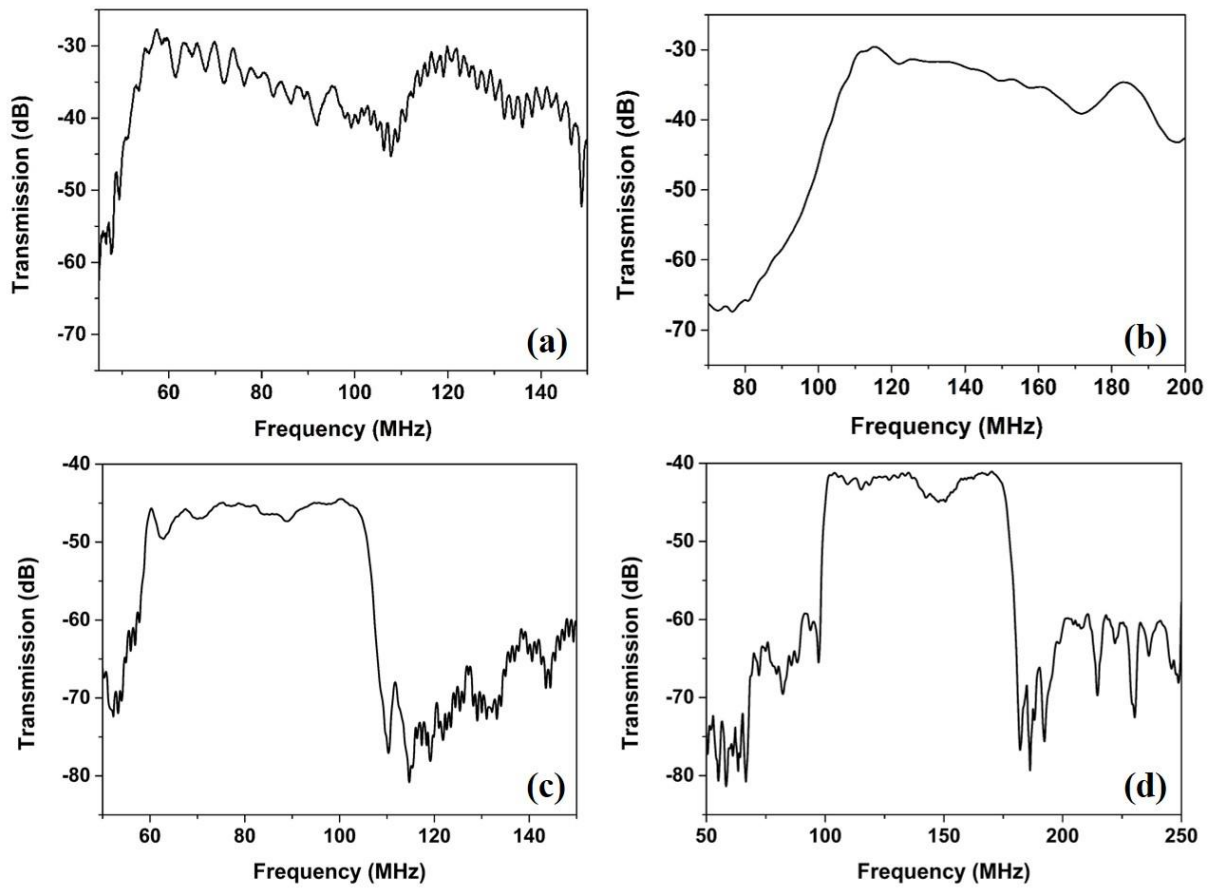


FIG. 4.19. Experimental response of dispersive IDTs (a and b) on a Y128-X LiNbO₃ substrate and slanted IDTs (c and d) a Y-Z LiNbO₃ substrate for low frequency (left) and high frequency (right) measured by a network analyzer.

4.4.2.2 Experimental results of 4 μm high pillar-based PnCs

The results of low frequency relative transmission spectrum (ΔS_{21}) of PnCs composed of square, triangular-X, triangular-Y, hexagonal-X and hexagonal-Y arrays of nickel pillars with

dispersive IDTs deposited on a Y128-X LiNbO₃ substrate are shown in Figure 4.20. The relative transmission spectrum (ΔS_{21}) is the difference between the transmission spectrum with a PnC (S_{21}) and without a PnC (S_{21ref}). We call the latter case a reference. The calculation of ΔS_{21} is shown in Equation 4.2.

$$\Delta S_{21} = S_{21} - S_{21ref} \quad (4.71)$$

The SEM pictures on the left bottom describe the samples which were characterized corresponding to the relative transmission spectrum. The white axis x and axis y in the triangular case represent respectively the propagation directions for triangular-X and triangular-Y lattices, and similarly for the case of hexagonal relative transmission spectrum.

First, two picks can be observed in the low frequency relative transmission spectrum of the PnC with square lattice (Figure 4.20a). The first pick appears around 81MHz with an insertion loss about 30dB and the second pick appears around 89MHz with an insertion loss about 35dB. These two picks correspond to the first two modes due to the local resonance. Quite similar results have been observed in the relative transmission spectrum of the PnC with triangular-Y lattice (blue curve in Figure 4.20b). As we have seen in the part of effect of anisotropy, because of the similarity of the square lattice and the triangular-Y lattice, the relative transmission spectrum of these two structures are very similar, resulting in two picks appearing at the quasi same frequencies. However, when the triangular-Y lattice is rotated 90 degrees, turning to a triangular-X lattice, the relative transmission spectrum becomes different (black curve in Figure 4.20b). Two more narrow picks appear respectively around 85MHz and 88MHz with an insertion loss of about 35dB. These results well demonstrate experimentally that the lattice symmetries have an effect in the locally resonant band gaps. Similar evidence can be found in the comparison of the relative transmission spectrum for the PnCs with hexagonal-X and hexagonal-Y lattices. For hexagonal-X lattice, only one pick can be found around 88MHz with an insertion loss about 40dB. For the case of hexagonal-Y lattice, two picks are found around 84MHz and 88MHz with insertion losses about 35dB and 38dB.

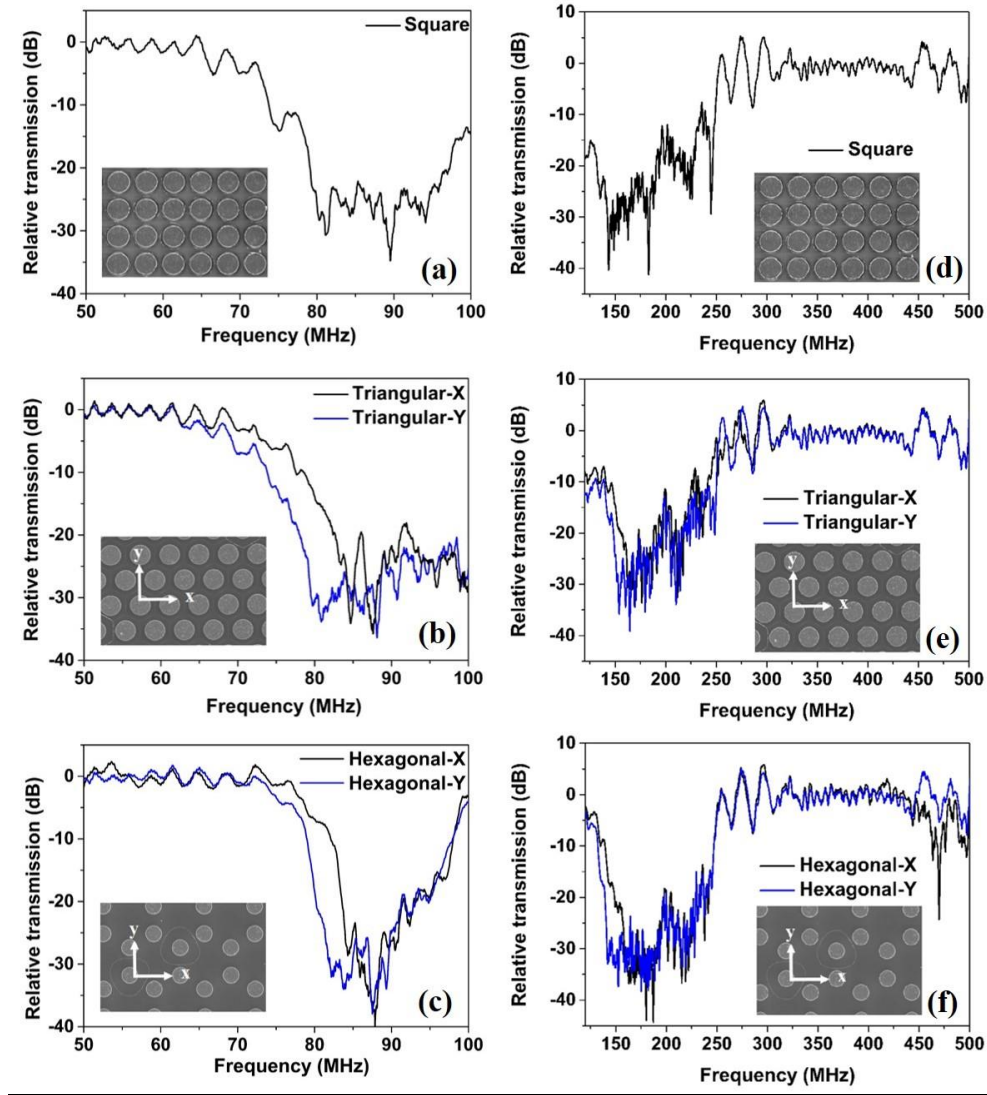


FIG. 4.20. Low frequency (left) and high frequency relative (right) transmission spectrum of PnCs with square (a and d), triangular (b and e), hexagonal (c and f) arrays of nickel pillars.

The results of high frequency relative transmission spectrum (ΔS_{21}) of PnCs composed of square, triangular-X, triangular-Y, hexagonal-X and hexagonal-Y arrays of nickel pillars with dispersive IDTs deposited on a Y128-X LiNbO₃ substrate are shown in Figure 4.20 (right part). Different from the low frequency relative transmission spectrum within which locally resonant modes can be clearly observed, in the case for high frequency, locally resonant modes are mixed up with Bragg scattering band gap and noise, resulting in a wide band gap from 150MHz to 250MHz. In addition, some surface waves are no longer localized on the surface and turn to be bulk waves which propagate in the substrate. We call this phenomenon the radiation. Moreover, a pick of about 25dB is observed at about 470MHz only for the PnC with hexagonal-X lattice, different from the other lattice symmetries.

For the design of masks, a linear defect was added for PnCs with square, triangular-X and hexagonal-Y lattices to work as a filter. To realize the propagating mode exactly in the band gap, much calculation is required. Since the waveguide is not the main subject of this work, we just added a linear defect in the crystal without the calculation to see if something special happens. The relative transmission spectrum measured by both low frequency IDTs and high frequency IDTs is shown in Figure 4.21. Comparing the relative transmission spectrum for PnCs with and without a linear defect, we can't find the result of a waveguide. That means the propagating mode due to the linear defect does not happen to be in the band gap.

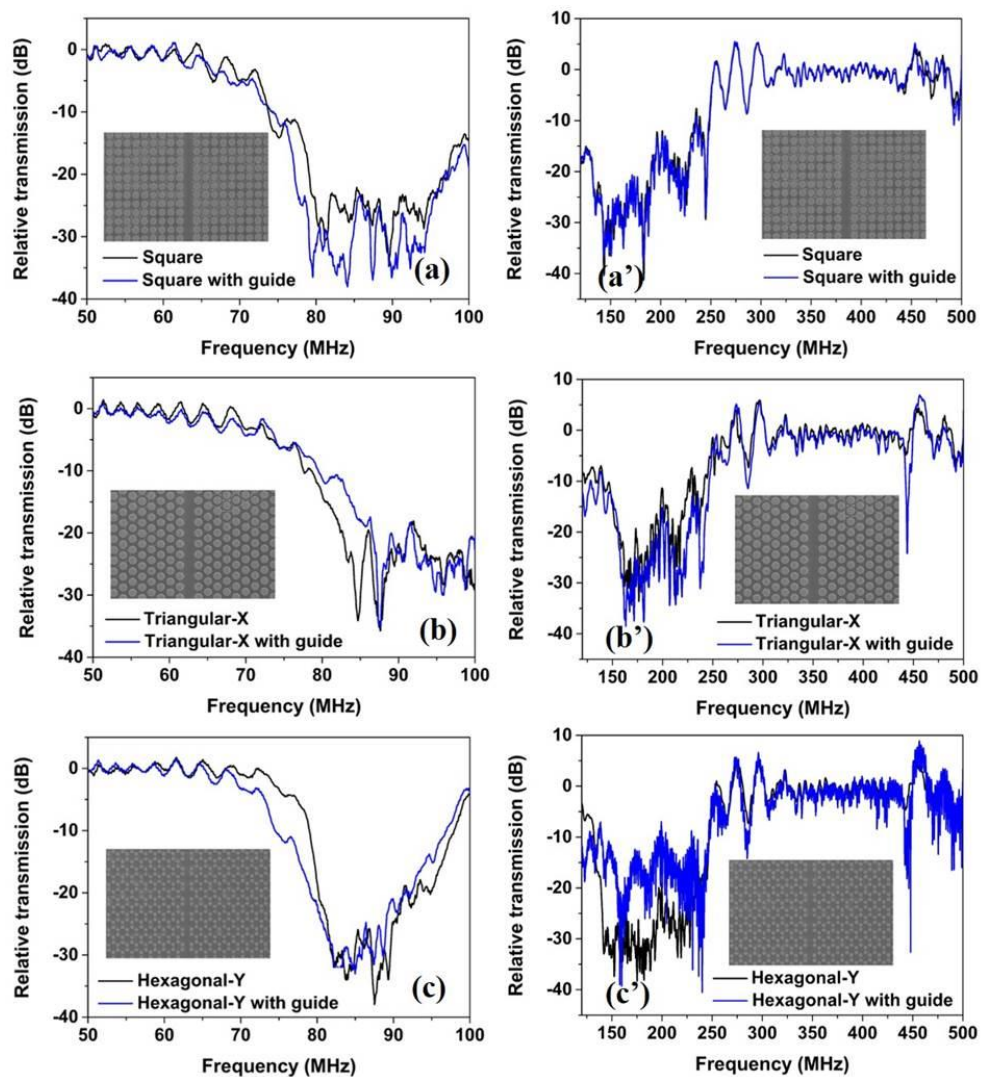


FIG. 4.21. Relative transmission spectrum of PnCs with a linear defect for square (a and a'), triangular-X (b and b') and hexagonal-Y (c and c') lattices measured low frequency IDTs (left) and high frequency IDTs (right).

Besides the dispersive IDTs, slanted IDTs have also been designed. Different from the case for dispersive IDTs, the slanted IDTs were deposited on a Y-Z LiNbO₃ substrate which can generate pure sagittal Rayleigh waves. The transmission spectrum with and without PnCs composed of square and hexagonal-X arrays of pillars is depicted in Figure 4.22. Comparing the transmission spectrum with and without PnCs, evident band gaps can be observed for both the two structures.

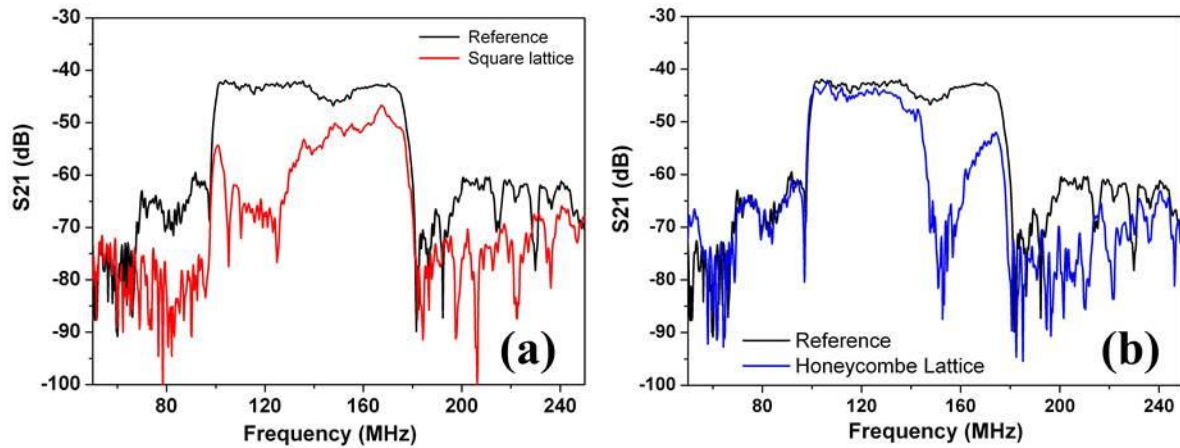


FIG. 4.22. The transmission spectrum with and without PnCs composed of square (a) and hexagonal-X (b) arrays of pillars.

4.4.2.3 Experimental results of 2.3 μm and 3.4 μm high pillar-based PnCs

Besides the PnCs composed of 4 μm high pillars, PnCs composed of nickel pillars with two heights 2.3 μm and 3.4 μm were also fabricated in this work. The electrodes were dispersive IDTs and the substrate was Y128-X LiNbO₃. The difference between the two fabrication processes is the selection of exposure modes for the photo lithography of resist AZ15nXT. For the former case, vacuum mode was chosen. For the latter case, the sample was exposed in a hard contact mode. As a result, the fabrication of PnCs composed of hexagonal-X and hexagonal-Y arrays of pillars whose size is the smallest was not succeeded. Consequently, the experimental results of PnCs with square, triangular-X and triangular-Y lattices will be presented here.

The theoretical and experimental study for square lattices has been presented in Sergey Yankin's work in 2014 [76]. In this work, not only the transmission spectrum, but also the cumulative phases were calculated and measured. As we know, the energy is stored inside the pillars at the resonant frequency. The transmission spectrum is static so that we can't know more about the dispersion relation $\omega = ck$ (ω is the angular frequency, k is the

wave number and c is the sound velocity) inside the inhomogeneous medium. Nevertheless we can be well-informed by the study of the phase delay. Indeed, we have the relation $k = \Delta\phi/L$, where $\Delta\phi$ is the cumulative phase delay and L is the distance between the input and output IDTs. The calculation of cumulative phase delay is a very convenient way to evaluate the difference of the phase and group velocities between the inhomogeneous medium and the free surface.

Figure 4.23 illustrates the treated experimental and theoretical results of the relative transmission ΔS_{21} and the phase delay $\Delta\phi_{21}$. As it is seen from the relative transmission spectra of the $2.3\mu\text{m}$ pillar-based PnC, for the theoretical curve, the local gap begins at 133MHz and leads to about 40dB of loss. The Bragg gap appears after 175MHz and the loss is about 50dB. From the phase delay graph (Figure 4.23(b)), large growth of the phase delay is clearly visible near 133MHz which corresponds to the start of the first forbidden zone. Furthermore, inside the band gaps the phase difference stops to rise and remains almost constant. For the second case $h=3.4\mu\text{m}$, first band gap is observed at frequencies ranging between 108MHz and 140MHz, and the Bragg band gap starts around 161MHz. Clearly, for a given set of parameters, the two stop bands are well separated, at least a separation of 20MHz. The behavior of the phase difference becomes more complex than for the first case. It increases in the frequency range between the two observed gaps. For the comparison of the theoretical and experimental results, we observe that the measured first band gap, corresponding to the local resonant mode in pillars, agrees quite well with the frequency range band gap obtained by the calculation. However, the second band gap is shifted by about 10MHz-15MHz. A possible explanation of this shift is the difference between the elastic properties of the pillar material used in the calculation and the actual values of the density and elastic constants of deposited nickel.

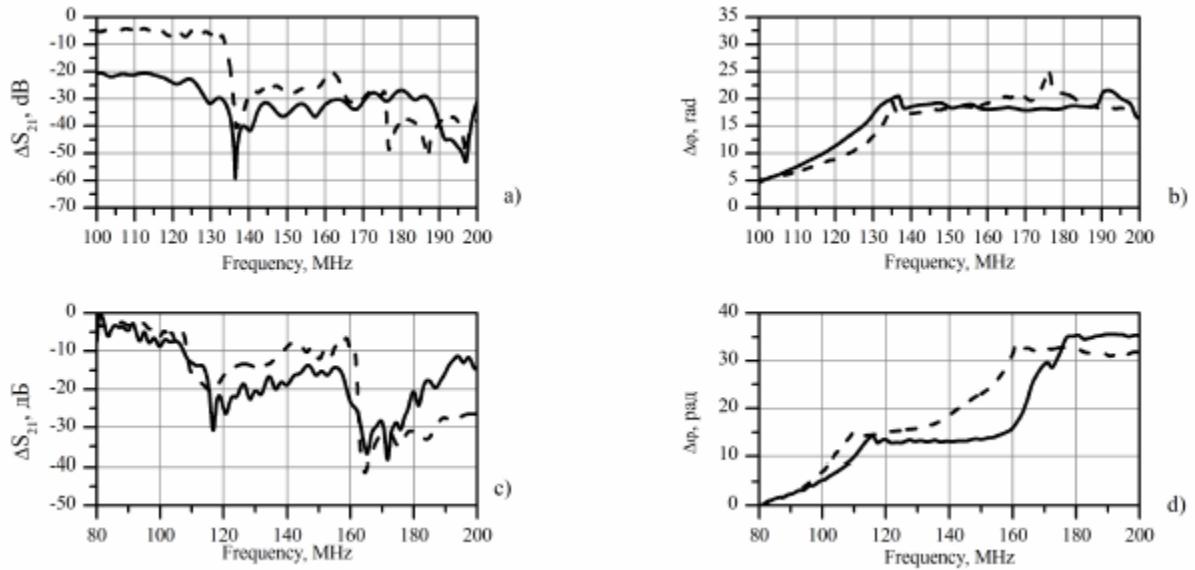


FIG. 4.23. Frequency dependence of relative transmission ΔS_{21} (a and c) and the phase delay $\Delta\phi_{21}$ (b and d) measured experimentally (solid line) and obtained by FEM calculation (dashed line) for pillar height $h=2.3\ \mu\text{m}$ (a and b) $h=3.4\ \mu\text{m}$ (c and d) [76].

The sample of PnCs composed of triangular-X and triangular-Y arrays of nickel pillars is a little different from the PnCs with square lattice. First, the pillar's form is not exactly cylindrical. It is more like a truncated cone which has a larger top diameter. That is because with the reduction of the diameters, hard contact exposure is not powerful enough to act properly at the bottom of the holes, even though a longer development process was followed. Secondly, the rate of electroplating deposition is different for the square lattice and the two triangular lattices. For example, when the height of pillars in square lattice reached to about $2.3\ \mu\text{m}$, the one in triangular lattices has already reached to $2.5\ \mu\text{m}$ and also begin to spill over the photo resist to form a nickel film.

The experimental relative transmission spectrum for triangular-X and triangular-Y lattices and the SEM picture of the sample are depicted in Figure 4.24. The theoretical relative transmission spectrum and the band structures for triangular-X and triangular-Y lattices are depicted in Figure 4.25. To best simulate the experimental sample, we used a truncated cone instead of the cylindrical pillar in the calculation. The top and bottom radius are respectively $3.5\ \mu\text{m}$ and $3\ \mu\text{m}$. The height is $2.5\ \mu\text{m}$. From Figure 4.25, four resonant modes are observed in the relative transmission spectra for triangular-X lattice. The eigenfrequencies are respectively 131MHz, 133MHz, 181MHz and 200MHz. For the case of triangular-Y lattice, only three resonant modes can be observed in the transmission spectra because the second mode shown in the band structure is not a sagittal mode. The eigenfrequencies are respectively 126MHz,

181MHz and 197MHz. And the Bragg band gaps begin to appear at about 200MHz for both the two lattices. Comparing the experimental results shown in Figure 4.24, we can well observe all the resonant modes predicted in the calculation but the resonant frequencies for some modes have little shifts of several megahertz. Furthermore, the Bragg band gaps don't appear before 220MHz. We have reasons to believe that the variation of the theoretical and experimental results is because of the spilling out of the electroplated nickel layer. Some pillars have already connected at the top.

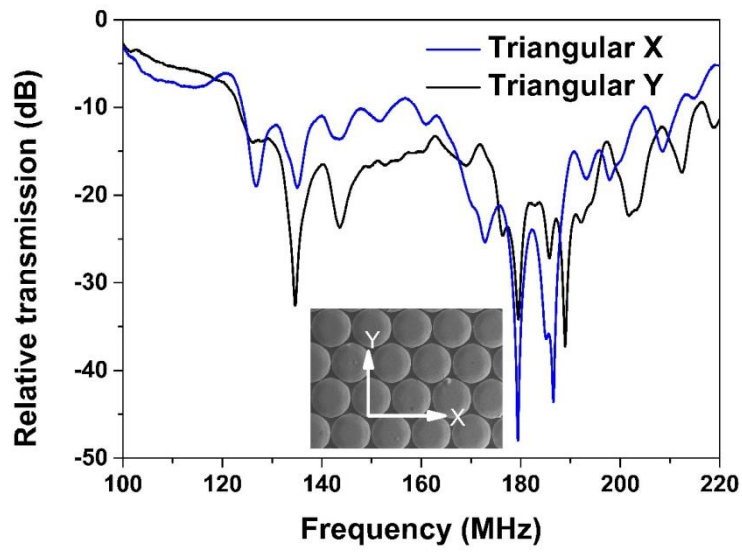


FIG. 4.24. The experimental relative transmission spectrum for triangular-X and triangular-Y lattices and the SEM picture of the sample.

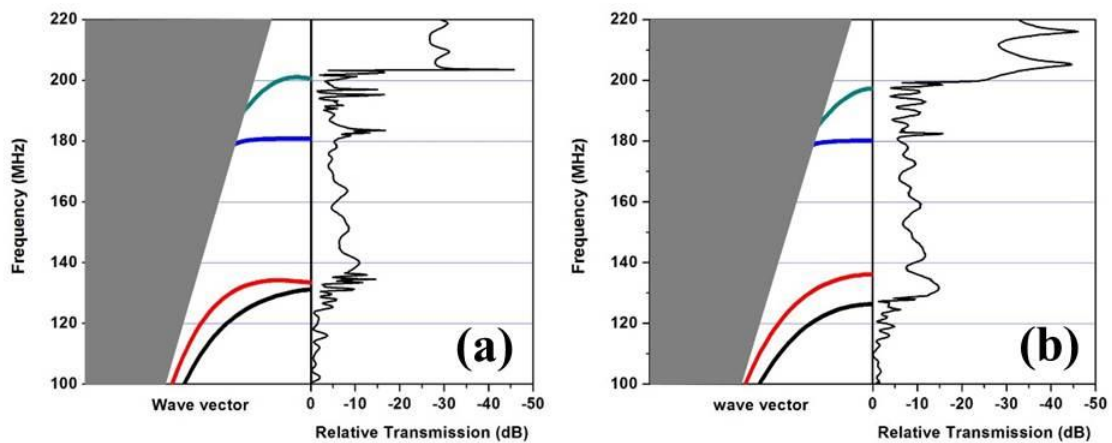


FIG. 4.25. Theoretical relative transmission spectrum and the band structures for triangular-X and triangular-Y lattices. The top and bottom radius of the pillars are respectively $3.5\ \mu\text{m}$ and $3\ \mu\text{m}$. The height is $2.5\ \mu\text{m}$.

4.5 Conclusion

In this chapter, we first talked about the selection of materials. In this work we chose LiNbO_3 Y128-X cut and LiNbO_3 Y-Z cut to generate the quasi sagittal and pure sagittal Rayleigh waves and the reason to select nickel as the pillar's material is that nickel has good magnetic property which may lead to some magnetic applications.

Following with the selection of materials, we have talked about the device design idea for the inter-digital transducers and the phononic crystals with different lattice symmetries.

Then a micro-fabricating process of two dimensional pillar-based phononic crystals was presented. Some micro-fabricating techniques used in this work were introduced including photolithography, metallic deposition, PECVD, etching, as well as electroplating.

At last, PnCs morphology was observed by a scanning electronic microscope and the transmission spectrum were measured by a network analyzer. According to the characterization, the devices were well fabricated and some results well coincided with the simulation prediction.

Chapter 5: Ongoing work

Besides the investigation of two dimensional phononic crystals based on nickel pillars and LiNbO_3 substrate, the study of some other micro and nano periodic structures were also involved in this work. For example, the two dimensional phononic crystals based on high silicon pillars realized by microsystem fabricating techniques such like lithography, sputtering, etching, etc. Secondly, with the collaboration of the material laboratory in Ecole Centrale de Pekin, we have explored the self-assembly of magnetic nanoparticles synthesized by hydrothermal method. Furthermore, the fabrication of nickel nanowires realized by electroplating through an anodic aluminum oxide template is also a part of this work. However, because of the limitation of time, during my Ph-D thesis, these works have not been yet investigated further enough but they give me an inspiration of my following work.

5.1 Fabrication of 2D Si pillar-based phononic crystals

Inspired by the study of 2D nickel pillar-based PnCs, we desired to fabricate the pillar-based PnCs for lower frequency ranges which needs the pillars to have a greater height. The original plan was to fabricate the PnCs composed of nickel pillars with a height of $50\mu\text{m}$ realized by electroplating through an etched silicon template. Nevertheless, we didn't succeed because the doped silicon used as the template was not an insulator. Nickel is always electroplated on the silicon template, as shown in Figure 5.1. Therefore, we changed our mind and decided to fabricate the silicon pillars instead of silicon holes. Consequently, the idea is to fabricate the PnCs based on silicon pillars.

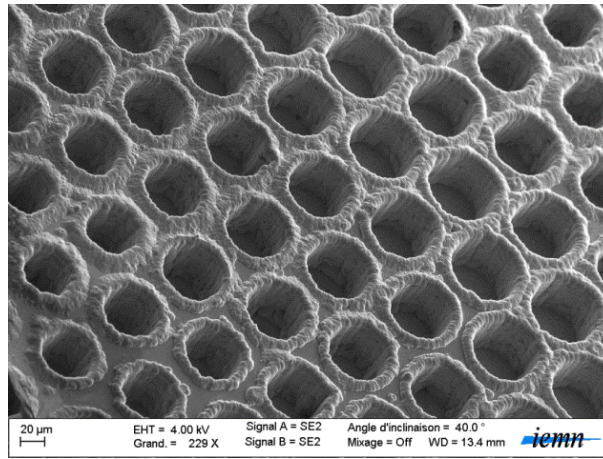


FIG. 5.1. Nickel electroplating through a 50µm thickness silicon plate.

The whole fabrication process is illustrated in Figure 5.2. Similar with the fabrication process of nickel pillar-based PnCs, for this work, the first step was also the fabrication of inter-digital transducers started with the deposition of an aluminum layer of 200nm, followed by a photo lithography process and aluminum wet etching. In parallel, a silicon plate with a thickness of 50µm should be well cleaned and rinsed before the sputtering of a thin aluminum layer. Then the PnC was patterned on the aluminum layer which was deposited on the silicon plate. The patterning was different from the one for nickel pillar-based PnCs. In this case, the positive photo resist S1818 and a positive mask were used to form the pillars instead of holes. Then the aluminum wet etching was followed by the patterning. The next step was the deposition of a layer of SU8 on the surface of the LiNbO₃ substrate. After a soft bake and exposure, the patterned silicon plate was put slightly on the surface of the substrate during the post exposure bake to paste the silicon plate on the substrate. Then a process of silicon anisotropic etching was realized by surface technology systems (STS). The aluminum on the silicon plate worked as the etching mask. The parts without aluminum were etched. To finish the whole fabrication process, the last step was the etching of SU8 to expose the IDTs.

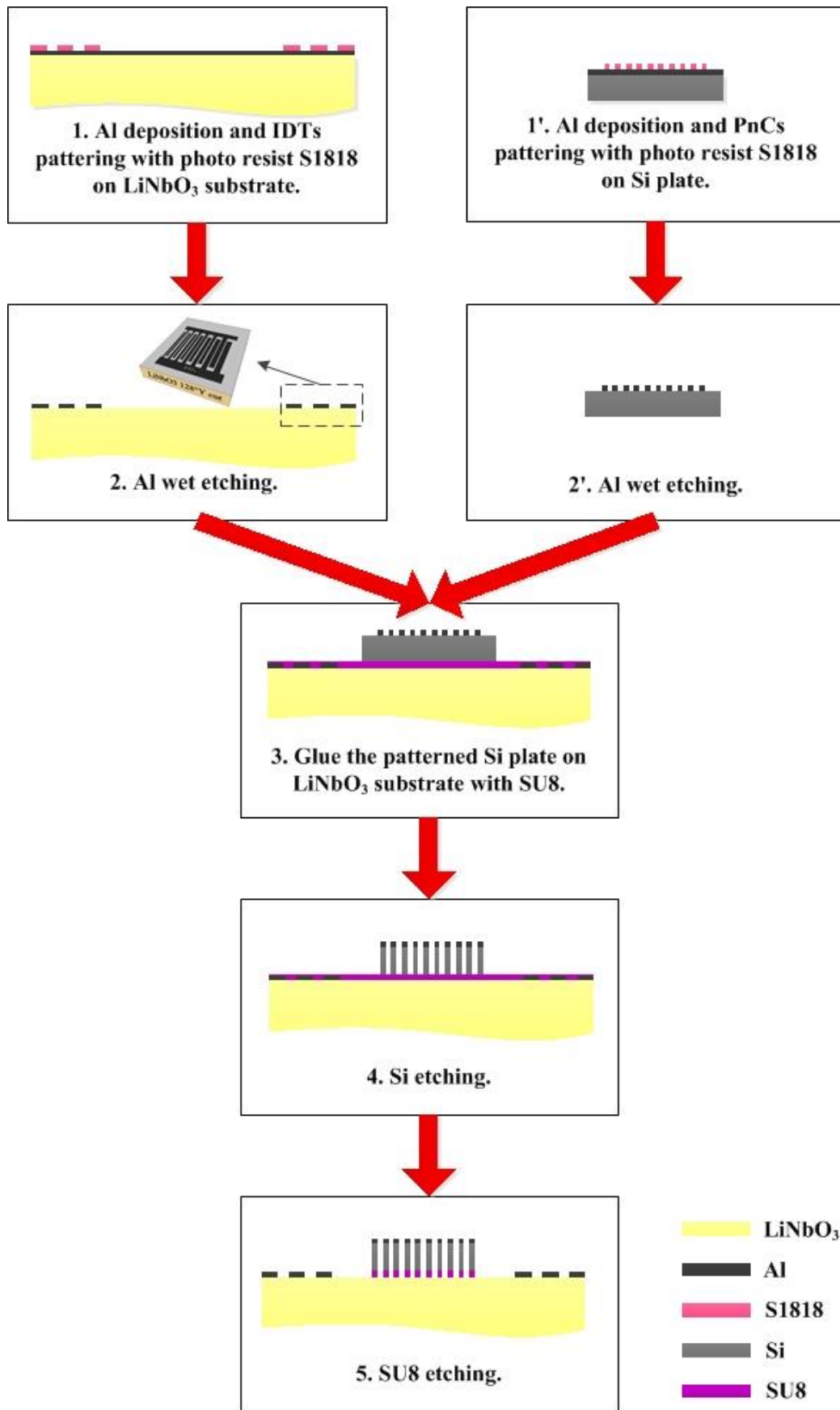


FIG. 5.2. Fabrication process of the silicon pillar-based phononic crystals.

The SEM pictures of silicon pillar-based PnCs with square lattice is depicted in Figure 5.3. The pillar is cylindrical. The diameter is $8\mu\text{m}$ and the height is $50\mu\text{m}$. The relative transmission spectra and the cumulative phase difference measured by the network analyzer are shown in Figure 5.4. Two resonant modes are clearly observed at about 15MHz and 17MHz .

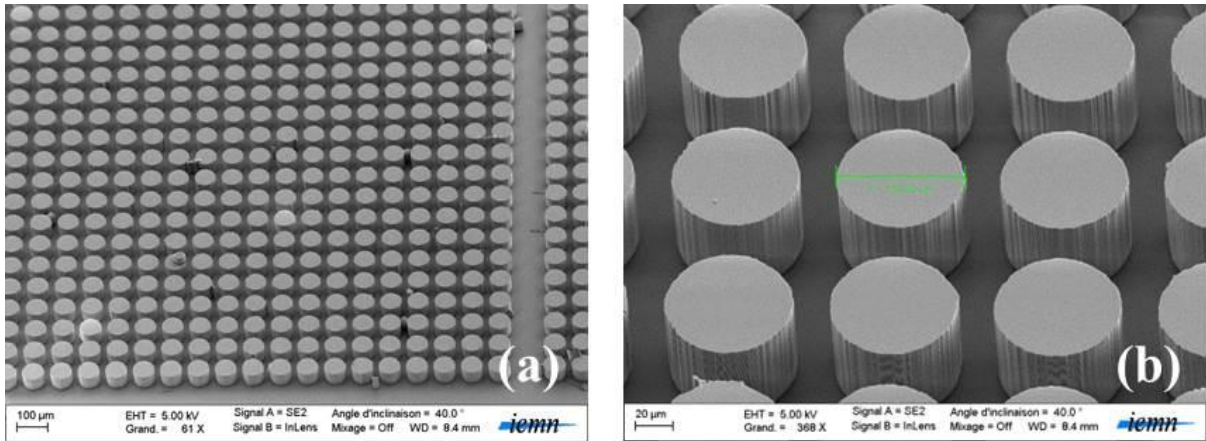


FIG. 5.3. SEM picture of silicon pillar-based PnCs.

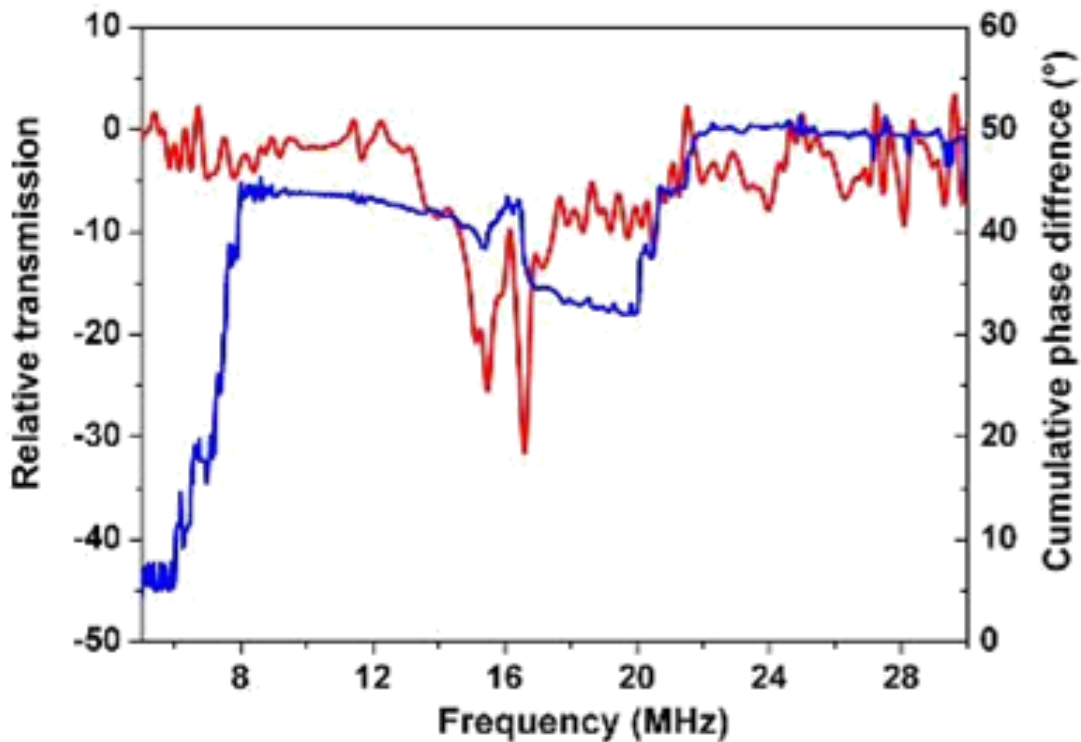


FIG. 5.4. The relative transmission spectra and the cumulative phase difference of the silicon pillar-based PnC with square lattice.

For further work, some theoretical calculation will be required. More characterization methods will be used such as the interferometry.

5.2 Self-assembly of magnetic nanoparticles

It is interesting to create the periodic structures by the self-assembled nanoparticles instead of nickel pillar-based PnCs fabricated by micro-fabricating techniques. Because the nanoparticles can be synthesized by a simple, accessible and pollution-free chemical reduction method, which is less expensive and easier to achieve in nanoscale than the method that we have presented above to fabricate the PnCs. Furthermore, the magnetic nanoparticles can be induced in a magnetic field, which gives us the possibility to control the structure by controlling the magnetic field. Therefore, it is very meaningful to assemble the magnetic nanoparticles to form a periodic structure.

The magnetic nanoparticles used in this work were the iron nanoparticles synthesized by the material laboratory of Ecole Centrale de Pekin in Beihang University. The nanoparticles were prepared by the chemical reduction method [109, 110]. NaBH_4 was used as the reducing agent for $\text{FeCl}_2 \cdot 4\text{H}_2\text{O}$. The concentration of the solution of NaBH_4 and $\text{FeCl}_2 \cdot 4\text{H}_2\text{O}$ was changed and NaOH of different quantities was added. NaBH_4 ($0.02 \text{ mol} \cdot \text{L}^{-1} \cdot \text{N}$) (N represents the multiple of reagents used) and NaOH ($\text{Xg} \cdot \text{L}^{-1}$) were added into deionized water at room temperature to form a homogeneous solution, which was then transferred into the FeCl_2 solution ($0.005 \text{ mol} \cdot \text{L}^{-1} \cdot \text{N}$). The mixed solution was then stirred using a magnetic stirrer for 10 min. after stirring, the precipitate was washed three times with deionized water, then three times with absolute ethyl alcohol. The precipitate was then dried in a vacuum drying oven at 140°C for 15 min.

We found that by controlling the concentration of reagents, the arrangement of Fe nanoparticles can be controlled to form the Fe nanochains, which give us the inspiration to form 1D PnCs. The SEM pictures of the Fe nanoparticles with different concentration of reagents are depicted in Figure 5.5. From these pictures we can find that the nanochains are already self-assembled and they are controllable. Magnetic hysteresis loops of the Fe nanoparticles and nanochains for different concentration of reagents measured by the vibrating sample magnetometer (VSM) to characterize the magnetic properties shown in Figure 5.6.

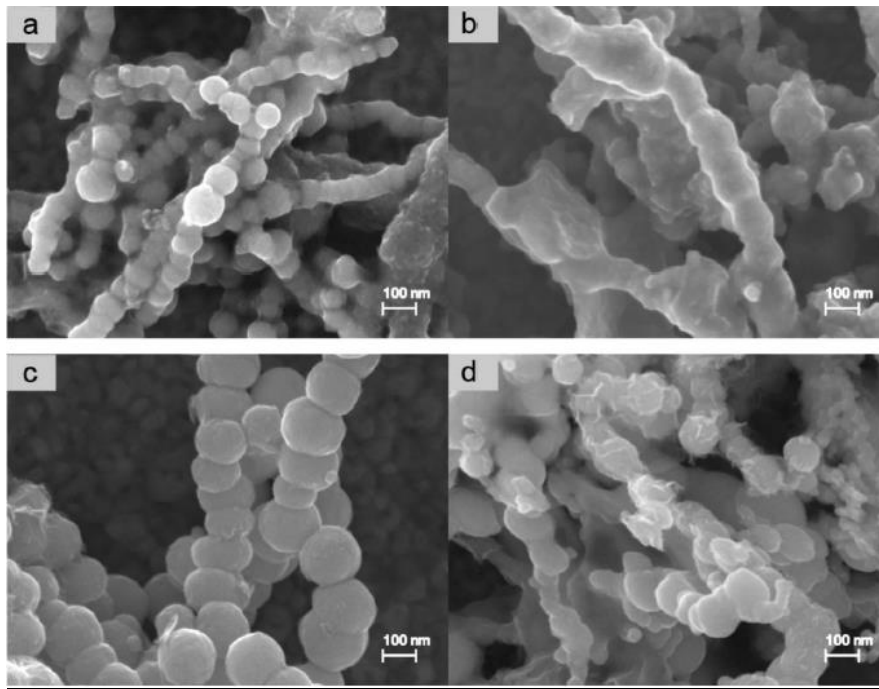


FIG. 5.5. SEM pictures of the Fe nanoparticles and nanochains: (a) N=1, X=0; (b) N=10, X=0; (c) N=5, X=0.05; (d) N=10, X=0.1 [109].

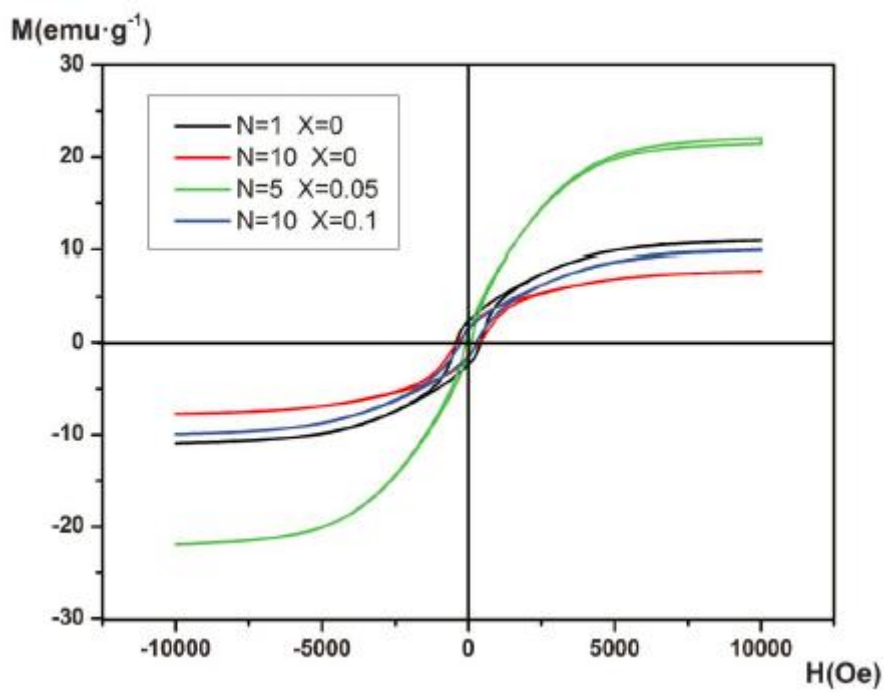


FIG. 5.6. Magnetic hysteresis loops of the Fe nanoparticles and nanochains for different concentration of reagents measured by VSM.

By using this kind of Fe nanochains, we have explored the possibility to form the 1D periodic structure in a magnetic field. However we have not succeeded to well separate the nanochains. That is the problem that should be solved in the future study.

5.3 Fabrication of nickel nanowires by electroplating

For the exploration of nano periodic structures, we have also explored the possibility to fabricate the nanowires by electroplating through an anodic aluminum oxide (AAO) template.

The fabrication process started with the deposition of a thin gold film on the silicon wafer before pasting a Whatman anodisc inorganic filter membrane by a physical method on the substrate as a mask. The Whatman anodisc inorganic filter membrane is shown in Figure-5.7. The diameter of the whole membrane was 25mm. The average diameter of the hole was about 200nm. And the thickness of the membrane was about 60 μ m. Then nickel electroplating was applied through the AAO template. The last step was to put the sample into NaOH aqueous solution to remove the AAO template. SEM pictures of the AAO template before electroplating (a), nickel nanowires before NaOH bath (b) and nickel nanowires after NaOH bath (c) (d) are depicted in Figure 5.8.

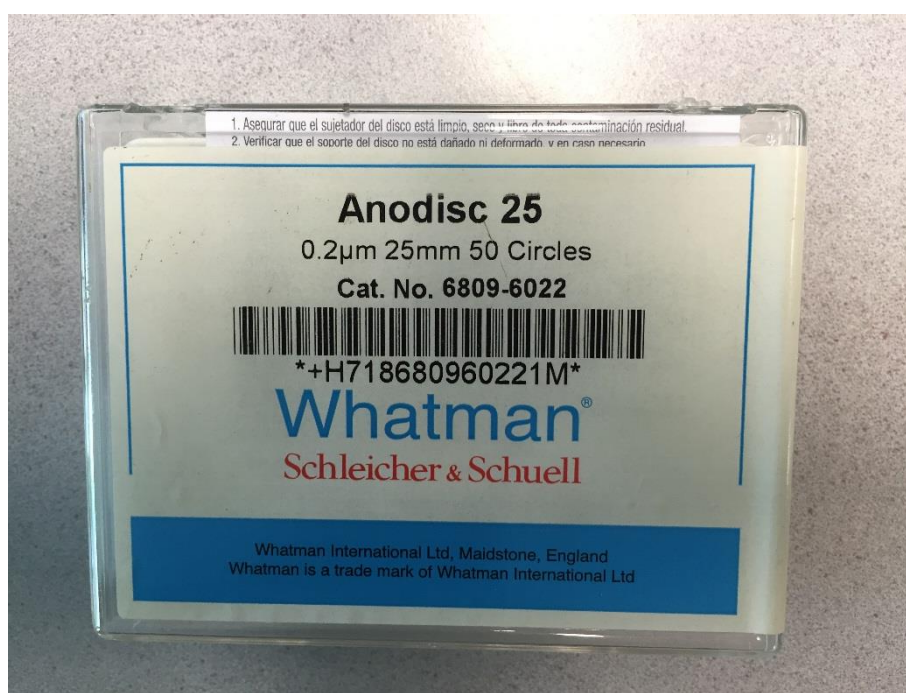


FIG. 5.7. The Whatman anodisc inorganic filter membrane used in this work.

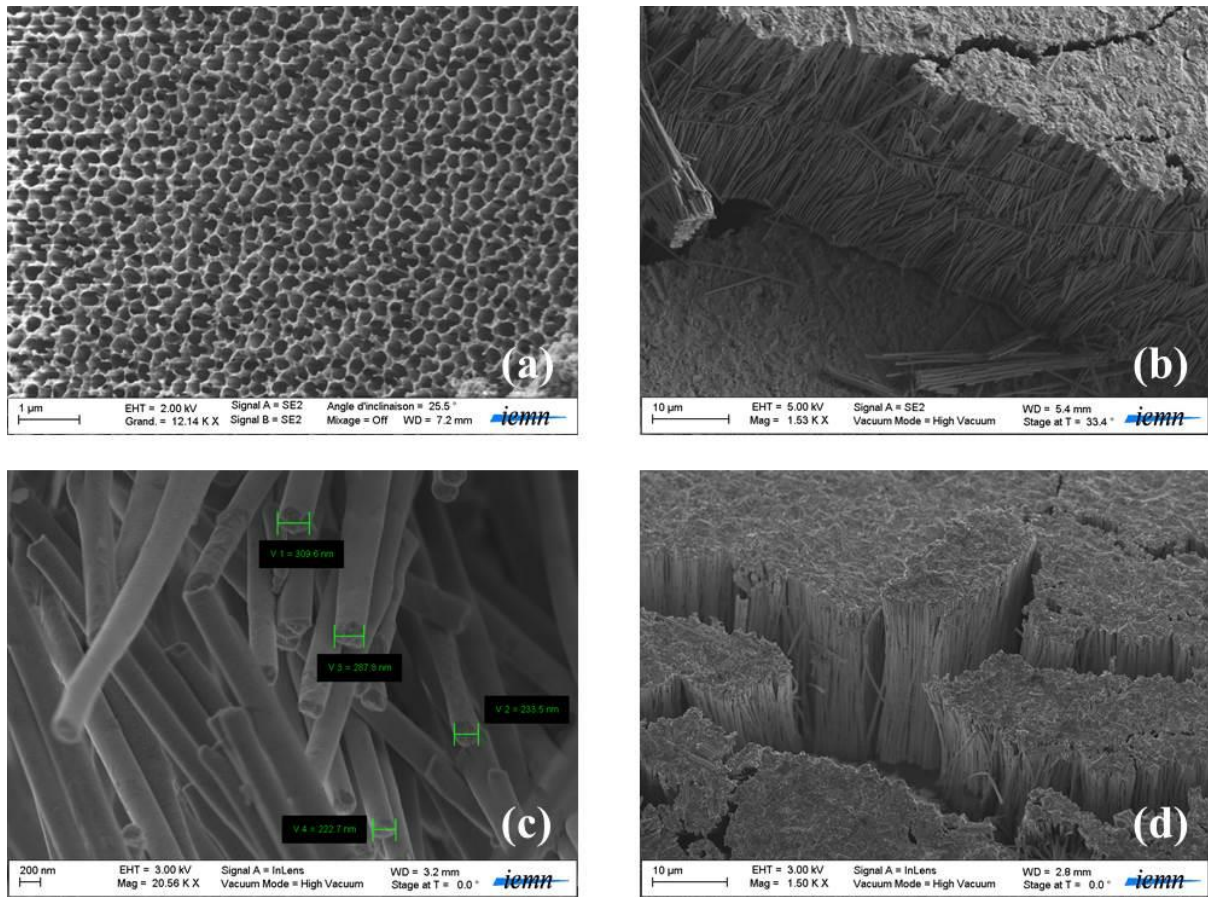


FIG. 5.8. SEM pictures of the AAO template before electroplating (a), nickel nanowires before NaOH bath (b) and nickel nanowires after NaOH bath.

We have tested the magnetic property of a electroplated nickel film and the nickel nanowire by VSM. The magnetic hysteresis loops for both the film and the nanowires are depicted in Figure 5.9. We observed that the nickel film keeps good magnetic property but the nickel nanowires don't show a clear magnetism.

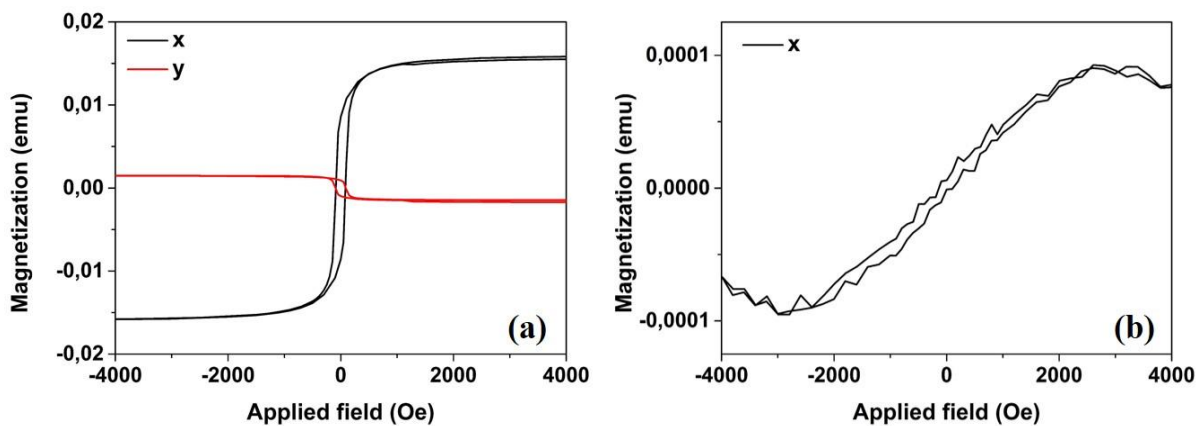


FIG. 5.9. Magnetic hysteresis loops for both the nickel film (a) and the nickel nanowires (b) fabricated by electroplating.

For further research, there are several problems to solve. First, different from the electrodeposition applied in the fabrication of nickel pillar-based PnCs, to realize the electroplating through the holes with a diameter 200nm and a height 50 μ m is much more difficult. A pulsed current should be used. Consequently, the parameters of electroplating should be confirmed after many tests. Secondly, as the nanowires have a large length-diameter ratio, they are very easy to be broken off during the NaOH bath. Therefore we need to find a better way to remove the AAO mask. Thirdly, it is very difficult to separate one nanowire which has a diameter of 200nm. In addition, the size of the nanowire is limited by the bought AAO template. In order to fabricate the nanowires which has our expected size and periodic structures, we need to fabricate the AAO template by ourselves, which bring us a new challenge.

5.4 Conclusion

In this chapter, we have talked about other achievements of periodic micro and nano structures which have been explored but not finished yet during the Ph-D period, including two-dimensional silicon pillar-based phononic crystals, self-assembly of magnetic nanoparticles and electroplated nickel nanowires.

These micro and nano periodic structures have been explored in fabrication. Basically, the fabrication was achieved but there is still the room for improvement, such as the separation of nanochains or nanowires, the removal of the AAO template, etc. All these works give us the inspiration of the future research.

Conclusion and Perspectives

Conclusion

In this thesis, the investigation of micro and nano structured materials for acoustic band gaps engineering in electro-acoustic devices was presented, especially for the study of two-dimensional nickel pillar-based phononic crystals. Some characteristics about the elastic wave propagation in the periodic structures due to local resonances was introduced. From the point of view of the pillar's polarization, some problems were proposed and analyzed theoretically. In addition, a complete fabrication process based on micro-fabricating techniques was presented in details. Therefore this work can be regarded as the optimization of the study of pillar-based PnC.

The state of art of the phononic crystals was presented in the first chapter, as well as the existing technologies and the applications to create a basis of conception of the PnCs.

The theoretical background introduced in Chapter 2 is the fundamental knowledge accumulation for this work. In this part, we systematically talked about the elasticity, the surface acoustic waves considering piezoelectric materials, the lattice and band theories, as well as the mechanisms of PnCs.

In Chapter 3, the theoretical modeling of band structures and transmission spectrum was calculated by the finite element method. The effects of geometrical parameters and elastic parameters on the locally resonant PnCs band gaps were proposed and analyzed. Different from the previous work, the analysis was from the point of view of the pillar's polarization, which represented the intrinsic properties. The coupling of propagating modes within different lattice symmetries was observed and well explained. As a potential application, the temperature coefficient of frequency was firstly studied for PnCs.

The design and micro-fabrication process of the inter-digital transducers and the two-dimensional nickel pillar-based PnCs were introduced in Chapter 4. Some micro-fabricating techniques used in this work were presented, especially for the nickel electroplating. The morphology and transmission spectrum were characterized respectively by a scanning

electron microscope and a network analyzer. The results further proved our theoretical arguments.

Besides the 2D nickel pillar-based PnCs, some other periodic micro and nano structures were also involved in this work, such as 2D silicon pillar-based PnCs, self-assembly of magnetic nanoparticles and electroplated nickel nanowires, which were presented in Chapter 5.

Perspectives

This work induced much ongoing and unfinished research. As perspectives, the first work should be done is the theoretical analysis about the coupling of the propagating modes. Until now, we have only observed the phenomena and gave a visualized explanation. A theoretical model is required to be built to deeply explain this problem.

Secondly, since the concept of PnCs first proposed more than two decades ago, much work has been achieved for the investigation of the mechanism and the properties of PnCs. However few achievements were realized for the applications. In this work, we have proposed an idea about thermal PnC sensors which can be regarded as a potential application of PnCs. But the study was not perfect. There is still the room for improvement.

Besides these, in Chapter 5, we have presented much ongoing works which need to be finished and further investigated. Although this is the end of my Ph-D thesis, this is also a new start of the research for periodic materials and structures.

Reference

- [1] M.M.Sigalas and E.N.Economou, "Elastic and acoustic wave band structure," *Journal of Sound and Vibration*, vol. 158, pp. 377-382, 1992.
- [2] M. Kushwaha, P. Halevi, L. Dobrzynski, and B. Djafari-Rouhani, "Acoustic band structure of periodic elastic composites," *Physical Review Letters*, vol. 71, pp. 2022-2025, 1993.
- [3] E. Yablonovitch, "Inhibited Spontaneous Emission in Solid-State Physics and Electronics," *Physical Review Letters*, vol. 58, pp. 2059-2062, 1987.
- [4] Z. Liu, "Locally Resonant Sonic Materials," *Science*, vol. 289, pp. 1734-1736, 2000.
- [5] Brillouin L.. Wave Propagation in Periodic Structures, 2nd edition. New York: Dover Publications, 1953
- [6] W.N.Newell, "Face-Mounted Piezoelectric Resonators," *Proceedings of the Institute of Electrical and Electronics Engineers*, vol. 53, p. 575, 1965.
- [7] E.Yablonovitch, "Inhibited Spontaneous Emission in Solid-State Physics and Electronics," *Physical Review Letters*, vol. 58, pp. 2059-2062, 1987.
- [8] J. Sajeev, "Strong localization of photons in certain disordered dielectric superlattices," *Physical Review Letters*, vol. 58, pp. 2486-2489, 1987.
- [9] M. S. Kushwaha and P. Halevi, "Band-gap engineering in periodic elastic composites," *Applied Physics Letters*, vol. 64, p. 1085, 1994.
- [10] R. Martinez-Sala, J. Sancho, J. V. Sanchez, V. Gomez, J. Llinares, and F. Meseguer, "Sound attenuation by sculpture," *Nature*, vol. 378, p. 241, 1995.
- [11] J. O. Vasseur, P. A. Deymier, G. Frantziskonis, G. Hong, B. Djafari-Rouhani, and L. Dobrzynski, "Experimental evidence for the existence of absolute acoustic band gaps in two-dimensional periodic composite media," *Journal of Physics: Condensed Matter*, vol. 10, p. 6051, 1998.
- [12] J. V. Sanchez-Perez, D. Caballero, R. Martinez-Sala, C. Rubio, J. Sanchez-Dehesa, F. Meseguer, *et al.*, "Sound Attenuation by a Two-Dimensional Array of Rigid Cylinders," *Physical Review Letters*, vol. 80, p. 5325, 1998.
- [13] R. Sprik and G. H. Wegdam, "ACOUSTIC BAND GAPS IN COMPOSITES OF SOLIDS AND VISCOUS LIQUIDS," *Solid State Communications*, vol. 106, pp. 77-81, 1998.
- [14] T.-T. Wu, L.-C. Wu, and Z.-G. Huang, "Frequency band-gap measurement of two-dimensional air/silicon phononic crystals using layered slanted finger interdigital transducers," *Journal of Applied Physics*, vol. 97, p. 094916, 2005.
- [15] B. Bonello, C. Charles, and F. Ganot, "Velocity of a SAW propagating in a 2D phononic crystal," *Ultrasonics*, vol. 44 Suppl 1, pp. e1259-63, Dec 22 2006.

Reference

- [16] X. Zhang, T. Jackson, E. Lafond, P. Deymier, and J. Vasseur, "Evidence of surface acoustic wave band gaps in the phononic crystals created on thin plates," *Applied Physics Letters*, vol. 88, p. 041911, 2006.
- [17] I. El-Kady, R. H. Olsson, and J. G. Fleming, "Phononic band-gap crystals for radio frequency communications," *Applied Physics Letters*, vol. 92, p. 233504, 2008.
- [18] S. Mohammadi, A. A. Eftekhar, A. Khelif, W. D. Hunt, and A. Adibi, "Evidence of large high frequency complete phononic band gaps in silicon phononic crystal plates," *Applied Physics Letters*, vol. 92, p. 221905, 2008.
- [19] M. Oudich, Y. Li, B. M. Assouar, and Z. Hou, "A sonic band gap based on the locally resonant phononic plates with stubs," *New Journal of Physics*, vol. 12, p. 083049, 2010.
- [20] M. Plihal and A. A. Maradudin, "Photonic band structure of two-dimensional systems: The triangular lattice," *Physical Review B*, vol. 44, pp. 8565-8571, 1991.
- [21] Z.-Y. Li and K.-M. Ho, "Light propagation in semi-infinite photonic crystals and related waveguide structures," *Physical Review B*, vol. 68, 2003.
- [22] L. M. Li and Z. Q. Zhang, "Multiple-scattering approach to finite-sized photonic band-gap materials," vol. 58, pp. 9587-9590, 1998.
- [23] Z. Hou and B. M. Assouar, "Modeling of Lamb wave propagation in plate with two-dimensional phononic crystal layer coated on uniform substrate using plane-wave-expansion method," *Physics Letters A*, vol. 372, pp. 2091-2097, 2008.
- [24] J. B. Pendry and A. MacKinnon, "Calculation of photon dispersion relations," *Physical Review Letters*, vol. 69, pp. 2772-2775, 1992.
- [25] K. Schmidt and P. Kauf, "Computation of the band structure of two-dimensional Photonic Crystals with hp Finite Elements," *Comp. Meth. App. Mech. Engr.*, vol. 198, p. 1249, 2009.
- [26] Z. Liu, C. T. Chan, P. Sheng, A. L. Goertzen, and J. H. Page, "Elastic wave scattering by periodic structures of spherical objects: Theory and experiment," *PHYSICAL REVIEW B*, vol. 62, p. 2446, 2000.
- [27] M. M. Sigalas and N. García, "Theoretical study of three dimensional elastic band gaps with the finite-difference time-domain method," *Journal of Applied Physics*, vol. 87, p. 3122, 2000.
- [28] Y. Tanaka, Y. Tomoyasu, and S. Tamura, "Band structure of acoustic waves in phononic lattices: Two-dimensional composites with large acoustic mismatch," *PHYSICAL REVIEW B*, vol. 62, p. 7387, 2000.
- [29] A. Khelif, B. Aoubiza, S. Mohammadi, A. Adibi, and V. Laude, "Complete band gaps in two-dimensional phononic crystal slabs," *Physical Review E*, vol. 74, 2006.
- [30] T.-C. Wu, T.-T. Wu, and J.-C. Hsu, "Waveguiding and frequency selection of Lamb waves in a plate with a periodic stubbed surface," *Physical Review B*, vol. 79, 2009.
- [31] Y. Cao, Z. Hou, and Y. Liu, "Convergence problem of plane-wave expansion method for phononic crystals," *Physics Letters A*, vol. 327, pp. 247-253, 2004.

Reference

- [32] T.-T. Wu, Z.-G. Huang, and S. Lin, "Surface and bulk acoustic waves in two-dimensional phononic crystal consisting of materials with general anisotropy," *Physical Review B*, vol. 69, 2004.
- [33] Z. Hou, X. Fu, and Y. Liu, "Singularity of the Bloch theorem in the fluid/solid phononic crystal," *Physical Review B*, vol. 73, 2006.
- [34] J. O. Vasseur, P. A. Deymier, B. Chenni, B. Djafari-Rouhani, L. Dobrzynski, and D. Prevost, "Experimental and Theoretical Evidence for the Existence of Absolute Acoustic Band Gaps in Two-Dimensional Solid Phononic Crystals," *Physical Review Letters*, vol. 86, pp. 3012-3015, 2001.
- [35] F. R. M. d. Espinosa, E. Jiménez, and M. Torres, "Ultrasonic band gap in a periodic two-dimensional composite," *Phys. Rev. Lett.*, vol. 80, p. 1208, 1998.
- [36] W. M. Robertson and J. F. R. III, "Measurement of acoustic stop bands in two-dimensional periodic scattering arrays," *J. Acoust. Soc. Am.*, vol. 104, p. 694, 1998.
- [37] T. Miyashita, "Sonic crystals and sonic wave-guides," *Measurement Science and Technology*, vol. 16, pp. R47-R63, 2005.
- [38] F.-L. Hsiao, A. Khelif, H. Moubchir, A. Choujaa, C.-C. Chen, and V. Laude, "Complete band gaps and deaf bands of triangular and honeycomb water-steel phononic crystals," *Journal of Applied Physics*, vol. 101, p. 044903, 2007.
- [39] S. Yang, J. H. Page, Z. Liu, M. L. Cowan, C. T. Chan, and P. Sheng, "Ultrasound Tunneling through 3D Phononic Crystals," *Physical Review Letters*, vol. 88, 2002.
- [40] A. Khelif, A. Choujaa, S. Benchabane, B. Djafari-Rouhani, and V. Laude, "Guiding and bending of acoustic waves in highly confined phononic crystal waveguides," *Applied Physics Letters*, vol. 84, p. 4400, 2004.
- [41] A. Khelif, A. Choujaa, B. Djafari-Rouhani, M. Wilm, S. Ballandras, and V. Laude, "Trapping and guiding of acoustic waves by defect modes in a full-band-gap ultrasonic crystal," *Physical Review B*, vol. 68, 2003.
- [42] A. Khelif, P. A. Deymier, B. Djafari-Rouhani, J. O. Vasseur, and L. Dobrzynski, "Two-dimensional phononic crystal with tunable narrow pass band: Application to a waveguide with selective frequency," *Journal of Applied Physics*, vol. 94, p. 1308, 2003.
- [43] S. Benchabane, A. Khelif, A. Choujaa, B. Djafari-Rouhani, and V. Laude, "Interaction of waveguide and localized modes in a phononic crystal," *Europhys. Lett.*, vol. 71, p. 570, 2005.
- [44] F. V. D. Biest, A. Sukhovich, A. Tourin, J. H. Page, B. A. v. Tiggelen, Z. Liu, *et al.*, "Resonant tunneling of acoustic waves through a double barrier consisting of two phononic crystals," *Europhysics Letters (EPL)*, vol. 71, pp. 63-69, 2005.
- [45] S. Yang, J. H. Page, Z. Liu, M. L. Cowan, C. T. Chan, and P. Sheng, "Focusing of Sound in a 3D Phononic Crystal," *Physical Review Letters*, vol. 93, 2004.
- [46] M. Ke, Z. Liu, C. Qiu, W. Wang, J. Shi, W. Wen, *et al.*, "Negative-refraction imaging with two-dimensional phononic crystals," *Physical Review B*, vol. 72, 2005.

Reference

- [47] R. H. O. III and I. El-Kady, "Microfabricated phononic crystal devices and applications," *Measurement Science and Technology*, vol. 20, p. 012002, 2009.
- [48] L. Dhar and J. A. Rogers, "High frequency one-dimensional phononic crystal characterized with a picosecond transient grating photoacoustic technique," *Applied Physics Letters*, vol. 77, p. 1402, 2000.
- [49] C. W. W. J, J. U, F. G, and S. N, "Observation and tuning of hypersonic bandgaps in colloidal crystals," *Nat. Mater.*, vol. 5, p. 830, 2006.
- [50] S. Mohammadi, A. A. Eftekhar, W. D. Hunt, and A. Adibi, "High-Q micromechanical resonators in a two-dimensional phononic crystal slab," *Applied Physics Letters*, vol. 94, p. 051906, 2009.
- [51] P. E. Hopkins, C. M. Reinke, M. F. Su, R. H. Olsson, E. A. Shaner, Z. C. Leseman, *et al.*, "Reduction in the thermal conductivity of single crystalline silicon by phononic crystal patterning," *Nano Lett*, vol. 11, pp. 107-12, Jan 12 2011.
- [52] B. Kim, J. Nguyen, C. Reinke, E. Shaner, C. T. Harris, I. El-Kady, *et al.*, "Thermal conductivity manipulation in lithographically patterned single crystal silicon phononic crystal structures," in *Ultrasonics Symposium (IUS), 2011 IEEE International*, Orlando, 2011, pp. 1308-1311.
- [53] M. Ziaei-Moayyed, M. F. Su, C. Reinke, I. F. El-Kady, and R. H. O. III, "Silicon carbide phononic crystal cavities for micromechanical resonators," in *Micro Electro Mechanical Systems (MEMS), 2011 IEEE 24th International Conference on*, Cancun, 2011, pp. 1377-1381.
- [54] S. Hemon, A. Akjouj, A. Soltani, Y. Pennec, Y. E. Hassouani, A. Talbi, *et al.*, "Hypersonic band gap in an AlN-TiN bilayer phononic crystal slab," *Applied Physics Letters*, vol. 104, p. 063101, 2014.
- [55] S. Benchabane, A. Khelif, J. Y. Rauch, L. Robert, and V. Laude, "Evidence for complete surface wave band gap in a piezoelectric phononic crystal," *Physical Review E*, vol. 73, 2006.
- [56] K. Kokkonen, M. Kaivola, S. Benchabane, A. Khelif, and V. Laude, "Scattering of surface acoustic waves by a phononic crystal revealed by heterodyne interferometry," *Applied Physics Letters*, vol. 91, p. 083517, 2007.
- [57] S. Benchabane, L. Robert, G. Ulliac, S. Queste, A. Khelif, and V. Laude, "Lithium Niobate surface structuration for phononic crystal fabrication.pdf," in *IEEE International Ultrasonics Symposium Proceedings*, 2008, p. 2201.
- [58] Y. M. Soliman, M. F. Su, Z. C. Leseman, C. M. Reinke, I. El-Kady, and R. H. Olsson, "Phononic crystals operating in the gigahertz range with extremely wide band gaps," *Applied Physics Letters*, vol. 97, p. 193502, 2010.
- [59] R. H. Olsson, I. F. El-Kady, M. F. Su, M. R. Tuck, and J. G. Fleming, "Microfabricated VHF acoustic crystals and waveguides," *Sensors and Actuators A: Physical*, vol. 145-146, pp. 87-93, 2008.
- [60] R. H. O. III, S. X. Griego, and I. El-Kady, "Ultra high frequency (UHF) phononic crystal devices operating in mobile communication bands," in *Ultrasonics Symposium (IUS), 2009 IEEE International*, Rome, 2009, pp. 1150-1153.

Reference

- [61] R. H. O. III, J. G. Fleming, I. F. El-Kady, M. R. Tuck, and F. B. McCormick, "Micromachined bulk wave acoustic bandgap devices," presented at the Solid-State Sensors, Actuators and Microsystems Conference, 2007. TRANSDUCERS 2007. International, Lyon, 2007.
- [62] Y. M. Soliman, D. F. Goettler, Z. C. Leseman, I. El-Kady, and R. H. O. III, "Effects of release hole size on microscale phononic crystals.pdf," presented at the SEM 2009 Annual Conference & Exposition on Experimental & Applied Mechanics, 2009.
- [63] M. F. Su, R. H. Olsson, Z. C. Leseman, and I. El-Kady, "Realization of a phononic crystal operating at gigahertz frequencies," *Applied Physics Letters*, vol. 96, p. 053111, 2010.
- [64] C. M. Reinke, M. F. Su, R. H. Olsson, and I. El-Kady, "Realization of optimal bandgaps in solid-solid, solid-air, and hybrid solid-air-solid phononic crystal slabs," *Applied Physics Letters*, vol. 98, p. 061912, 2011.
- [65] S. Mohammadi, A. A. Eftekhari, A. Khelif, W. D. Hunt, and A. Adibi, "Evidence of the existence of complete phononic band gaps in phononic crystal plates," *NSTI-Nanotech*, vol. 3, p. 481, 2008.
- [66] T.-W. Liu, Y.-C. Tsai, Y.-C. Lin, T. Ono, S. Tanaka, and T.-T. Wu, "Design and fabrication of a phononic-crystal-based Love wave resonator in GHz range," *AIP Advances*, vol. 4, p. 124201, 2014.
- [67] B. Wu, A. Kumar, and S. Pamarthy, "High aspect ratio silicon etch: A review," *Journal of Applied Physics*, vol. 108, p. 051101, 2010.
- [68] F. Meseguer, M. Hologado, D. Caballero, N. Benachas, J. Sanchez-Dehesa, C. Lopez, *et al.*, "Rayleigh-wave attenuation by a semi-infinite two-dimensional elastic-band-gap crystal," *PHYSICAL REVIEW B*, vol. 59, p. 12169, 1999.
- [69] Y. Tanaka and S. Tamura, "Surface acoustic waves in two-dimensional periodic elastic structures," *Physical Review B*, vol. 58, pp. 7958-7965, 1998.
- [70] B. Manzanares-Martínez and F. Ramos-Mendieta, "Surface elastic waves in solid composites of two-dimensional periodicity," *Physical Review B*, vol. 68, 2003.
- [71] V. Laude, M. Wilm, S. Benchabane, and A. Khelif, "Full band gap for surface acoustic waves in a piezoelectric phononic crystal," *Physical Review E*, vol. 71, 2005.
- [72] D. M. Profunser, E. Muramoto, O. Matsuda, and O. B. Wright, "Dynamic visualization of surface acoustic waves on a two-dimensional phononic crystal," *Physical Review B*, vol. 80, 2009.
- [73] Y. Achaoui, V. Laude, S. Benchabane, and A. Khelif, "Local resonances in phononic crystals and in random arrangements of pillars on a surface," *Journal of Applied Physics*, vol. 114, p. 104503, 2013.
- [74] Y. Achaoui, A. Khelif, S. Benchabane, L. Robert, and V. Laude, "Experimental observation of locally-resonant and Bragg band gaps for surface guided waves in a phononic crystal of pillars," *Physical Review B*, vol. 83, 2011.
- [75] A. Khelif, Y. Achaoui, and B. Aoubiza, "Locally Resonant Structures for Low Frequency Surface Acoustic Band Gap Applications," vol. 166, pp. 43-59, 2013.

Reference

- [76] S. Yankin, A. Talbi, Y. Du, J. C. Gerbedoen, V. Preobrazhensky, P. Pernod, *et al.*, "Finite element analysis and experimental study of surface acoustic wave propagation through two-dimensional pillar-based surface phononic crystal," *Journal of Applied Physics*, vol. 115, p. 244508, 2014.
- [77] A. Khelif, Y. Achaoui, and B. Aoubiza, "Surface acoustic waves in pillars-based two-dimensional phononic structures with different lattice symmetries," *Journal of Applied Physics*, vol. 112, p. 033511, 2012.
- [78] R. Pourabolghasem, A. Khelif, S. Mohammadi, A. A. Eftekhar, and A. Adibi, "Physics of band-gap formation and its evolution in the pillar-based phononic crystal structures," *Journal of Applied Physics*, vol. 116, p. 013514, 2014.
- [79] R. Pourabolghasem, S. Mohammadi, A. A. Eftekhar, A. Khelif, and A. Adibi, "Experimental evidence of high-frequency complete elastic bandgap in pillar-based phononic slabs," *Applied Physics Letters*, vol. 105, p. 231908, 2014.
- [80] C. Goffaux and J. P. Vigneron, "Spatial trapping of acoustic waves in bubbly liquids," *Physica B*, vol. 296, p. 195, 2001.
- [81] M. M. Sigalas, "Elastic wave band gaps and defect states in two-dimensional composites," *J. Acoust. Soc. Am.*, vol. 101, p. 1256, 1997.
- [82] M. M. Sigalas, "Defect states of acoustic waves in a two-dimensional lattice of solid cylinders," *Journal of Applied Physics*, vol. 84, p. 3026, 1998.
- [83] M. Torres, F. M. d. Espinosa, and J. Aragón, "Ultrasonic Wedges for Elastic Wave Bending and Splitting without Requiring a Full Band Gap," *Physical Review Letters*, vol. 86, pp. 4282-4285, 2001.
- [84] T.-T. Wu, W.-S. Wang, and J.-H. Sun, "A layered SAW device using phononic-crystal reflective gratings," *Ultrasonics Symposium, 2008. IUS 2008. IEEE*, p. 709, 2008.
- [85] M. Maldovan, "Sound and heat revolutions in phononics," *Nature*, vol. 503, pp. 209-17, Nov 14 2013.
- [86] T. Gorishnyy, C. K. Ullal, M. Maldovan, G. Fytas, and E. L. Thomas, "Hypersonic Phononic Crystals," *Physical Review Letters*, vol. 94, 2005.
- [87] J. K. Yu, S. Mitrovic, D. Tham, J. Varghese, and J. R. Heath, "Reduction of thermal conductivity in phononic nanomesh structures," *Nat Nanotechnol*, vol. 5, pp. 718-21, Oct 2010.
- [88] B. Liang, B. Yuan, and J.-c. Cheng, "Acoustic Diode: Rectification of Acoustic Energy Flux in One-Dimensional Systems," *Physical Review Letters*, vol. 103, 2009.
- [89] B. Liang, X. S. Guo, J. Tu, D. Zhang, and J. C. Cheng, "An acoustic rectifier," *Nat Mater*, vol. 9, pp. 989-92, Dec 2010.
- [90] B. Li, "Acoustics: Now you hear me, now you don't," *Nat Mater*, vol. 9, pp. 962-3, Dec 2010.
- [91] S. Narayana and Y. Sato, "Heat Flux Manipulation with Engineered Thermal Materials," *Physical Review Letters*, vol. 108, 2012.

Reference

- [92] H. Zhou, "Etude théorique et expérimentale de système à ondes de surface dans des structures multicouches piézomagnétiques pour des applications en contrôle santé intégré de MEMS par imagerie acoustique non linéaire," 2014.
- [93] N. Gasmi, "Propagation des ondes magnéto-électro-élastiques dans les systèmes multicouches et les cristaux phononiques," 2014.
- [94] A. Pavlova, "Préparation et étude des propriétés des films magnétiques nanostructures pour des applications en dispositifs magneto-acoustiques et spintroniques," 2014.
- [95] S. Yankin, "Surface acoustic waves interaction with systems of topographical irregularities comparable to a wavelength," 2014.
- [96] Q. ROLLAND, "Couplage acoutic-optiques dans les cristaux photoniques et phononiques," 2014.
- [97] S. Benchabane, "Elastic wave guiding and filtering in phononic band gap materials," 2007.
- [98] W. L. Bragg, "The diffraction of chort electromagnetic waves by a crystal," *proceedings of the Cambridge Philosophical Siciety*, vol. 17, pp. 43-57, 1913.
- [99] C. Goffaux and J. Sánchez-Dehesa, "Two-dimensional phononic crystals studied using a variational method: Application to lattices of locally resonant materials," *Physical Review B*, vol. 67, 2003.
- [100] C. Goffaux, J. Sánchez-Dehesa, A. Yeyati, P. Lambin, A. Khelif, J. Vasseur, *et al.*, "Evidence of Fano-Like Interference Phenomena in Locally Resonant Materials," *Physical Review Letters*, vol. 88, 2002.
- [101] C. Goffaux, J. Sánchez-Dehesa, and P. Lambin, "Comparison of the sound attenuation efficiency of locally resonant materials and elastic band-gap structures," *Physical Review B*, vol. 70, 2004.
- [102] M. Hirsekorn, "Small-size sonic crystals with strong attenuation bands in the audible frequency range," *Applied Physics Letters*, vol. 84, p. 3364, 2004.
- [103] M. Hirsekorn, P. P. Delsanto, N. K. Batra, and P. Matic, "Modelling and simulation of acoustic wave propagation in locally resonant sonic materials," *Ultrasonics*, vol. 42, pp. 231-5, Apr 2004.
- [104] R. D. Cook, D. S. Malkus, and M. E. Plesha, *Concepts and Applications of Finite Element Analysis*, 3rd ed., 1989.
- [105] K. H. Huebner and E. A. Thornton, *The Finite Element Method for Engineers*, 2nd ed., 1982.
- [106] D. P. Elford, "Band Gap Formation in Acoustically Resonant Phononic Crystals," 2010.
- [107] S. A. Watson, "NickelElectroplatingSolutions," 1989.
- [108] C. P. Watts, *Trans. Electrochem. Soc.*, vol. 395, p. 29, 1916.
- [109] X. Zhan, H. Tang, Y. Du, A. Talbi, J. Zha, and J. He, "Facile preparation of Fe nanochains and their electromagnetic properties," *RSC Advances*, vol. 3, p. 15966, 2013.

Reference

- [110] H. Tang, X. Zhan, Z. Wu, Y. Du, A. Talbi, and P. Pernod, "Controllable and facile fabrication of Fe nanoparticles/nanochains and their magnetic properties," *Journal of Magnetism and Magnetic Materials*, vol. 377, pp. 472-476, 2015.

Etude et développement de matériaux micro/nano structurés pour l'ingénierie des bandes interdites dans les dispositifs électro-acoustiques à ondes de surface

RESUME

Ce travail porte sur l'étude de matériaux micro/nano structurés permettant l'ingénierie des structures de bande dans le domaine des ondes élastiques. Nous nous sommes intéressés en particulier à l'intégration de ces matériaux dans les dispositifs électro-acoustiques et l'étude de l'interaction avec les ondes acoustiques de surface.

La démarche consiste à mener des simulations par la méthode des éléments finis, pour calculer les structures de bande et les spectres de transmission. Nous avons étudié l'effet des paramètres géométriques et élastiques des micro-plots sur les branches acoustiques représentant les modes de surface. Nous avons ensuite discuté l'effet de la symétrie de l'arrangement sur la polarisation des modes de surface. Nous avons également étudié l'effet de la symétrie sur la sensibilité des modes de surface. Cet effet est représenté par la variation des constantes élastiques et de la densité en fonction de la température.

Sur le plan expérimental, Nous avons élaboré des transducteurs inter-digités sur un substrat piézoélectrique de LiNbO_3 . Nous avons intégré divers cristaux phononiques composés de micro-plots de Ni, obtenues par électro-déposition. Les spectres de transmission ont été mesurés par un analyseur de réseau.

En dehors des cristaux phononiques basés sur des plots du nickel, d'autres structures de micro et nano périodiques ont également été présentées dans ce travail, tel que les cristaux phononiques bidimensionnels à base de plots du silicium, des nanoparticules magnétiques auto-assemblées et des nanofils du nickel électro-déposés à travers des membranes nano-poreuses d'alumine.

Mots-Clés:

- Cristaux phononiques
- Ondes acoustiques de surface
- Bandes interdites
- Résonance locale
- Electro-déposition
- Polarisation
- Micro-plots
- Transducteurs interdigités

Investigation of micro and nano structured materials for acoustic band gaps engineering in electro-acoustic devices

ABSTRACT

This work concerns the study of micro/nano structured materials for the engineering of band structures in the field of elastic waves. We were interested in particular to the integration of these materials in electro-acoustic devices and the study of the interaction with the surface acoustic waves.

The approach is to carry out the simulation using the finite element method to calculate the band structures and the transmission spectra. We studied the effect of geometrical and elastic parameters of micro-pillars on acoustic branches representing surface modes. Then we discussed the effect of the symmetry of the arrangement on the polarization of the surface modes. We also investigated the effect of the symmetry on the sensitivity of surface modes. This effect is represented by the variation of the elastic constants and the density as a function of the temperature.

Experimentally, we have developed interdigital transducers on a piezoelectric substrate of LiNbO_3 . We have fabricated various phononic crystals composed of nickel micro-pillars, obtained by electrodeposition. The transmission spectra were measured by a network analyzer.

Besides the phononic crystals based on nickel pillars, some other periodic micro/nano structures were also involved in this work, such as two dimensional silicon pillar-based phononic crystals, self-assembled magnetic nanoparticles and nickel nanowires electroplated through nano-porous alumina membranes.

Keywords:

- Phononic crystals
- Surface acoustic waves
- Band gaps
- Local resonance
- Electroplating
- Polarization
- Micro-pillars
- Interdigital transducers